



UNIVERSITÄT ZU LÜBECK

From the Institute of Biomedical Optics  
of the University of Lübeck  
Director: Prof. Dr. Alfred Vogel

**„Enhanced metabolic quantification of cells and  
tissue by label-free fluorescence lifetime imaging  
microscopy“**

Dissertation  
for Fulfillment of  
Requirements  
for the Doctoral Degree  
of the University of Lübeck

from the Department of Natural Sciences

Submitted by

Michael Evers  
from Wismar

Lübeck 2019





Chairperson:	Prof. Dr. Thomas Peters
First referee:	Prof. Dr. Reginald Birngruber
Second referee:	Prof. Dr. Christian Hübner
Guest referee:	Prof. Dr. Dieter Manstein
Date of oral examination:	Lübeck, June 18 <sup>th</sup> 2019
Approved for printing:	Lübeck, June 21 <sup>st</sup> 2019

## **Statutory Declaration**

I declare that I have authored this thesis independently, that I have not used other than the declared sources / resources, and that I have explicitly marked all material which has been quoted either literally or by content from the used sources.

---

(Michael Evers)  
Lübeck 2019

**Abstract** Metabolic analysis of heterogeneous cell cultures and complex tissues carries many analytical difficulties using current evaluation methods due to their procedural limitations, destructive nature, and lack of visual information. Therefore, the objective of this work was to use fluorescence lifetime imaging microscopy (FLIM) of intrinsic fluorophores such as nicotinamide adenine dinucleotide (NADH) for label-free quantification of metabolic activity. Two-photon FLIM experiments were carried out to measure metabolic changes in response to various external stimuli of individual cells, cell cultures, and tissues over time. Special focus was on adipocyte metabolism and increasing its energy expenditure which make it a desirable prospect for treating obesity and related disorders. Expanding from the traditional two-lifetime model of NADH to a four-lifetime model using exponential fitting and phasor analysis of the fluorescence decay results in an increased dynamic range to metabolic changes and a superior metabolic assessment as compared to traditional FLIM analysis. The four lifetime components can be mapped to specific cellular compartments to create a novel optical biomarker named the mitochondrial-cytoplasmic-ratio (MCR) that accurately reflects shifts in mitochondrial and cytoplasmic NADH distribution and binding states. Additionally, the new MCR metric correlates well with the oxygen consumption rate as measured by an extracellular flux analyzer. It therefore provides a highly sensitive, non-destructive, label-free biomarker for real-time quantitative assessment of metabolic activity with subcellular resolution. This widely applicable approach constitutes a powerful tool for studies where monitoring cellular metabolism is of key interest.

---

**Kurzfassung** Die metabolische Analyse heterogener Zellkulturen und komplexer Gewebe weist bei der Verwendung aktueller Bewertungsverfahren erhebliche Einschränkungen auf wie zum Beispiel aufwendige Prozeduren mit teilweise destruktiven Auswirkungen und Mangel an visuellen Informationen. Ziel dieser Arbeit war es daher, Fluoreszenzlebensdauer-Mikroskopie (FLIM) von intrinsischen Fluorophoren wie Nicotinamid-Adenin-Dinukleotid (NADH) zur markierungsfreien Quantifizierung der Stoffwechselaktivität zu verwenden. Zweiphotonen-FLIM-Experimente wurden an einzelnen Zellen, Zellkulturen und Gewebe durchgeführt, um metabolische Veränderungen als Reaktion auf verschiedene äußere Reize zu messen. Besonderer Fokus lag auf dem Fettstoffwechsel und dessen Aktivierung, da der damit verbundene erhöhte Energieverbrauch das Potential zur Behandlung von Fettleibigkeit und damit verbundenen Erkrankungen hat. Die Erweiterung vom traditionellen Zwei-Lebenszeit-Modell von NADH zu einem Vier-Lebenszeit-Modell unter Verwendung von exponentiellem Fitting und der Phasor-Analyse der Fluoreszenzabklingkurve erhöht die Messgenauigkeit und den dynamischen Bereich von metabolischen Veränderungen im Vergleich zu herkömmlichen FLIM-Analysen. Die vier Lebenszeitkomponenten können eindeutig spezifischen zellulären Bereichen zugeordnet werden, wodurch sich ein neuartiger optischer Biomarker mit dem Namen Mitochondrial-Cytoplasmic-Ratio (MCR) erzeugen lässt. Dieser spiegelt die Verschiebungen in der Mitochondrien- und Cytoplasma-NADH-Verteilung und den Bindungszuständen genau wider. Darüber hinaus korreliert das neue MCR-Verhältnis gut mit der Sauerstoffverbrauchsrate, die von einem extrazellulären Fluxanalysator gemessen wurde. Das Verhältnis bietet daher einen hochempfindlichen, zerstörungs- und markierungsfreien Biomarker zur quantitativen Bestimmung der Stoffwechselaktivität in Echtzeit mit subzellulärer Auflösung. Diese weitreichend anwendbare Methodik stellt ein leistungsfähiges Instrument für Studien dar, bei denen die Messung des Zellstoffwechsels von zentralem Interesse ist.

# Contents

<b>1</b>	<b>Introduction</b>	<b>1</b>
<b>2</b>	<b>Background</b>	<b>7</b>
2.1	Physical Principles of Fluorescence and Phosphorescence . . . . .	7
2.1.1	Fluorescence . . . . .	7
2.1.2	Multiphoton Fluorescence . . . . .	10
2.1.3	Phosphorescence . . . . .	13
2.1.4	Fluorophores . . . . .	13
2.1.5	Fluorescence Lifetime . . . . .	15
2.2	Fluorescence Lifetime Imaging Microscopy (FLIM) . . . . .	18
2.2.1	Time Domain Lifetime Measurements . . . . .	19
2.2.2	Frequency Domain Lifetime Measurements . . . . .	20
2.2.3	Phosphorescence Lifetime Imaging Microscopy . . . . .	22
2.2.4	Phasor Analysis . . . . .	22
2.2.5	Resolution and Imaging Depth . . . . .	26
2.3	Raman Microscopy . . . . .	28
2.3.1	Spontaneous Raman Microscopy . . . . .	28
2.3.2	Stimulated Raman Scattering Microscopy . . . . .	30
2.4	Cell Metabolism . . . . .	35
2.4.1	Aerobic Cellular Respiration . . . . .	36
2.4.2	Anaerobic Cellular Respiration . . . . .	39
2.4.3	Lipid Metabolism . . . . .	40
2.5	Optical Analysis of Cell Metabolism . . . . .	41
2.5.1	Metabolic Biomarkers NADH and FAD . . . . .	41
2.5.2	Optical Redox Ratio . . . . .	43
2.5.3	Optical Free-to-Bound Ratio . . . . .	44
2.6	Function and Therapeutic Potential of Adipose Tissue . . . . .	45
2.6.1	Anatomy and Physiology of Adipose Tissue . . . . .	45
2.6.2	Activation and Therapeutic Potential of Brown/Beige Fat . . . . .	49
<b>3</b>	<b>Materials and Methods</b>	<b>53</b>
3.1	Optical Methods and Parameters . . . . .	53
3.1.1	Fluorescence Microscopy . . . . .	53
3.1.2	Fluorescence Lifetime Imaging Microscopy . . . . .	53
3.1.3	Raman Scattering Microscopy . . . . .	56

3.1.4	Damage Threshold . . . . .	60
3.1.5	Photobleaching . . . . .	61
3.1.6	Apoptosis . . . . .	63
3.1.7	Solution and pH Measurements . . . . .	66
3.2	Image Acquisition and Processing . . . . .	67
3.2.1	Lifetime Fitting . . . . .	67
3.2.2	Instrument Response Function . . . . .	70
3.2.3	Phasor Analysis . . . . .	74
3.2.4	Multi-Harmonic Phasor Analysis . . . . .	76
3.2.5	Phasor Calibration . . . . .	78
3.2.6	NADH FLIM Phasor . . . . .	79
3.2.7	Region of Interest Selection . . . . .	80
3.2.8	Spatial and Temporal Binning . . . . .	81
3.3	Cell Lines and Tissues . . . . .	83
3.3.1	Murine Adipocytes . . . . .	83
3.3.2	Murine White and Brown Adipose Tissue . . . . .	84
3.3.3	HEK 293 Cultures . . . . .	85
3.3.4	3T3-L1 Fibroblast . . . . .	85
3.3.5	Mixed Cell Cultures . . . . .	85
3.3.6	Human Skin Equivalent . . . . .	86
3.4	Quantitative Analysis of Cell Metabolism . . . . .	86
3.4.1	Western Blotting . . . . .	86
3.4.2	Cellular Respiration and Extracellular Acidification . . . . .	87
<b>4</b>	<b>Results</b>	<b>93</b>
4.1	NADH Lifetime Solution Experiments . . . . .	93
4.1.1	Temperature and Solvents . . . . .	93
4.1.2	Concentration . . . . .	93
4.1.3	Binding Enzymes . . . . .	95
4.1.4	Reagents . . . . .	97
4.2	NADH Lifetime Analysis . . . . .	98
4.2.1	Spatial Binning . . . . .	98
4.2.2	Temporal Binning . . . . .	100
4.2.3	Lifetime Localization . . . . .	101
4.2.4	Isolated Mitochondria . . . . .	102
4.2.5	Detection of Lipids and Lipofuscin . . . . .	105
4.2.6	Mitochondrial Movement . . . . .	106
4.2.7	NADH Phasor Plot . . . . .	108
4.3	Assessment of Metabolic Activity . . . . .	109
4.3.1	Mitochondrial Cytoplasmic Ratio . . . . .	109
4.3.2	Mitochondria Stress Test - Individual Injections . . . . .	109
4.3.3	Mitochondria Stress Test - Consecutive Injections . . . . .	112

4.3.4	Glycolysis Stress Test . . . . .	113
4.3.5	Redox Ratio . . . . .	115
4.3.6	Browning of Adipocytes . . . . .	118
4.4	Quantification of the new MCR Metric . . . . .	119
4.4.1	MCR of Adipocytes . . . . .	119
4.4.2	Mixed Cell Cultures . . . . .	121
4.4.3	MCR of HEK cells . . . . .	122
4.5	Adipose Tissue . . . . .	126
4.5.1	Epididymal, Inguinal, and Interscapular Mouse Fat . . . . .	126
4.5.2	Storage Influence on Fluorescence Lifetime . . . . .	128
4.5.3	Metabolic Changes of Tissue . . . . .	130
4.5.4	Wound healing of Human Skin Equivalent . . . . .	133
<b>5</b>	<b>Discussion</b>	<b>135</b>
5.1	NADH Lifetime Parameters and Localization . . . . .	135
5.2	MCR of Adipocytes, HEK 293 Cells, and Tissue . . . . .	141
5.3	Tissue Preparation, Imaging, and Wound Healing . . . . .	147
<b>6</b>	<b>Conclusion</b>	<b>149</b>
<b>7</b>	<b>Outlook</b>	<b>151</b>
<b>8</b>	<b>Abbreviations</b>	<b>155</b>
	<b>Resume</b>	<b>183</b>
	<b>Publications and Presentations</b>	<b>185</b>
	<b>Acknowledgements</b>	<b>187</b>





# 1 Introduction

The past couple of decades have seen an increasing interest in the development of a wide range of new optical biomarkers and imaging techniques for biomedical diagnostics. These biomarkers represent a powerful tool in bio-photonics, cell biology as well as a new approach for cell sorting, metabolomics and drug screening. These relatively new and hot topic research areas show an increasing need for metabolic studies in real time on a sub-cellular level. Therefore, this thesis has analyzed the role of a relatively limited set of key-molecules of energy metabolism. In this study, we demonstrate the applications of two-photon fluorescence lifetime imaging microscopy in assessment of metabolism in biological samples such as mono-layer cell cultures, fresh tissue as well as tissue engineered skin models. The work presented here, puts special focus on the fluorescence analysis of endogenous fluorophore nicotinamide adenine dinucleotide (NADH) of adipocytes.

## Imaging of NADH as a Metabolic Indicator

NADH is a coenzyme which is crucial for several metabolic pathways, as well as intracellular biosynthesis in living cells. Already in 1954, Chance et al used NADH as a reporter of metabolism in living samples and have proposed promising implications and applications for metabolic analysis [1]. The measurement of NADH was further improved by the development of laser scanning confocal microscopy which allowed for investigation of complex structures by adding spatial resolution [2]. Additionally, in 1992 Lakowicz et al. developed a technique to generate images of cells and tissues, in which the contrast parameter is the fluorescence lifetime [3]. One of the first applications of this fluorescence lifetime imaging microscopy (FLIM) approach was demonstrated on NADH [4]. The fluorescence lifetime of NADH and other fluorophores is sensitive to changes in its local environment which enables quantitative measurements of metabolic changes from inside living systems. Commercial fluorescence lifetime setups for conventional confocal microscopes made fluorescence lifetime imaging commonly available, leading to an increasing number of NADH FLIM studies [5]. Numerous observations of different NADH lifetime characteristics between healthy, abnormal and diseased cells and tissues have been shown and now shifted the focus to the development of clinical and laboratory diagnostic devices [6, 7]. However, few devices and applications have transcended into laboratories

and clinics as the standard tool for bioenergetics since technical challenges and analytical difficulties of quantification resulting in conflicting outcomes still remain [8].

NADH acts as an electron carrier, transporting electrons between redox reactions as the principal electron donor in oxidative phosphorylation and electron acceptor in glycolysis. It therefore plays crucial roles in both oxidative metabolism and glycolysis and monitoring its auto-fluorescence is useful as an indicator of metabolic activity and mitochondrial function [9]. While NADH is fluorescent, its oxidized counterpart,  $\text{NAD}^+$ , is not. Using two photon microscopy, NADH can be excited within the 710 to 780 nm range which enables deeper tissue imaging and improved imaging signal-to-noise ratios than one-photon excitation while reducing the potential for light-induced cell damage [10]. Fluorescence lifetime imaging microscopy (FLIM) has been used extensively to analyze NADH via both its fluorescence intensity and lifetime. Within the cell, NADH can be found as either a free molecule or bound as a cofactor to a variety of enzymes [10].

FLIM has been used extensively to analyze NADH via both its fluorescence intensity and lifetime. Within the cell, NADH can be found as either a free molecule or bound as a cofactor to a variety of enzymes [10]. While the fluorescence spectrum of free and bound NADH is very similar, the lifetimes of these species differ significantly. Free NADH in solution has two fluorescence lifetime components, which can be attributed to a folded and extended conformation of the molecule. Binding to an enzyme prolongs the fluorescence lifetime of NADH, and this lifetime varies slightly for each of NADH's multiple binding partners [11]. While traditional assessment of NADH only shows two fluorescence lifetimes components, one free and one bound, recent studies in cancer cells and cerebral tissue suggest that there are likely four distinct NADH species [9, 12]. The NADH fluorescence decay can be modeled as the sum of two or more decaying exponentials, with each term representing a different conformation or enzymatic bound formulation of NADH [9].

An alternative method of analyzing lifetime data is the Fourier-based phasor approach, which calculates phasor coordinates describing the fluorescence decay [13]. These methods can be used for distinguishing dynamic changes in metabolism with much higher specificity than traditional methods. In this study, the phasor approach to FLIM analysis of NADH was applied to verify results gathered by exponential fitting models and to simplify the fluorescence lifetime analysis. The phasor approach to FLIM is a fit-free technique which does not require a priori knowledge of the fluorescent species in the sample [14]. However, interpretation of phasor plots composed of more than two fluorescence lifetime species exposed difficulties. Therefore, a new analysis methodology using a combination of segmentation of exponentially derived

---

lifetime histograms and the phasor approach was introduced in this thesis. Using this technique, the potential of the NADH FLIM-phasor approach to differentiate metabolic states at the single-cell level was demonstrated. The FLIM-phasor plots capture information about metabolic activity and demonstrate that this method can provide distinct and nuanced information about metabolic states. Nevertheless, a complete understanding of the underlying biochemical processes that are observed during FLIM imaging of NADH is required for an accurate interpretation.

This thesis provides both an introduction to the field of NADH fluorescence imaging and an overview of the relevant biochemical pathways required to interpret the data that such experiments generate. Primary mechanisms of NADH production and consumption are discussed as well as introduction of basic photo-physics and practical considerations of NADH fluorescence applications for metabolic imaging and how the specific findings of this dissertation can be used to improve future label free metabolic imaging for individual cells..

## **Assessment of Adipose Tissue Function**

In this study, NADH fluorescence lifetime measurements are mainly applied on adipocytes. Lately, the understanding of fat metabolism has become more important as the number of obese children and adults has increased dramatically worldwide over the past three decades [15]. Obese individuals have an increased risk of developing numerous diseases, such as hypertension, hyperglycemia, type 2 diabetes and many forms of cancer [15, 16]. This obesity epidemic is driving a demand for innovative and effective treatments for the condition. In the human body, there are at least three types of fat cells with distinctive specialized metabolic functions. Excessively accumulated fat is known as white adipose tissue (WAT), whose main function is to store excess energy. WAT can be found in humans mainly intra-abdominally (visceral) and subcutaneously, while smaller deposits are found throughout the human body [17]. White adipose cells are structured with a single large lipid droplet and contain few mitochondria. In contrast, brown adipose tissue (BAT) is specialized to dissipate energy as heat through nonshivering thermogenesis and is mostly found in the neck and shoulder areas (cervical, supraclavicular, axillary, and paravertebral regions) [18]. Brown adipocytes contain multilocular lipid droplets and many mitochondria that contain the BAT-specific protein known as uncoupling protein 1 (UCP1). UCP1 plays an important role in increasing energy expenditure through the uncoupling of oxidative phosphorylation from adenosine triphosphate (ATP) production, which leads to heat generation [19, 20].

While a clear anatomical difference can be drawn between WAT and BAT, the cellular origin of the recently discovered beige adipose tissue (BeAT) has not been completely clarified. Beige fat consists of brown-like adipocytes that are mainly found in subcutaneous white fat depots and share many characteristics of BAT, such as enriched mitochondria, multiple lipid droplets, and expression of UCP1. Activation and recruitment of brown and beige adipocytes by various stimuli, including mild cold exposure, increases lipolysis and upregulates UCP1 causing increased whole-body energy expenditure [18]. Therefore, brown and beige adipocytes are promising therapeutic targets to reduce obesity, and numerous research groups are investigating the effects leading to their activation [20].

Even though the interest in this field of research is growing rapidly, traditional methods have great difficulty in detecting the activation of beige and brown fat within a heterogeneous environment. A recent publication by Alonzo et al. showed, for the first time, the use of two-photon excited fluorescence (TPEF) microscopy to distinguish WAT from BAT [21]. Our goal was to further investigate the potential of label-free TPEF microscopy to quantify changes in adipose metabolism and activation of brown and beige adipocytes with subcellular-resolution. One approach is the optical detection of the metabolic co-factor nicotinamide adenine dinucleotide (NADH), which allows for non-invasive functional imaging of cellular metabolism and has been used to monitor a wide variety of cells, tissues, and organs in vitro as well as in vivo [22].

Here we present our results using FLIM to investigate heterogeneous changes in NADH activity of adipocytes. We hypothesize that different enzymatic binding states and free-to-bound ratios detected by FLIM might be used as specific biomarkers of molecular pathways associated with glycolysis or oxidative phosphorylation. To test this theory and create a new method for assessing cellular metabolism and metabolic changes, NADH fluorescence lifetime data was acquired while cells were treated with a range of pharmacological agents known to affect key cellular metabolic processes. In particular, changes in NADH were studied following pharmacological alteration of mitochondrial respiration and cellular acidification. Switching from the traditional two-lifetime model of NADH to a four-lifetime model and locating the four lifetime components to specific cellular components allows for the analysis of mitochondrial and cytosolic NADH concentration resulting in superior metabolic assessment compared to traditional FLIM analysis. Additionally, it was evaluated whether changes in fluorescence lifetime correlate with gene expression of BAT- and BeAT-related markers such as UCP1. By understanding how the fluorescence lifetime can be related to specific metabolic pathways of white and brown fat, this study provides an imaging toolkit for future investigations and a valuable research tool in obesity research. It is noteworthy that as the energy metabolism of cells

---

is linked to their functional and physiological state, the ability to probe the energy metabolism of individual cells can provide meaningful insights in the real time study of cellular function. This ability proves especially useful in immunology and oncology where individual cells such as activated immune cells and cancer cells have changed metabolism.

In addition to differences in metabolism of adipocyte cell cultures, metabolic differences exist between individual cells as well as mixed cellular populations. The current gold standard for measuring cellular metabolism, the Seahorse XF flux analyzer assay, was compared to FLIM measurements. The flux analyzer directly quantifies oxidative phosphorylation (OXPHOS) through the measurement of oxygen consumption rate (OCR), and measures glycolytic function by determining the extracellular acidification rate (ECAR) in the culture media surrounding the cells. Induced cellular metabolic changes through pharmacological injections consisted of glycolysis as well as respiratory inhibitors and maximizers. NADH FLIM data from adipocytes and HEK 293 cells were compared to flux analyzer derived OCR data and showed a strong correlation. These results suggest that NADH FLIM can be used to predict metabolic respiration of individual cells in pure and mixed cell populations. FLIM's ability to measure cellular metabolic states in combination with visual information and spatial resolution makes it an ideal tool for studying cellular heterogeneity. Besides cell cultures, ex-vivo tissue and 3D engineered tissue were also investigated using the FLIM analysis methodology since tissue analysis is an important and rapidly developing area of modern therapeutic and regenerative applications [23]. Therefore, freshly excised WAT, scWAT, and BAT depots were analyzed by FLIM and an extracellular flux analyzer. Additionally, preliminary data of functional skin equivalents were analyzed as it has been shown to be a promising field of research since fluorescence lifetime distribution can be used to diagnose several skin diseases and abnormalities such as inflammation, cancer, and psoriasis [24]. The results of this work are suitable to improve projects that investigate the role of metabolic activity for such applications.



## 2 Background

### 2.1 Physical Principles of Fluorescence and Phosphorescence

#### 2.1.1 Fluorescence

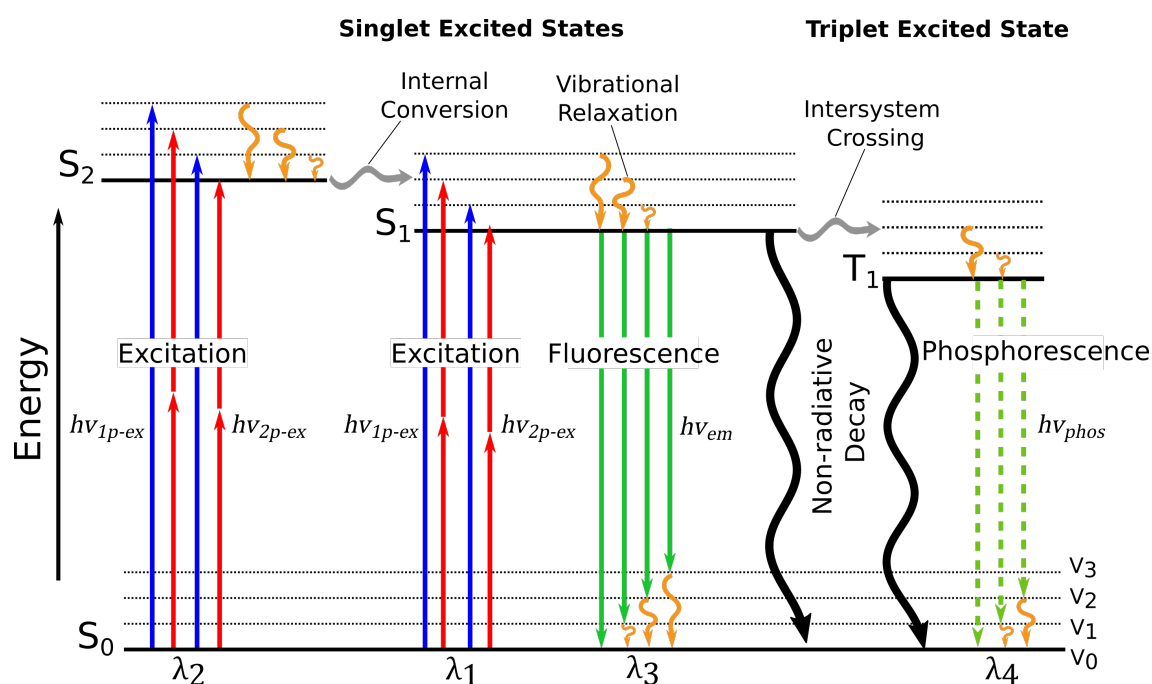


**Figure 2.1:** Jablonski energy diagram illustrating the transitions between electronic states of a molecule for the processes of fluorescence and phosphorescence. Waved lines mark non-radiative transitions such as internal conversion and vibrational relaxation. Fluorophores that absorb one or multiple photons can get excited to a higher vibrational energy level in the excited state such as  $S_1$  and  $S_2$ . Once the fluorophore reaches its lowest vibrational level of the first excited state it releases the energy by radiative decay as fluorescence or by non-radiative relaxation as heat. For phosphorescence the electron undergoes a spin conversion into a "forbidden" triplet state  $T_1$ . Emission from the triplet state occurs with lower energy relative to fluorescence, hence emitted photons have longer wavelengths.

## 2 Background

---

Fluorescence is a phenomenon which can be described as the excitation of a molecule by absorption of a photon and its de-excitation by spontaneous emission of another photon of a longer wavelength, typically within a few nanoseconds after excitation. The process of fluorescence can be described by the Jablonski diagram (Fig. 2.1). An orbital electron of a molecule in its lowest singlet electronic state ( $S_0$ , ground state) absorbs the energy ( $hv_{1p-ex}$ ) of a single photon to go to one of its higher singlet electronic states ( $S_n$ , excited state). The Energy  $E$  can be expressed as the frequency  $v$  of the photons by the Planck relation  $E = hv$  with  $h$  as the Planck's constant. Each of the electronic states is subdivided into several vibrational energy levels. At room temperature, most molecules exist on the lowest vibrational level ( $V_0$ ) of the ground state ( $E_0$ ), and thus, in order to induce the transition to the excited state, the energy of the absorbed photon has to match the difference in the energy levels of  $V_0$  in  $E_0$  and some vibrational level ( $V_n$ ) in an excited state ( $E_n$ ).

$$hv_{1p-ex} \geq E_1V_0 - E_0V_0 \quad (2.1)$$

Where  $hv_{1p-ex}$  represents the energy of the absorbed photon with  $h$  as the Planck's constant and  $v$  as the frequency. Due to several excited states and vibrational levels, the fluorophore can be excited by a continuous range of wavelengths, which is called the absorption spectrum (blue arrows in Fig. 2.1). Any molecule in its excited energy state is not stable and will return to the ground state, emitting the absorbed energy by various pathways [25]. Vibrational relaxation is one of these pathways bringing the excited fluorophores energy back to the lowest vibrational level of  $S_1$ . Non-radiative processes such as vibrational relaxation and internal conversion are indicated by wavy arrows in the Jablonski diagram. During internal conversion, a radiationless de-excitation, a molecule in the ground vibrational level of an excited electronic state passes directly into a high vibrational energy level of a lower excited state. Once the fluorophore reaches its lowest vibrational level of the first excited state it releases the energy by radiative decay as emission of a photon (fluorescence) or by non-radiative relaxation as heat. Molecules usually return to their ground state by the fastest mechanism, which is why fluorescence is only observed if it is a more efficient way of relaxation than the combination of the non-radiative processes. Low temperature and high viscosity lead to enhanced fluorescence due to the reduced number of collisions between molecules, thus reducing the possibility of radiationless de-excitation. Due to loss of energy during vibrational relaxation and internal conversion, emitted photons have lower energy ( $hv_{em}$ ) and longer wavelengths than the excitation photons. The fluorescent transition of the lowest vibrational level of the first excited electronic state to any vibrational level of the ground state produces photons of several wavelengths, called the emission spectrum (red arrows in Fig. 2.1). The difference between absorption maxima and emission maxima with its longer wavelength of lower energy is called Stoke's shift (Fig. 2.2). While in most



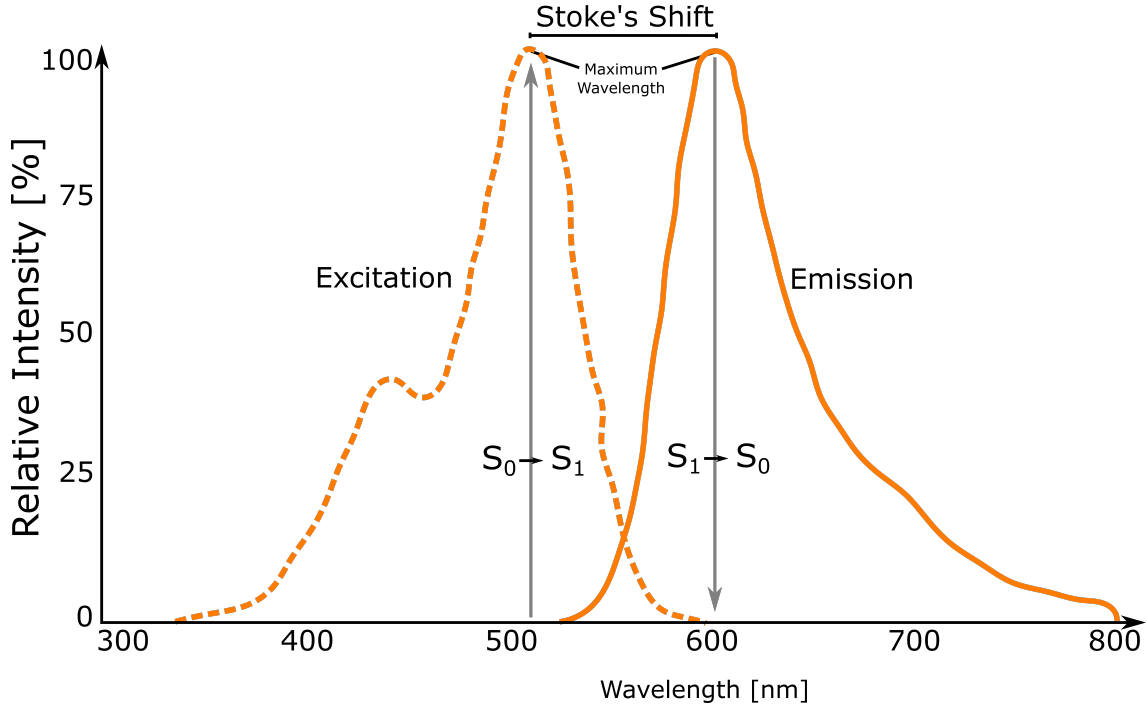


**Figure 2.2:** Exemplary Stokes shift schematic of the fluorophore tetramethylrhodamine, ethyl ester (TMRE). The Stokes shift is the difference in wavelength between the excitation and emission maxima of the same electronic transition. The magnitude of the Stokes shift is determined by the electronic structure of the fluorophore as well as the environment and protein binding state.

cases, radiative decay occurs from the lowest vibrational level of the excited state  $S_1$  to the ground state, some rare exceptions exist where fluorescence occurs from higher excited states. The emission spectrum tends to have a similar and mirrored shape to the absorption spectrum since the probability  $P$  of reaching the  $n$ th vibrational level of an excited state during excitation matches the probability of reaching the  $n$ th vibrational level of the ground state during relaxation [3].

$$P([S_0, V_0] \rightarrow [S_1, V_n]) \approx P([S_1, V_0] \rightarrow [S_0, V_n]) \quad (2.2)$$

It is worth mentioning that due to vibrational relaxation the emission spectrum is usually independent of the excitation wavelength [26]. The Stoke's shift plays a crucial role in the heating of the active laser media. Three-level laser systems have high lasing thresholds, low Stoke's losses (difference between pump energy and emission energy), and a reduced heat production [27]. On the other hand, four-level laser systems have lower lasing thresholds, higher Stoke's losses, and higher heat production. For fluorophores, the Stoke's shift can be used for spectral analysis to rapidly recognize spectral fingerprints as it changes depending on emission wavelength as

well as the fluorophore environment such as temperature, pH-value, and viscosity [28].

### 2.1.2 Multiphoton Fluorescence

Multiphoton excitation of molecules is a nonlinear process of simultaneous absorption of two or more photons. The combined energy of these photons is sufficient to induce a molecular transition to an excited electronic state. Since the energy of a photon is inversely proportional to the wavelength, the absorbed photons during multiphoton excitation must have a significantly longer wavelength as for one photon excitation. This means that a fluorophore which under one-photon techniques is excited by UV or visible light, can be excited by two photons of near-infrared light. Therefore, this technique allows for the use of longer wavelengths, which can be utilized to excite chromophores in a single quantum event and subsequently emit secondary radiation at lower wavelengths. For two-photon excitation of a conventional fluorophore in its lowest singlet electronic state, the energy of two photons ( $h\nu_{2p-ex}$ ) has to be absorbed to go to one of its higher singlet electronic states [29]:

$$2h\nu_{2p-ex} \geq E_1V_0 - E_0V_0 \quad (2.3)$$

In general, these photons have a wavelength around twice as long as for one photon excitation, but many fluorophores have a blue-shifted two-photon excitation which makes it very challenging to theoretically determine the excitation spectrum. The probability for two-photon excitation depends on both spatial and temporal overlap between the incident photons, and therefore high photon densities and a maximum absorption time difference of  $10^{-18}$  seconds are required. Quantum mechanically, the first absorbed photon excites the molecule to a virtual intermediate state in which it can stay for  $10^{-17}$  or 0.01 femtoseconds, and the absorption of the second photon brings it to the final excited state [30].

Interestingly, the photons do not have to be of identical wavelength to induce multiphoton excitation, but most experimental systems are designed with a single laser source and therefore the two excitation photons usually have a narrow wavelength distribution. The number of absorbed photons per fluorophore per pulse can be calculated by [31]:

$$n_a = \frac{p_0^2 \delta}{\tau_p f_p^2} \left( \frac{NA^2}{2\hbar c \lambda} \right)^2 = \frac{p_0^2}{\tau_p f_p^2} \times S \quad (2.4)$$

where  $p_0$  is the average power of the laser pulse train,  $\delta$  the two photon absorption cross section,  $\tau_p$  the pulse width,  $f_p$  the laser repetition rate,  $NA$  the numerical aperture,  $c$  the speed of light,  $\hbar$  the reduced Planck constant and  $\lambda$  the wavelength.

Variable	Symbol	Unit
Number of Absorbed Photons	$n_a$	Photons
Average Power	$p_0$	W
Two Photon Absorption Cross Section	$\delta$	$\text{cm}^4 \text{ s}$
Pulse Width	$\tau_p$	ns
Laser Repetition Rate	$f$	Hz
Numerical Aperture	$NA$	-
Reduced Planck Constant	$\hbar$	J s
Speed of Light	$c$	m/s
Wavelength	$\lambda$	nm
Simplification Factor	$S$	$\text{s/J}^2$

**Table 2.1:** Variables and symbols for calculating the number of absorbed photons per pulse per fluorophore in Eq. 2.4

With the simplification factor  $S = \delta \left( \frac{NA^2}{2\hbar c \lambda} \right)^2$ , the assumption of rectangular pulses, and with  $p_0 = p_{peak} \tau_p f_p$  the Eq. 2.4 can be displayed as:

$$n_a = p_{peak}^2 \times \tau_p \times S \quad (2.5)$$

While the fluorescence intensity and the excitation power have a linear dependency for one photon excitation, it has a quadratic dependence under two-photon excitation. In order to produce significant multiphoton excitation events high-power mode-locked lasers in combination with high numerical aperture objectives are used. These lasers generate short pulses with high peak powers to induce two-photon excitation while still having an average power low enough to not thermally damage the sample. The resulting emission occurs in the same singlet state as that obtained during one-photon emission and is therefore indistinguishable from that as seen in Fig. 2.1. Typically, pulse durations of around 100 fs are used for two-photon excited fluorescence (TPEF) of biological specimen. Literature shows that increasing peak laser power and reduction of the pulse duration while maintaining average laser power improves the number of absorbed photons and the signal levels of TPEF [32]. However, increasing peak power results in higher cell damage and therefore might not always be beneficial [33, 32]

Three-photon excitation is another multiphoton and nonlinear optical process which is increasingly used for biomedical experiments. While the photon density required for two-photon excitation ( $> 10^{24} \text{ photons cm}^{-2} \text{ s}^{-1}$ ) has to be a million-fold greater than the density needed for one-photon excitation, due to quantum-mechanical properties the energy density for three-photon excitation only has to be 10-fold higher than for two-photon excitation [34, 29]. A benefit of three-photon excitation is that often the same laser setup can be used as for two photon excitations while it can

penetrate deeper into highly scattering tissue with a higher axial resolution since the excitation volume along the axial direction is reduced due to a cubic excitation power dependence compared to two photon excitation where there is a quadratic power dependence. Deeper penetration is possible since the photons would be less susceptible to scattering and additionally, three-photon excitation dramatically reduces the out-of-focus background in regions far from the focal plane, improving the signal-to-background ratio by orders of magnitude when compared to two-photon excitation [35]. However, when wavelengths approach the 1300-nm range, water in the specimen begins to absorb the photons, limiting the penetration depth Fig. 2.3. The parameters of a typical setup include a wavelength range from 680 to

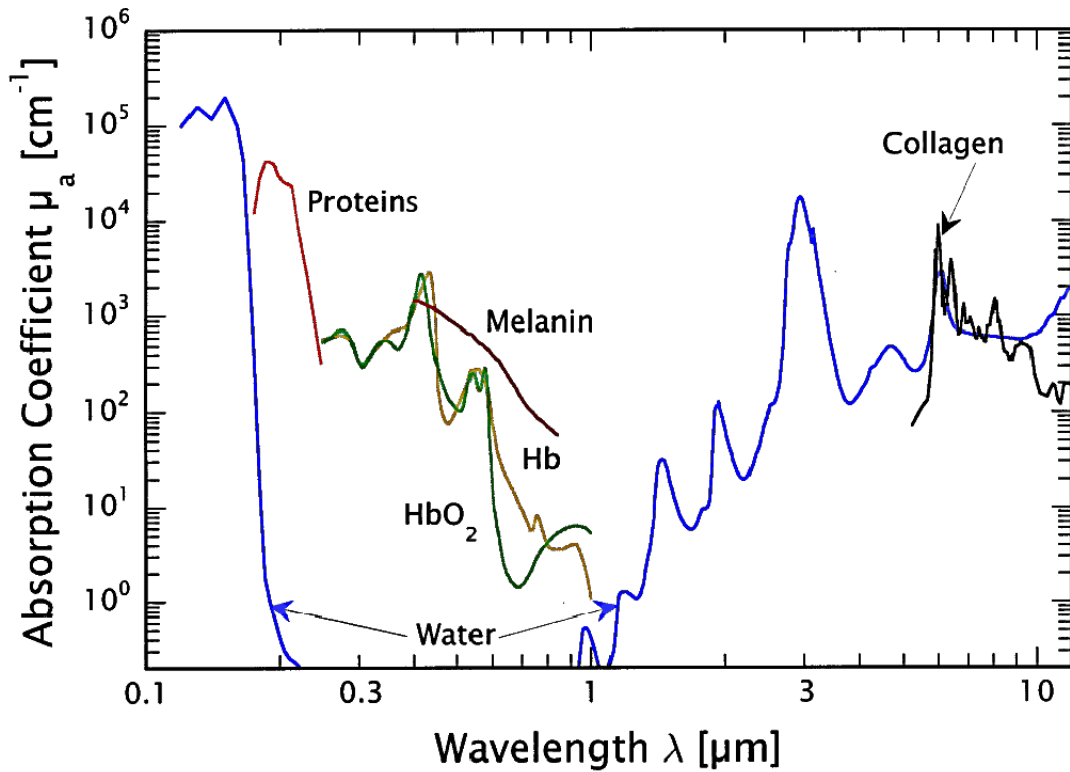


**Figure 2.3:** Optical absorption coefficients  $\mu_a$  of principal soft tissue chromophores are water, proteins, melanin, oxygenated hemoglobin ( $\text{HbO}_2$ ), deoxygenated hemoglobin (Hb), and collagen, in the wavelength range from 100 nm to 10  $\mu\text{m}$  [36]

1100 nm, 80 to 150 fs pulsewidth, 80 to 100 MHz repetition rate, and on sample power of around 1 to 50 mW. This setup allows to induce three-photon excitation at for example 720 nm wavelength of chromophores which usually excite in the UV range at 240 nm. This is an important improvement to the ability of conventional microscopy since ultraviolet wavelengths below approximately 300 nanometers are

very problematic for regular microscope optics. Even though higher-order excitations are theoretically possible and have been demonstrated, it is not clear if there are any advantages to use these techniques for biological imaging [37].

### 2.1.3 Phosphorescence

Intersystem Crossing is a third form of radiationless relaxation in which a molecule in the lowest vibrational level of the first excited state undergoes a transition towards its triplet state (Fig. 2.1). Phosphorescence occurs when a molecule in the lowest excited vibrational level of the triplet state ( $T_1V_0$ ) transitions to the singlet ground state ( $S_0V_n$ ) by emitting a photon. In comparison to the singlet excited state, the triplet excited state is long lived due to the quantum mechanically forbidden nature of this transition. Therefore, phosphorescence can continue to emit photons in the region of milliseconds to seconds after excitation. The  $T_1 \rightarrow S_0$  transition violates the selection rule and is spin forbidden which renders the phosphorescence process to be of low probability and less intense than spin allowed processes such as fluorescence emission. When a quantum mechanical model forbids a transition mathematically, they can still occur in reality. Whether transitions are allowed or forbidden, and to what degree they may be forbidden depends on selection rules such as the spin selection rule. This rule states that the spin on the electron that gets excited has to be the same after excitation as it was before excitation. Another selection rule states electronic transitions that conserve either symmetry or antisymmetry for a molecule are forbidden. Nevertheless, in reality most forbidden transitions have exceptions and for example the symmetry selection rule can be broken by vibrational movement. Therefore, phosphorescence often relies on external stimuli such as vibronic perturbation, thermal activation, and magnetic fields [38]. However, in order for phosphorescence to be favored over other transitions, the system must be protected from other potential mechanisms of de-excitation. Intermolecular collisions or the presence of dissolved oxygen causes quenching, which lowers the efficiency of the phosphorescence process. Additionally, since external and internal conversion effectively reduce phosphorescence, the molecule quantum yields are higher at lower temperature in highly viscous media to protect the triplet state.

### 2.1.4 Fluorophores

Biological laser scanning microscopy relies heavily on fluorescence as an imaging method, primarily due to high sensitivity of the technique coupled with the ability to specifically target structural components and dynamic processes in chemically fixed as well as living cells and tissues. Fluorophores are chemical compounds capable of absorbing and re-emitting photons through fluorescence. Fluorophores that

## 2 Background

are naturally found in biological samples are termed intrinsic or endogenous while fluorophores that are used to artificially produce fluorescence are called extrinsic. Intrinsic fluorophores such as aromatic amino acids, collagen, flavin adenine dinucleotide (FAD) and nicotinamide adenine dinucleotide (NADH) can be used as natural indicators to study the structure, the dynamics, and the metabolism of living cells without altering the cells environment Table 2.2. Fluorescence microscopy and metabolic analysis of a single fluorophore in samples such as skin which contain several fluorophores can be challenging as their emission and excitation spectra overlap. Therefore, changes in fluorescence intensity and lifetime can have several metabolic or morphological reasons and one has to be careful with the choice of excitation wavelength and bandwidth of detection filters.

Endogenous fluorophore	Excitation maxima [nm]	Emission maxima [nm]
<b>Amino acids</b>		
Tryptophan	280	350
Tyrosine	275	300
Phenylalanine	260	280
<b>Structure proteins</b>		
Collagen	360	405
Elastin	290,325	340,400
<b>Enzyme and coenzymes</b>		
FAD	450	535
NADH	290,350	460
<b>Lipids</b>		
Phospholipids	436	540,560
Lipofuscin	340-395	540, 430-460

**Table 2.2:** Common endogenous fluorophores at the 1-photon excitation wavelength range from 250 to 450 nm [39]

Extrinsic fluorophores are inserted into samples and are designed to bind with specific biological macromolecules or structures for monitoring of localization, dynamic processes, or cellular integrity. Fluorescent probes such as rhodamine, fluorescein and numerous other substances are described according to their absorption and fluorescence properties including spectral profiles, wavelengths, fluorescence intensity, molar attenuation coefficient and quantum yield. The quantum yield  $\phi_F$  is especially important for both, intrinsic and extrinsic fluorophores, since it describes a quantitative measure of fluorescence efficacy [40].

$$\phi_F = \frac{\text{number of emitted photons}}{\text{number of absorbed photons}} \quad (2.6)$$

The quantum yield can range from 1, when every absorbed photon results in an emitted photon, to 0 when fluorescence does not occur. In general, a high quantum yield is desirable in most microscopic applications. The fluorescence quantum yield can be related to the fluorescence lifetime  $\tau$  by [41, 42]

$$\phi_F = \frac{k_r}{k_r + k_{nr}} = k_r \tau \quad (2.7)$$

Where  $k_r$  is the radiative decay rate which mostly depends on the chemical structure of the fluorophore whereas the non-radiative decay rate  $k_{nr}$  varies, sometimes to large degrees, with environmental factors such as temperature, pH, and viscosity [43, 44]. The earlier mentioned molar attenuation coefficient measures how strongly a chemical species attenuates light at a given wavelength  $\lambda$ .

The Beer-Lambert law describes the exponential decrease in intensity of light as a function of sample thickness  $d$ , and concentration  $c$ , as it passes through a sample [45]:

$$\varepsilon cd = \log_{10} \left( \frac{I_0}{I} \right) \quad (2.8)$$

Where  $I$  and  $I_0$  are the intensities of the transmitted and incident light, respectively, and  $\varepsilon$  is the molar attenuation coefficient. The conversion of the molar attenuation coefficient to the absorption cross section  $\sigma$  is solely a unit conversion. Therefore,  $\varepsilon$  expressed in units  $Lmol^{-1}cm^{-1}$  can be directly converted to  $\sigma$  in units of  $cm^2$  via the Avogadro constant  $N_A$  [3]:

$$\sigma = 1000 \ln(10) \frac{\varepsilon}{N_A} \quad (2.9)$$

### 2.1.5 Fluorescence Lifetime

Fluorescence lifetime is defined as the average time an excited molecule needs to return to the ground state. In a time-resolved measurement, the fluorescence intensity is recorded rather than the number of excited fluorophores [3]. Mostly, their relationship is proportional and in the simplest case of a mono-exponential decay

## 2 Background

---

function, the lifetime  $\tau$  is the time it takes for the intensity  $I(t)$  to decrease to  $1/e$  or 36.85% of the maximum intensity value  $I_0$ . The intensity at time  $t$  is given by:

$$I(t) = I_0 e^{\frac{-t}{\tau}} \quad (2.10)$$

For more complicated samples that have several fluorescent components and therefore follow a multi-exponential decay, the decay equation takes the form:

$$I(t) = \sum_i \alpha_i e^{\frac{-t}{\tau_i}} \quad (2.11)$$

Where  $\alpha$  is the pre-exponential factor. When  $I(t)$  is normalized to a peak value of 1, the sum of the lifetime components weight is  $\sum \alpha_i = 1$ . However, in reality the experimentally measured fluorescence decay signal  $I_{exp}(t)$  includes the fluorescence decay convolved with the instrument response function  $IRF(t)$  [3, 46].

$$I_{exp}(t) = IRF(t) \otimes I(t) \quad (2.12)$$

Where  $I_{exp}(t)$  can be described as the histogram of detected photons and the IRF is the response of the system to the excitation laser pulse. The IRF of a system depends on several parameters by the excitation- and the detection-system such as excitation pulse, cable length, and electronics. For the experimental measurement of the IRF, the excitation laser pulse can be detected or an instantaneous event such as second-harmonic generation or Hyper-Rayleigh scattering [47]. Both methods deliver ultrafast signals at a wavelength detectable by the FLIM system.

However, the convolution integral cannot be reversed, meaning that there is no analytical expression of  $I(t)$  for a given  $I_{exp}(t)$  and  $IRF(t)$ . Therefore, the standard approach to solve the deconvolution is through iterative reconvolution of a predicted model function such as a 1, 2, or 3 component exponential decay. Meaning that the convolution of the model function and the IRF are calculated, and the result is compared with the measured data. Then the parameters of the model function are varied until the least squares residuals are minimized. A bi-exponential decay can be expressed as:

$$I(t) = \alpha_1 e^{\frac{-t}{\tau_1}} + \alpha_2 e^{\frac{-t}{\tau_2}} \quad (2.13)$$

The above equation is derived with the assumption that the excitation pulse is infinitely narrow. In reality, femto-second excitation pulses are used, causing the decay to be broadened (Fig. 2.4).

In multi-exponential decay, it is often useful to determine the mean lifetime  $\tau_m$ . The mean lifetime is an average of the lifetimes of the components of a multi-exponential decay weighted by their amplitude coefficients.



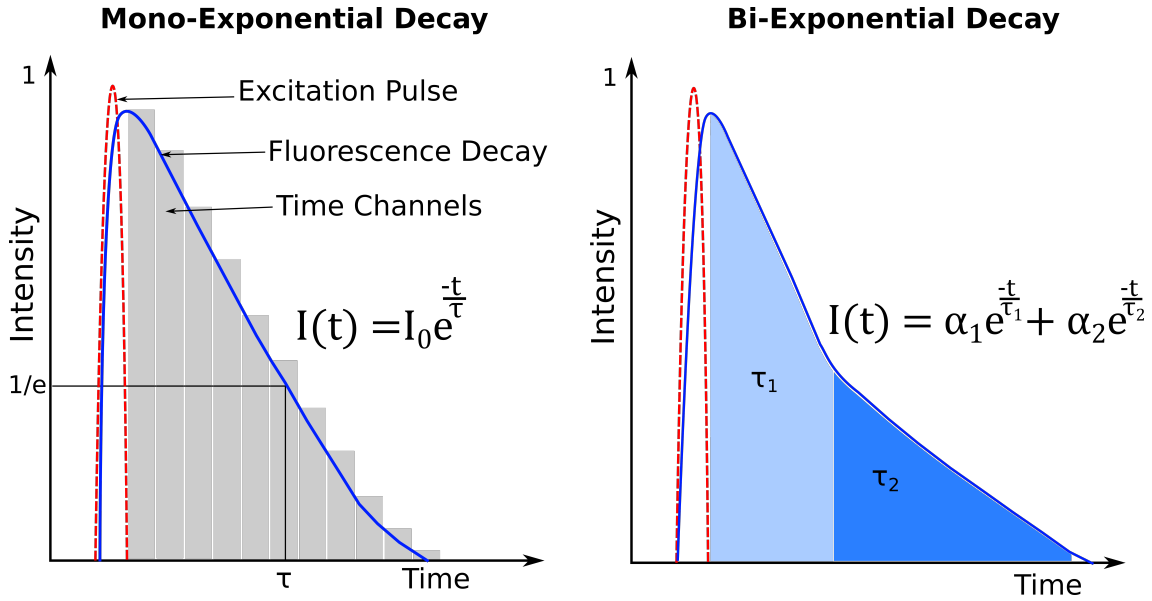


**Figure 2.4:** Simple representation of time domain lifetime analysis for mono- and bi-exponential fluorescence decays. The measured fluorescence decay signal includes the true fluorescence decay convolved with the fluorescence of the laser excitation pulse. The temporal resolution of the measured fluorescence decay curve is determined by the number of discrete time channels that are used. In case of a bi-exponential decay, the fluorescence intensity at time  $t$  after an excitation pulse can be expressed by the lifetime of each component  $\tau_1$  and  $\tau_2$  and their relative contribution  $\alpha_1$  and  $\alpha_2$ . Depending on the number of fluorescence lifetime components, different exponential fittings can be used to approximate the fluorescence decay.

$$\tau_m = \frac{\sum_{i=1}^N \alpha_i \tau_i}{\sum_{i=1}^N \alpha_i} \quad (2.14)$$

To check if a fit produces appropriate results for a given dataset the reduced chi-squared  $\chi_r^2$  is calculated, which is used to represent the goodness of a fit:

$$\chi_r^2 = \frac{1}{n - p} \sum_{i=1}^n \frac{(d_i - f_i)^2}{d_i} \quad (2.15)$$

Where  $d_i$  are the observed data points,  $f_i$  are the predicted fitting points,  $n$  are the number of data points limited by the number of time bins, and  $p$  are the number of parameters and constraints in the model. One of the major advantages of the fluorescence lifetime of a molecule is the fact that it is an absolute measurement, unlike the fluorescence intensity, which is relative. Fluorescence lifetime is, within

certain constraints, independent of fluorescence intensity and fluorophore concentration [3, 25, 48]. The duration a molecule spends in their excited state on the other hand, can be sensitive to a great variety of internal factors such as fluorophore structure and conformation, and external factors like temperature, polarity, and the presence of fluorescence quenchers. Thus, the fluorescence lifetime is useful in elucidating changes in the environment as well as size and shape of molecules, molecular interactions, inter- and intramolecular distances, and kinetic and dynamic rates.

## 2.2 Fluorescence Lifetime Imaging Microscopy (FLIM)

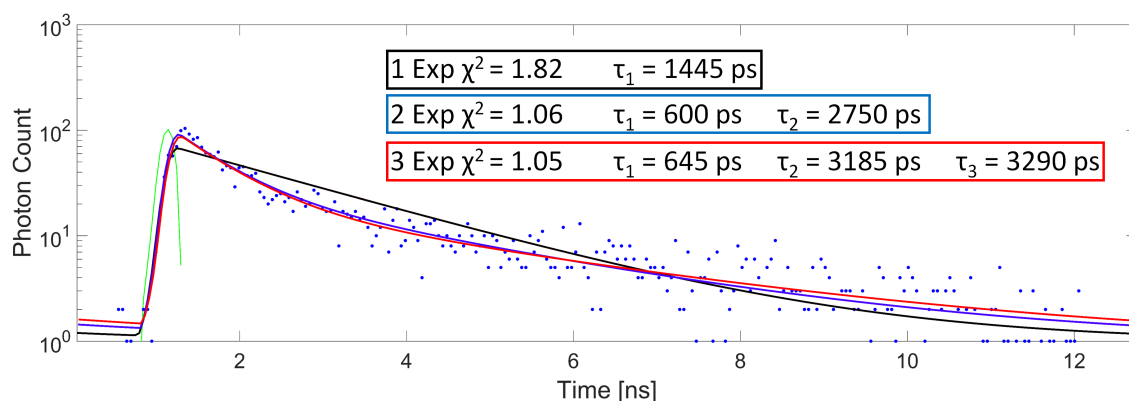


**Figure 2.5:** Using single-, double-, and triple-exponential fits on the same fluorescence decay to determine the correct fitting model. An attempt to fit the data with a single exponential results in poor  $\chi^2$  values. Double exponential fitting results in good  $\chi^2$  values. Triple exponential fitting delivers a small improvement in  $\chi^2$  values, but the third lifetime component  $\tau_3$  is almost identical to lifetime component  $\tau_2$ , which suggests overfitting.

FLIM is a technique used to form an image based on the fluorescence lifetime of fluorophores. However, in the FLIM analysis process it is often not clear which model, in particular which number of exponential components, should be used to fit the data. One way to verify model accuracy is by fitting the decay curve with a varying number of exponential components, and comparing the chi-squared ( $\chi^2$ ) value as well as the residuals, which represent the goodness of fit. A good fit is characterized by a  $\chi^2$  close to 1, and residuals showing no noticeable systematic variations [49]. If more exponential components are defined than needed to fit the data, the fitting returns two components of almost identical lifetime, or an extremely long lifetime component of very low relative amplitude. Most often, fitting data with a minimal

number of components delivers acceptable  $\chi^2$  values, while adding supplemental exponential components only results in minor improvements in fit. This is another indication that the model cannot be made more accurate by adding exponential components. Fig. 2.5 shows the lifetime distribution of NADH of adipocytes for a different number of exponential fits. The single exponential fit results in poor  $\chi^2$ , which is markedly improved by using a double exponential fit. Even though a triple exponential fit further improves the  $\chi^2$  value, the additional lifetime component  $\tau_3$  is almost identical to lifetime component  $\tau_2$ , which suggests overfitting. The two most common methods for fluorescence lifetime measurements are the frequency domain method and the time domain method. Detailed explanation of both techniques are shown in the following subsections.

### 2.2.1 Time Domain Lifetime Measurements

Generally, time-domain fluorescence lifetime imaging microscopy (FLIM) is based on the photon counting approach, called time correlated single photon counting (TCSPC). Each point in the sample is excited sequentially by a laser pulse that has to be short relative to the lifetime of the fluorophore. Individual emitted photons are recorded by photo multiplier tubes (PMTs) to create an electrical pulse measured by a time-to-amplitude converter (TAC) (Fig. 2.6). The TAC generates a voltage that is proportional to the photon arrival time relative to the laser pulse which is converted to a digital value by an analogue to digital converter (ADC) [42]. Large numbers of photon arrival times have to be accumulated to generate histograms representing the fluorescence decay time at each spatial location. Therefore, excitation sources with high repetition rate are necessary. However, due to an instrumental dead-time associated with the electronics during the processing of a photon counting event, the excitation light and detection rate must be low. Only a single photon can be processed at a time, which means any additional photons that arrive between two pulses are lost. This would distort the fluorescence lifetime towards shorter arrival times and therefore, the standard detection rate should not exceed 10% of the excitation rate [50]. The collected decay histograms consist of a range of time bins which normally correspond to the temporal resolution of the system. Fluorescence lifetimes can be derived from exponential fits to the decay data. The advantage of TCSPC is its high sensitivity, dynamic range and well defined statistics as well as decay histograms with great temporal resolution to indicate the presence of more than one decay pathway.

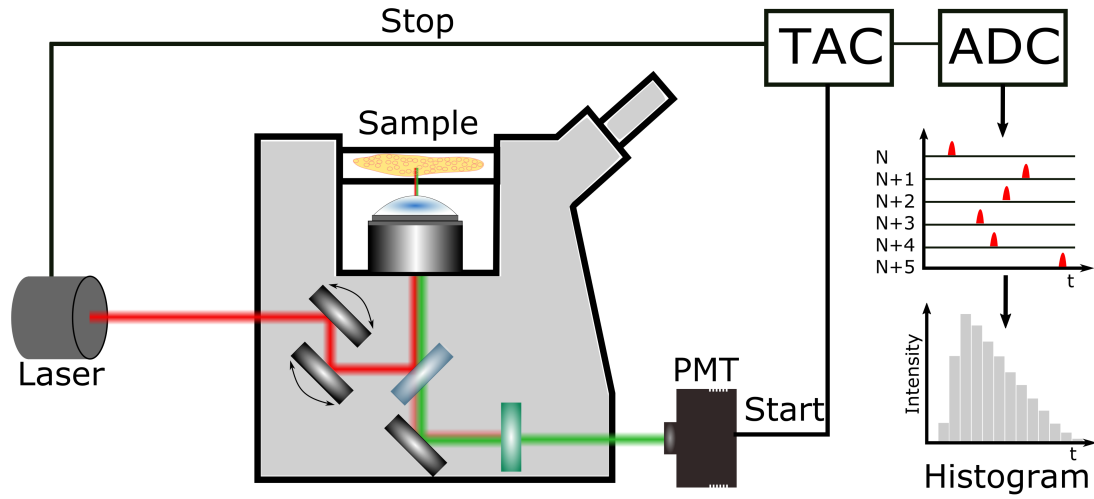


**Figure 2.6:** Time-Correlated Single Photon Counting (TCSPC) schematic. TCSPC FLIM requires a short-pulsed excitation source to excite a sample. The emitted photons pass through an emission filter and are detected by a single-photon sensitive detector such as a photomultiplier tube (PMT). The spatial information and the time between sample excitation and the arrival of the emitted photon at the detector is recorded. TCSPC requires a defined “start”, provided by the electronics steering the laser pulse and a defined “stop” signal, achieved by detection with the PMT. The measurement of this time delay is repeated numerous times to account for the statistical nature of the fluorophores emission. With the use of time-to-amplitude converter (TAC) and analog-to-digital converter (ADC) the delay times are sorted into a histogram that plots the occurrence of emission over time after the excitation pulse.

### 2.2.2 Frequency Domain Lifetime Measurements

An alternative method to time domain FLIM is frequency domain FLIM which is well established and has many appealing aspects for biological applications. This technique requires a modulated excitation source and detector of any repetitive waveform. Usually, Pockels cells are used to create intensity based sinusoidal waveforms with frequencies of 10 to 200 MHz [51]. After exciting the sample, the emission waveform shows a difference in amplitude and a phase delay (Fig. 2.7). Therefore, the demodulation ratio  $M$  and phase-angle shift  $\phi$  represent parameters that are related to the fluorescence lifetime  $\tau$  and the initial fluorescence intensity of the fluorophore [52]. For an absolute lifetime determination of a fluorophore, the system needs to be calibrated with a FLIM measurement of a reference fluorophore of known lifetime. The advantage of frequency domain over time domain FLIM is the rapid data acquisition since it is not constrained by the single-photon detection limit of TCSPC, which makes it suitable for measuring molecular kinetics.

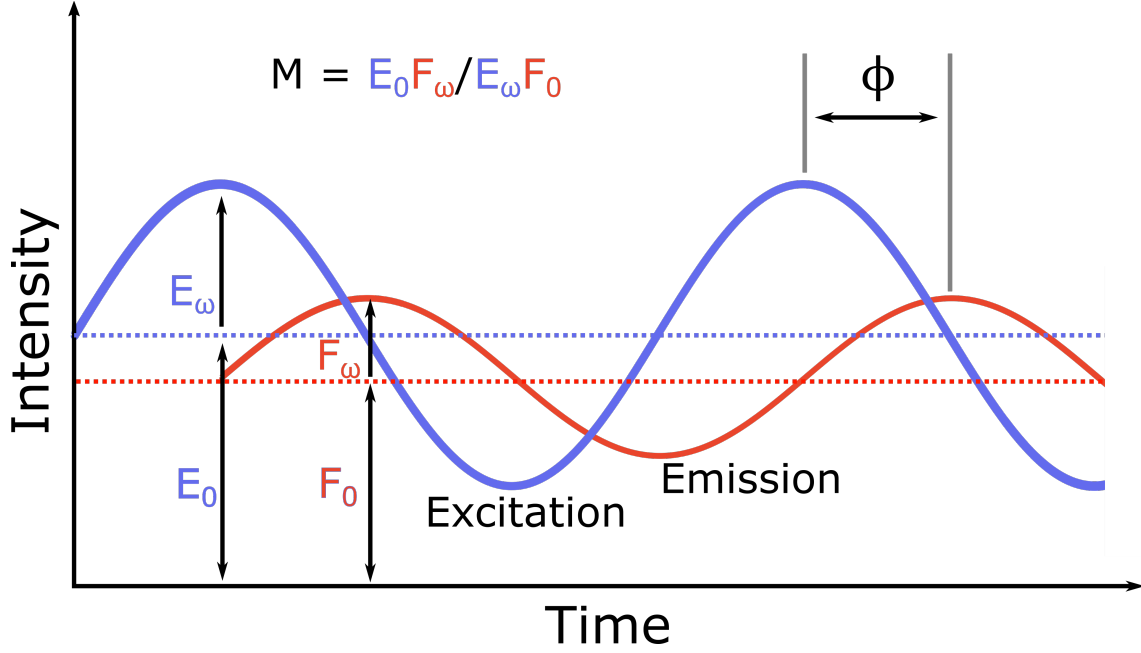


**Figure 2.7:** Frequency domain FLIM scheme. Excitation is achieved using a light source that is intensity modulated at high frequencies to excite the specimen. The basic principle is illustrated, showing the phase delay  $\phi$  and changes in modulation  $M = E_0 F_\omega / E_\omega F_0$  of the emission relative to the excitation source, which are used to estimate the fluorescence lifetime. The modulation frequency is selected based on the lifetime of the fluorophore and usually ranges between 10 to 200 MHz. Compared to time domain FLIM, frequency domain FLIM does not required short laser pulses.

The Intensity  $I$  for a single exponential decaying system after time  $t$  is given by Eq. 2.10 and the corresponding phase is given by:

$$\phi = \arctan(\omega\tau_\phi) \quad (2.16)$$

and the modulation is expressed by:

$$M = \frac{1}{\sqrt{1 + (\omega\tau_M)^2}} \quad (2.17)$$

where  $\omega$  is the modulation frequency. The lifetime determined from the phase  $\tau_\phi$  is equal to the lifetime from the modulation  $\tau_M$  for single exponential processes. For multi-exponential decay processes the lifetimes of the phase is biased towards the faster decay components and the lifetime of the modulation is weighted toward

slower components. Therefore, resolving separate fluorescence lifetime parameters for mixtures requires multi-frequency methods using a minimum of  $N$  frequencies to discern  $N$  lifetime components to be statistically valid. The approach whereby phase and modulation measurements are obtained sequentially over a set of modulation frequencies has not found application in FLIM of biological samples, principally because the sequential collection of lifetime images at every frequency is prohibitively costly, both in terms of data collection times and in terms of the total time that the sample is exposed to the excitation light [53]. Instead, in practice, measurements of multi-exponential fluorescence decays are performed at a single modulation frequency in combination with the phasor analysis. The phasor analysis is a useful and convenient 2D visualization of the phase and modulation and is further described in Subsection 2.2.4.

### 2.2.3 Phosphorescence Lifetime Imaging Microscopy

Phosphorescence Lifetime Imaging Microscopy (PLIM) is similar to Fluorescence Lifetime Imaging Microscopy (FLIM), with the difference that it images the phosphorescence of a sample and therefore covers time ranges up to milliseconds. Like in FLIM, the contrast in PLIM images are based on the excited state lifetime of the phosphorescent compound. Compared to fluorescence, phosphorescence of endogenous fluorophores in biological samples is very weak and often not detectable. Therefore, live-cell phosphorescence imaging relies on dyes such as cell-penetrating small molecule phosphors and conjugates [54]. These exogenous phosphors have the intrinsic ability to efficiently stain cells or 3D tissue models and are strongly quenched by oxygen which enables real-time imaging of intracellular oxygen concentration dynamics [54]. In most applications, PLIM and FLIM measurements are performed simultaneously to capture cellular metabolism as well as oxygen consumption [55]. Therefore, a burst of multiple laser pulses is used to excite fluorescence, and, pulse by pulse, build up phosphorescence which is far higher than for a single laser pulse.

### 2.2.4 Phasor Analysis

The phasor plot analysis is a graphical representation of raw FLIM data which can be applied to both time domain and frequency domain FLIM. For frequency domain FLIM, the decay data is expressed as amplitude and phase values at the repetition rate  $f$  with  $\omega = 2\pi f$  as the laser repetition angular frequency:

$$\text{Excitation Signal : } E(t) = E_0 + E_\omega \cos(\omega t + \phi_E) \quad (2.18)$$

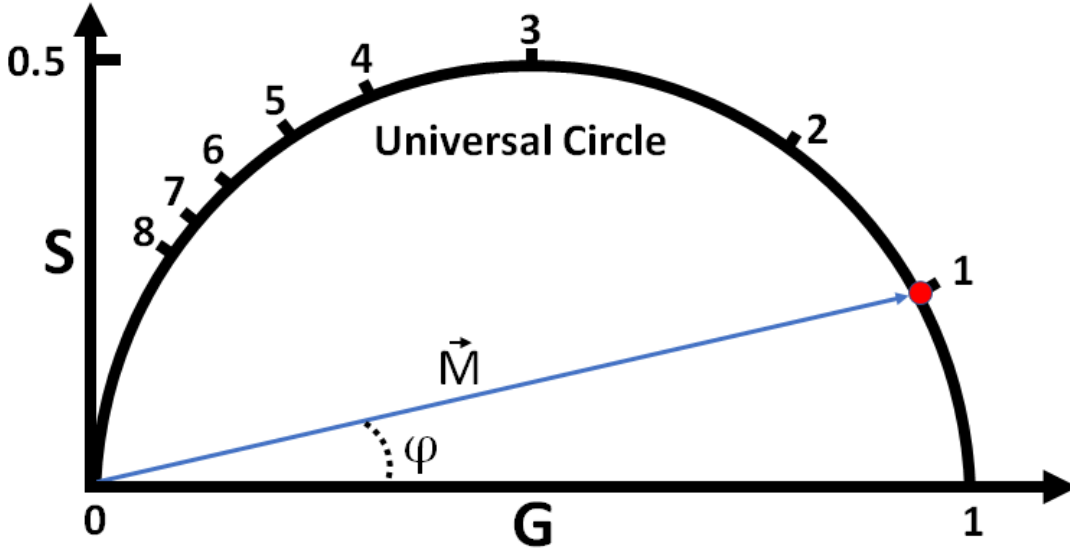


**Figure 2.8:** A schematic phasor plot of lifetime locations measured at 80 MHz. The semicircle is the single lifetime curve. The location 1,0 represents a lifetime of 0 ns and coordinates 0,0 represent an infinite long lifetime. In this coordinate system the measured value is a single exponential lifetime of 1 ns.

$$\text{Fluorescence Signal : } F(t) = F_0 + F_\omega \cos(\omega t + \phi_F) \quad (2.19)$$

were  $M_E$  and  $M_F$  are the modulation and  $\phi_E$  and  $\phi_F$  are the phase of the excitation and fluorescence signal, respectively. The relative demodulation ratio  $M = E_0 F_\omega / E_\omega F_0$  and the relative phase-angle shift  $\phi = \phi_F - \phi_E$  express the difference in amplitude and phase delay between excitation and emission and are directly related to the fluorescence lifetime  $\tau$  by Eq. 2.16 and Eq. 2.17. The phasor approach transforms the phase and the amplitude at the fundamental repetition frequency to polar coordinates by [13]

$$G(\omega) = M \cos(\phi) \quad G = \frac{1}{1 + \omega^2 \tau^2} \quad (2.20)$$

$$S(\omega) = M \sin(\phi) \quad S = \frac{\omega \tau}{1 + \omega^2 \tau^2} \quad (2.21)$$

Using the coordinates  $G$  and  $S$ , a decay trace can be graphically represented by the vector  $\vec{M} = (G, S)$  as a single point (“phasor”) in the phasor plot. The vector

## 2 Background

---

$\vec{M}$  has modulation  $M$  as a modulus and the phase  $\phi$  as an angle. The universal semicircle of the phasor representation shows a single lifetime phasor for fast and slow decaying fluorescence lifetimes and can be expressed by

$$S^2 + (G - 0.5)^2 = 0.25 \quad (2.22)$$

In this representation the longer lifetimes fall near the coordinates (1, 0) while the shorter lifetimes are closer to (0, 0). In this representation, all single exponential components are represented by the semi-circle. An alternative way of representing the modulated excitation and emission signal which can be a train of laser pulses or any repetitive wave with a fundamental period, is a complex notation as a Fourier series [56]:

$$\text{Excitation Signal : } E(t) = E_0 + \sum_{-\infty}^{\infty} E_{\omega} e^{i(\omega t + \phi_E)} \quad (2.23)$$

$$\text{Fluorescence Signal : } F(t) = F_0 + \sum_{-\infty}^{\infty} E_{\omega} F_{\omega} e^{i(\omega t + \phi_E - \phi_F)} \quad (2.24)$$

where  $F(t)$  is the measured fluorescence signal in response to the excitation signal  $E(t)$ . The Fourier transformation of the fluorescence signal also results in the phasor coordinates  $G$  and  $S$ :

$$\mathcal{F}(F(t)) = \frac{\int_0^{\infty} F(t) e^{-i\omega t} dt}{\int_0^{\infty} F(t) dt} \quad (2.25)$$

$$= \frac{\int_0^{\infty} F(t) \cos(\omega t) dt - \int_0^{\infty} F(t) \sin(i\omega t) dt}{\int_0^{\infty} F(t) dt} \quad (2.26)$$

$$= \frac{1}{1 + \omega^2 \tau^2} - \frac{i\omega \tau}{1 + \omega^2 \tau^2} \quad (2.27)$$

$$= G - iS \quad (2.28)$$

In the time-domain, the phasor approach is especially useful for fluorescence lifetime data from heterogenous samples with several fluorophores which show multi-exponential decays and are generally very complex to analyze using exponential fitting methods. In addition, the fluorescence decay of time domain measurements is convolved with the instrument response function (IRF). Traditional analysis of



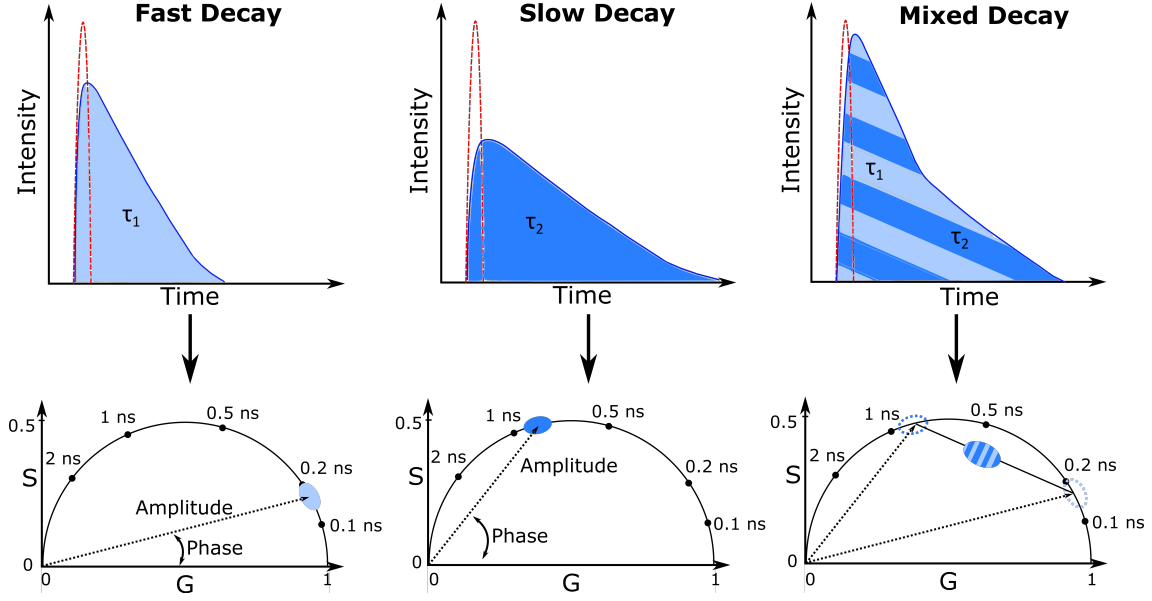


**Figure 2.9:** Three different fluorescence lifetime decays are illustrated for the comparison of time domain and phasor FLIM analysis. A decay trace can be graphically represented as a single point (“phasor”) in the phasor plot by applying the real (G) and imaginary (S) components of the Fourier transform of the decay data. Applying this technique to every FLIM image pixel generates a phasor cloud. The universal semicircle of the phasor representation shows a single lifetime phasor for fast and slow decaying fluorescence lifetimes. In this representation the longer lifetimes fall near the coordinates (1, 0) while the shorter lifetimes are closer to (0, 0). The phasor arising from the mixed lifetime decay follows the rule of linear addition of phasors and is therefore located inside the semicircle. Here, lifetimes can be determined by a straight line connecting the two lifetime locations on the universal circle. The position on the straight line will be determined by the relative fractional contribution of each lifetime component.

these data sets involves multi-exponential non-linear least square fitting and deconvolution of the IRF, which often require a priori knowledge and computationally costly fitting algorithms [3]. The advantage of the phasor plot representation is its fitting free data analysis of FLIM raw data and immediate visualization [57, 58]. Analyzing a FLIM image with this technique results in data points in a 2D histogram, the so called phasor plot, for every single pixel of the image to create the phasor distribution. This allows analysis of different lifetime phasor clusters with similar decay signature. The advantage of the phasor plot is that the clusters are usually more clearly defined than in decay parameter histograms, or do not depend on amplitude ratios which may vary with filters, detectors, and absorption in the sample [50]. For time domain FLIM the fluorescence decay of each pixel of the image can also be plotted as a single point in the phasor plot by applying the Fourier trans-

## 2 Background

---

form. Normally, a single fluorescence decay is not periodic; however, by excitation of fluorescence using a pulsed laser, exponential decay can be repeated periodically at a laser repetition frequency  $f$  and a period length of  $T = 1/f$ , which results in

$$\mathcal{F}(I(t)) = \int_0^T I(t)e^{-ik\omega t} dt \quad (2.29)$$

According to Euler's formula  $e^{ix} = \cos(x) + i\sin(x)$  the result is a complex number, which, for further calculations, is separated in the real and complex part:

$$G = \text{Re}(R) = \frac{\int_0^T I(t)\cos(k\omega t)dt}{\int_0^T I(t)dt} = \frac{1}{1 + (k\omega\tau)^2} \quad (2.30)$$

$$S = \text{Im}(R) = \frac{\int_0^T I(t)\sin(k\omega t)dt}{\int_0^T I(t)dt} = \frac{i\omega\tau}{1 + (k\omega\tau)^2} \quad (2.31)$$

Where  $G$  and  $S$  represent the phasor coordinates and  $k$  the harmonic frequency number. All phasor points from a fluorescence signal with a mono-exponential decay lie on the universal semicircle of the polar plot which is centered at  $(x, y) = (0.5, 0)$  and has a radius of 0.5. A short lifetime with a smaller phase will lie near the point  $(1, 0)$  which corresponds to  $\tau = 0$ , while a long lifetime will fall close to the coordinates  $(0, 0)$  which corresponds to  $\tau = \infty$  Fig. 2.9. Phasors of combinations of several decay components are linear combinations of the phasors of the individual components. This means that phasors of pixels with multi-exponential decay profiles are located inside the semicircle. For example, a mixture of two different pure single exponential fluorophores lie inside of the semicircle on a straight line connecting the two lifetime locations on the universal circle. The position on the straight line will be determined by the relative fractional contribution of each lifetime component [57]. The combination of phasor plot and traditional FLIM analysis allows for identification of pixels with similar decay characteristics for further analysis and as an image segmentation function.

### 2.2.5 Resolution and Imaging Depth

According to the Rayleigh criterion the lateral resolution  $\Delta\rho_{ideal}$  and axial resolution  $\Delta z_{ideal}$  of a conventional fluorescence microscope under ideal conditions can be expressed as:

$$\Delta\rho_{ideal} = \frac{0.61\lambda_{em}}{NA} \quad (2.32)$$

$$\Delta z_{ideal} = \frac{2n\lambda_{em}}{NA^2} \quad (2.33)$$

Where  $NA$  is the numerical aperture,  $\lambda$  a specific wavelength, and  $n$  the refractive index of the immersion medium. The spatial resolution of a confocal microscope under ideal conditions allows for a 30% smaller point spread functions and high quality objective lenses with high  $NA$  ensure that the fundamental restriction to the lateral  $\Delta\rho_{conf}$  and axial  $\Delta z_{conf}$  spatial resolution is close to the size of the diffraction limit [59].

$$\Delta\rho_{conf} = \frac{0.46\lambda_{em}}{NA} \quad (2.34)$$

$$\Delta z_{conf} = \frac{1.4n\lambda_{em}}{NA^2} \quad (2.35)$$

However, in case of two-photon microscopy the lateral  $\Delta\rho_{tpm}$  and axial  $\Delta z_{tpm}$  spatial resolution are broader than those of conventional one-photon excitation. The reason for that is that the resolution in all microscopy is limited by the spot diameter, and that diameter is dependent on the longest wavelength. While in one-photon confocal microscopy the longer wavelength is the emission light, the resolution limiting factor in two-photon microscopy is the longer excitation light. Therefore, the lateral and axial resolutions in two-photon microscopy are given by:

$$\Delta\rho_{tpm} = \frac{0.7\lambda_{em}}{NA} \quad (2.36)$$

$$\Delta z_{tpm} = \frac{2.3n\lambda_{em}}{NA^2} \quad (2.37)$$

While it is still true that resolution is dependent on the wavelength of emitted light, the increased constants show the disadvantage of two-photon microscopy resulting in lower spatial resolution. However, the optics and wavelengths typically used to excite endogenous biomarkers such as FAD and NADH result in a 500 nm focused spot size. If an object or feature of interest is smaller in size than the focused spot size, then two-photon microscopy will be unable to resolve that object. The advantage of two-photon excitation is that images can be acquired to a greater depth (up to 1 mm) compared to single-photon methods (100  $\mu\text{m}$ ) due to lower absorption, scattering, and excitation irradiances in the focal plane [60].

Near-infrared photons of two-photon excitation are less susceptible to Mie scattering which scales as  $\lambda^{-b}$  and causes the majority of light attenuation. The exponent  $b$  varies with particle size and a recent study by Jacques showed that the values

of  $b$  for skin and brain are 0.7 and 1.1, respectively [61]. There is a fundamental imaging depth limit at which images can be acquired. For confocal imaging scattering causes excitation and emission photons not to reach the focus and the pinhole, respectively. At a certain depth, even for high excitation power, the signal-to-noise ratio and signal-to-background ratio become too low to extract the actual signal information. Additionally, high intensities can cause photodamage and phototoxicity, since fluorescence is excited throughout the sample. For two-photon microscopy imaging depth can be increased since out of focus photons are not causing fluorescence and therefore not contributing to phototoxicity. Additionally, the absence of a pinhole results in higher detection efficiency and reduces the loss of signal. Therefore, higher excitation radiant exposure can be tolerated to achieve greater imaging depth compared to one-photon excitation.

The fundamental depth limit for two-photon excitation is reached as soon as the energy density of ballistic photons at the surface exceeds the energy of ballistic photon at the focus. This means that as the focus of the excitation beam of constant power moves deeper into the sample, the fluorescence generated in the focal plane decreases proportionally to the square of the fraction of ballistic excitation photons while the energy density will decrease exponentially with depth due to scattering. Therefore, the effect of scattering will always outweigh the effect of focusing, and thus fluorescence will start to be excited closer to the surface of the sample [62]. The maximum imaging depth  $z_m$  can be defined as the depth at which the ratio of fluorescence signal to fluorescence background falls to one. In literature this depth is described in units of the scattering mean free path  $l_s$  which is the distance the unscattered light travels to decrease to  $1/e$  of its original power [63]. While in weakly scattering material such as neuronal tissue 6 to 7  $l_s$  distances of 200  $\mu\text{m}$  can be resolved, in highly scattering tissue such as epithelial tissue only up to 4  $l_s$  distances of 90  $\mu\text{m}$  have been demonstrated [64].

## 2.3 Raman Microscopy

### 2.3.1 Spontaneous Raman Microscopy

When photons hit molecules, the energy can be scattered elastically and inelastically. When for example focused light from a laser beam interacts with a sample, most photons will experience elastic scattering (Rayleigh scattering) which preserves the energy of the incident light  $h\nu_{\text{Rayleigh}}$ . Nevertheless, there is a small portion of photons that will inelastically scatter (spontaneous Raman scatter) by an exchange of energy through the interaction with vibrational states of the molecule. Differences in these vibrational states are determined by the chemical bonds and composition of the molecules. The energy of the incident pump photons  $h\nu_{\text{pump}}$  is absorbed

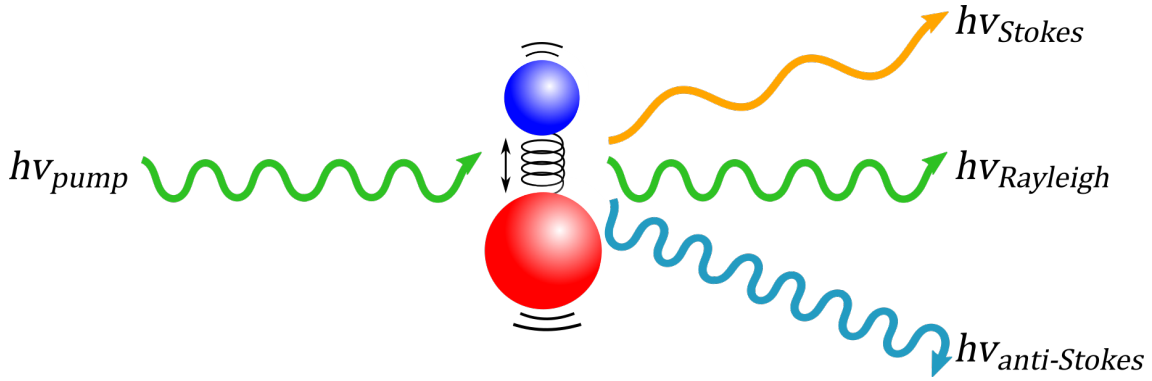


**Figure 2.10:** A diagram that focuses on Rayleigh and Raman scattering processes. Most photons that hit molecules experience elastic scattering (Rayleigh scattering) which preserves the energy of the incident light. A small portion of photons will inelastically scatter (spontaneous Raman scatter) by an exchange of energy through the interaction with vibrational states of the molecule. Inelastically scattered photons that are of lower energy than the incident pump photons are called Stokes Raman photons. Pump photons that interact with chemical bonds already in an excited vibrational state, are called anti-Stokes Raman photons with higher energy than the pump photons.

by chemical bonds to get excited to a higher vibrational energy level. Then, the scattered photons are called Stokes Raman photons  $h\nu_{Stokes}$  which will be of lower energy than the incident pump photons. By contrast, pump photons that interact with chemical bonds existing in an excited vibrational state, will have scattering photons called anti-Stokes Raman photons  $h\nu_{anti-Stokes}$  with higher energy than the pump photons. The difference in frequency between the incoming and scattering light is known as the Raman shift [65]. For a molecule to experience Raman transition several conditions must be fulfilled. For spontaneous Raman scattering, these conditions can be described by a linear electromagnetic field description where the dipole moment  $P$  induced in a molecule by an external electric field  $E$  is proportional to the field [66]:

$$P = \varepsilon_0 \chi^{(1)} E \quad (2.38)$$

Where  $\varepsilon_0$  is a physical constant called the vacuum permittivity and the electric susceptibility  $\chi$  is a proportionality constant that indicates the degree of polarization of a molecule in response to an applied electric field. The electric susceptibility relates to the molecular polarizability  $\alpha$  by  $\chi = N\alpha$  with  $N$  as the number of molecules contributing to the polarization. The Raman effect depends on the polarizability that is defined by the difficulty with which the electron cloud around a molecule can be distorted. An atom in which the electron cloud is further away from the nucleus has a larger polarizability than an atom where the electron cloud is closer to the

nucleus. For Raman scattering, the molecular polarizability must change during the molecular vibration. The Raman spectrum of each molecule provides a characteristic fingerprint defined by its chemical bonds. Therefore, a complex molecule with several vibrational energy levels of the chemical bonds will produce an extensive Raman spectrum containing the information of several combined Raman shift peaks. Spontaneous Raman scattering microscopy uses a laser with a single excitation frequency. The disadvantage of this approach is the signal strength which is extremely weak with typical photon conversions of 1 in  $10^{18}$  making it 10 orders of magnitude weaker than fluorescence due to spontaneous vibrational transition [65, 67]. This low photon yield makes spontaneous Raman scattering microscopy impractical for live imaging due to the requirement of long acquisition times and high laser power.

### 2.3.2 Stimulated Raman Scattering Microscopy

In conventional Raman microscopy, a single frequency of excitation laser beam is used for spontaneous Raman scattering. However, Raman signals can be amplified by using two coherent excitation laser beams at  $\nu_{pump}$  and  $\nu_{Stokes}$  for non-linear interaction between the two beams and the molecules [68]. When the Raman shift  $\Delta\nu = \nu_{pump} - \nu_{Stokes}$ , matches a particular molecular vibrational frequency, amplification of the Raman signal is achieved through stimulated excitation [69]. This provides the principle for coherent non-linear optical imaging techniques including coherent anti-Stokes Raman scattering (CARS) and stimulated Raman scattering (SRS). These techniques provide signal amplification to overcome the low signal levels associated with spontaneous Raman imaging, and therefore enable real-time imaging of living cells and organisms. Compared to spontaneous Raman scattering, CARS and SRS are enhanced processes with an amplified signal which is several orders of magnitude higher. Additionally, the signal intensity of SRS is also orders of magnitude higher than of CARS since the occurrence of the two-photon SRS process is higher than the three-photon process of CARS. The energy processes which occur in SRS and CARS are provided in Fig. 2.11 for comparison. The basic idea of non-linear Raman scattering techniques is that vibrational scattering is used to produce contrast for microscopic images, which is typically achieved by coupling two laser beams with different frequencies and intensities  $I_{pump}$  and  $I_{Stokes}$  into a multiphoton fluorescence microscopy experiment Fig. 2.12.

In SRS, non-linear interaction between the pump and Stokes photons stimulate the chemical bonds into an excited vibrational state. This results in the disappearance of a pump photon and the creation of a Stokes photon and as a consequence the intensity of the Stokes beam undergoes a gain known as stimulated Raman gain (SRG) and the intensity of the pump beam experiences a loss namely the stimulated Raman loss (SRL) [69]. To generate a contrast image in SRS microscopy, typically

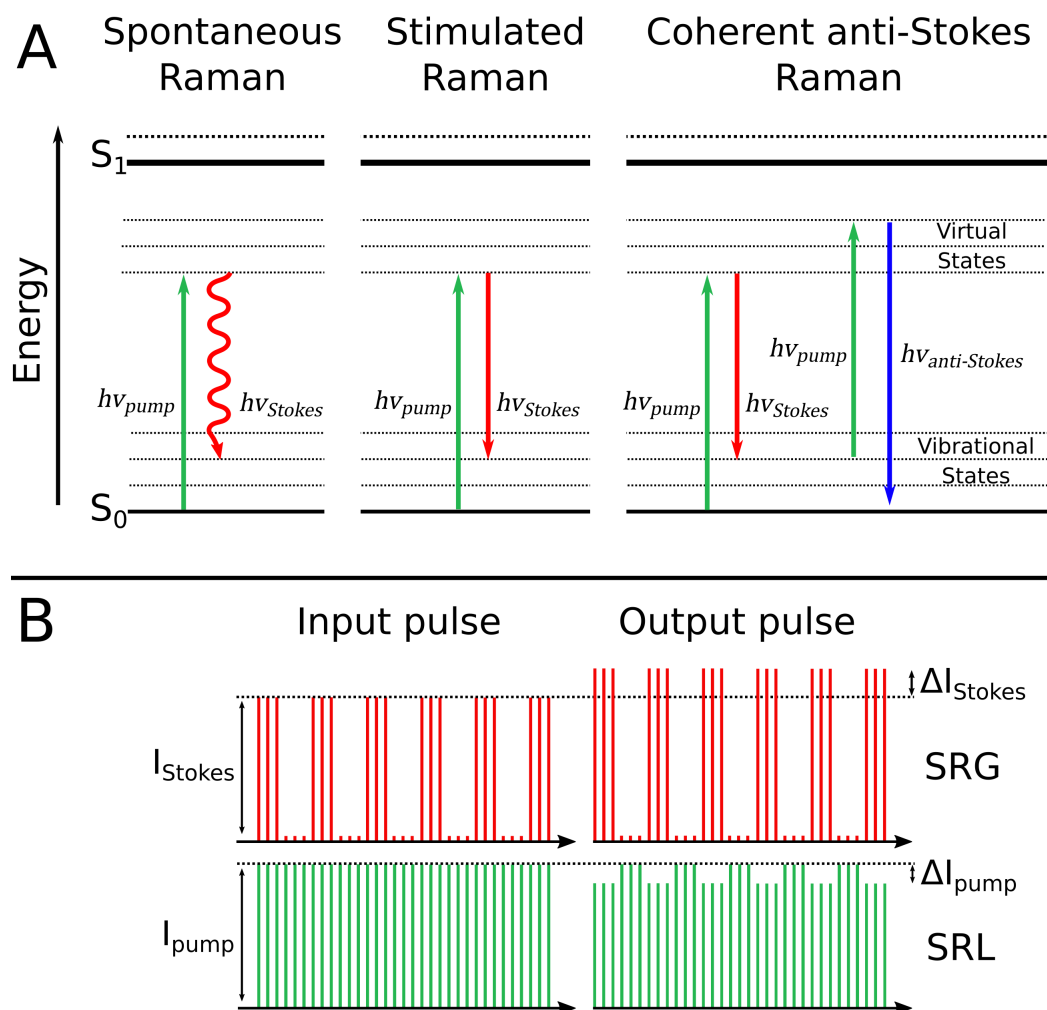


**Figure 2.11:** Schematic energy level diagrams for spontaneous Raman, stimulated Raman scattering (SRS) and coherent anti-Stokes Raman scattering (CARS) processes. **A:** In spontaneous Raman, the pump beam, is directed on to the sample generating a red-shifted signal, due to inelastic scattering. During SRS two laser beams at frequencies  $\nu_{pump}$  and  $\nu_{Stokes}$  are used, such that when the frequency difference ( $\Delta\nu = \nu_{pump} - \nu_{Stokes}$ ) matches a molecular vibration in the sample, amplification of the Raman signal is achieved through stimulated excitation. CARS microscopy causes vibrational resonance of the chemical bonds and the excited vibrational bonds further interacts with a second pump photon, resulting in the coherent emission of an anti-Stokes photon. **B:** To generate a contrast image in SRS microscopy, typically the Stokes beam is modulated and the change in pump beam (SRL) or Stokes beam (SRG) is measured.

## 2 Background

---

the Stokes beam is modulated and the change in pump beam (SRL) or Stokes beam (SRG) is measured using radio-frequency lock-in detection.

In CARS microscopy non-linear interaction between pump and Stokes photons causes vibrational resonance of the chemical bonds in the molecule. This excited vibrational chemical bond further interacts with a second pump photon, resulting in the coherent emission of an anti-Stokes photon. The emitted photons are blue-shifted to the frequency  $\nu_{CARS} = 2\nu_{pump} - \nu_{Stokes}$  which is different compared to the incidence laser beam and background fluorescence [68]. This spectral separation allows for an easy optical detection of the CARS signal. During the CARS process, no energy is transferred to the sample, rather, the energy difference between the pump- and Stokes-photons is emitted at the anti-Stokes frequency. Consequently, CARS processes can occur when there are no resonant molecules in the field of view, giving rise to non-resonant background effects. Instead, it has a complicated dependence on the geometrical structure and local concentration of the sample. Additionally, interference between non-resonant background and resonant signal may distort the CARS spectrum, limiting detection sensitivity and specificity.

The Raman signal for SRS and CARS is strongest, if a resonance condition between the excitation light and the sample molecules under investigation is met. In the case of non-linear optics, the optical response to an electric field can be described by expressing the polarization as a power series in the field [66]:

$$P = P_0 + \varepsilon_0\chi^{(1)}E + \varepsilon_0\chi^{(2)}E^2 + \varepsilon_0\chi^{(3)}E^3 + \dots \quad (2.39)$$

Where the first susceptibility term  $\chi^{(1)}$  corresponds to the linear susceptibility, and the quantities  $\chi^{(2)}$  and  $\chi^{(3)}$  are known as the second- and third-order non-linear optical susceptibilities, respectively. The signal intensity for both, SRS and CARS, can be represented in a simple relation with the number of molecules contributing to the scattering effect [70]:

$$I_{SRS} \propto I_{pump}I_{Stokes}N\sigma_{Raman} \quad (2.40)$$

$$I_{CARS} \propto I_{pump}^2I_{Stokes}|\chi^{(3)}|^2 \quad (2.41)$$

Where  $\sigma_{Raman}$  represents the Raman scattering cross section and  $\chi$  is proportional to the number of molecules of interest as shown in Subsection 2.3.1. A significant difference for SRS and CARS can be observed in Eq. 2.40 and Eq. 2.41, highlighting the linear dependence on the concentration of probed molecules for SRS and the quadratic dependence for CARS. Another difference is that SRS cannot occur when  $\Delta\nu$  does not match any vibrational resonance that absorbs the difference energy from the fields. As a result, SRS does not have a non-resonant background signal, rendering image analysis much simpler than in CARS imaging. Yet, CARS microscopy in many cases is still the preferred choice. The reason for this is that it



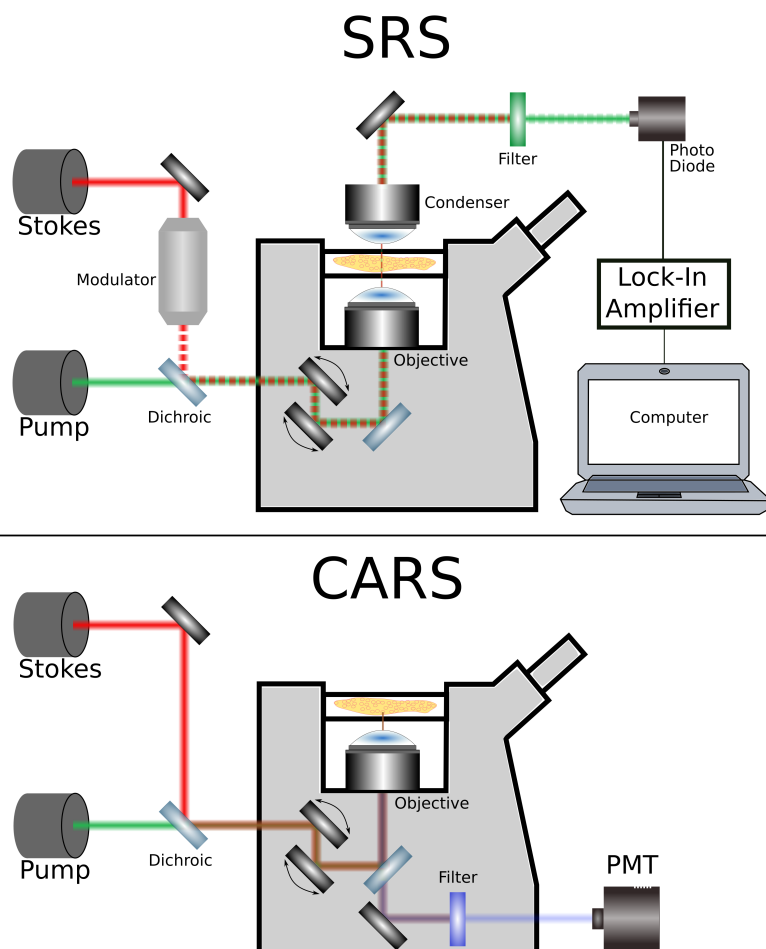


**Figure 2.12:** SRS and CARS microscopy setup. Both setups have spatially and temporally synchronized Stokes and pump laser beam which are aligned to a common focus spot. Typically the Stokes laser beam has a fixed wavelength (1064 nm), while the pump beam is tunable (803 nm for lipid imaging). The combined pump and Stokes laser beams is scanned over the sample by a XY scanner. **SRS:** The intensity of the Stokes beam is modulated with an electro-optic modulator at a high frequency ( $\sim 20$  MHz). The Stokes beam is blocked completely with a filter and the transmitted pump beam containing SRL signals is detected with a large-area photodiode. The SRL signal is extracted with a lock-in amplifier that detects at the same frequency of the modulation of the Stokes beam. **CARS:** The laser setup is very similar to SRS, except that the Stokes laser beam is not intensity modulated. CARS signal is collected using a photomultiplier tube (PMT). In front of the PMT, filters are used to block the pump and Stokes beams and any induced two-photon fluorescence. While SRS signals are typically detected in forward direction and CARS signals in epi-direction, both techniques can be detected in both directions.

offers the advantage that the detection of CARS signals is much easier than that of SRS signals [70]. Owing to the strongest signal arising from lipid molecules, one area in which CARS and SRS have quickly been applied is the study of lipid metabolism [65]. To image a particular chemical such as lipids, the wavelength of the pump laser  $\lambda_p$  can be tuned to match the Raman shift  $\Delta\omega$  of the corresponding chemical bond. Raman shifts which are typically expressed in wavenumbers, can be calculated by following equation [65]:

$$\Delta\omega = \frac{1}{\lambda_p} - \frac{1}{\lambda_s} \quad (2.42)$$

Where  $\lambda_s$  is the wavelength of the Stokes beam. Most commonly, the Raman shift of the target chemical is known (e.g.  $2845 \text{ cm}^{-1}$  for lipids), and the wavelength of the Stokes beam is typically fixed (1040 nm in this work). Based on Eq. 2.42, the wavelength of the pump beam can be calculated as followed:

$$\lambda_p = \frac{1}{\Delta\omega + \frac{1}{\lambda_s}} \quad (2.43)$$

Solving Eq. 2.44 for lipids which contain large amounts of fatty acid side chains that have abundant C-H bonds and a specific  $\text{CH}_2$  stretching frequency at a Raman shift of  $2845 \text{ cm}^{-1}$ ,  $\lambda_s=803 \text{ nm}$ . This information can than be used to calculate the wavelength of the CARS signal:

$$\lambda_{\text{CARS}} = \frac{1}{\frac{2}{\lambda_p} - \frac{1}{\lambda_s}} \quad (2.44)$$

The coherent nature of the CARS and SRS signal is dependent on parameters such as the size and shape of the scattering objects, the nonlinear susceptibilities of the object, and the local environment [68]. Each vibrationally oscillator can be considered as a Hertzian dipole at the used frequency (Fig. 2.13a). For thin portions of dipoles, the signal pattern becomes more directional, and generates radiation equally in the forward and epi directions (Fig. 2.13b). As the thickness of the sample increases, constructive interference arises in the forward direction (Fig. 2.13c). Simultaneously, destructive interference arises in the backward direction, resulting in no epi-CARS/SRS signal for larger objects (Fig. 2.13d). The incomplete destructive interference in backward direction increases with the size of the object. However, a sample with many local changes in the index of refraction, such as tissue, can redirect forward-propagating photons in the epi direction (Fig. 2.13e). It was shown that the percentage of forward signals redirected backward increased as the thickness of the turbid sample was increased [68]. Another mechanism that generates a signal in epi-direction is the discontinuity of the third-order nonlinear susceptibility  $\chi^{(3)}$  at the interface of two media.

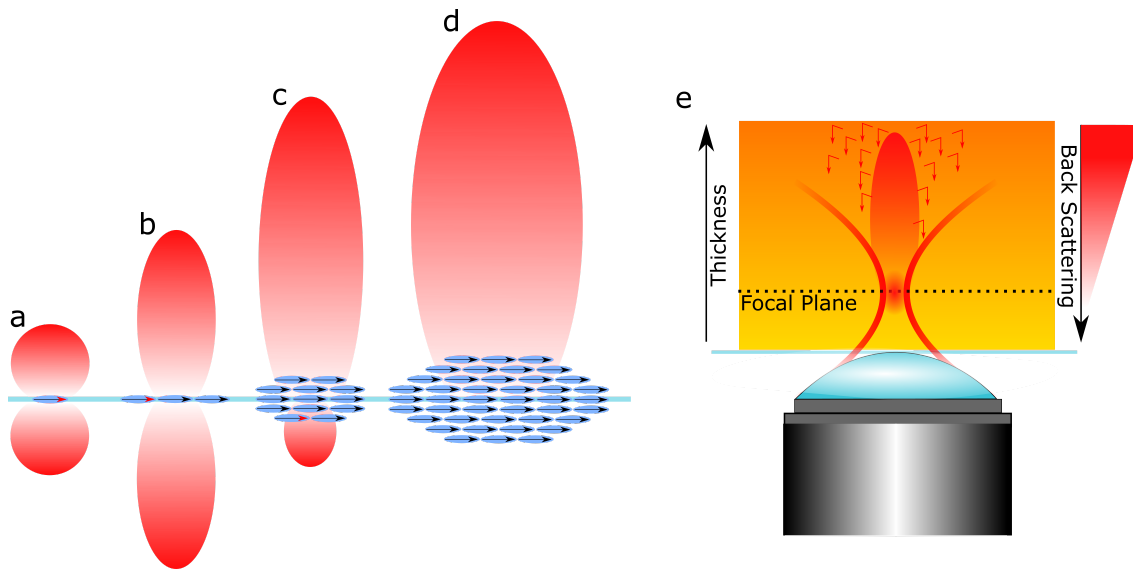


**Figure 2.13:** The effects of coherent signal buildup in the focal volume. **a:** The signal strength of a single oscillating dipole is equal in both the forward and backward (epi) directions. **b:** A thin layer of dipoles coherently generate equal signal levels in the forward and epi directions. **c:** Several dipoles collectively generate a forward-propagating part as well as a weak epi-directed signal. **d:** A thick layer of dipoles in the focal spot coherently interfere to generate only a strong forward signal. **e:** In samples with strong destructive interference in the epi-direction, signals can be detected as photons are scattered backwards. The effect is especially prominent in turbid samples such as tissue and increases with sample thickness.

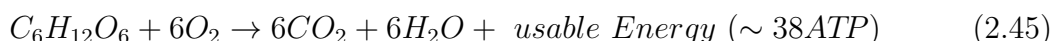
## 2.4 Cell Metabolism

Metabolic research is of immense importance since the metabolic activity of cells plays a crucial role in normal as well as diseased cell physiology, cellular function and cell fate. Scientists are dedicated in understanding every aspect of cellular metabolism such as the metabolic pathways of cell proliferation, growth, differentiation and cell death. Metabolism contains numerous biochemical pathways catalyzed by a sequence of enzymes which result in either consumption or production of energy. These pathways of cellular metabolism can be categorized in two major groups: catabolic and anabolic cellular metabolism. Catabolic metabolism involves the degradation of complex organic molecules such as lipids and proteins into smaller and simpler molecules like fatty acids and amino acids. These exergonic reactions are characterized by the release of energy or in other words release of ATP,  $\text{CO}_2$  and  $\text{H}_2\text{O}$  which are produced by oxidative phosphorylation and the citric acid cycle. Anabolic cellular metabolism uses the simple constituents broken down by catabolic

metabolism, to combine them into more complex substances such as amino acids into proteins. These pathways typically use energy and are useful for building cell structures and maintaining the cell. Although catabolism and anabolism occur independently of each other, they are inextricably linked and cells need to balance and monitor the needs and surpluses of all their different metabolic pathways. To regulate a particular pathway, cells can increase or decrease the amount of necessary activator or inhibitor enzymes. This regulation of metabolic enzyme production often occurs in response to changes in concentration of key metabolites such as lactic acids and amino acids within the cell.

### 2.4.1 Aerobic Cellular Respiration

Cellular respiration is the process where cells acquire energy by breaking down nutrient molecules and it's one of the most robust and elegant metabolic pathways. Cellular respiration is a specific series of enzyme controlled chemical reactions in which oxygen is involved in the gradual breakdown of glucose into carbon dioxide and water. During the reaction that breaks down glucose, the chemical-bond energy adenosine triphosphate (ATP) is produced directly and released into the cell. Instead of heat or light, cells run on chemical energy which is temporarily stored in the form of ATP molecules. Cellular respiration transfers chemical energy from the large fuel molecule glucose to many smaller molecules of ATP. A molecule of glucose can easily be transported through the bloodstream and it contains a large amount of chemical energy (38 ATP) in a small package. However, the amount of energy of a single glucose molecule is too high to work within the cell. Therefore, the chemical energy is transferred from glucose to ATP, which can be used to do work in the cell [71].



This process of breaking down glucose to generate energy while consuming oxygen is known as aerobic cellular respiration. The step-by-step breakdown of glucose to  $CO_2$  and  $H_2O$  usually makes a maximum yield of 36 to 38 ATP molecules. Enzymes of specific importance during this reaction are NADH and FAD. These coenzymes of oxidation and reduction are also known as redox coenzymes. NADH is generated when a metabolite is oxidized and  $NAD^+$  accepts two electrons and a hydrogen ion ( $H^+$ ).



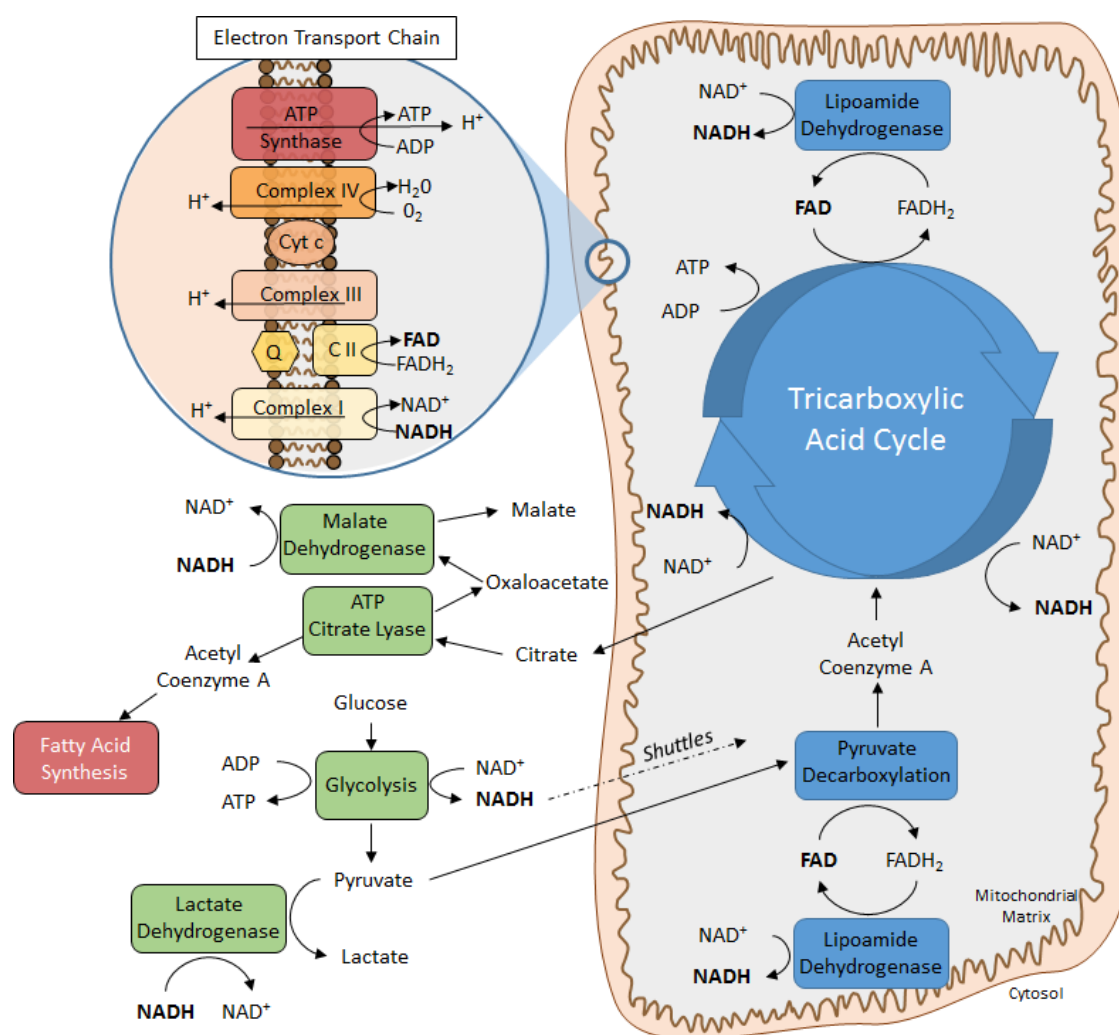


**Figure 2.14:** Simplified schematic of glycolysis and oxidative metabolism that highlights the roles of the intrinsic fluorophores NADH and FAD and shows the electron transport chain. During glycolysis which takes place in the cytosol of a cell, glucose is catabolized to pyruvate, which is then shuttled into the mitochondria or converted to lactic acid. During these processes, NADH can reduce a metabolite by giving up electrons while NAD<sup>+</sup> can oxidize a metabolite by accepting electrons. Inside the mitochondrial matrix, pyruvate is catabolized further, and its products enter the tricarboxylic acid cycle. The eight steps of the cycle are a series of redox, dehydration, hydration, and decarboxylation reactions. Citrate is one of the products of this cycle and when it is shuttled through the mitochondrial membrane into the cytoplasm it initiates the fatty acid synthesis. NADH and FADH<sub>2</sub> molecules are additional products of the tricarboxylic acid cycle which are carried to the electron transport chain where they transfer their electrons through protein complexes for oxidative phosphorylation. During that process energy is released to pump protons out of the mitochondrial matrix to create a proton gradient. ATP is synthesized when protons flow back to the mitochondrial matrix through the enzyme complex ATP synthase.

## 2 Background

---

While NADH can reduce a metabolite by giving up electrons,  $\text{NAD}^+$  can oxidize a metabolite by accepting electrons. The same principle applies to the coenzyme FAD which can accept two electrons and two hydrogen ions to become  $\text{FADH}_2$ . Therefore, NADH and FAD are involved in numerous steps of cellular respiration and can be used repeatedly by cycling back and forth between their oxidized and reduced form. Cellular respiration involves many individual metabolic reactions which can be grouped into four stages: 1. Glycolysis 2. Pyruvate oxidation 3. Citric acid cycle and 4. Oxidative phosphorylation.

During glycolysis, the six-carbon molecule glucose undergoes a series of chemical transformations and ultimately gets converted into two three-carbon molecules of pyruvate. Glycolysis takes place in the cytosol of a cell, and it can be broken down into the energy-requiring phase, and the energy-releasing phase. During the energy-requiring phase, two molecules of ATP are spent to form an unstable sugar, which then splits to form two three-carbon molecules that are isomers of each other. In the energy-releasing phase, the two three-carbon molecules turn into pyruvate and four ATP molecules are produced, along with two molecules of NADH. Overall, the net products are two pyruvate molecules, two ATP and two NADH molecules Fig. 2.14.

In the next step, the pyruvate oxidation, the three-carbon molecule pyruvate is transported into mitochondria and converted into acetyl CoA, a two-carbon molecule attached to Coenzyme A. This conversion produces one NADH and one carbon dioxide molecule for each pyruvate molecule. This step takes place inside the matrix, the innermost compartment of the mitochondria. This preparatory reaction converts products from glycolysis into products that enter the citric acid cycle.

The citric acid cycle also known as the tricarboxylic acid (TCA), or also Krebs cycle, is a central driver of cellular respiration which takes place in the mitochondrial matrix. The citric acid cycle is a series of enzyme-controlled reactions to release stored energy through the oxidation of acetyl CoA. Unlike glycolysis, the citric acid cycle is a closed loop where the last part of the pathway regenerates the compound used in the first step. The eight steps of the cycle are a series of redox, dehydration, hydration, and decarboxylation reactions that produce two carbon dioxide molecules, one ATP molecule, three NADH molecules, and one  $\text{FADH}_2$  for each acetyl group [71]. Together with the pyruvate oxidation all six carbon atoms originally located in a glucose molecule have turned into carbon dioxide. NADH and  $\text{FADH}_2$  captured the high-energy electrons released during the breakdown of glucose and carry them to the electron transport chain for oxidative phosphorylation.

During oxidative phosphorylation (OXPHOS) the reduced electron carriers NADH and  $\text{FADH}_2$  transfer their electrons to molecules in the beginning of the electron transport chain (ETC). The flow of electrons from NADH or  $\text{FADH}_2$  to  $\text{O}_2$  through the protein complexes of the ETC follows the direction from a higher to a lower energy level. Energy is released in these electron transfers and several protein complexes use the released energy for the pumping of protons out of the mitochondrial

matrix into the intermembrane space [72]. The resulting uneven distribution of protons generates a pH gradient and a transmembrane electrical potential that creates a proton gradient. The pH gradient proceeds along the inner mitochondrial membrane with the inside negative and the outside positive, and with the pH higher in the matrix than in the cytosol, where the pH is generally close to 7. Small molecules equilibrate freely across the outer membrane of the mitochondrion, and therefore the pH in the intermembrane space is the same as in the cytosol [73]. Oxygen is the final acceptor of electrons from the electron transport chain and after receiving electrons, oxygen combines with hydrogen ions, and forms water.

The critical role of oxygen as the final acceptor of electrons during cellular respiration is demonstrated by noting that if oxygen is not present, the chain does not function, and no ATP is produced by mitochondria. ATP is synthesized when protons flow back to the mitochondrial matrix through the enzyme complex ATP synthase. Thus, the oxidation of fuels and the phosphorylation of ADP are coupled by a proton gradient across the inner mitochondrial membrane [74]. Importantly, the mechanism by which the energy derived from these electron transport reactions is coupled to ATP synthesis is fundamentally different from the synthesis of ATP during glycolysis or the citric acid cycle. While in the latter cases, a phosphate is transferred directly to ADP in an energy-yielding reaction, such direct transfer of phosphate groups does not occur during electron transport [75]. Instead, the energy derived from electron transport is coupled to the generation of a proton gradient across the inner mitochondrial membrane. Besides the maximum production of between 32 to 34 ATP molecules, the ETC regenerates the electron carriers back to their oxidized form of six  $\text{NAD}^+$  and two FAD molecules which then again can be used in glycolysis and in the citric acid cycle.

### 2.4.2 Anaerobic Cellular Respiration

Pyruvate oxidation and the citric acid cycle rely on oxidative phosphorylation which uses oxygen as the final electron acceptor of the electron transport chain. Therefore, complete glucose breakdown requires an input of oxygen to keep cellular respiration working. However, glycolysis can take place and produce ATP without oxygen due to the conversion of  $\text{NAD}^+$  to NADH as an electron carrier. Since glycolysis cannot occur without this reaction and cells only hold a limited amount of  $\text{NAD}^+$ , a mechanism to convert NADH into  $\text{NAD}^+$  is needed or glycolysis will come to a standstill and ultimately result in cell death. In aerobic cellular respiration the ETC regenerates NADH back to its oxidized form  $\text{NAD}^+$  but without oxygen the ETC cannot operate. As a result, cells may use other, simpler pathways to regenerate  $\text{NAD}^+$ . In these pathways, NADH donates its electrons to an acceptor molecule in a reaction that doesn't make ATP but does regenerate  $\text{NAD}^+$ , so glycolysis can continue. Typically, glucose proceeds through the glycolysis pathway, producing



pyruvic acid. The pyruvic acid then undergoes one of several alternative changes, depending on the kind of organism and the specific enzymes it possesses. In humans, most cells can return the electrons removed from glucose in the earlier stages of glycolysis to the pyruvic acid formed at the end of glycolysis. When this occurs, the pyruvic acid is converted into lactic acid (Fig. 2.14). The formation of molecules such as lactic acid is necessary to regenerate  $\text{NAD}^+$ . This process is known as lactic acid fermentation and it occurs completely within the cytoplasm with a net profit of only 2 ATPs per glucose [72]. The buildup of the waste product, lactic acid, eventually interferes with normal metabolic functions. Lactic acid must ultimately be metabolized, which requires oxygen. Therefore, the accumulation of lactic acid represents an oxygen debt, which must be repaid in the future [Ref Holt 2009]. When oxygen is available, the lactic acid that has accumulated is converted back into pyruvic acid. The pyruvic acid can then continue through the Krebs cycle and the ETC.

### 2.4.3 Lipid Metabolism

Lipid metabolism entails the oxidation of fatty acids to either generate energy or synthesize new lipids from smaller constituent molecules. For the generation of energy, the first step in lipid metabolism is lipolysis which is the hydrolysis of triglyceride in the cytoplasm to produce glycerol and three fatty acids. Glycerol is a three-carbon molecule that is metabolized into glyceraldehyde-3-phosphate, an intermediate in glycolysis. This reaction is readily reversible if glycerol is needed for the synthesis of a lipid. Before the fatty acids can be used to release energy, they must be converted to even smaller units as they are long molecules with typically 14 to 20 carbons [72]. This breakdown of fatty acids, called fatty acid oxidation or  $\beta$ -oxidation, occurs within the mitochondria. Fatty acids are oxidized into 2-carbon fragments in the form of acetyl CoA, which are used by the citric acid cycle and then ultimately converted into ATP,  $\text{CO}_2$ , and  $\text{H}_2\text{O}$  in the ETC [76]. Along with the breakdown of long chained fatty acids, the reduced electron carriers NADH and  $\text{FADH}_2$  are produced for each 2-carbon fragment. One triglyceride molecule is converted into three fatty acid molecules and therefore each molecule of fat has the potential to yield several times as much ATP as a molecule of glucose. Each glucose molecule has 6 pairs of hydrogen which are used in the ETC during respiration, whereas a typical molecule of fat has up to 10 times that number. Thus, fat makes a good long-term energy storage for cells and when glucose levels are low, triglycerides can be converted into acetyl CoA molecules which are used to produce ATP in the same way as acetyl CoA derived from pyruvate.

When glucose levels are plentiful, the excess acetyl CoA generated by glycolysis can be converted into fatty acids and triglycerides. This process, called lipogenesis, creates lipids from the acetyl CoA and takes place in the cytoplasm of adipocytes



[76]. Lipogenesis begins with acetyl CoA and repeatedly advances by the subsequent addition of two carbon atoms from another acetyl CoA until fatty acids are the appropriate length. Even though this bond-creating anabolic process uses ATP, it is an efficient way of storing the energy available. Although lipogenesis occurs in the cytoplasm, the necessary acetyl CoA is created in the mitochondria and cannot be transported across the mitochondrial membrane. To solve this problem, citrate which is produced in the citric acid cycle and can cross the mitochondrial membrane is shuttled into the cytoplasm. In the cytoplasm, citrate is converted into oxaloacetate and acetyl CoA. Oxaloacetate is then converted into malate and the acetyl CoA is used to synthesize fatty acids (Fig. 2.14).

## 2.5 Optical Analysis of Cell Metabolism

### 2.5.1 Metabolic Biomarkers NADH and FAD

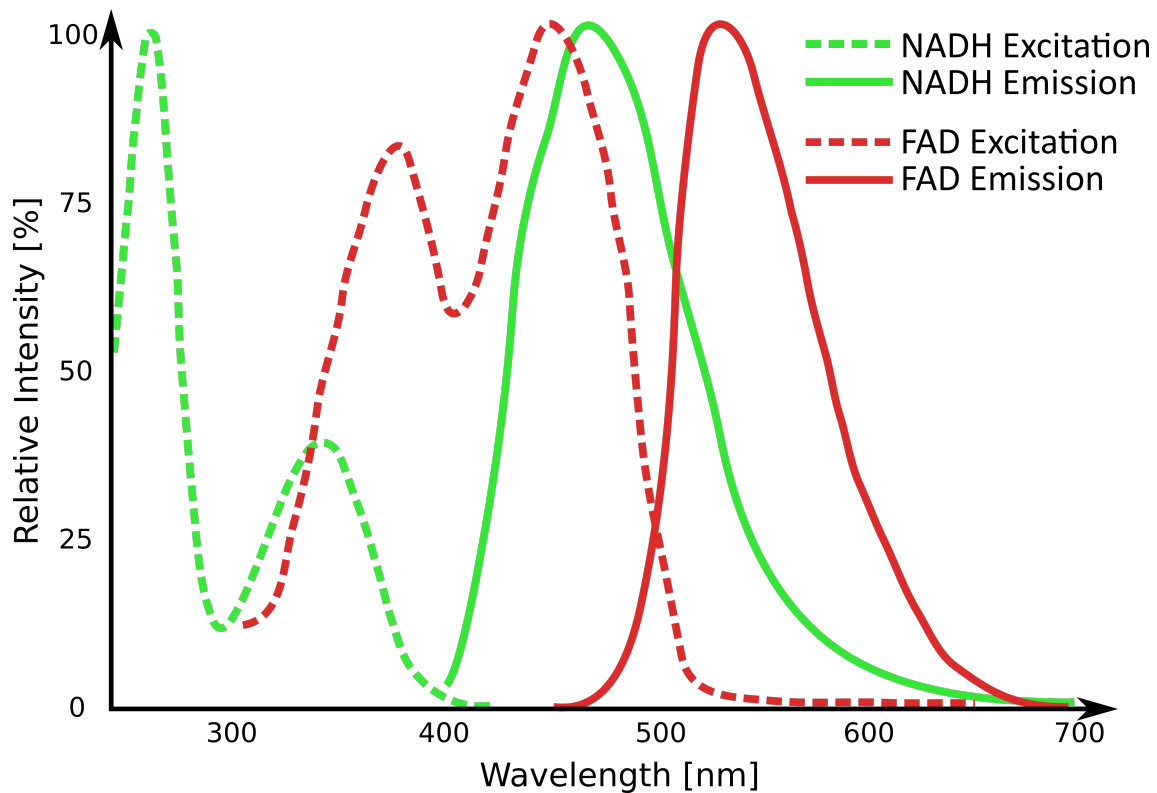


**Figure 2.15:** One-photon excitation (dotted lines) and emission (solid lines) spectra of NADH and FAD autofluorescence in aqueous solution [77]. The maximum intensity is normalized.

## 2 Background

Intrinsic fluorophores in biological tissue have been of particular interest since they can be exploited as a label-free method for monitoring intracellular changes associated with metabolism. These intrinsic fluorophores include tryptophan, collagen, nicotinamide adenine dinucleotide (NADH), flavins, and porphyrins and their analysis represents a powerful tool to understand biochemical pathways in cells. Two of these fluorophores, NADH and the flavin FAD, are electron carriers and essential in the metabolic pathway of the cells as they are involved in several key processes. The one-photon excitation and emission spectrum of these coenzymes is shown in Fig. 2.15 [78]. It can be seen that excitation and emission of FAD are shifted towards longer wavelengths compared to NADH so the two fluorophores can be spectrally isolated. This is not the case for NADH phosphate (NADPH) and NADH which both have a nicotinamide ring responsible for their fluorescence and therefore, making their spectral properties indistinguishable Fig. 2.16. Consequently, the mixed

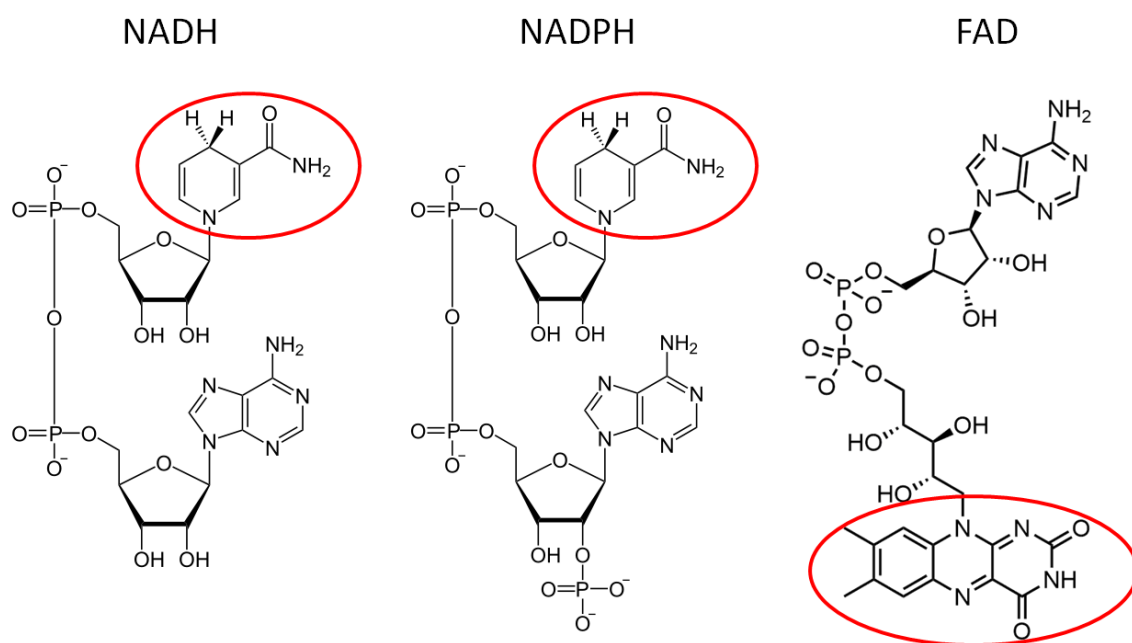


**Figure 2.16:** Molecule structure of NADH, NADPH and FAD. The fluorescent nicotinamide ring of NADH and NADPH, and the isoalloxazine ring of FAD are highlighted.

signal is often referred to as NAD(P)H. Even though NADPH is involved in several metabolic processes such as fatty acid biosynthesis, it is often neglected in microscopic studies for many cell lines since the quantum yield and intracellular concentration of NADH is significantly higher compared to NADPH [79, 80]. While NADH is fluorescent in its reduced biochemical state and not in its oxidized state as  $\text{NAD}^+$ , FAD is only fluorescent in its oxidized form and not in the reduced form as  $\text{FADH}_2$ . This allows non-invasive metabolic imaging of cells and tissue in their native physi-

ological environment avoiding perturbation of the biological system. Therefore, the fluorescent signals of NADH and FAD have been used as indicators of cellular redox reactions, energy metabolism, mitochondrial anomalies under different pathophysiological conditions, calcium homeostasis, gene expression and cell death. It is worth noting that even though NAD in its oxidized form is written as  $\text{NAD}^+$  since the adenine portion of nicotinamide adenine dinucleotide has a positive charge, the entire molecule is negatively charged due to the phosphate groups.  $\text{NAD}^+$  has one negative charge and NADH has two negative charges Fig. 2.16.

### 2.5.2 Optical Redox Ratio

The autofluorescence of endogenous coenzymes NADH and FAD can be used to optically determine and monitor cellular metabolism. The most common method for optical metabolic imaging is the redox ratio, which is the fluorescence intensity ratio of FAD and NADH [81, 82, 83]. Measuring ratio changes of  $\text{FAD}/(\text{FAD}+\text{NADH})$  can be interpreted as a relative change in the rate of glucose catabolism to oxidative phosphorylation. The optical redox ratio has been used and studied extensively and an increase in the ratio can typically be described as followed: NADH fluorescence intensity decreases during oxidative phosphorylation due to the conversion to non-fluorescent  $\text{NAD}^+$ , and FAD fluorescence intensity increases due to the transformation from its reduced and non-fluorescent form  $\text{FADH}_2$  Fig. 2.14. This shows that the redox ratio is highly sensitive to changes in metabolic rate and oxygenation. Factors for a decreased ratio can be caused by hypoxia, impairment of the electron transport chain or a need to increase glucose catabolism which leads to a build up of NADH that does not get oxidized to  $\text{NAD}^+$ .

In cancer cells, the metabolism is shifted from highly energy efficient oxidative phosphorylation to less efficient glycolysis as the primary source of energy production even though oxygen is present. This shift is known as the “Warburg effect” which causes an enhanced production of lactate in an aerobic environment and results in lower optical redox ratios [84]. In this scenario, glucose is metabolized into two molecules of pyruvate, which results in the generation of two ATP and two NADH molecules. Some of the pyruvate molecules are then further converted into lactate under regeneration of two NADH molecules to  $\text{NAD}^+$ . In healthy oxygenated tissue, glucose is converted to water and carbon dioxide through oxidative phosphorylation, resulting in the generation of 30 to 36 ATP molecules and the oxidation of 10 NADH molecules to  $\text{NAD}^+$ . This involvement and change in NADH quantity can be used to describe and distinguish cellular metabolism based on the optical redox ratio. In addition to various cancer cell lines such as bladder, ovarian and breast cancer, the optical redox ratio has been used to distinguish metabolic changes due to the effects of hormones, viruses and drugs [85, 86, 87].

Even though the optical redox ratio has been used for many years in hundreds of

studies in vitro and in vivo to track metabolic changes of cells, it has just recently been shown that the ratio does not correlate with the actual concentrations of FAD molecules but rather with the intracellular concentration ratio of  $\text{NAD}^+ / (\text{NADH} + \text{NAD}^+)$  [79]. This could be explained by inconsistent changes in FAD fluorescence intensity with increasing total intracellular FAD concentration which are caused by quenching effects and different fluorescence quantum yields among flavoproteins [88, 79]. Another change of up to one order of magnitude in fluorescence quantum yield and intensity of FAD and NADH can arise due to protein binding.

Additionally, in adipose tissue it has been shown that besides glycolysis and oxidative phosphorylation, the redox ratio changes with fatty acid synthesis [79]. These findings show the need for a more detailed and robust interpretation of the fluorescence signal than the fluorescence intensity. Nevertheless, the ability to non-destructively measure metabolic changes on a cell-by-cell basis provides great biochemical insight and makes it a particularly useful research tool.

### 2.5.3 Optical Free-to-Bound Ratio

The endogenous fluorescence of biomarkers such as NADH is affected by local environment and protein binding which is dependent on metabolism. The optical free-to-bound ratio is a fluorescence lifetime-based measurement of the ratio of free and protein-bound NADH. For NADH, binding to proteins only causes a relatively small spectral shift towards longer wavelengths of 10 – 20 nm compared to the total spectral width of 150 nm [89]. However, the fluorescence lifetime of NADH can increase several-fold after protein binding, making it a sensitive biomarker. While free NADH in solution has lifetimes between 0.4 and 0.9 ns, protein-bound NADH usually has lifetimes between 1 to 6.5 ns, where the lifetime increase is dictated by the enzyme it binds to. Prolonged NADH lifetimes after binding to proteins are caused by higher levels of conformational restriction of the molecule at the protein binding site which increase rigidity and shut down internal conversion pathways [90]. NADH is distributed throughout the entire cell and most (>60%) of the intracellular NADH is typically localized within the mitochondria, where it participates in oxidative phosphorylation and the tricarboxylic acid cycle (TCA), while the remainder is found in the cytoplasm taking part in glycolysis and the nucleus where it is involved in transcriptional pathways [10].

In solution, free NADH displays two lifetimes and a broad variety of lifetimes when bound to different enzymes [12]. FLIM imaging allows the analysis of the fluorescence lifetime of NADH in each pixel with subcellular resolution. The pixel-wise analyzed fluorescence lifetime data can be averaged on a cell-by-cell or field-by-field basis to provide average fluorescence lifetimes that are representative of individual cells or cultures. FLIM studies in cells or tissues traditionally use a two-component decay curve to resolve two lifetimes at each pixel to represent free and protein-bound

conformations of NADH. The short fluorescence lifetime component  $\tau_{free}$  usually has values between 0.4 and 0.9 ns, while the protein-bound lifetime component  $\tau_{bound}$  is longer with typical lifetime of 2 to 4 ns. Recently, Yaseen et al. used a different approach by fitting their fluorescence lifetime data of NADH in cerebral tissue to four different components ( $C_1$  to  $C_4$ ) [9]. Component  $C_1$  exhibited the shortest lifetime of 0.4 ns and  $C_2$  showed a lifetime of 1 ns, which were assigned to the different folding conformations of free NADH.  $C_3$  and  $C_4$  exhibited lifetimes of 1.7 ns and 3.2 ns, respectively, which were associated with lifetimes for NADH bound to different enzymes such as malate dehydrogenase or lactate dehydrogenase.

Independently of the use of two or four lifetime components, the lifetime differences are thought to reflect NADH in different cell locations (e.g. cytoplasm and mitochondria) with different microenvironments (e.g. pH, temperature, and viscosity). Furthermore, many studies suggest that the short and free NADH fluorescence lifetimes are predominately found in the cytoplasm while the long protein-bound lifetimes are associated with mitochondrial fluorescence [91, 92].

## 2.6 Function and Therapeutic Potential of Adipose Tissue

### 2.6.1 Anatomy and Physiology of Adipose Tissue

#### White Adipose Tissue

White adipose tissue (WAT) consist of white adipocytes which primary task is to store energy for times of starvation or great exertion. In healthy, non-overweight humans, WAT composes around 20% of the body weight in men and 25% of the body weight in women [93]. In the human body, WAT is mainly found in subcutaneous (scWAT) depots such as around the thighs and buttocks and visceral depots (vWAT) such as adipose tissue that surrounds the internal organs, but also in deposits between the muscles, around the heart, the bone marrow and elsewhere. White adipocytes transform excess dietary nutrients into densely packed triacylglycerols stored in a single large lipid droplet, the morphology therefore named unilocular. The large lipid droplet forces the nucleus and the cytoplasm to be squeezed into a thin rim at the periphery of the cell containing small amounts of mitochondria. When circulating fuels or stored carbohydrate cannot prevent an imminent energy shortage in muscles and other tissues, certain hormones bind to adipocytes to start lipid mobilization through the process of lipolysis [94]. During lipolysis, a breakdown of triglycerides into energy-rich free fatty acids and glycerol is initiated. The free fatty acids provide fuel for muscles and cardiac tissue, and the glycerol is

## 2 Background

---

delivered to the liver for gluconeogenesis. The enzyme that triggers the hydrolysis of triglycerides is called lipase and it is activated by hormones and catecholamines such as epinephrine, norepinephrine, glucagon, and adrenocorticotropin [94]. In addition to that, other hormones such as insulin and catecholamines but also nutritional status like feeding and fasting, and exercise regulate the lipid metabolism. Once blood sugar levels are increasing insulin is released from the pancreas and white adipose cells' insulin receptors cause the inactivation of hormone-sensitive lipase. Further, insulin increases the anabolic actions of white adipocytes by enhanced free fatty acid and glucose uptake, inhibition of lipolysis, and increased de novo fatty acid synthesis (lipogenesis). As described, WAT is not only responsible for energy storage and thermal insulation to help maintain body temperature, but it also plays a crucial role in metabolic health and endocrine functions [95]. Obese individuals accumulate an excessive amount of WAT which leads to an increased risk of developing numerous diseases, such as hypertension, hyperglycemia, many forms of cancer and type 2 diabetes which is a defective body responsiveness to insulin [15, 16]. However, the specific type of adipose tissue that accumulates in the body is critically important with regard to health risks. While the accumulation of vWAT is related to most of the health risks mentioned before, the accumulation of scWAT is not [96, 97]. This suggest different compositions, functions and characteristics of WAT which could be utilized to decrease obesity related health risks.

### Brown Adipose Tissue

Compared to WAT, brown adipose tissue (BAT) does not store lipids to provide fuel for other cells but primarily to dissipate them as heat. This direct conversion of chemical into thermal energy is called non-shivering thermogenesis and is of special importance in young and small mammals due their large body surface and high heat loss compared to big animals. The heat generated by BAT is crucial for the survival of these animals in low temperatures and for hibernating mammals, increased BAT activity has been seen in conjunction with arousal from hibernation [98]. Newborn human infants also have large amounts of BAT to prevent hypothermia since their nervous system is too slow to respond to cold conditions and they are not able to shiver yet. For human adults some of the brown fat depots disappear such as the interscapular BAT, while other depots remain but decrease in size such as in the supraclavicular, para aortic and neck region. Morphologically, brown adipocytes are large multilocular cells with a diameter of approximately 25-50  $\mu\text{m}$  [99]. Multiple small lipid droplets create a high surface to volume ratio which enables fast release of fatty acids from stored triacylglycerols. Brown adipocytes exhibit a large number of mitochondria in which both  $\beta$ -oxidation of fatty acids as well as dissipation of extracted energy as heat takes place.

The mitochondria of brown adipocytes contain significant amounts of uncoupling

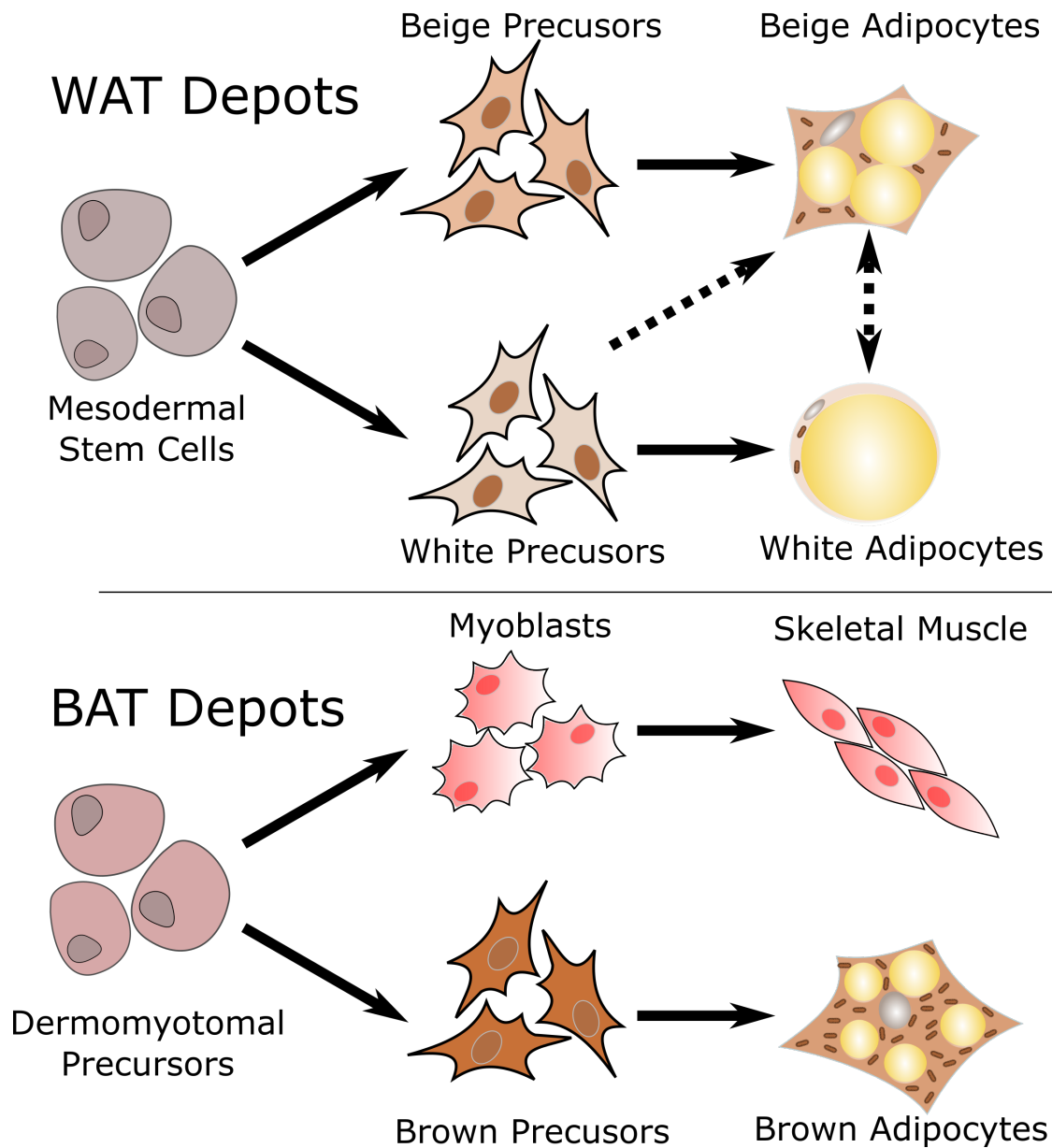


**Figure 2.17:** Developmental lineages of brown, beige, and white adipocytes. Brown adipocytes share a progenitor cell with skeletal muscle and differentiate during development from dermomyotomal precursors that express Myf5 and Pax7. The development of mature white adipocytes is well defined by differentiation of PPAR $\gamma$  expressing white preadipocytes. While the development of beige adipocytes is not fully determined. Beige adipocytes which develop in response to external stimuli such as cold in WAT depots can originate from Myf5-negative precursors of mesodermes. The dotted arrows indicate the uncertainty of the recruitment pathways. Beige adipocytes may be derived from directed differentiation from white precursors, or a reversible transdifferentiation from mature white adipocytes.



protein-1 (UCP1) which is a crucial protein for non-shivering thermogenesis. UCP1, when activated, short circuits the electrochemical gradient that drives ATP synthesis and thereby stimulates respiratory chain activity [100]. This process generates a substantial amount of heat which is distributed to the rest of the body via circulation. The size and number of mitochondria in BAT in combination with higher vascularization than WAT contribute to its brownish macroscopic color. BAT has been considered as an attractive target to promote weight loss due to its high metabolic activity. Genetic fate-mapping experiments indicate that there are two different origins for human BAT. Classical brown fat is one of them and it originates from precursor cells in the embryonic mesoderm which express Myf5 and Pax7, two genes previously assumed to be present almost exclusively in committed skeletal muscle precursors [101] Fig. 2.17.

The developmental relationship between brown fat and muscle is also evident in a common gene signature and related mitochondrial proteomes. The other origin of brown or brown-like adipocytes are called beige adipocytes which arise from Myf5-negative cells within WAT. That means, despite the morphological similarity, beige adipocytes are distinct from brown adipocytes in their developmental origin and regulation. In addition, beige adipocyte differentiation is highly induced in response to a variety of environmental cues, such as cold exposure, exercise, and tissue injury. Therefore, effective recruitment of beige adipocytes is the target of new therapeutic strategies to fight obesity. Brown and beige adipocytes can be detected non-invasively utilizing their high glucose uptake by the label glucose analogue  $^{18}\text{F}$ -fluorodesoxyglucose ( $^{18}\text{F}$ -FDG) in positron emission tomography - computed tomography (PET-CT) measurements [102].

### Beige Adipose Tissue

In recent years, research showed that in addition to the classical brown adipocytes, clusters of adipocytes with brown characteristics also develop in WAT in response to various stimuli. These cells have been named brown-like, brite (brown-in-white), recruitable or beige adipocytes and will be called beige adipocytes hereafter [20]. Even though beige fat cells share many features with classical brown adipocytes they come from different cell lineages with a distinct beige adipocyte gene expression profile which does not include the expression of Myf5 [103]. Early research suggested that beige adipocytes found in WAT, actually result from reversible white-to-brown transdifferentiation [104].

However, recent studies show that most, if not all, beige adipocytes, arise through de novo differentiation/maturation from a precursor population rather than from pre-existing adipocytes [105]. The precursor cells that give rise to beige adipocytes are not the same embryonic precursors responsible for classic brown fat. Another significant difference is that brown adipocytes have a high expression of UCP1 and other



thermogenic genes under basal (unstimulated) conditions, while beige adipocytes only express these genes in response to activators like cold,  $\beta$ -adrenergic receptor agonists, PPAR $\gamma$  agonists, or fibroblast growth factor 21 (FGF21) analogs [106]. Like adipocytes in BAT, the beige cells in murine WAT are defined by their multilocular lipid droplet morphology, high mitochondrial content, and expression of a core set of brown vs. white fat-specific genes (e.g. UCP1, Cidea, PGC-1 $\alpha$ ). Available data suggests that the function of fully stimulated beige adipocytes is similar to that of classical brown adipocytes in terms of thermal regulation, providing non-shivering thermogenesis to maintain body temperature [19]. Aside from thermogenesis, it has yet to be studied if WAT depots that undergo “browning” by recruiting beige adipocytes have the same cell type-specific actions of BAT. While it has been shown that beige adipocytes can arise in almost all WAT depots throughout the body, there are significant differences in the number of recruited cells after stimulation such as cold exposure, exercise, and tissue injury. In rodents, beige adipocytes are most abundant in the subcutaneous inguinal WAT.

Another special feature of beige adipocytes is, that their thermogenic profile is reversible, meaning that activated beige adipocytes with high amounts of UCP1 return to low UCP1 expression once the stimulation is over until they are activated again. This could mean that these cells act as both beige or white fat cells for a certain period of time depending on the conditions and stimulation. While some studies suggest that the gene profiles of beige and white cells are distinct making direct transformation of white into beige adipocytes unlikely, other studies suggest that beige adipocytes in the inguinal WAT were derived from white adipocytes [20, 107]. Therefore, further investigations and improved measurement methods are required

### 2.6.2 Activation and Therapeutic Potential of Brown/Beige Fat

Rising obesity is a worldwide problem with several hundred million adult humans affected. Obesity is a major risk factor for several diseases which are often collectively called the metabolic syndrome. Many strategies to fight obesity are focused on limiting the caloric input or increasing the energy consumption. One of these strategies to combat obesity is activation and recruitment of beige and brown adipose tissue since both tissues are responsible for a considerable amount of energy expenditure during acute cold exposure. Even though the fundamental regulatory mechanisms and the means of recruitment especially of beige adipocytes are not fully understood, numerous stimuli that can induce brown and beige adipocyte activity or increase their growth have already been discovered [108, 109]. The list of agents that induce browning or activate brown and beige fat cells is growing rapidly. Besides weight loss, mice with increased brown and beige fat activity display improvements in systemic metabolism such as higher metabolization of large quantities

of lipid from the bloodstream, improved insulin sensitivity, and increased glucose tolerance. The focus of many research groups lies in pharmacological molecules, such as  $\beta_3$ -adrenergic ( $\beta_3$ -AR) agonists, the PPAR $\gamma$  agonists thiazolidinediones and the cannabinoid antagonist rimonabant [110]. However, the browning process has been proven successful through several dietary compounds derived from plant or animal origins such as powdered scallop shells, hydrolyzed salmon protein, capsaicin found in chili peppers, and olive oil. These compounds establish an appealing approach for increased metabolic activity since they do not produce side effects compared with pharmacological drugs.

Additionally, it has been shown that irisin, a myokine induced through exercise, powerfully activates browning of WAT in mice [111]. This increase in beige fat development and UCP1-induction in WAT due to exercise reports a new regulatory circuit of beige adipocyte recruitment which does not necessarily demand thermogenesis. This is another indication that the biological significance of beige adipocytes may go beyond just heat generation in response to sympathetic stimulation [112]. It has been long known, that many types of cancers are accompanied by weight loss which is called cancer cachexia. This type of weight loss is typically associated with chronic inflammation, muscle and adipose atrophy and increased resting energy expenditure. Recently it has been shown that the increased resting energy expenditure is partly caused by cancer related hormones and proteins such as interleukin-6, UCP1, and Pgc1 $\alpha$  inducing browning of WAT [113]. Similar to cancer cachexia, beige adipocytes in the human subcutaneous WAT and high levels of urinary epinephrine and norepinephrine have been reported after severe burn injuries [114].

Interestingly, up to this point the simplest and most effective way for stimulation are physiological agents such as noradrenaline and epinephrine stimulation by chronic cold exposure. Especially for obese and elder people who do not possess sufficient amount of BAT, recruitment is highly desired but also challenging. While it has been demonstrated that cold acclimation is able to recruit activated BAT in lean adult humans, it fails to recruit necessary amounts in obese and elderly study participants [115]. Chronic cold induces BAT thermogenesis through the  $\beta_3$ -AR agonist pathway, which can also be administered pharmacologically. However, initial clinical treatment with the  $\beta_3$ -AR agonist accompanied several significant side effects such as impairment of the cardiovascular system [116]. Recent studies using oral administration of a selective  $\beta_3$ -AR agonist named Mirabegron show promising results in increased resting energy expenditure with limited undesirable cardiovascular effects [117]. Further investigations particularly in obese and elderly patients are required to understand the underlying mechanisms of BAT activation resistance. While there is a consensus that brown and beige adipocytes affect the energy balance, the magnitude of this effect in humans is still uncertain. Calculation in rodents suggest that cold-induced BAT thermogenesis could account for over 40% of whole-body energy expenditure which explains the immense therapeutic interest for humans [118].

However, recent studies in humans showed that activated BAT only increases energy expenditure from as low as 7 kcal/day up to 123 kcal/day at room temperature [119]. Significant BAT contribution to energy expenditure is nevertheless supported by the  $\beta$ 3-adrenergic agonist mirabegron-mediated increase in energy expenditure ( $+203 \pm 40$  kcal/day), along with increased pulse rate and blood pressure, suggesting increased energy expenditure from the cardiovascular system [119]. Whether browning of WAT significantly contributes to a chronic shift of total body energy balance remains to be tested. Nonetheless, regardless of whether BAT and browning of white adipose tissue play a mayor role in body weight regulation, it is likely that increased active brown and beige fat is beneficial in treating metabolic diseases including type 2 diabetes, insulin resistance, atherosclerosis, lipid disorders, and others [120].



## 3 Materials and Methods

### 3.1 Optical Methods and Parameters

#### 3.1.1 Fluorescence Microscopy

For confocal imaging, adipocytes were stained with the mitochondrial stain Tetramethylrhodamine ethyl ester (TMRE) (Molecular Probes T669, Life Technologies) and MitoTracker Green FM (M7514, ThermoFisher) as per the manufacturer's instructions. Fluorescence images of the mitochondria stains were performed on living cells using an inverted confocal microscope (FV1000, Olympus). The optical setup of the confocal microscope consists of 5 laser diodes which can be operated simultaneously and are controlled individually (Fig. 3.1). Several dichroic mirrors, gratings and filter wheels in combination with 3 photo multiplier tubes (PMTs) allow for concurrent detection of multiple epi-fluorescence signals. The optical setup permits for confocal and fluorescence lifetime imaging on the same system by mechanically changing dichroic mirrors. Therefore, cytoplasmic and mitochondrial compartment images were determined by FLIM and confocal imaging. Correlations between FLIM images and confocal mitochondrial stain images were calculated using the CORR2 function in MATLAB which implements a linear correlation to 2-D arrays [121]. Multiple confocal fluorescence images of adipocytes using the TMRE mitochondrial stain were captured 6 seconds apart from each other to analyze the movement of individual mitochondria. The movement analysis in areas where the mitochondria were clustered within the cell was not feasible, therefore, less clustered areas were used to measure the displacement between frames. Additionally, to show regional differences of the NADH species, mitochondria of murine adipocytes were isolated and stained with mitochondrial stains to check for purity.

#### 3.1.2 Fluorescence Lifetime Imaging Microscopy

Fluorescence intensity and lifetime imaging of two-photon excited NADH were performed on a confocal microscope (FV1000, Olympus) equipped with a tunable (680–1300 nm) ultrafast laser system (InSight DeepSee+, Spectra-Physics) with a 60x water objective (NA 1.2) (UPLSAPO 60xW, Olympus) with a working distance

## Confocal and FLIM

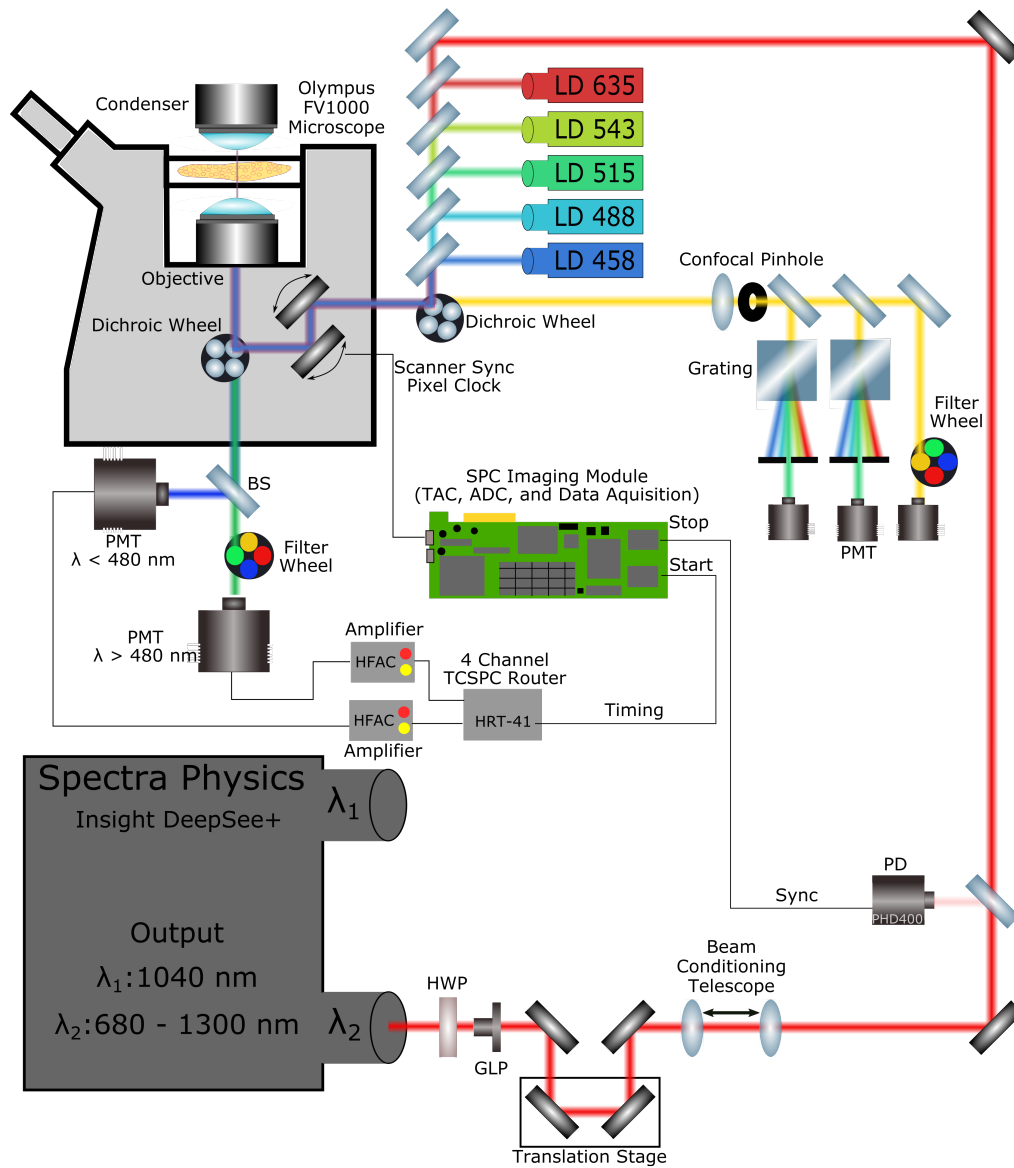


**Figure 3.1:** Confocal and FLIM microscope setup scheme. **Confocal:** Five laser diodes from 458 nm to 635 nm wavelength can be controlled and operated individually. Several dichroic mirrors guide the laser beams through a laser scanning unit into a 60x water objective (NA 1.2). Detection of the epifluorescence occurs by several PMTs through a confocal pinhole. A variety of gratings, dichroic mirrors, and filters allow for spectral division of the detected fluorescence light. **FLIM:** The tunable output channel of the femtosecond laser is used for fluorescence lifetime measurements. The half-wave plate in combination with the glan-laser polarizer attenuate the beam and the beam conditioning telescope expands the laser output. A photo diode is used as a stop signal to synchronize the laser pulse with a detected photon. A beam splitter divides fluorescent light at 480 nm to two PMTs which are connected to a TCSPC module through amplifiers and a 4-Channel router for simultaneous photon counting. For generation of 2D-images, the TCSPC module is synced with the laser scanning unit. BS: Beam splitter, GLP: Glan-laser polarizer, HWP: Half-wave plate, LD: Laser diode, PD: Photodiode, PMT: Photomultiplier tube

of 0.28 mm using a 2x digital zoom (Fig. 3.1). The tunable output channel of the laser generates  $<120$  fs pulses for the entire wavelength range of 680 nm to 1300 nm with a maximum average power of 1.3 W at 850 nm and 80 MHz repetition rate. The optical path consists of a half-wave plate in combination with a glan-laser polarizer to continuously attenuate the beam. A beam conditioning telescope expands the laser output for maximal illumination of the objective lens. A photo diode is used as a stop signal to synchronize the laser pulse with a detected photon. A beam splitter divides fluorescent light at 480 nm to two PMTs which are connected to a TCSPC module through amplifiers and a 4-Channel router for simultaneous photon counting. For generation of 2D-images, the TCSPC module is synced with the laser scanning unit. The intrinsic two-photon fluorescence associated with NADH and FAD was generated at excitation wavelengths of 755 nm and 860 nm, respectively, with average laser powers maintained below 15 mW at the microscope objective for all imaging experiments. Thus, the theoretical lateral and axial resolution of this system at 755 nm wavelength determined by the Rayleigh criterion is 383 nm and 1394 nm, respectively.

Confluent adipocytes in monolayer cell cultures on glass bottom dishes typically had a height of 25  $\mu\text{m}$  and therefore cellular images were taken at the center of the cell in 10 – 15  $\mu\text{m}$  depth. NADH and FAD emissions were first separated using a 480 nm dichroic mirror. For NADH detection, a  $475 \pm 30$  nm band-pass filter (HQ475/60M, Chroma) was placed following the dichroic mirror's reflected optical path, such that the effective detection ranged from 445 to 480 nm. For FAD detection, a  $525 \pm 25$  nm band-pass filter (HQ525/50M, Chroma) was placed following the dichroic mirror's transmitted optical path. Emission events were registered by external photomultiplier tubes (PMTs; H7422p-40 for NADH detection and H7422p-50 for FAD detection, Hamamatsu) attached to a commercial time-correlated single photon counting electronics module (SPC-150, Becker & Hickl GmbH). The samples were imaged using continuous scanning with a pixel dwell time of 2  $\mu\text{s}$  over a total acquisition time of 60 to 90 s to collect sufficient photon counts per pixel. For each field of view, images were acquired at a resolution of 256x256 pixels (105 x 105  $\mu\text{m}$ ). The scan of a single frame takes 375 ms including delays introduced by sawtooth scanning and flyback times of the galvanometer scanners. The PMT gain and laser power were kept constant and were measured for each image. Fluorescence intensity was used to create redox images, which were generated by computing pixel-wise ratios of  $\text{FAD} / (\text{FAD} + \text{NADH})$  (Fig. 3.2). Using different excitation wavelengths resulted in slightly different optical focuses due to chromatic aberrations. To determine the difference, Z-stacks with a step size of 0.1  $\mu\text{m}$  of well-defined fluorescent structures were taken for both wavelengths and images were compared and correlated. For the wavelengths 755 nm and 860 nm the axial position of the focus had a difference of 1  $\mu\text{m}$  which was mechanically compensated for in the redox ratio experiments.

Using this setup, cell cultures experiments were performed and maintained at 37°C

### 3 Materials and Methods

within a humidified 5%  $CO_2$  or ambient air environment using a microscope-compatible micro-incubator system (INUBTF-WSKM-F1, Tokai Hit). For experiments that were performed with long waiting periods in between the imaging sessions, the culture dishes were transferred into an incubator at 37°C.

To analyze the browning of adipocytes, cells were treated with forskolin (5  $\mu$ M) or epinephrine (0.5  $\mu$ M). One hour after treatment, cell cultures were imaged again to capture metabolic changes. For quantification of the fluorescence lifetime analysis, FLIM data was compared to oxygen consumption rate (OCR) and extracellular acidification rate (ECAR) derived by an extracellular flux analyzer.

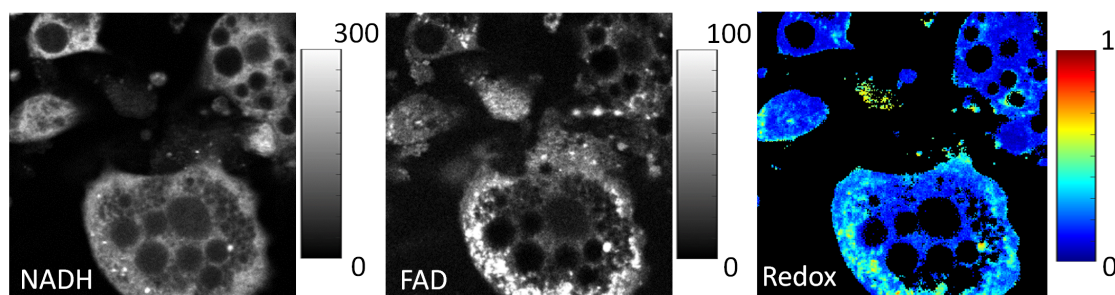


**Figure 3.2:** Fluorescence intensity image of NADH and FAD of adipocytes used to create a redox ratio image computed by the equation  $FAD / (FAD + NADH)$ .

#### 3.1.3 Raman Scattering Microscopy

CARS and SRS occur simultaneously, therefore it is common to implement both modalities on the same microscope. Additionally, the microscope (FV1000, Olympus) CARS and SRS were performed on, is the same microscope as for the confocal and FLIM experiments (Fig. 3.3). Raman signals were obtained by combining a 1040 nm Stokes beam and a 803 nm pump beam using a dual output femtosecond pulsed laser system (InSight DeepSee+, Spectra-Physics). The laser beams were aligned using an optical setup as seen in (Fig. 3.4). Both beams can be continuously attenuated by using a combination of a rotating half-wave plate and a polarizer. The 1040 nm Stokes beam is modulated at 20 MHz using an electro-optic amplitude modulator (EO-AM-R-20-C2, ThorLabs). The temporal overlap between pump and Stokes beam can be fine-tuned with a translation stage and the spatial overlap is achieved with the use of mirrors and beam conditioning telescopes in each beam path to accomplish beams of identical size. The overlapping beams are then guided into the microscope objective. CARS signals were detected in the epi-direction using a combination of a shortpass filter and a thermoelectrically cooled photomultiplier tube (H7422PA-50, Hamamatsu). SRS imaging was performed simultaneously with CARS imaging on the same system, using the same wavelengths. The SRS signal



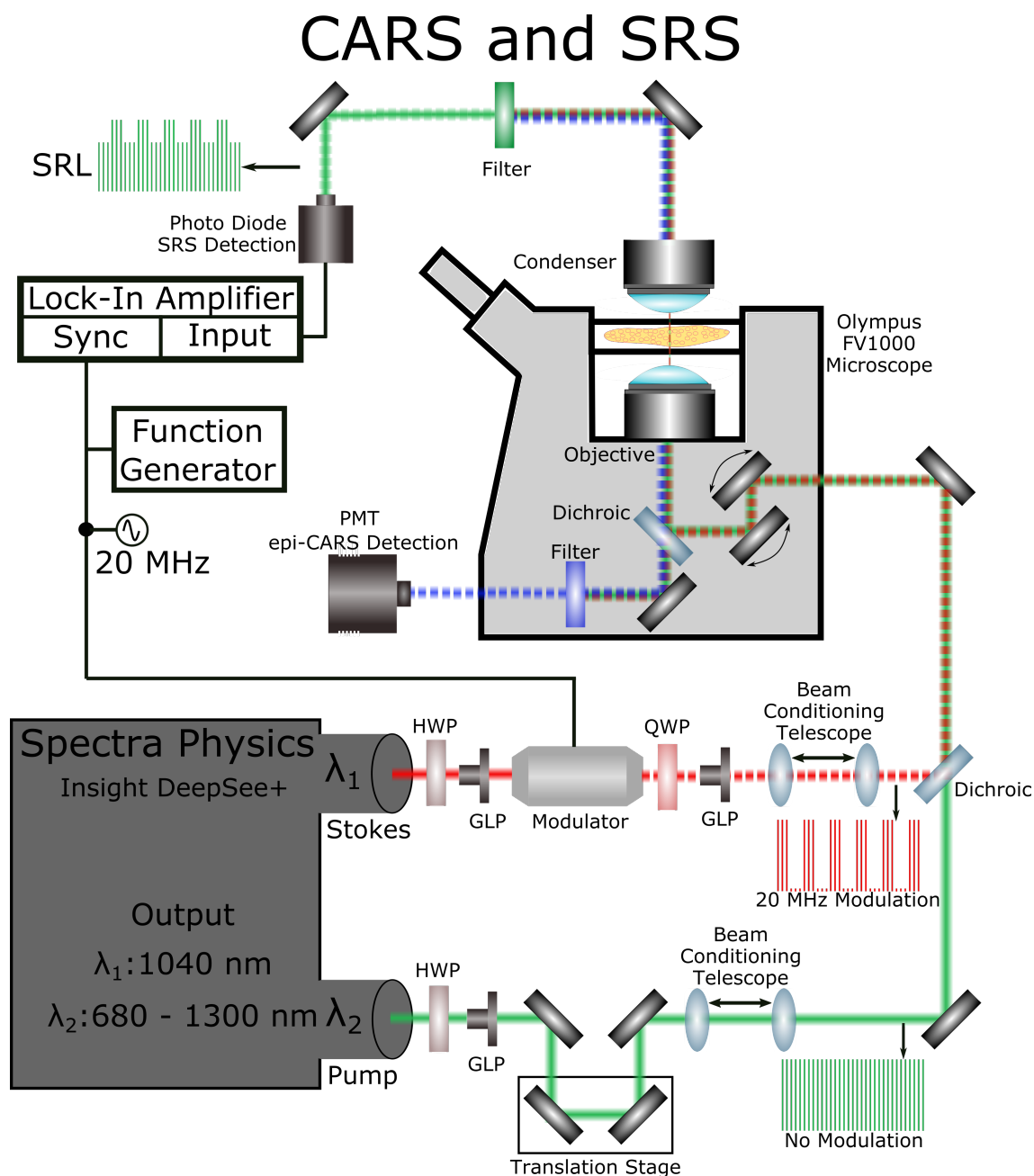


**Figure 3.3:** Optical setup for simultaneous CARS and SRS imaging. The Stokes and pump beam are continuously attenuated by a half-wave plate and a glan-laser polarizer. An adjustable translation stage enables temporal overlap of both beams. Adjustable mirrors and beam conditioning telescopes in each beam path accomplish beams of identical size with spatial overlap. **CARS:** Signals are detected in epi-direction by a combination of a shortpass filter and a PMT. **SRS:** An electro-optic amplitude modulator changes the intensity of the Stokes beam at a 20 MHz frequency. The SRS signal is detected in trans-direction by a photo diode. The photo diode and the modulator are synchronized through a function generator and lock-in amplifier to measure the stimulated Raman loss of the pump beam intensity. GLP: Glan-laser polarizer, HWP: Half-wave plate, PMT: Photomultiplier tube, QWP: Quarter-wave plate, SRL: Stimulated Raman loss

### 3 Materials and Methods

of the sample was detected in the trans-direction using a photodiode. The photodiode and the modulator are synchronized through a function generator and lock-in amplifier to measure the stimulated Raman loss of the pump beam intensity.

CARS signals have a complicated nonlinear relationship to the target molecule

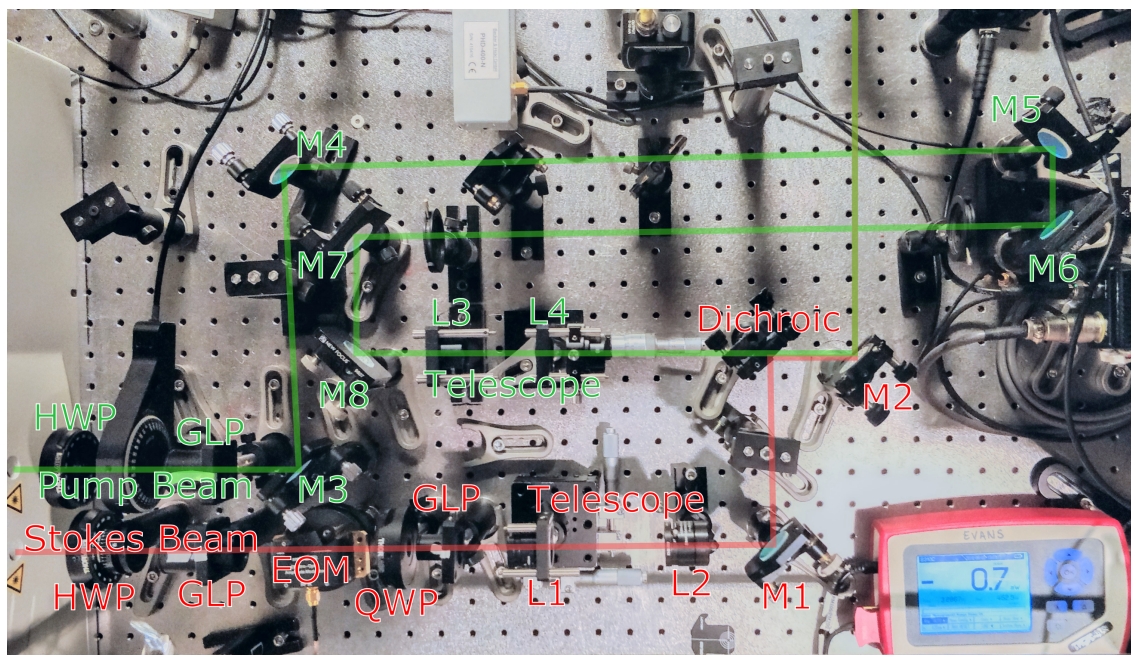


**Figure 3.4:** Optical setup of the pump and Stokes beam. The beams are attenuated by a half-wave plate and a glan-laser polarizer. Mirrors and beam conditioning telescopes in each beam path accomplish beams of identical size with spatial overlap. A modulator changes the intensity of the Stokes beam at 20MHz frequency. EOM: Electro-optic modulator, GLP: Glan-laser polarizer, HWP: Half-wave plate, L: Lens, M: Mirror, QWP: Quarter-wave plate, SRL: Stimulated Raman loss

concentration and are not suited for straightforward quantification. Optical setups where both CARS and SRS are measured, typically detect the CARS signal in epi-direction and the SRS signal in trans-direction. The reason for this is that the SRS signal exactly follows the pump and Stokes beam making it easy to detect in trans-direction [122]. The epi-detected CARS signal arises from small objects or from reflection of the forward signal, whereas the epi-detected SRS solely relies on the backscattered photons. Fig. 3.5 shows transillumination, FLIM, CARS and SRS images of adipocyte cell cultures and adipose tissue. While the thin periphery of the lipid droplets within the cell culture produce a measurable CARS signal, the middle of the droplets constitutes a thick layer of dipoles which results in strong destructive interference in the epi-direction. Therefore, no CARS signal can be detected in these areas even though a strong signal can be detected in trans-direction

by SRS. For thick tissue samples, CARS was the detection method of choice in this work. Even though SRS exhibits much higher detection sensitivity than CARS, the SRS signal in trans-direction through thick tissue samples was too low to detect. Compared to CARS images of cell cultures, the signal can be detected throughout the lipid droplets. While there is still destructive interference, the thickness of the lipid droplets and high scattering properties results in a significant amount of backscattering which can be detected. In this study, both CARS and SRS were used as a masking modality only. By identifying lipid rich areas within cells and tissue, these regions were excluded from the FLIM analysis. Fig. 3.5 shows that especially in tissue, lipid rich areas possess a strong fluorescence with a long fluorescence lifetime, which significantly would interfere with the NADH-FLIM analysis. In addition to lipid droplets, other lipid rich compounds such as lipofuscin were detected and masked out.

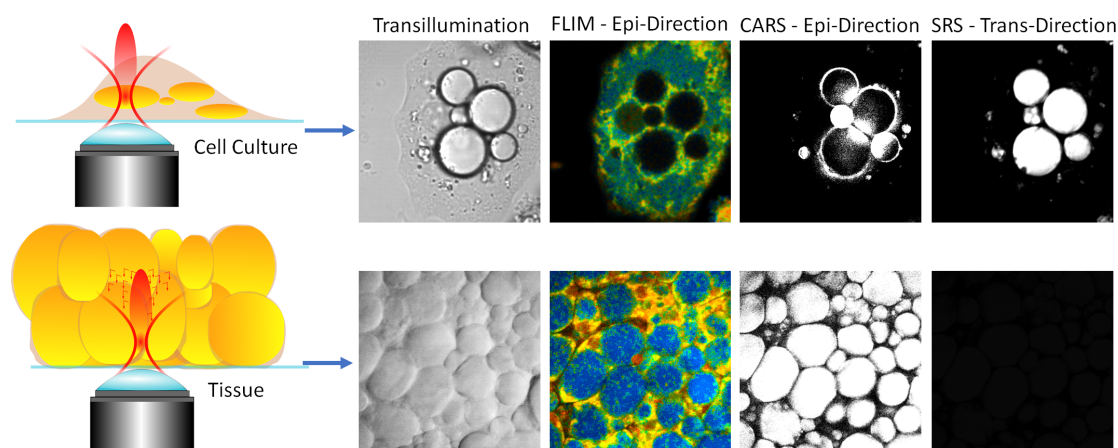


**Figure 3.5:** Image modalities for cell culture and tissue imaging. **Cell culture:** Transillumination-, FLIM-, CARS-, and SRS-Image of a single adipocyte. In this work, CARS (epi-direction) and SRS (trans-direction) are only used to detect lipids to remove these regions from the FLIM analysis. However, the lipid droplets in the FLIM image can easily be identified without the use of CARS and SRS by low fluorescence intensity. Additionally, in the CARS image, the inside of big lipid droplets is black due to destructive interference and therefore CARS is not suitable as a lipid mask in cell culture. **Tissue:** Transillumination-, FLIM-, CARS-, and SRS-Image of adipose tissue. Compared to cell cultures, it is not a straightforward to identify lipid droplets in the transillumination and FLIM image. Here, the CARS image is of great assistance in identifying lipid rich areas. Due to backscattering and refractive index changes, even large droplets produce a detectable CARS signal. In this thick tissue sample, the SRS signal in trans-direction is too weak to be detected.

### 3.1.4 Damage Threshold

Studies by Hopt and Neher on cellular photo-damage of mammalian cells induced by ultrafast near-infrared laser sources under typical in vitro imaging conditions, revealed that the number of scans before photo damage occurs is given by [33]:

$$m = \frac{f^{1.5} \lambda^2 \tau^{1.5}}{NA t_{dwell} A n (P(t))^{2.5}} \frac{1}{Cn_1 Cn_2 Cn_3 Cn_4} \quad (3.1)$$

The damage threshold proposed by Hopt and Neher observed in Chinese hamster ovary cells was empirically determined using both abrupt changes in basal  $\text{Ca}^{2+}$ , as measured by the membrane-permeable form of the fluorescence-indicator dye FURA-2, and morphological changes. Sudden decreases in the indicator dye fluorescence were observed, indicative of a sudden  $\text{Ca}^{2+}$  rise due to damage of proteins. Other experiments determining the damage threshold were carried out by König et al., observing the cloning efficiency of Chinese hamster ovary cells after exposure to laser irradiation in a two-photon microscope. Nan et al., for their part, evaluated laser-induced effects based on changes of cellular morphology such as breakdown of the cytoskeleton or extracellular matrix (ECM), seen as a collapse of the cell body or cell movements [123, 124]. These experiments indicated that photo-damage is a nonlinear function of the input beam and that higher order light-matter interactions contribute to the damaging process.

	Symbol	Hopt	König	Nan	Evers
Pulse width [ <i>fs</i> ]	$\tau$	190	150	2000	120
Wavelength [ <i>nm</i> ]	$\lambda$	840	800	711	755
Power [ <i>mW</i> ]	$P(t)$	10	7.1	63	11.25
Repetition Rate [ <i>MHz</i> ]	$f$	82	80	80	80
Dwell time [ $\mu\text{s}/\text{pixel}$ ]	$t_{dwell}$	10	80	3.3	2
Area of a cell [ <i>pixel</i> ]	$A$	1500	1500	4625	3250
Numerical Aperture	$NA$	0.9	1.25	1.2	1.2
Refractive Index	$n$	1.33	1.33	1.33	1.33
Constant 1 [ $\text{m}^2/\text{mW}^{2.5}\text{s}$ ]	$Cn_1$	$4.5 * 10^{-23}$	$4.5 * 10^{-23}$	$4.5 * 10^{-23}$	$4.5 * 10^{-23}$
Constant 2	$Cn_2$	$\pi^{2.5}$	$\pi^{2.5}$	$\pi^{2.5}$	$\pi^{2.5}$
Constant 3	$Cn_3$	0.216	0.216	0.216	0.216
Constant 4	$Cn_4$	0.576	0.576	0.576	0.576
Threshold Scan Number	$m$	75	10	10	40

**Table 3.1:** Laser settings of experiments of several studies and the maximum number of scans to reach the damage threshold.



Above the threshold, two-photon photochemical photodamage as well as immediate cell damage via optical breakdown may occur. Comparing the numbers of these previous experiments with our excitation conditions, using Eq. 3.1, we find a tolerable number of 40 scans for an average illumination power of 11.25 mW. In order to generate good enough photon statistics for low spatial binning, 160 scans at 11.25 mW power were used in our experiments which is 4-times the number of scans proposed by the damage threshold. The fact that we did not observe cellular responses such as change of morphology or increased rate of apoptosis to laser radiation at these laser parameters and high scan numbers might be explained by the choice of cells as well as excitation wavelength. Indeed, it is worth noting that the experiments by Hopt and Neher, as well as by König et al., were carried out on Chinese hamster ovary cells, which complicate a direct comparison with our results. Nan et al., on the other hand, used mouse adrenal cortical tumor (Y-1) and fibroblast cells (3T3-L1, ATCC), which are more similar to the cells used in our study. However, the experiments carried out by Nan et al. used a laser excitation wavelength of 711 nm compared to 755 nm in our study. Patterson et al. have reported that when the excitation wavelength for NADH was increased from a high two-photon cross section (710 nm) to a low two-photon cross section (760 nm) with matched intensities to yield similar photon excitation, the low two-photon cross section wavelengths had 3-fold lower photobleaching rates [125]. These findings support our observation of the absence of cellular photo-damage after laser irradiation that exceeds the empirical damage threshold by a factor of 4.

### 3.1.5 Photobleaching

Photobleaching experiments were carried out on 3T3-L1 adipocytes using four different powers in the focal plane for continuous measurement over 15 minutes. During this experiment 60 second FLIM images were taken continuously for 15 minutes and the total intensity of the field of view was analyzed for each image. While the fluorescence for powers of 11.25 mW did not show significant changes over the 15-minute duration, the fluorescence decreased for powers of 15mW and higher. It appears that the cells can compensate for photobleaching at low laser irradiation but after many frames or at higher laser powers, the cells become unable to adapt. Different than for one-photon excitation, photobleaching is restricted to the focal plane and therefore, two-photon excitation causes less photobleaching overall but higher photobleaching in the focal plane. For accurate fluorescence lifetime determination, many photons are required which means either a high excitation irradiation or a long acquisition time. Thus, photobleaching and photodamage occur and are likely to change the lifetimes. Both effects are nonlinear for two-photon excitation. Hence, photobleaching can be reduced by recording at lower excitation irradiation and correspondingly longer acquisition time. An example of photobleaching is shown in

### 3 Materials and Methods

Fig. 3.6 where photobleaching has no effect on the spatial structure of a sample. Fluorescence measurements for spatial imaging can therefore be performed at high

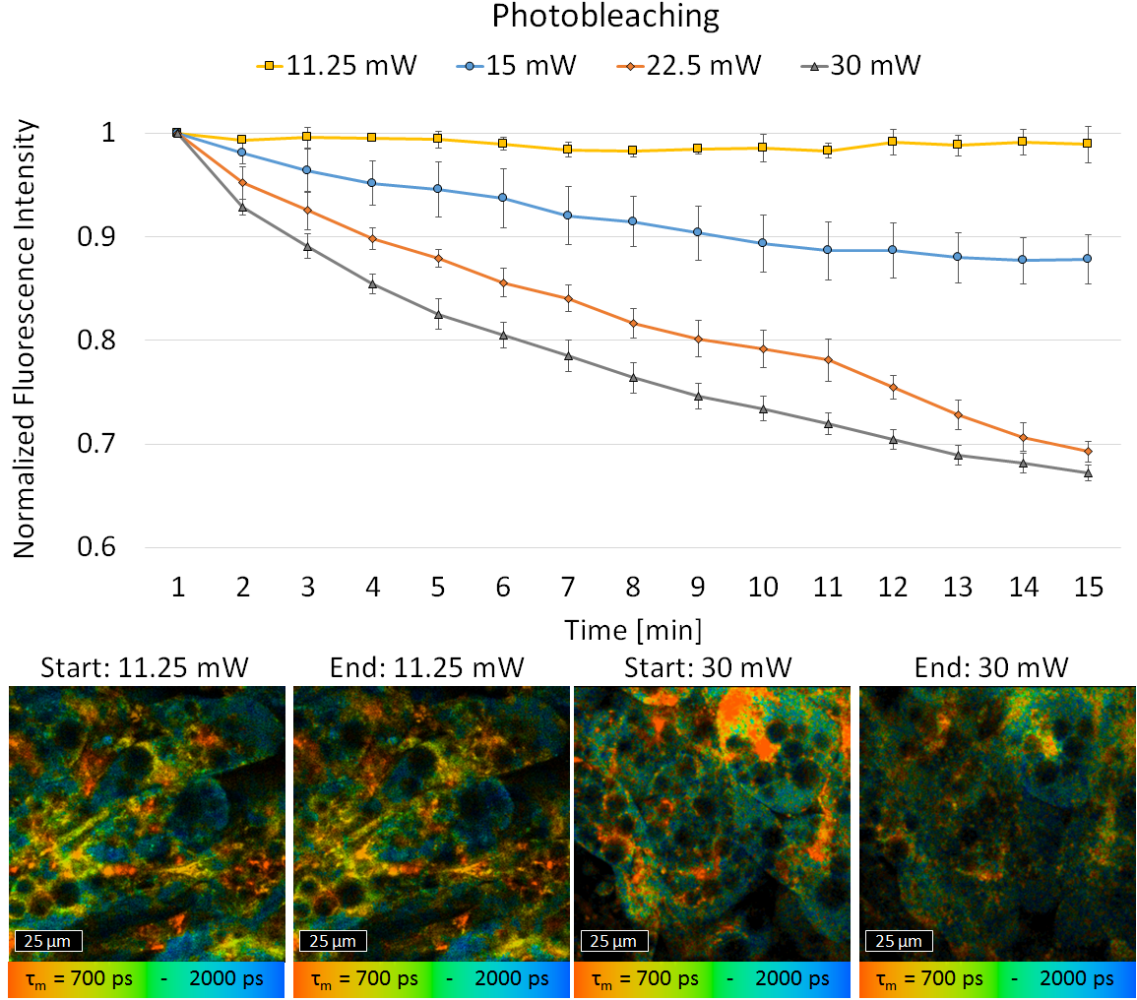


**Figure 3.6:** Average fluorescence intensity of 3T3-L1 adipocytes over a 15-minute duration at different laser excitation powers at the focal plane at 755 nm wavelength. FLIM images show adipocytes after 1 min and after 15 min of continuous imaging at 11.25 mW and 30 mW.

excitation irradiation. The lifetime image of the imaging area showed that the fluorescence intensity of the image decreased significantly even though the spatial structure of the sample is still perfectly preserved. However, the false color life-time image shows a blue shift, indicating an increased lifetime of the photobleached region. The reason for that is that biological samples normally contain several fluorophores, or fluorophores in different confirmation or binding states which bleach at different rates. Depending on which fluorophore is present, short and long lifetime components bleach at different rates and the lifetime distribution changes toward

the more stable fluorophore. It may also happen that photobleaching products are fluorescent themselves. In these cases the lifetime changes may become entirely unpredictable [49]. Additionally, photobleaching generates radicals which can have a destructive effect on the cell. Photobleaching may therefore not only change the fluorophores but also the molecular structure of the cell, ultimately leading to cell death. In a second set of experiments it was tested if the loss of fluorescence intensity is irreversible or if the fluorescence intensity recovers within a short period of time. Therefore, photobleaching experiments were carried out on 3T3-L1 adipocytes using a protocol of three imaging periods of 3 minutes with 3 minutes of break in between each imaging session. The results in Fig. 3.7 show that the fluorescence intensity does not recover during the short 3 minute break between each imaging session.

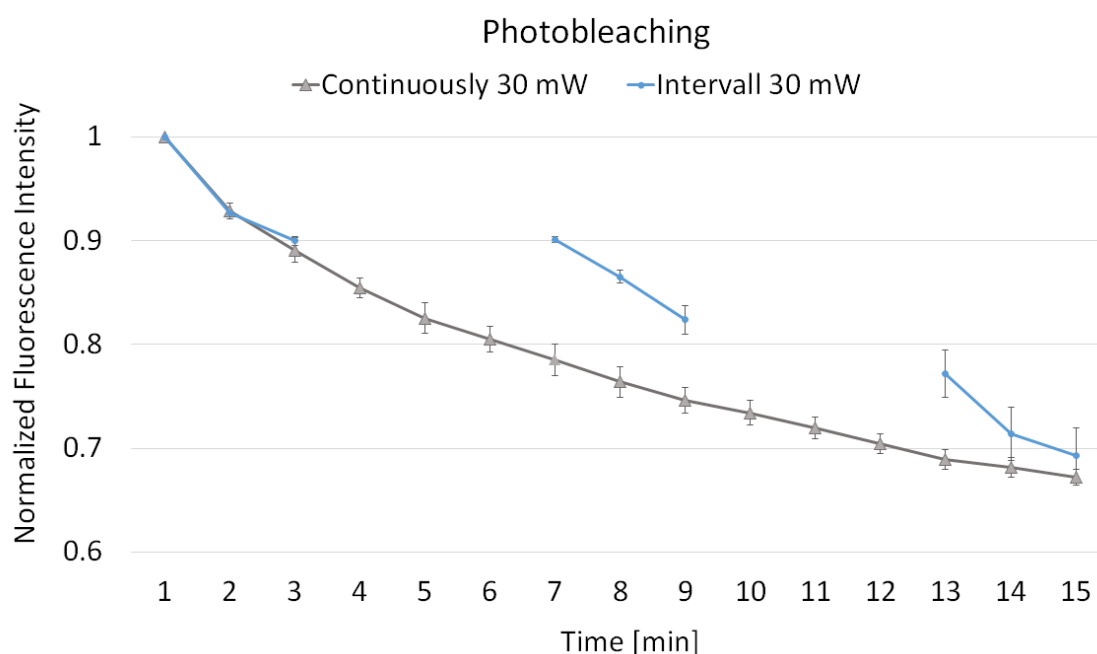


**Figure 3.7:** Fluorescence intensity of 3T3-L1 adipocytes for continuous imaging over 15-minute duration compared to alternating between 3 minutes of imaging and pausing. Using 30 mW laser excitation powers at the focal plane at 755 nm wavelength.

### 3.1.6 Apoptosis

The detection of laser induced cellular damage leading to programmed cell death (apoptosis) is of utmost importance in FLIM studies. Caspases are signaling molecules that are markers for cellular damage. Although the precise role in the initiation and

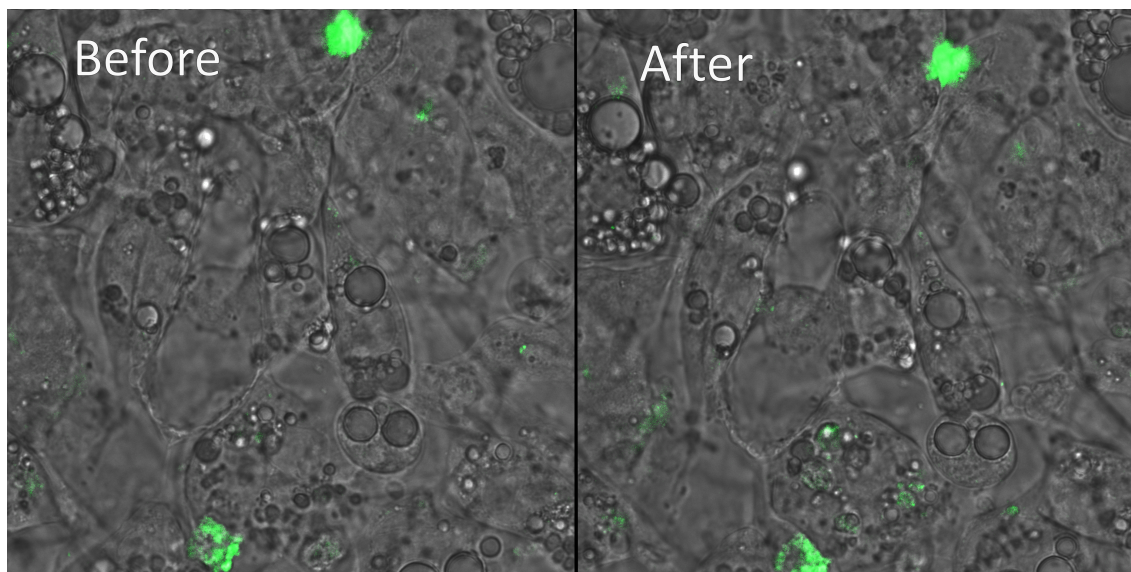


**Figure 3.8:** Combination of a trans-illumination image and a fluorescence image of apoptosis stain caspase-3/7 green. No apoptosis is induced by the image acquisition of a FLIM image using a mean power of 11.25 mW for 90 s.

progression of apoptosis is not yet known for all caspases, their use for the detection of apoptotic events is commonly used as a readout in apoptosis assays. 3T3-L1 adipocytes were stained with caspase-3/7 green detection reagent (CellEvent<sup>TM</sup>, ThermoFisher) as per the manufacturer's protocol. Trans-illumination images of the 3T3-L1 fat cells in combination with apoptosis stain fluorescence images were taken, prior to a 90 s FLIM image acquisition with the experimental laser settings at 755 nm wavelength and 11.25 mW power. More trans-illumination images in combination with apoptosis stain fluorescence images were taken 4 hours after the FLIM image acquisition to see if apoptosis was induced by the laser scanning microscope. Given the high degree of similarity between the two imaged timepoints in Fig. 3.8 and the relatively constant signal intensity from the fluorescent apoptosis marker, it can safely be concluded that the imaging conditions do not induce apoptosis. This indicates that these laser and imaging parameters do not induce any DNA strand breaks within the cell and hence are not deleterious.

However, higher laser excitation power and longer acquisition times induced pronounced apoptosis as detected by characteristic changes of cellular morphology and fluorescence lifetime (Fig. 3.9). Cells were irradiated with 755 nm wavelength for 180 s using mean powers of 30 mW. The trans-illumination image reveals the break of the cell membrane as well as the fusion of multiple lipid droplets. The FLIM image shows a significant shift to shorter fluorescence lifetimes with a significant fluorescence intensity loss. Therefore, it was shown that visible and near infrared two-photon laser irradiation of 3T3-L1 adipocytes under certain exposure conditions



## Photodamage

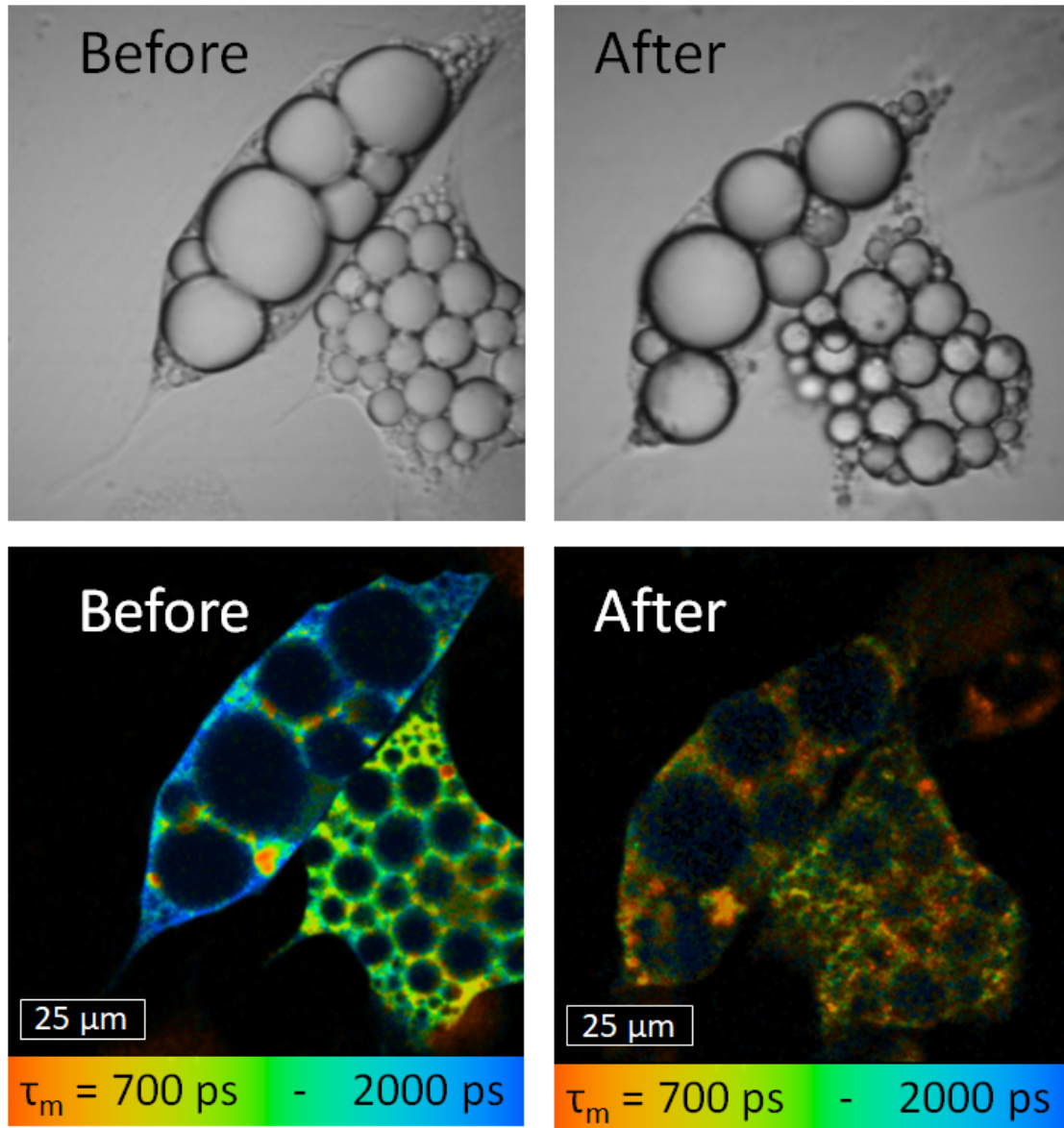


**Figure 3.9:** Trans-illumination and FLIM image of adipocytes before and 4 hours after photodamage was induced by excessive laser irradiation at 755 nm wavelength for 180 s using mean powers of 30 mW. Due to photodamage the cells show rupture of the outer membrane, reduced fluorescence and change of fluorescence lifetime.

lead to apoptosis-like cell death. Additionally, it has been demonstrated that mitochondria are the major targets of NIR femtosecond laser exposure and that excessive irradiation results in several abnormalities such as mitochondrial swelling, formation of electron dense bodies in the mitochondrial matrix, and rupture of the outer membrane [126, 127]. Typically, photodamage is a photochemical damage induced by the nonlinear excitation of absorbers followed by phototoxic reactions such as the formation of reactive oxygen species (ROS), which result in oxidative stress. ROS formation in mitochondria often leads to apoptosis, whereas ROS formation in lysosomes or other organelles may induce either necrosis or apoptosis [128].

#### 3.1.7 Solution and pH Measurements

Several NADH solution experiments were performed to investigate changes of fluorescence lifetime depending on the solvent media, concentration of NADH, as well as introduction of binding enzymes. To distinguish the effect of media on fluorescence lifetime, NADH disodium salt (Grade 1, Sigma Aldrich) was dissolved in 1 ml of culture media, phosphate buffered saline, and distilled water. A drop of the solution with a final concentration of 0.5 mM was placed on a microscope slide and analyzed. The influence of NADH concentration on the fluorescence lifetime was tested with seven different concentrations, starting at 30  $\mu$ M and going up to 200 mM. The effect of potential enzyme binding partners of NADH was investigated using NADH disodium salt in solution (48  $\mu$ M) and a 16:1 mixture of NADH (48  $\mu$ M) and lactate dehydrogenase (LDH, 3  $\mu$ M) in solution. LDH is a tetrameric molecule with four identical NADH binding sites. For both solutions, a double and a triple exponential fit of the fluorescence decay curve were used to describe the fluorescence decay.

The fluorescence lifetime is known to change significantly with the pH value of the solution. To induce metabolic changes in adipocytes, several metabolic modifiers were injected into the media resulting in significant changes of the oxygen consumption rate (OCR), extra cellular acidification rate (ECAR), and fluorescence lifetime parameters. To verify that the resulting changes were indeed caused by metabolic changes rather than by change of pH due to injection, pH measurements were performed. Therefore, the metabolic modifiers were injected individually into separate tubes of culture media and pH changes were measured by a pH meter. The ratios of media volume to injection volume were consistent with the actual cell experiments.

## 3.2 Image Acquisition and Processing

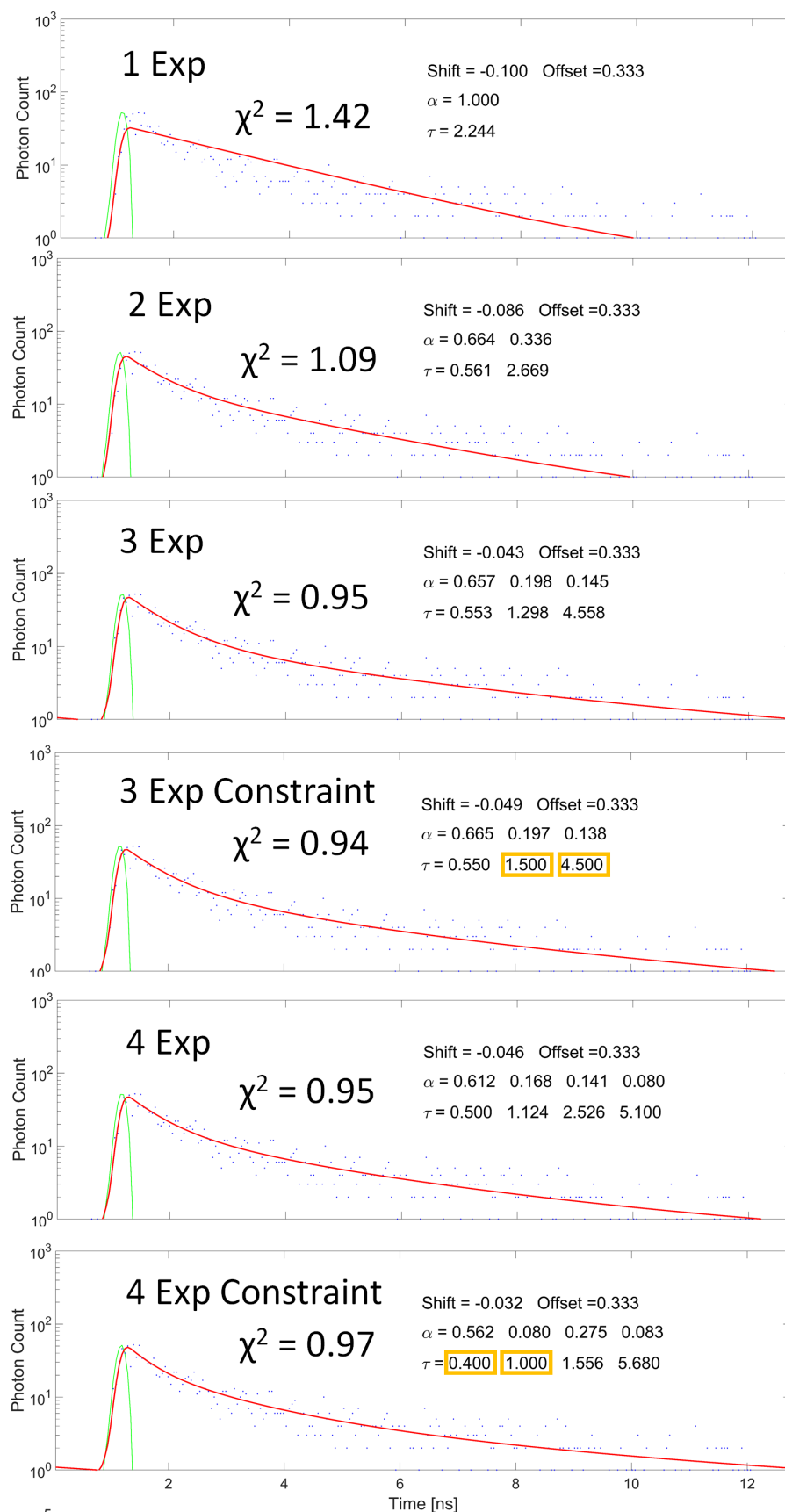
### 3.2.1 Lifetime Fitting

For the FLIM analysis it is often not clear which model, in particular which number of exponential components, should be used to fit the data. In literature, endogenous fluorescence of NADH in live cells has been fitted with double, triple and quadruple-exponential fits [9, 12, 129, 21]. The SPCImage (7.01, Becker & Hickl) software was used to fit the fluorescence signal at each area ( $3 \times 3$  pixels) with up to triple-exponential fits according to the following equation:

$$I_{fit}(t) = I_{offset} + \sum_{i=1}^N \alpha_i e^{\frac{-t}{\tau_i}} \quad (3.2)$$

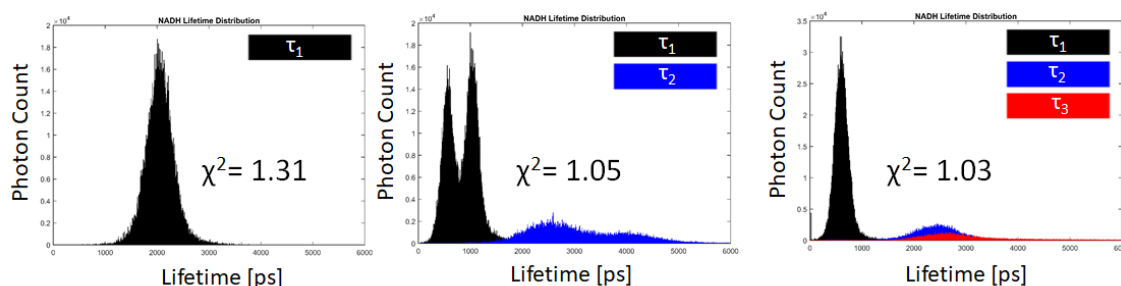
Where  $N = 1, 2$  or  $3$  is the number of exponentials and  $I_{offset}$  represents the noise coming from a detector and ambient light. The variables  $\alpha_i$  and  $\tau_i$  represent the relative contribution, and fluorescence lifetime of component  $i$ , respectively. The offset was determined by the number of photons which are in the time channels before the rise of the fluorescence decay trace starts and it must be taken into account to avoid the artificial generation of long-lifetime components by the fitting process. The shift denotes a linear shift between the calculated and the actually used response function and is determined by minimization of  $\chi^2$ . The shift that results in the best fit is fixed to the optimum value and used for the analysis of the entire image.

Fig. 3.10 shows a representative fluorescence decay which was described by a different number of exponential fits. For the three and four exponentials fits a free and a lifetime constrained fitting routine were used based on the work of Meleshina et al and Yaseen et al [129, 9]. Meleshina et al identified three fluorescence lifetimes in differentiated adipocytes at 750 nm wavelength and hypothesized that the shortest lifetime component around 300 ps represents free NADH, while a lifetime component around 1.5 ns represents bound NADH. The third lifetime component at 4.5 ns is associated with NADPH. The bound NADH and NADPH fluorescence lifetimes were fixed at 1.5 and 4.5 ns, respectively, enabling an analysis that significantly relaxes the requirements on the minimum photon numbers and speeds up the computational time. Yaseen et al concluded that the first two lifetime components of a four-exponential fit correspond to the different folding conformations of free NADH identified from NADH solution measurements. The lifetimes of these components remained the same between NADH measurements in solution and those measured



**Figure 3.10:** Using single-, double-, triple-, and quadruple-exponential fits on the same fluorescence decay of NADH. Triple- and quadruple-exponential fitting were performed free and constraint, meaning the fluorescence lifetime of two lifetime components were fixed to predefined values (yellow boxes).

in cerebral tissue of mice. Consequently, the fitting routine was modified so that  $\tau_1$  and  $\tau_2$  were constrained to lifetimes of 0.4 ns and 1 ns, respectively. Analysis of the fluorescence decays were performed with commercial software (SPCImage 7.01, Becker & Hickl). Attempts to fit the experimental fluorescence lifetime data at each pixel as the sum of more than three decaying exponentials are not available in the commercial software. This motivated the development of custom lifetime-fitting software in Matlab for data analysis as seen in Fig. 3.10 based on “Tcspcfits - A Matlab package for fitting multiexponential fluorescence decay curves” [130]. The optimization is based on a least-squares fitting routine including a Nelder-Mead simplex algorithm. Unfortunately, these iteration methods are very sensitive with respect to the initial guess values of the parameters such as lifetime and amplitude, and can be very time consuming for bad initial guesses, large data sets or larger numbers of exponential components [130]. Fig. 3.10 shows that a mono-exponential fit was found to be inadequate to model NADH fluorescence lifetime, as indicated by a poor residual profile and  $\chi^2$  value. While both 2-, 3- and 4-component models yielded more satisfactory residual profiles, the 4-component model consistently resulted in smaller fitting errors.



**Figure 3.11:** Using single-, double-, and triple-exponential fits on the same FLIM image of adipocytes to determine the correct NADH fitting model. An attempt to fit the data with a single exponential results in poor  $\chi^2$  values. Double exponential fitting results in good  $\chi^2$  values and triple exponential fitting delivers a small improvement in  $\chi^2$  values. However, the third lifetime component  $\tau_3$  is almost identical to lifetime component  $\tau_2$ , which suggests overfitting.

While the triple-exponential model yielded satisfactory residual profiles, the decaying exponentials routinely indicated the presence of four distinct NADH components, where each of the four components were found to be independently sensitive to metabolic perturbations. Additionally, after analyzing an entire image, the triple exponential just adds an additional lifetime component  $\tau_3$  which is almost identical to lifetime component  $\tau_2$  as seen in Fig. 3.11. Therefore, the triple-exponential model can be neglected.

Overall, the quadruple exponential fits constitute the best fitting results of the fluorescence decay. However, the use of the custom lifetime analysis software is very

time consuming compared to the commercially available software. Additionally, while double and quadruple exponential fitting identify different fluorescence lifetime parameters for each individual fluorescence decay, the overall NADH lifetime distribution and the parameters of the entire image are comparable with lifetime components  $C_1 = 0.5$  ns,  $C_2 = 1.0$  ns,  $C_3 = 2.6$  ns,  $C_4 = 3.7$  ns for the double exponential fitting and  $C_1 = 0.5$  ns,  $C_2 = 1.1$  ns,  $C_3 = 2.5$  ns,  $C_4 = 4.5$  ns for the quadruple exponential fitting. Taking this into account, we found the double-exponential fitting model to be appropriate for estimating NADH. It's more practical to use the commercial software and double exponential fitting compared to the quadruple exponential fit. Hence, almost all the subsequent images were analyzed with the commercial software.

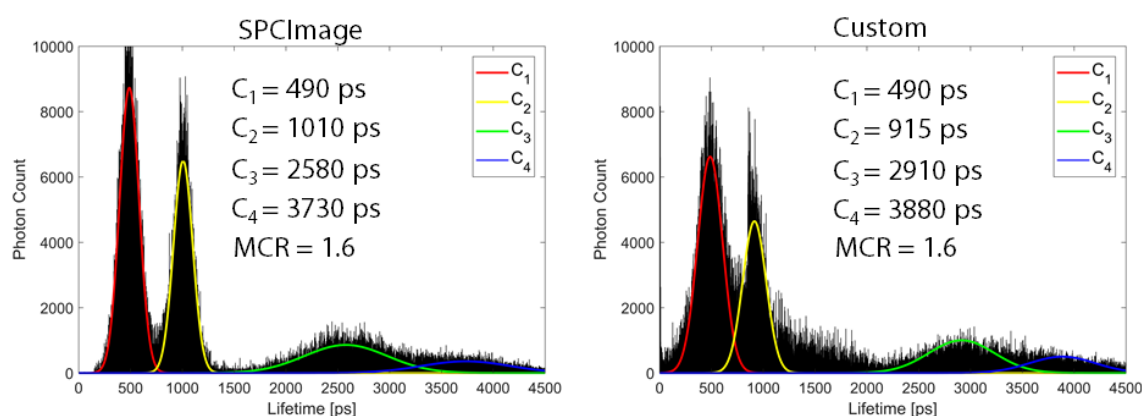


**Figure 3.12:** Comparison of the NADH lifetime distribution of a double exponential fit of an adipocyte FLIM image between the commercial SPCImage software results and the custom results. Fluorescence lifetime parameters and the MCR value are comparable for both methodologies. However, the commercial software data analysis is significantly faster.

### 3.2.2 Instrument Response Function

The instrument response function (IRF) is the function the FLIM system would record when it detected the laser pulse directly. For the measurement of the instrument response function on a multi-photon microscope setup, several ultrafast processes that change the excitation wavelength into a wavelength that passes the dichroic mirrors in the detection light path can be used. Unlike laser light reflection, the emission signal can be separated and detected. Fig. 3.13 shows the use of urea crystals on a microscope slide to produce second harmonic generation. Strong second harmonic generation (SHG) signals were generated at 780 nm wavelength, 20 mW laser output power, 0.73 V PMT gain and detected with a  $410 \pm 20$  nm



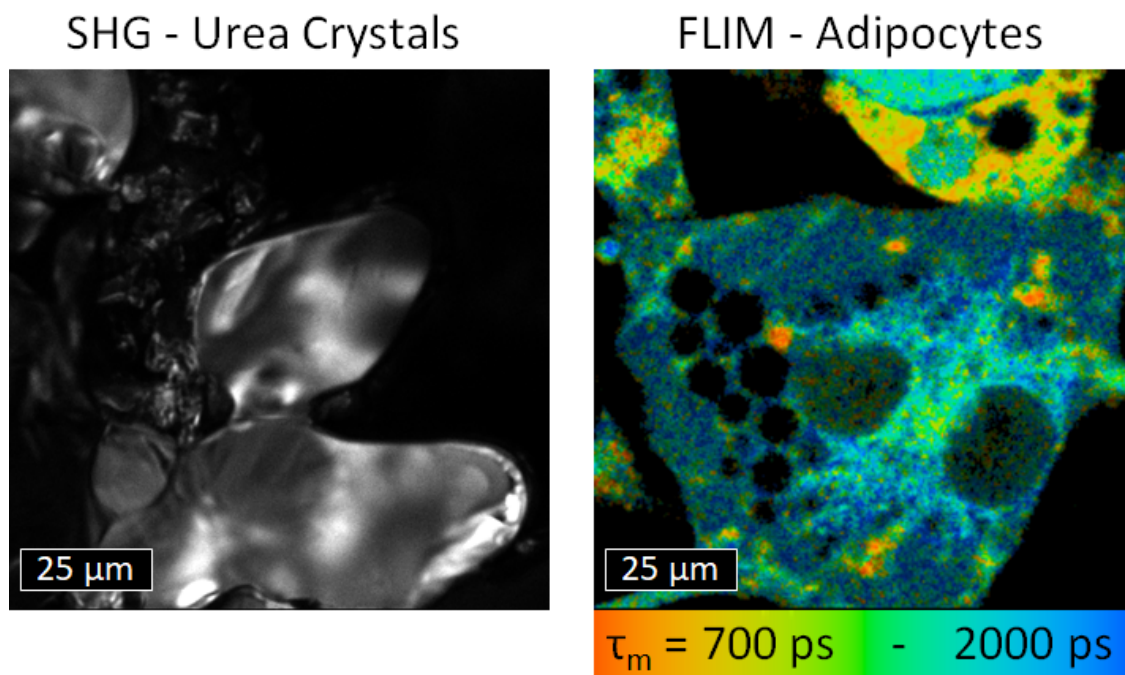


**Figure 3.13:** SHG of urea crystals for determination of the instrument response function of the FLIM setup. A FLIM image of 3T3-L1 adipocytes using the measured IRF

band-pass filter (HQ410/40M, Chroma) which was placed downstream of a 480 nm dichroic mirror. The detection PMT (H7422-50, Hamamatsu) is a high-speed, high-sensitivity PMT module that features excellent sensitivity in the red and near-infrared region with an IRF width from about 200 ps to 350 ps. The IRF width does not determine the minimum fluorescence lifetime detectable by TCSPC. The fluorescence lifetime is determined by the fitting model of the fluorescence decay data and depends on the signal-to-noise ratio of the raw data. Therefore, lifetimes considerably shorter than the IRF width can be determined [49]. Even though the used method delivers ultrafast signals at a wavelength detectable by the FLIM system, the use of SHG required a change in laser wavelength (780 nm) compared to the experimental use for NADH (755 nm). This can cause a shift in amplitude and phase of the timing reference pulses and thus a shift in the measured IRF [9]. However, measured fluorescence lifetimes of reference fluorophores fluorescein and NADH solution conform with lifetimes reported in literature. The fluorescence decay, the FLIM system records is the convolution of the true fluorescence decay profile with the IRF. Lifetime parameters are derived from the recorded decay by convoluting a model function with the IRF, and fitting the result to the data. Therefore, an estimated IRF is required to analyze fluorescence lifetime parameters from the

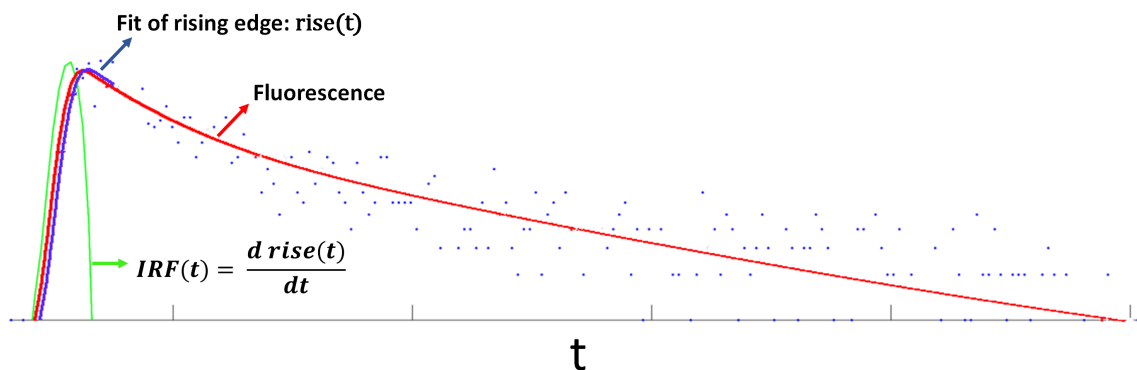


**Figure 3.14:** Calculation of the synthetic IRF (green) by using the rising edge (blue) of the fluorescence signal (red).

measured fluorescence data. The SPCImage software (7.1, Becker & Hickl) calculates an IRF from the fluorescence decay data themselves and uses this synthetic IRF for the data analysis Fig. 3.14. This technique assumes that the fluorescence lifetime is long compared to the width of the IRF. Therefore, the rising edge of the fluorescence signal can be fitted with a suitable function  $rise(t)$  and the integral of this function can be assumed to be the IRF. This calculation is performed on the brightest spot on the image and the resulting IRF is used for the entire image. Under the circumstance, that the brightest spot of the image is a dust fragment or some sort of artifact, a manual selection of a representative spot of fluorescence was performed. This procedure was used for almost all lifetime images presented in this thesis as it yields nearly identical fit results with a decay obtained with a measured IRF (green colored peak) as seen in Fig. 3.15. The lifetimes and amplitudes of the decay components do not differ by more than 10% even though the shortest lifetime component has a lifetime of about 500 ps, which is close to the width of the IRF. All the parameters are almost identical since the shape and width of the synthetic and real IRF are very similar and shorter than the fluorescence lifetimes. Thus, the IRF has no impact on the shape of the measured fluorescence decay after the first couple hundred picoseconds after the excitation maximum. Additionally, a comparison of NADH lifetime distribution of an entire image using the FLIM analysis with a synthetic IRF and the real IRF is shown in Fig. 3.16. As can be seen from the figure, the outcomes are practically undistinguishable. Therefore, the synthetic IRF was used and no effort of measuring a new IRF before each experiment had to be taken.



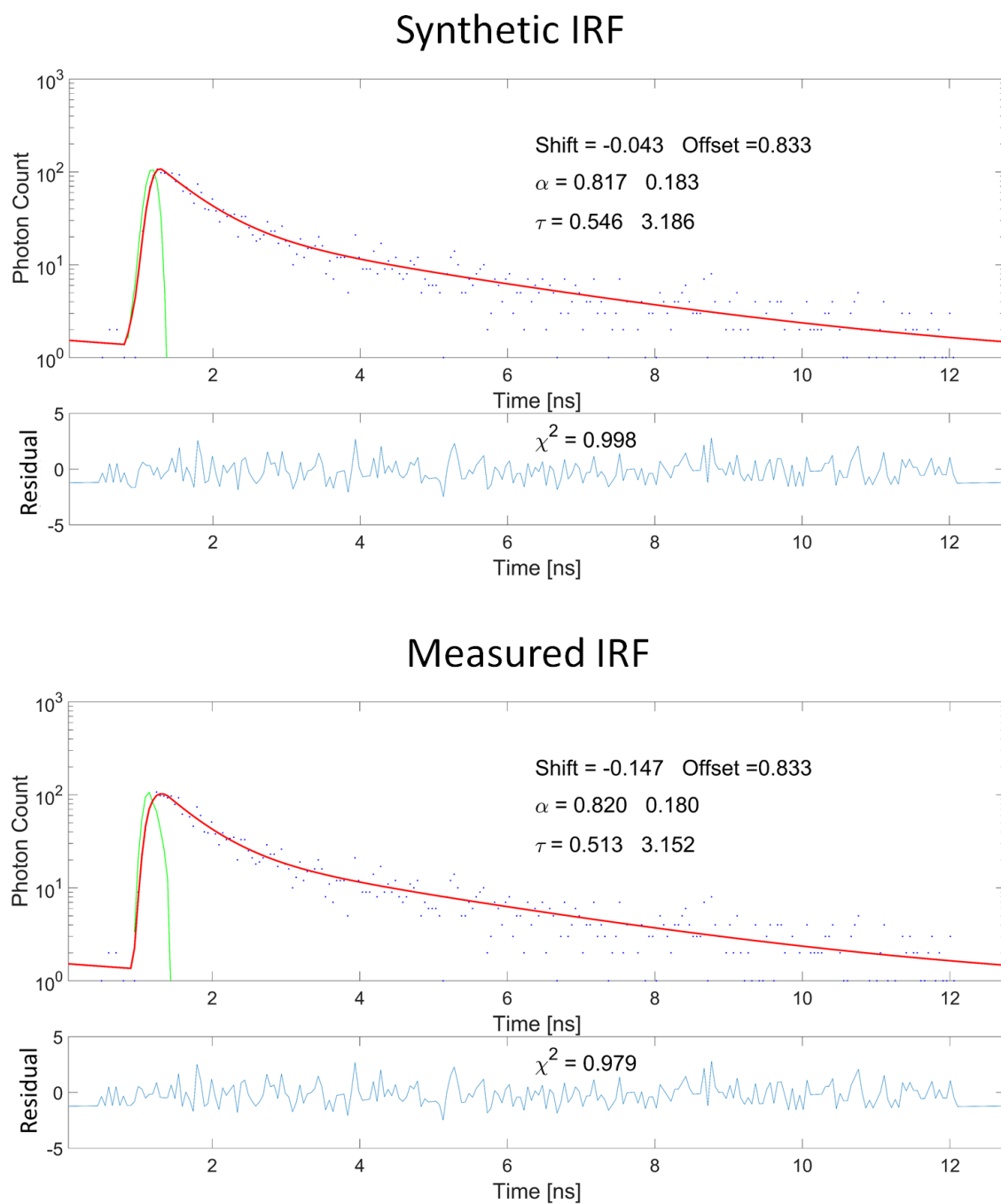


**Figure 3.15:** Comparison of the fluorescence lifetime decay of NADH of adipocytes using a synthetic IRF of SPCImage and a measured IRF determined by the SHG of urea crystals

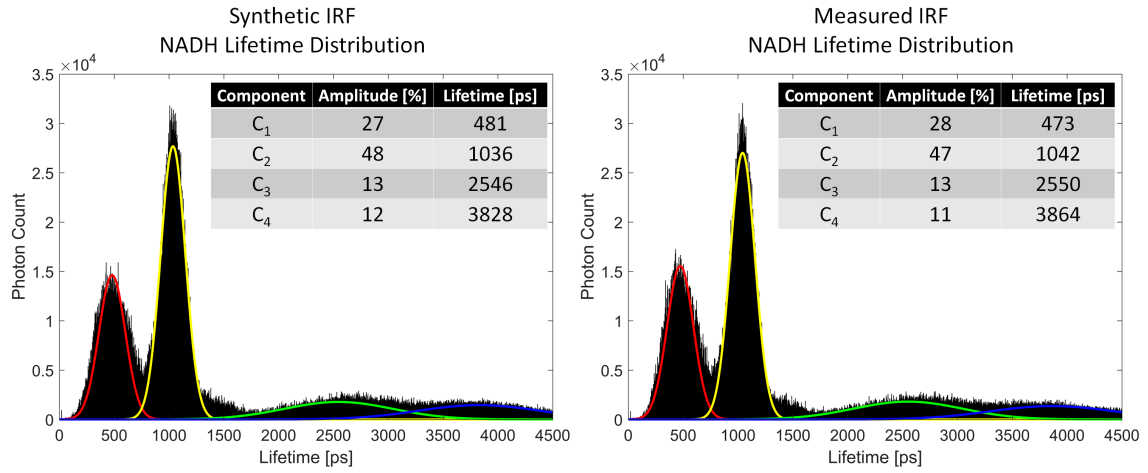


**Figure 3.16:** Comparison of the NADH fluorescence lifetime distribution of an entire FLIM image of adipocytes using a synthetic IRF and a measured IRF determined by the SHG of urea crystals

### 3.2.3 Phasor Analysis

The phasor plot is a graphical and fit-free representation of raw FLIM data. Phasor plots were generated by a custom designed software developed in Matlab based on the source code of Lanker et al [131]. Fig. 3.17 shows a typical FLIM image of adipocytes and its phasor plot generated by the commercially available software SPCImage and by the Matlab software. Even though the generation of the phasor plots is slower compared to the commercially available software, SPCImage is missing key functions necessary for the phasor analysis such as fluorescence lifetime and component determination. Therefore, the custom software was used for all subsequent phasor plot images and analysis. The intensity  $I(t)$  of a time-resolved fluores-

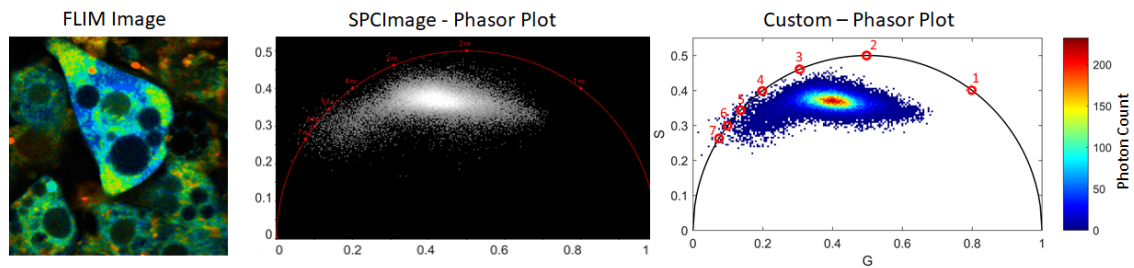


**Figure 3.17:** Phasor plot comparison of the SPCImage software and a custom phasor plot software in Matlab for data analysis.

cence decay recorded at each pixel location can be plotted as a single point in the phasor plot by applying the sine and cosine transforms to the measured decay data.

This is equivalent to the real and imaginary components of the Fourier transform of the decay data as described in Eq. 2.30 and Eq. 2.31. The universal semicircle is a lifetime ruler in the phasor plot, where the lifetimes increase counterclockwise from right (1,0) (lifetimes approaching zero) to left (0,0) (lifetimes approaching infinity). A phasor population falling on the semicircle indicates a mono-exponential decay, while multi-exponential decays fill the area inside the semicircle as linear combinations of their contributing mono-exponential components. Principal component analysis was used to create fitted linear functions on the universal circle to determine fluorescence lifetimes. As shown in Fig. 3.18, the schematic phasor plot, composed

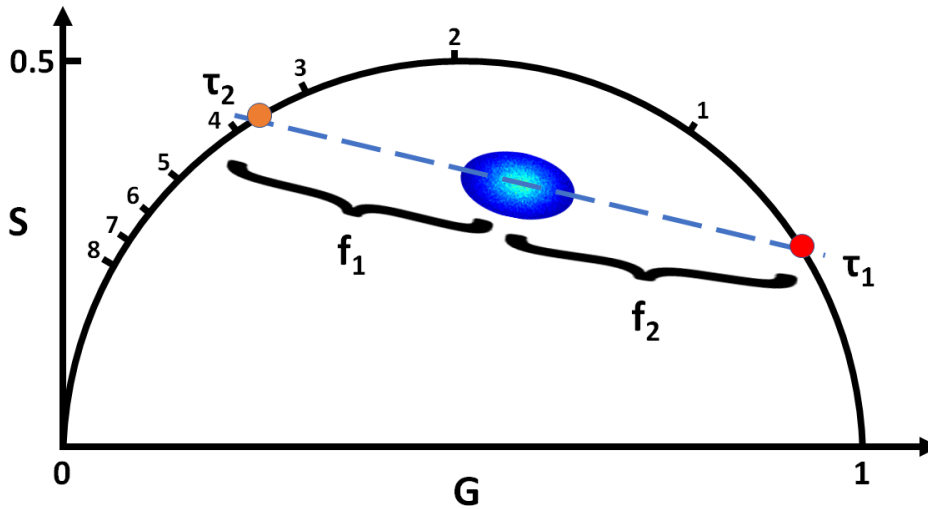


**Figure 3.18:** Schematic of phasor plot properties of a fluorophore with a bi-exponential decay showing the intersections of a linear fitted line with the universal circle representing lifetimes  $\tau_1$  and  $\tau_2$ . Lifetime fractions  $f_1$  and  $f_2$  show the distance of the mean of the phasor data to the universal circle. The shape of the phasor data is determined by a 95% confidence ellipse. Relative lifetime contribution  $\alpha_i$  ( $i = 1, 2$ ) is calculated by  $\alpha_i = f_i / (f_1 + f_2)$ .

of two lifetimes, lies on a fitted line connecting it to the universal circle, where the two intersecting points between the line and the semicircle represent each individual lifetime. While exponential fitting requires an assumption of the number of exponential components, the phasor approach does not require such initial assumptions for the purely graphical representation seen in Fig. 3.17. However, for the analysis and generation of lifetimes of the phasor plot, one has to decide the number of lifetime components. For two lifetime components as shown in Fig. 3.18, the fractional contribution of each of the two components to the total intensity is given by the length of the line connecting the mean of the phasor data with the intersection of the universal circle of the opposite component, divided by the length of the entire line uniting the two points (lifetimes) on the universal circle. The phasor plot used is represented by an intensity pseudo-color scale which takes advantage of the linear

addition property of the phasor representation. A continuous and linear color scale divided into 256 levels represents the amount of phasor points with the same G and S location. This allows not only to visualize shifts in lifetime but also shifts of the amplitude of the lifetime components induced by events such as enzyme binding and metabolic perturbations. If a sample has a multiexponential fluorescence decay or when several fluorophores with slightly different lifetime are present the phasor plots are not as straightforward to interpret. A common method to separate components having the same phasor location but different lifetime distributions is the multi-harmonic lifetime analysis, where higher harmonics of the laser repetition rate are used.

#### 3.2.4 Multi-Harmonic Phasor Analysis

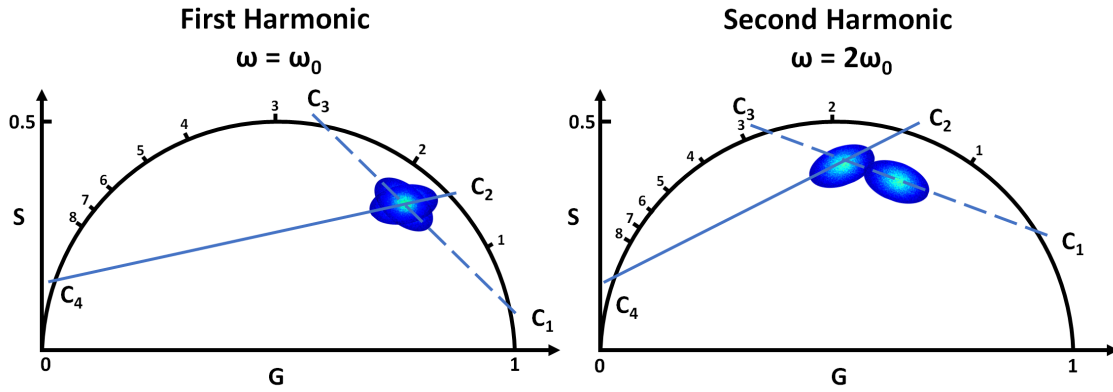


**Figure 3.19:** Schematic of the principle of separating phasors having the same location but different lifetimes by multi-harmonic analysis. In the first harmonic, the phasor points for each fluorescent species are overlapping. Adjusting the scale of the phasor plot by using the second harmonic of the laser repetition rate  $\omega_0$  results in two distinct clusters without changing the values of the individual lifetime components  $C_1$ ,  $C_2$ ,  $C_3$ , and  $C_4$ .

Given a mono-exponential lifetime value, the phasor shifts to the left along the semicircle for a lower angular modulation frequency  $\omega$  (equal to  $2\pi f$ , where  $f$  is the laser repetition rate) which results in an increase of the  $S/G$  ratio as seen in the following equations:

$$G = \frac{1}{1 + \omega^2 \tau^2} \quad S = \frac{\omega \tau}{1 + \omega^2 \tau^2} \quad \tau = \frac{1}{\omega} \left( \frac{S}{G} \right) \quad (3.3)$$

These equations show that the scale of the universal circle can be simply adjusted by varying the modulation frequency to generate the phasor plot, making the phasor plot very flexible to visualize different lifetimes and highlight the contrast upon the lifetime values. When applying phasor analysis to frequency-domain-based lifetime measurements, the modulation frequency of excitation light affects the phasor plot by mapping lifetimes on different regions of the phasor universal circle. For time-domain lifetime measurements, similar practices have been implemented, where available modulation frequencies are integer multiples of the fundamental modulation frequency called harmonics. Those harmonics of the laser repetition rate are often used for complex lifetime analysis of several fluorescence species with multi-exponential decays.

A common way to separate components having overlapping phasor locations but different lifetime distributions is to perform a multi-harmonic analysis of the fluorescence lifetime data (Fig. 3.19) with higher harmonics of the angular modulation frequency, wherein the harmonics are  $\omega = n\omega_0$  with  $n = 2, 3$  [132]. The phasor analysis can be performed with any harmonics of the original modulation frequency without changing the lifetime value. The idea of this method is that once the frequency is increased, the phasor plot shifts along the universal circle toward the (0,0) coordinate. The best frequency for maximal sensitivity to changes in the phasor location is when the phasor is in the central region of the phasor plot. If the harmonic repetition rate applied is too high or too low, the phasors of various molecular species will be crowded in a small area of the phasor plot, and their separation becomes problematic. Additionally, this method can be performed to validate if a fluorophore is pure and if it for example has a truly bi-exponential decay. If that is the case the phasor plot results in the same lifetimes for each harmonic. Therefore, the phasor plots of NADH of adipocytes at higher harmonics (2 and 3) of the laser repetition rate were analyzed. Each of the three phasor plots in Fig. 3.20 was analyzed by a single linear fit.

If NADH had a bi-exponential decay, each of the harmonics would result in the same fluorescence lifetime. However, each harmonic resulted in different fluorescence lifetimes, indicating more than two fluorescence species or the decay of one fluorescent species is higher than bi-exponential. By assuming two fluorescence species (mitochondrial and cytosolic NADH), the same approach of applying multi-harmonic analysis, can then be used to separate the phasor clusters (Fig. 3.19). However, higher harmonics of the laser repetition rate did not result in a separation of two potential (mitochondrial and cytosolic) NADH populations Fig. 3.20. This inability of further separating the phasor points was expected since the phasor cluster of the first harmonic already had a central position within the semicircle which results in maximum sensitivity.

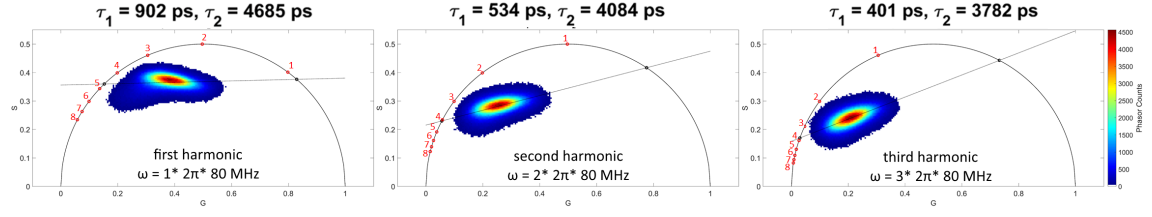


**Figure 3.20:** Phasor analysis of NADH of adipocytes at different harmonics of the laser repetition rate. First harmonic of the original modulation frequency  $f$  at 80 MHz with  $n = 1$  in  $\omega = n\omega_0$ , second harmonic with  $n = 2$ , and third harmonic with  $n = 3$ . Different fluorescence lifetimes  $\tau_1$  and  $\tau_2$  at each harmonic mean that **a:** more than bi-exponential fluorescent species is present or **b:** the decay of one fluorescent species is higher than bi-exponential. Higher harmonics of the laser repetition rate did not result in further separation of two potential (mitochondrial and cytosolic) NADH populations.

#### 3.2.5 Phasor Calibration

For time domain FLIM, the phasor must be computed from the measured decay. This decay is distorted by the width of the instrument response function (IRF). Similar to the curve-fitting analysis, phasor analysis requires a calibration procedure to account for this. In order to establish the correct scale for the plotted phasor points, the coordinates of the phasor plot are calibrated by using a standard sample of known mono-exponential lifetime such as fluorescein (4.1 ns) or alternatively, a directly recorded IRF data trace for the zero lifetime. By applying the Fourier transform to the reference data, the phasor location of the IRF can be determined [133]. This location can then be used to calculate a correction value to the amplitude  $M_{cor}$  and a phase  $\phi_{cor}$  about the origin [133]:

$$G = \frac{G_r * \cos(\phi_{cor}) - S_r * \sin(\phi_{cor})}{M_{cor}} \quad (3.4)$$

$$S = \frac{G_r * \sin(\phi_{cor}) + S_r * \cos(\phi_{cor})}{M_{cor}} \quad (3.5)$$

where  $G_r$  and  $S_r$  are the phasor coordinates before the IRF calibration is applied. This correction method is not an addition or subtraction of a phasor vector but is a rotation and rescaling of the phasor. Fig. 3.21 shows the phasor plot of fluorescein before and after calibration.

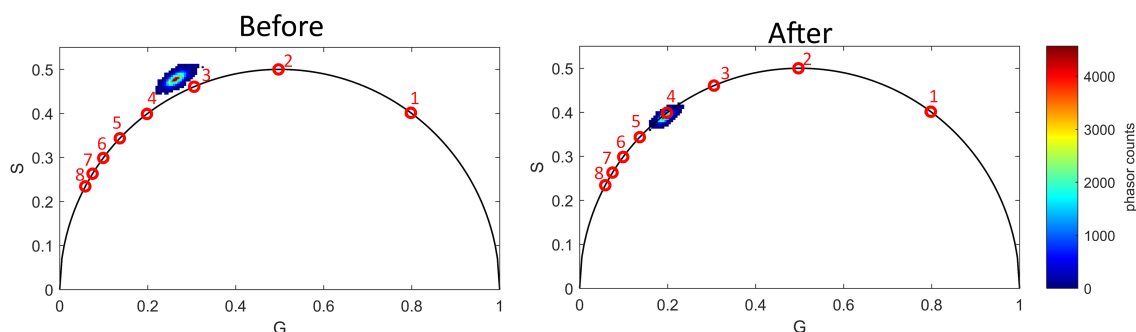


**Figure 3.21:** Phasor plot of fluorescein with a fluorescence lifetime of 4.1 ns before and after calibration of the IRF.

### 3.2.6 NADH FLIM Phasor

The main application of the phasor approach employed in this thesis is the NADH phasor plot. In biological samples with multiple fluorophores present and for the analysis of more than two fluorescence lifetimes components the interpretation of the phasor plot is often not possible using the standard principle component analysis. Therefore, one way of representing specific areas in the FLIM image of a phasor plot is the cursor selection method. In the cursor selection method, specific areas of the phasor plot can be manually selected by outlining areas which are then highlighted in the FLIM image. This technique allows to select the phasor cluster of interest with the cursor and the corresponding pixels in the image will be color coded. This method can also be used reciprocal, meaning the manual selection can also be used on the FLIM image to create a phasor plot of a specific area. For the traditional two-lifetime model of NADH, this method can be used to distinguish between free and bound NADH and follow the metabolic trajectory along phasor line [11]. For the 4-lifetime model of NADH this feature is of limited use due to heterogenous and overlapping lifetimes within the phasor plot as well as the FLIM image.

Therefore, a combination of exponential fitting and phasor analysis was tested. The lifetimes of phasor plots that arrange in broad clusters are analyzed by combining an exponential fitting lifetime distribution with the phasor analysis. A segmentation of the exponentially fitted NADH lifetime distribution can be performed by manual selection of ranges of lifetimes (histogram splitting) or using markers of specific features in the FLIM image such as mitochondrial stains to create masks.

For histogram splitting, specific ranges of the lifetime distribution such as the NADH lifetime component  $C_1$  from 0 to 700 ps and therefore its corresponding pixel in the FLIM image are manually selected (Fig. 3.22.). The FLIM image pixels that were segmented by that method, are then analyzed by the phasor approach. The phasor points generated by that segmentation result in a phasor distribution along a single line joining the exponentials. From this simplified phasor plot, parameters like

lifetimes and fraction ratios can be identified. Finally, the lines representing the fluorescence lifetimes of multiple segmentations can also be used to describe the original broad phasor plot cluster.

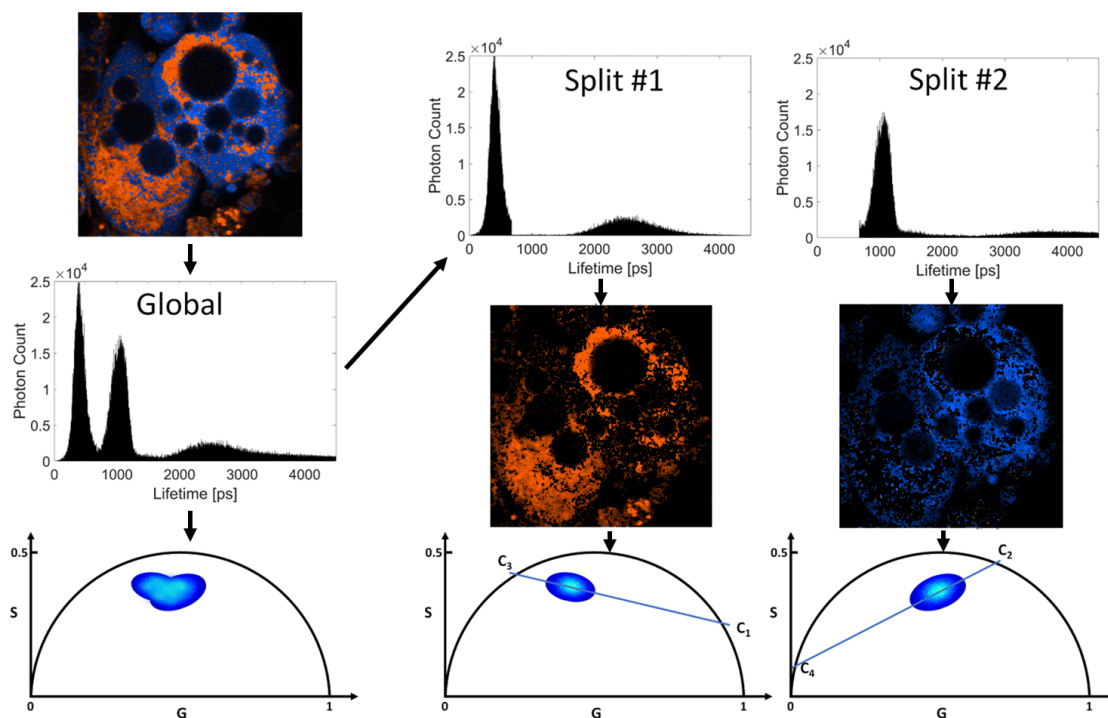


**Figure 3.22:** Schematic NADH lifetime distribution defined by exponential fitting and the corresponding phasor plot. Two fluorescence species (cytoplasm in blue and mitochondria in red) with a bi-exponential fluorescence decay are present. However, interpretation and analysis of the global phasor plot of both NADH species is not possible since the phasor points are overlapping. Therefore, manual splitting of the lifetime distribution histogram is performed, and corresponding images are generated. The phasor analysis of these images creates plots that can be interpreted with conventional methods.

#### 3.2.7 Region of Interest Selection

Regions of interest (ROI) were manually selected using the selection tool in SPCImage or the `impoly` function in MATLAB. In SPCImage the manual selection is achieved by clicking the polygonal ROI symbol and outlining an area. Similar to that, the MATLAB function `impoly` encapsulates an interactive polygon over an image. It allows the user to add vertices and adjust the size and position of the polygon by using the mouse. Defining ROIs save computation time since only the selected area is processed and therefore, the parameter histogram is calculated from



the pixels inside the ROI only. The ROI selection can thus be used to obtain lifetime histograms from selected regions of the image. Both tools were used to enable the analysis of individual cells as well as distinguishing different cells within the same field of view. Additionally, it was used to remove unwanted structures such as highly fluorescent dust and particles which interfered with the lifetime analysis.

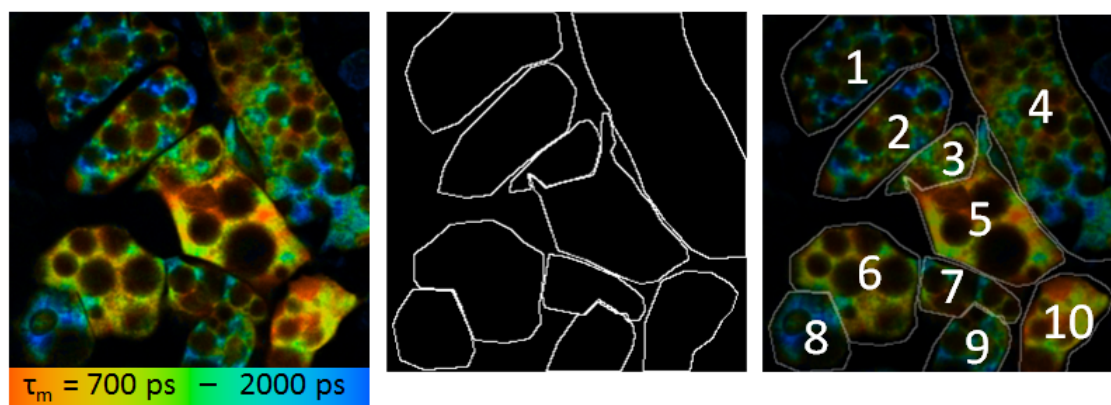


**Figure 3.23:** Manual region of interest selection of several cells in one field of view for individual cell analysis.

### 3.2.8 Spatial and Temporal Binning

Spatial binning defines an area of pixels that is added to the pixel of interest to increase the photon count for lifetime analysis. The binning factor can be adjusted according to the number of photons in the raw data, the desired spatial resolution, and the complexity of the decay model used [49]. For endogenous autofluorescence such as FAD and NADH, usually lifetime data should be calculated from several binned pixels to improve photon statistics. The applied binning of the FLIM images presented in this thesis does only affect the lifetime but not the intensity. Spatial binning yields considerably enhanced lifetime accuracy while slightly decreasing the effective resolution and spatial detail. Additionally, faster acquisition can be achieved and the noise of the FLIM images is reduced. However, a balance between the speed of the data acquisition and required resolution has to be determined depending on the strength of the fluorescence signals. A quadratic shape was used for the binning to increase the number of pixels around the pixel of interest. The number of pixels used for spatial binning does not change the total amount of pixels that are analyzed of a FLIM image. Fig. 3.24 shows the effect of spatial binning on the fluorescence lifetime distribution of NADH of adipocytes. Exactly like spatial binning, temporal binning can be used to improve lifetime accuracy and image acquisition speed. While TCSPC provides the highest temporal resolution of flu-

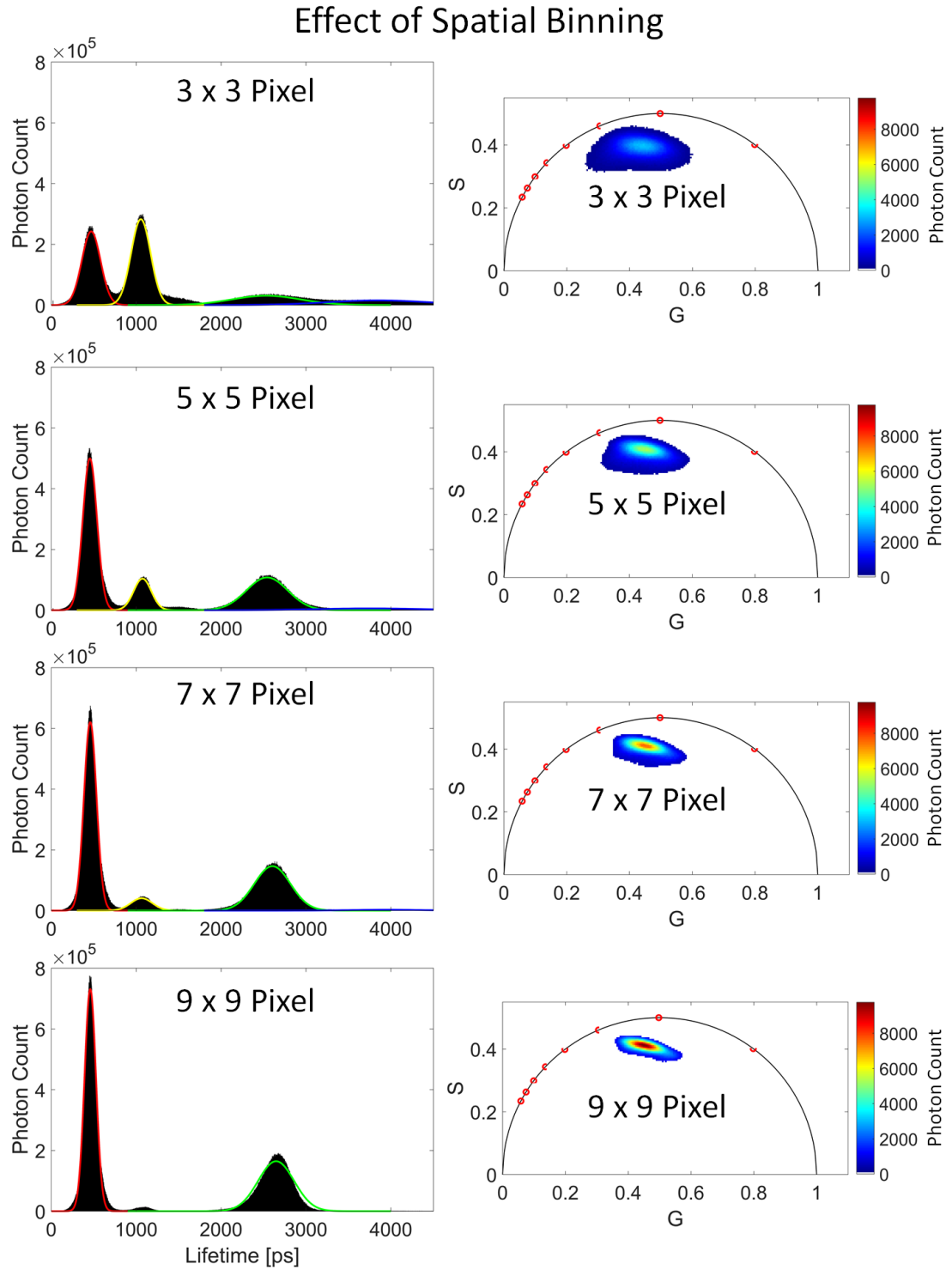


**Figure 3.24:** NADH fluorescence lifetime distribution of the same FLIM image using different sizes of spatial binning. The NADH histogram based on the intensity and lifetime of all pixels of the FLIM image using bi-exponential fitting with a spatial binning of 9 x 9 pixels (14  $\mu\text{m}^2$ ), 7 x 7 pixels (8.5  $\mu\text{m}^2$ ), 5 x 5 pixels (4.3  $\mu\text{m}^2$ ), and 3 x 3 pixels (1.5  $\mu\text{m}^2$ ).

orescence lifetime decays, image acquisition and data analysis are inherently slow. Thousands of photons per pixel are required for accurate exponential decay fitting, especially for multi-exponential decays. Furthermore, only one photon per laser pulse can be resolved, yet photon yield must be much less, around 10%, in order to avoid bias towards early arrival photons [46]. Therefore, it is often useful to reduce the number of time channels to decrease the required memory space, or to obtain more photons per time channel. Temporal binning means combining several analogue to digital converter (ADC) channels or time bins into one. For the analysis shown in Fig. 3.25, the temporal resolution was reduced from the standard 256 time bins over 12.5 ns to 64 time bins, summing the number of photons in 4 consecutive time bins. The new fluorescence decay curves were analyzed to extract fluorescence lifetime parameters, which were compared to the traditional analysis with 256 time bins. Temporal binning of fluorescence decay curves was evaluated as a method to improve fitting accuracy and reduce acquisition time.

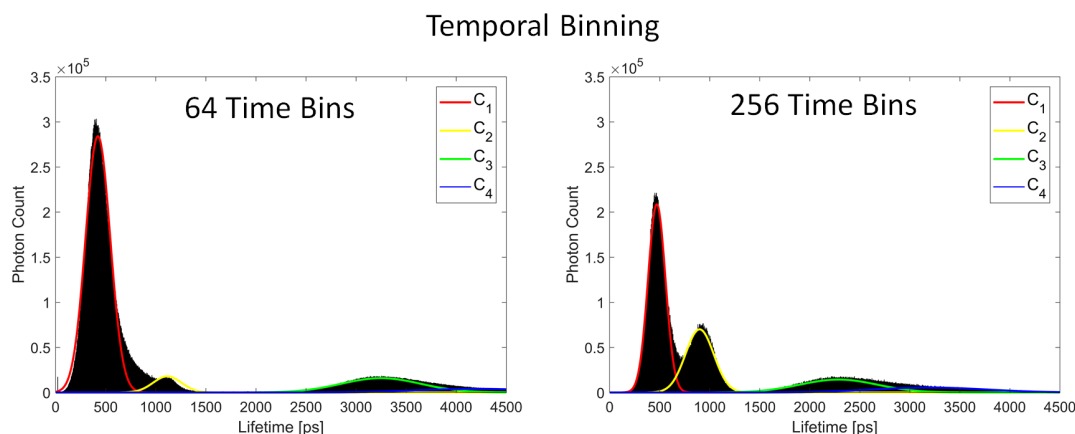


**Figure 3.25:** Fluorescence lifetime distribution of the same FLIM image using different numbers of time bins. The lifetime distribution histogram based on the intensity and lifetime of all pixels of a FLIM image using 64 and 256 time bins over 12.5 ns.

## 3.3 Cell Lines and Tissues

### 3.3.1 Murine Adipocytes

Mouse embryo 3T3-L1 preadipocytes were maintained in Dulbecco's modified Eagle medium (DMEM) supplemented with 10 % bovine calf serum and penicillin-streptomycin. To induce differentiation into mature adipocytes, confluent cells were

### 3 Materials and Methods

---

cultured in DMEM containing 10 % fetal bovine serum (FBS), 5  $\mu$ M dexamethasone, 0.5  $\mu$ g/mL insulin, and 0.5 mM isobutylmethylxanthine for 48 h to induce adipogenesis. Cells were then refed every other day with DMEM containing FBS and 0.5  $\mu$ g/mL insulin for 7 days REF [Wu 1995].

For primary murine preadipocytes, young mice were euthanized and epididymal, inguinal, and interscapular adipose pads were dissected, minced, and digested with collagenase at 1 mg/mL in HEPES-buffered solution at 37 °C under agitation for 45 minutes. After filtration, the cell suspension was centrifuged for 10 minutes at 100 G and the pellet containing the stromal vascular fraction was washed with DMEM media. Cells were plated in DMEM media supplemented with 10% FBS and penicillin-streptomycin. When cells reached confluence, adipocyte differentiation was initiated by addition of 5  $\mu$ M dexamethasone, 0.5  $\mu$ g/mL insulin, 0.5 mM isobutylmethylxanthine, and rosiglitazone 1  $\mu$ M for 48 hrs. Then, cells were fed every other day with DMEM containing FBS and 0.5  $\mu$ g/mL insulin.

For FLIM experiments, cells were seeded into coated 96 well glass bottom culture plates. The cells were grown to confluency, and differentiated as described above. On day 7 of differentiation, medium was refreshed 8 to 12 hours before the mature adipocytes were ultimately imaged.

#### 3.3.2 Murine White and Brown Adipose Tissue

6 to 10 week old male C57BL6 mice were sacrificed by cervical dislocation. Epididymal, subcutaneous inguinal, and interscapular adipose depots were excised and non-adipose tissue were removed. Each fat pad was cut into small sections using a scalpel resulting in 3 to 4 mg tissue samples as determined by a scale for each piece. The tissues were rinsed in fresh media and a pair of sterile forceps was used to place the samples into different containers, depending on the required condition. Three different tissue conditions were tested for imaging: fresh, cooled for 24 hours, and frozen for 24 hours.

Fresh: tissue specimen were imaged immediately after excision. Therefore, the samples were placed in glass bottom petri dishes with assay media at 37°C. Additionally, to prevent drying out and floating movements of the tissue specimen, a glass cover slip was placed on top. For the fresh samples, it was of great importance to work quickly and in a sterile environment and immediately image the tissue after excision. From euthanization of the mouse to imaging the samples, usually less than 15 min passed and the imaging sessions were kept under 30 minutes.

Cooled: tissue specimen were placed in 4°C media and transferred to a 4°C refrigerator for 24 hours. Then the tissue was placed into in glass bottom petri dishes with assay media at 37°C and the imaging was performed using the same protocol as for fresh tissue.

Frozen: fat samples were placed into Eppendorf tubes and were snap frozen with

liquid nitrogen and stored at  $-80^{\circ}\text{C}$  for 24 hours. The tissue samples were thawed and hydrated in  $37^{\circ}\text{C}$  assay media. Again, the same imaging protocol as for fresh and cooled samples was used afterwards.

### 3.3.3 HEK 293 Cultures

Human embryonic kidney cells 293 (HEK 293) were grown in advanced Dulbecco's modified Eagle Medium (Gibco) supplemented with 10% fetal bovine serum and penicillin-streptomycin. The cells were grown as monolayers in sterile 10 cm tissue culture dishes in a  $37^{\circ}\text{C}$ , 5%  $\text{CO}_2$  incubator. Cells were harvested with 5 ml of trypsin-EDTA (0.25% (w/v)) applied for a 2 min incubation, following removal of the culture medium. For imaging, cells were transferred to a 96 well glass bottom dish 24 hours before start. The surface area of the 96 well plate, is identical to the surface area of the 24 well Seahorse XF cell culture V7-PS plates. However, the well volume of the 96 well plates is smaller compared to the V7 plate, which contain  $525\ \mu\text{l}$  of media and each injection contains  $75\ \mu\text{l}$ . Therefore, only one third of the media ( $175\ \mu\text{l}$ ) and  $25\ \mu\text{l}$  of the injection was applied in the 96 well plate.

### 3.3.4 3T3-L1 Fibroblast

NIH 3T3 mouse embryonic fibroblast cells are an immortal cell line that has become a standard fibroblast cell line. Cells become confluent at a density of approximately  $40,000\ \text{cells}/\text{cm}^2$ , and a saturation density of about 50,000 cells can be reached. However, in culture, cells should not become completely confluent as this results in cells becoming senescent. NIH 3T3 cells do not adhere well to certain types of glass, therefore glass bottom dishes were coated with collagen. Cells were grown in DMEM formulated with the addition of 10% FBS at  $37^{\circ}\text{C}$  in 5%  $\text{CO}_2$ .

### 3.3.5 Mixed Cell Cultures

NIH 3T3 mouse embryonic fibroblast cells and differentiated 3T3-L1 adipocytes were used in mixed cell cultures. For FLIM imaging and OCR measurements, the cells were counted and seeded into collagen coated glass bottom 96 well plates and Seahorse XF cell culture V7-PS plates, respectively 24 hours before the experiment. For the FLIM imaging session, 10,000 adipocytes and 10,000 fibroblasts were seeded into the same well counted with a hemocytometer. For the OCR measurements with the flux analyzer, four conditions with different amounts of fibroblasts and adipocytes were tested: condition 1 was 10,000 adipocytes, condition 2 was 10,000

### 3 Materials and Methods

---

fibroblasts, condition 3 was 5,000 adipocytes and 5,000 fibroblasts, and condition 4 was 10,000 adipocytes and 10,000 fibroblasts in the same well.

#### 3.3.6 Human Skin Equivalent

The EpiDerm full thickness-400 (EFT-400) skin equivalent was obtained from Mat-Tek Corporation (Ashland, MA). The skin equivalent was engineered to enable in vitro skin research in which fibroblast-keratinocyte cell interactions are important. The EFT-400 system consists of normal, human epidermal keratinocytes and normal, human dermal fibroblasts cultured to form a multilayered model of the human dermis and epidermis. The epidermal and dermal layers are mitotically and metabolically active and exhibit in vivo-like morphological and growth characteristics. A Dulbecco's Modified Eagle (DME) based medium for maintaining cultures was supplied by manufacturer (EFT-400-MM). The skin samples are cultured at an air-liquid interface in tissue culture inserts. Upon arrival, while still at 4°C, epidermal-only wounds were induced using a sterile 1 mm dermal biopsy punch and the epidermis was mechanically removed using forceps. Afterwards, the EFT-400 culture inserts were placed in 6-well plates and equilibrated with 1 ml of EFT-400-MM medium at 37°C. Following overnight pre-incubation, the culture medium was replaced with fresh 5 ml of medium and skin cultures were placed with the epidermal side down on a microscope slide for imaging. Using a cover glass and 1 ml of culture media allowed stable positioning and hydration throughout the imaging session of up to 45 min.

### 3.4 Quantitative Analysis of Cell Metabolism

#### 3.4.1 Western Blotting

Western blot analysis was used to measure the expression of traditional markers of thermogenesis such as uncoupling protein 1 (UCP1). After treatment with forskolin and epinephrine, adipocytes were washed with phosphate-buffered saline (PBS) and lysed using mammalian protein extraction reagent containing a protease inhibitor cocktail. Protein concentration was measured using a Coomassie Plus assay kit. 100  $\mu$ g of each supernatant sample of protein was separated by electrophoresis and transferred to a 0.2  $\mu$ m trans-blot transfer medium nitrocellulose. Following transfer, membranes were blocked with 5% skim milk dissolved in tris-buffered saline (TBS) at room temperature for 1 h. Then, membranes were incubated overnight with primary UCP1 and GAPDH antibodies at 4 °C. Blots were washed 3 times with TBS and then incubated with horseradish peroxidase-conjugated secondary antibodies

for 1 h at room temperature. Blots were washed 3 times with TBS and then treated with chemiluminescent western blotting substrate (ECL Plus, Thermo Fisher). Finally, the blots were exposed to X-ray films and developed. Expression levels were quantified and normalized to housekeeping gene glyceraldehyde 3-phosphate dehydrogenase (GAPDH). Changes with respect to the control expression were computed and the normalized fold change in expression was compared to optical metabolic analysis and results of the extracellular flux analyzer.

### 3.4.2 Cellular Respiration and Extracellular Acidification

#### Seahorse XFe24 Analyzer

Oxygen consumption rate (OCR) and extracellular acidification rate (ECAR) were determined in mono-layer cell cultures and tissues, using a XFe24 analyzer (Seahorse Bioscience). The analyzer measures the rate of change of dissolved oxygen and pH in the media immediately surrounding living cells. The flux analyzer works with a microplate system having a cell culture plate at the bottom and a disposable biosensor cartridge on top, creating a 2  $\mu$ l to 6  $\mu$ l microchamber in which rapid changes in oxygen consumption rate and extracellular acidification rate can be measured. The changes are measured by the biosensor cartridge which sits 200  $\mu$ m above the mono-layer cell culture and that contains oxygen and proton biosensors. These biosensors are fluorophores embedded in a polymer where one fluorophore is quenched by oxygen and measures mitochondrial metabolism, while the other fluorophore is sensitive to protons and indicates glycolysis. Fiber optic bundles of light emitting diodes are simultaneously lowered into the cartridge and emit light, resulting in excitation of the embedded fluorophores. Changes in fluorescence emission due to alterations in oxygen and proton levels are then detected by the sensors. Changes in the extracellular media are caused by the consumption or production of chemical compounds by the cells. Measurements of the media above the cell monolayer can be used to determine rates of cellular metabolism in a non-invasive and label-free procedure. This indirect measurement of the cellular metabolism is typically performed for 5-8 minutes. Here, during the measurement cycle, the media is mixed for 3 minutes, then a waiting period of 2 minutes is initiated, followed by measurements for 3 minutes in which the dissolved oxygen and pH levels are measured. The measurement is performed using optical fluorescent biosensors and are reported in pmol/min for OCR and in mpH/min for ECAR. One metabolic compound at a time is injected to the media and mixed, and then the OCR and ECAR measurements are performed and repeated. As cells change their metabolic activity, the relationship between OCR and ECAR changes. The non-destructive behavior of the measurement and the temperature control of the analyzer allow for several consecutive injections over a period of hours or days.



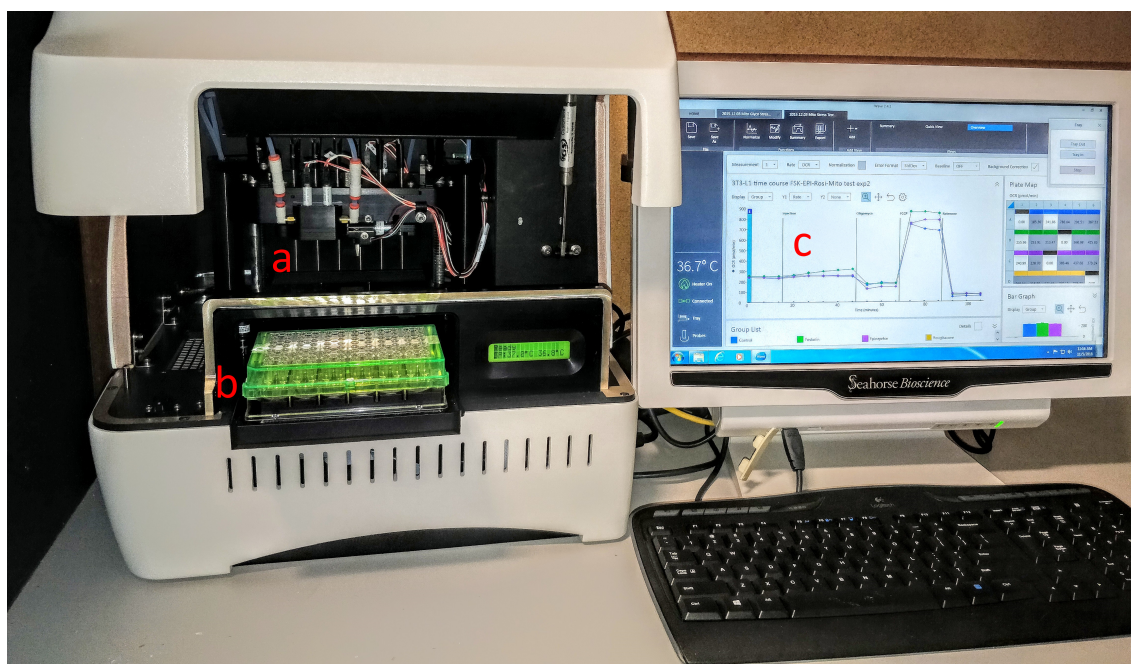


**Figure 3.26:** Picture of the XFe24 analyzer. **a:** 24 fiberoptic bundles which simultaneously insert themselves into the sensor cartridge at 200  $\mu\text{m}$  above the cells. The fiber optics emit light that excites the fluorophores of the sensor cartridge and then reads the changes in fluorophore emission based on the changes of oxygen and protons. **b:** 24 well disposable sensor cartridge with integrated fluorophores. The fluorescence of the first fluorophore is quenched in the presence of oxygen and the second fluorophores fluorescence is sensitive to protons. The cartridge has drug injection ports which enable the injection and measurement of pharmacological reagents. **c:** The software (Waves, Agilent) illustrates changes in oxygen concentration and pH which are automatically calculated and reported as Oxygen Consumption Rate (OCR) and ExtraCellular Acidification Rate (ECAR) in real time, enabling time-resolved, kinetic data of cell metabolism.

#### Mitochondrial Respiration Stress Test

The mitochondrial respiration stress test is a kit of several reagents for assessing mitochondrial function. The stress test measures multiple parameters in one assay as seen in Fig. 3.27. The measurement protocol to determine mitochondrial respiration consisted of injections of: (1) oligomycin (1  $\mu\text{M}$ ) to inhibit mitochondrial ATP production and probe uncoupled respiration; (2) carbonyl cyanide-4-(trifluoromethoxy)-phenylhydrazone (FCCP, 1  $\mu\text{M}$ ) to induce maximal mitochondrial respiration; and (3) rotenone/antimycin (0.5  $\mu\text{M}$ ) to inhibit mitochondrial respiration. The compounds are reconstituted directly in assay medium and therefore, eliminating the need for DMSO or other solvents. The assay provides insight into the mechanism



of mitochondrial function and allows to investigate functional differences among cell types.

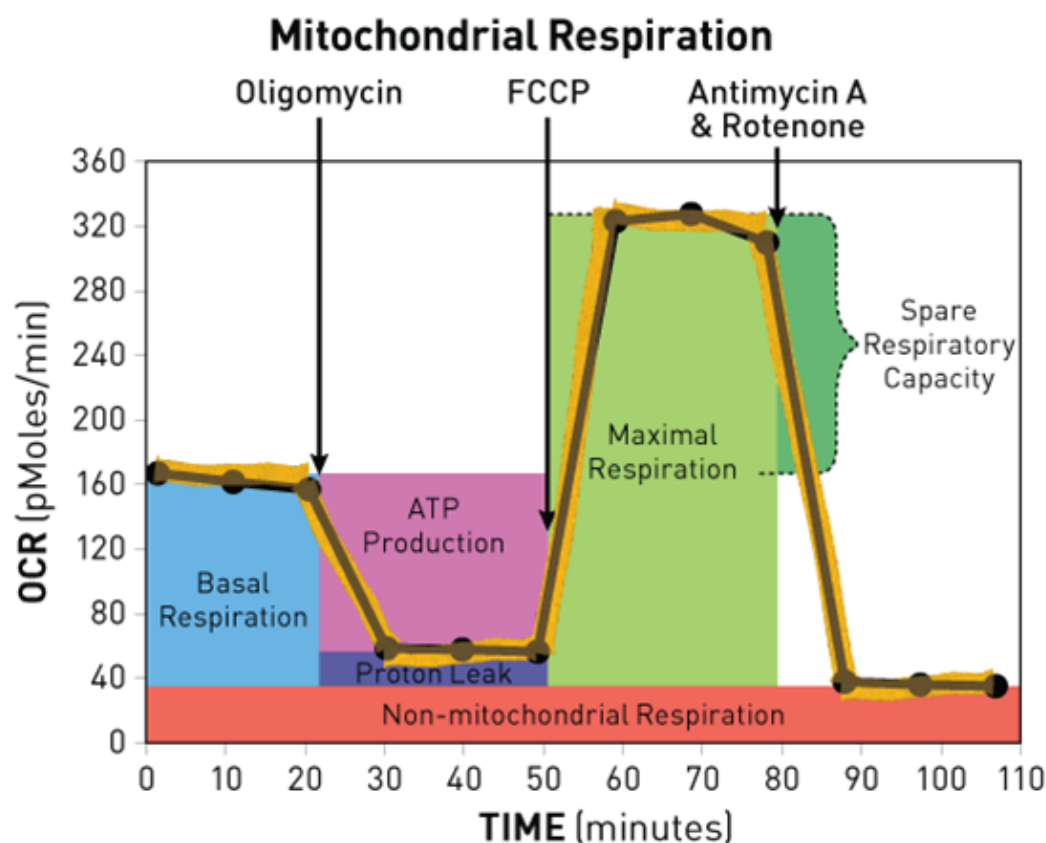


**Figure 3.27:** Mitochondrial Respiration Stress Test profile of consecutive injections and key parameters of mitochondrial respiration.

### Glycolytic Function Stress Test

The glycolytic function stress test is the standard test to measure glycolytic function of live cells. During glycolysis glucose in the cell is converted to pyruvate, and then converted to lactate in the cytoplasm, or  $CO_2$  and water in the mitochondria. The conversion of glucose to pyruvate, and subsequently lactate, results in a net production and extrusion of protons into the extracellular medium. This results in the acidification of the medium surrounding the cell which the flux analyzer directly measures. Injections consisted of glucose, oligomycin and 2-deoxy-D-glucose (2-DG) as shown in Fig. 3.28. Glucose (10 mM) is taken up by the cells and represents the rate of glycolysis under basal conditions. The cells utilize the glucose and extrude protons into the surrounding medium causing a rapid increase in ECAR. Oligomycin

(1  $\mu$ M) shifts the energy production to glycolysis and with the subsequent increase in ECAR revealing the maximum glycolytic capacity of the cell. 2-DG (50 mM) is a glucose analog that inhibits glycolysis and decreases ECAR.

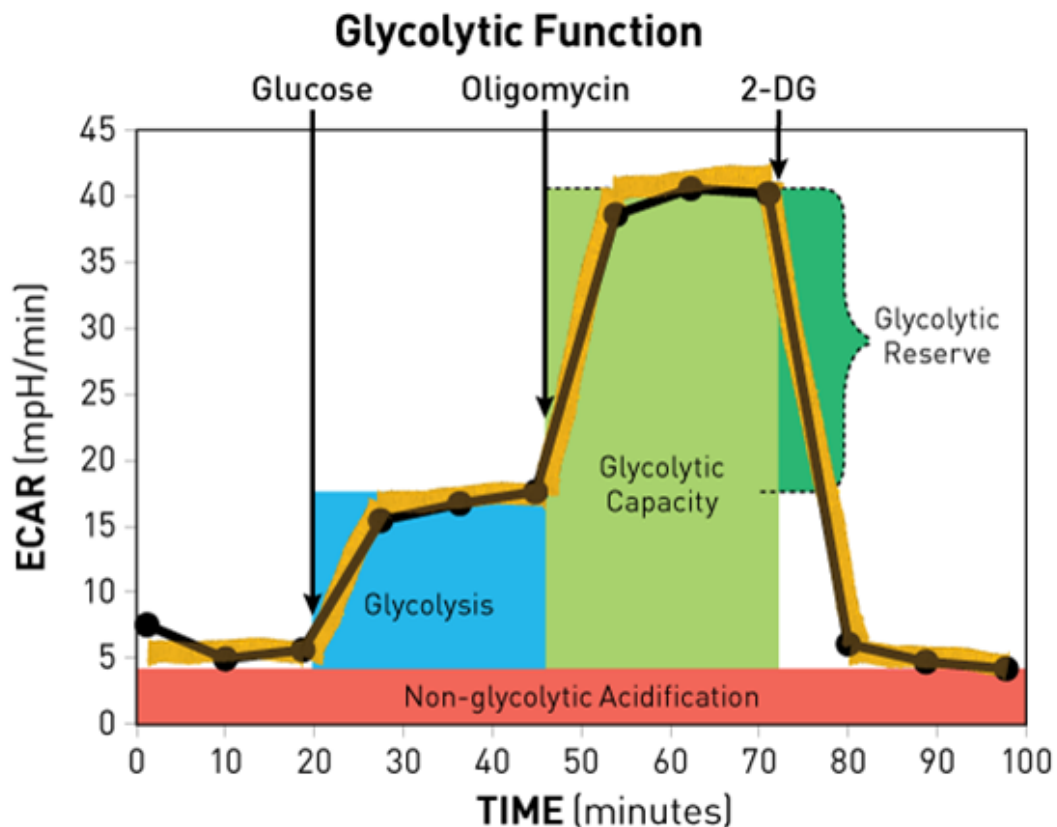


**Figure 3.28:** Glycolytic Function Stress Test profile of consecutive injections and key parameters of glycolytic function. [134]

### OCR and ECAR of Cell Cultures

All cell cultures were plated into Seahorse XF cell culture V7-PS plates coated with collagen at 10,000 or 20,000 cells per well one day before the OCR and ECAR measurements were performed. For mouse embryo 3T3-L1 preadipocytes the plating took place at day 6 of differentiation. On day 7 of differentiation the metabolic measurements were carried out. All other cell lines were plated in low passages before growing to complete confluency. For plate preparation the growth media has been exchanged for assay media in the tissue culture plate wells. The assay media is Seahorse XF base medium with 1 mM glutamine added for the glycolysis stress test and 1 mM pyruvate, 2 mM glutamine, and 10 mM glucose added for the

mitochondria stress test. The pH is adjusted to 7.4 with 0.1 N NaOH. For 3T3-L1 cells, 1 mM of insulin was added to the media. To examine the browning of mature inguinal adipocytes, epinephrine (0.5  $\mu$ M) and forskolin (5  $\mu$ M), which both are known to induce browning, were also added to the assay media. After exchange of media, cells were kept at 37 °C in a non- $CO_2$  environment for one hour. The 24 well plates are then transferred into the XFe24 Analyzer where the injection and measurement protocol is performed. Depending on the experiment subsequent or individual injections of the mitochondria and glycolysis stress test were applied.

#### OCR and ECAR of Tissue

6 to 10-week old male C57BL6 mice were euthanized by cervical dislocation and epididymal, inguinal, and interscapular fat pads were dissected. Adipose depots were excised and placed in small petri dishes with assay media at 37°C. Each fat pad was sampled into small sections using a scalpel resulting in 3 to 4 mg tissue samples. The fat pads were taken from the same section of tissue as close together as possible and cleaned of any blood vessels and non-adipose material. Samples were transferred into an XFe24 islet capture microplate (Seahorse Bioscience, North Billerica, MA) and covered with the customized screens that allow free perfusion while minimizing tissue movement during measurements. A total of 2 tissue samples resulting in 7 mg were placed onto the screens for each well. Once in position, all the tissue samples were rinsed once with assay media to a final amount of 525  $\mu$ l. Several experiments were carried out to compare between different sizes (3 – 10 mg) of tissue and concentration of reagents for their OCR levels of the measurements to be in the dynamic range. The OCR and ECAR of the tissue pieces were analyzed on the XFe24 immediately as they are only viable for a few hours after euthanasia of the mouse. Animal care and experiment protocols relevant to tissue dissection of euthanized mice were approved by the Institutional Animal Care and Use Committee of Massachusetts General Hospital, in accordance with NIH guidelines.



## 4 Results

### 4.1 NADH Lifetime Solution Experiments

#### 4.1.1 Temperature and Solvents

The molecular conformation of NADH and thus its fluorescence behavior such as its lifetime is influenced by the solvent, especially the solvent polarity. Moreover, when a molecule enters the excited state the solvent molecules around it rearrange. Thus, energy is transferred to the solvent, with the result that the emission spectrum is shifted. Solvent relaxation can happen on the time scale of a few picoseconds up to the same order as the fluorescence lifetime depending on polarity and viscosity. The effect of temperature induced viscosity changes and solvent dependent polarity can be seen in Table 4.1. The temperature change from 4°C, to 25°C, and up to 37°C did not induce any significant changes. NADH in different solvents however, showed changes in lifetime as well as lifetime component contribution to the fluorescence intensity.

Solvent	Temperature	Lifetime $C_1$	Lifetime $C_2$	Contr. $C_1$	Contr. $C_2$
DMEM	4°C	390 ps	995 ps	87%	13%
DMEM	25°C	395 ps	985 ps	87%	13%
PBS	25°C	370 ps	970 ps	84%	16%
Water	25°C	360 ps	850 ps	86%	14%
DMEM	37°C	385 ps	985 ps	87%	13%

**Table 4.1:** Fluorescence lifetime and the relative contribution of the lifetime components of NADH (100  $\mu$ M) dissolved in DMEM, PBS and water at different temperatures.

#### 4.1.2 Concentration

Calibration measurements were made with NADH dissolved at concentrations ranging from 30  $\mu$ M to 200 mM in phosphate buffered saline (PBS) and distilled water.

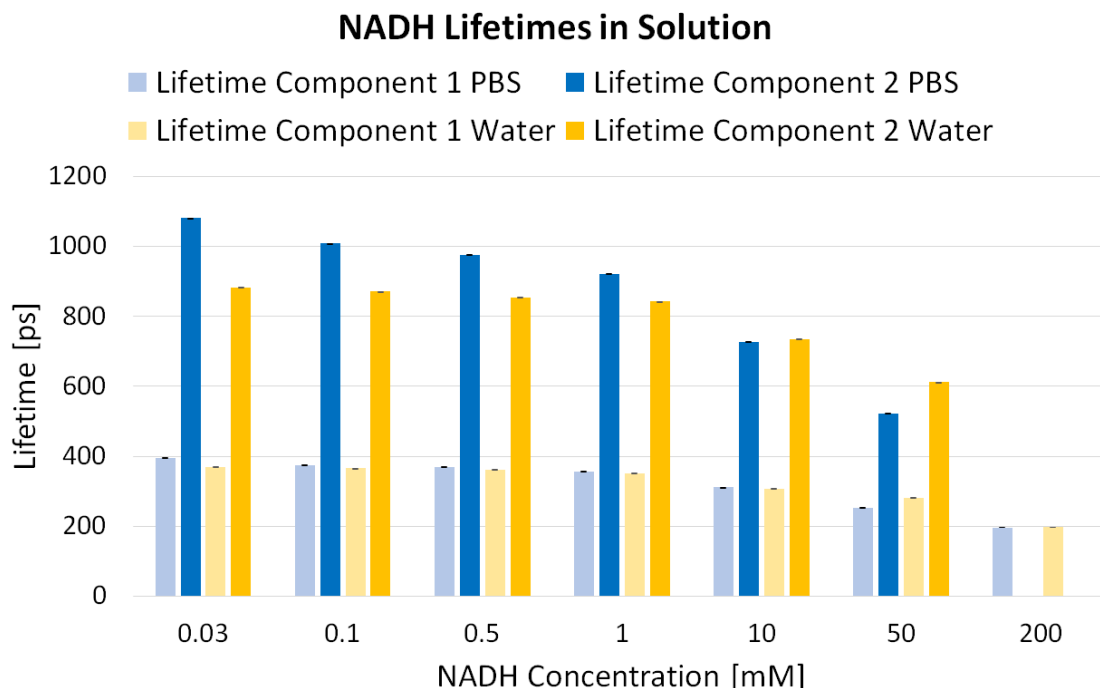


**Figure 4.1:** Free NADH dissolved in PBS and distilled water is characterized by a short and a long fluorescence decay time, which are caused by a folded and extended conformation, respectively. Increasing concentrations of NADH in solution decrease the fluorescence lifetimes due to self-quenching and the pile-up effect. Concentrations higher than 1 mM are above the physiological range. At 200 mM, only one lifetime component can be detected.

Calibration solutions were imaged following the same imaging protocols as were used for cell and tissue culture. For low concentrations of up to 1 mM, NADH in PBS has two characteristic lifetimes, a short decay of  $375 \pm 15$  ps and a longer decay of  $1000 \pm 60$  ps (Fig. 4.1). Approximately 85% of the total NADH concentration was associated with the short lifetime while 15% was associated with the longer (Fig. 4.2). As shown in Table 4.1, the fluorescence lifetimes for NADH dissolved in water are shorter while the contribution of the short and long lifetime components are similar to NADH dissolved in PBS. The fact that there are two lifetimes reveals that there are two distinct environments for the nicotinamide fluorophore. These lifetimes can be attributed to a folded and an extended conformation of the molecule. In the folded conformation light absorption initiates an effective energy transfer within the molecule resulting in shorter fluorescence lifetimes compared to the extended conformation [135, 136, 137, 138, 3]. While fluorescence lifetimes should be independent of the concentration of NADH, increasing NADH concentration in the solution produced a steady decrease in fluorescence lifetime and increase

of the contribution of the short lifetime component. There are two reasons for this behavior. First, due to the electronics and dead time of the TCSPC detector, only one photon per excitation cycle can be registered. However, at high concentrations and high photon count rates, it can happen that more than one photon per cycle is emitted. The system would only detect the first photon and miss the following ones. This measurement error causing artificial shortening of the fluorescence lifetime is known as pile-up effect, which leads to an over-representation of early photons in the histogram [42]. Second, at high concentrations, NADH fluorescence can lead to self-quenching, resulting in shorter lifetimes and lower quantum yields.

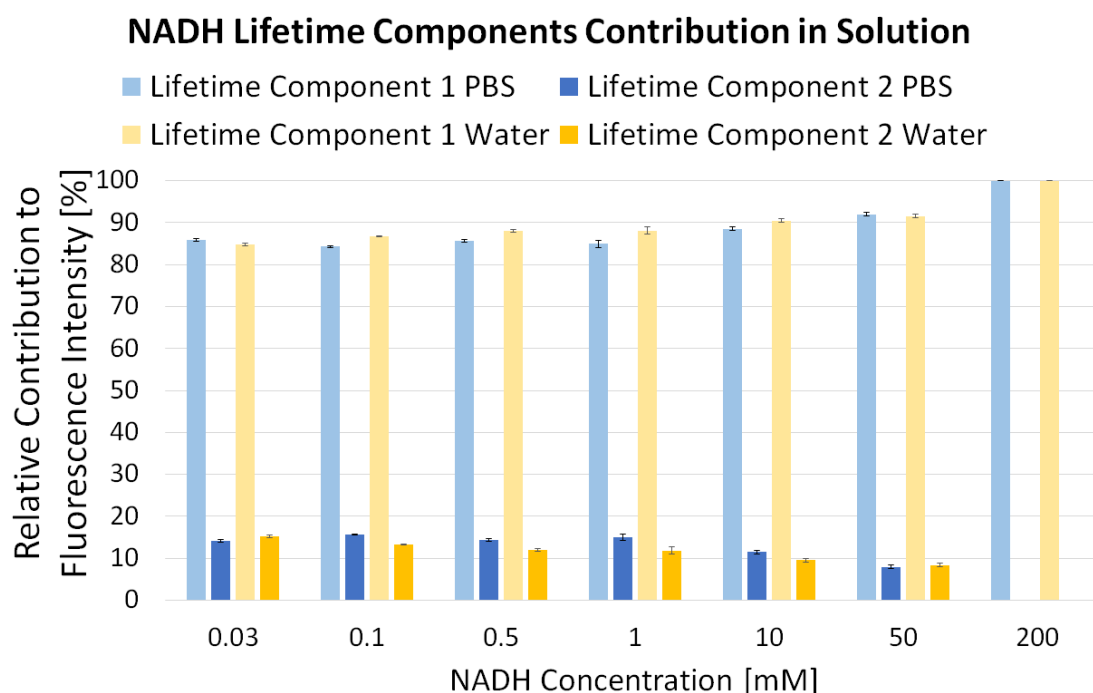


**Figure 4.2:** Free NADH dissolved in PBS and distilled water is characterized by a short and a long fluorescence decay time. The short lifetime components relative contribution to the total fluorescence intensity is significantly higher than the long lifetime components contribution. Increasing NADH concentration increases the contribution of the short lifetime component.

### 4.1.3 Binding Enzymes

To enhance the understanding of the fluorescence lifetime parameters exhibited in monolayer cell culture, well-characterized solutions of free and protein bound NADH were imaged using the same analysis procedure. Pure NADH in solution and a

mixture of NADH and LDH (16:1) in solution were analyzed. For both solutions, a double and a triple exponential fit of the fluorescence decay curve were applied to evaluate which model is the appropriate model to generate accurate fluorescence lifetimes.

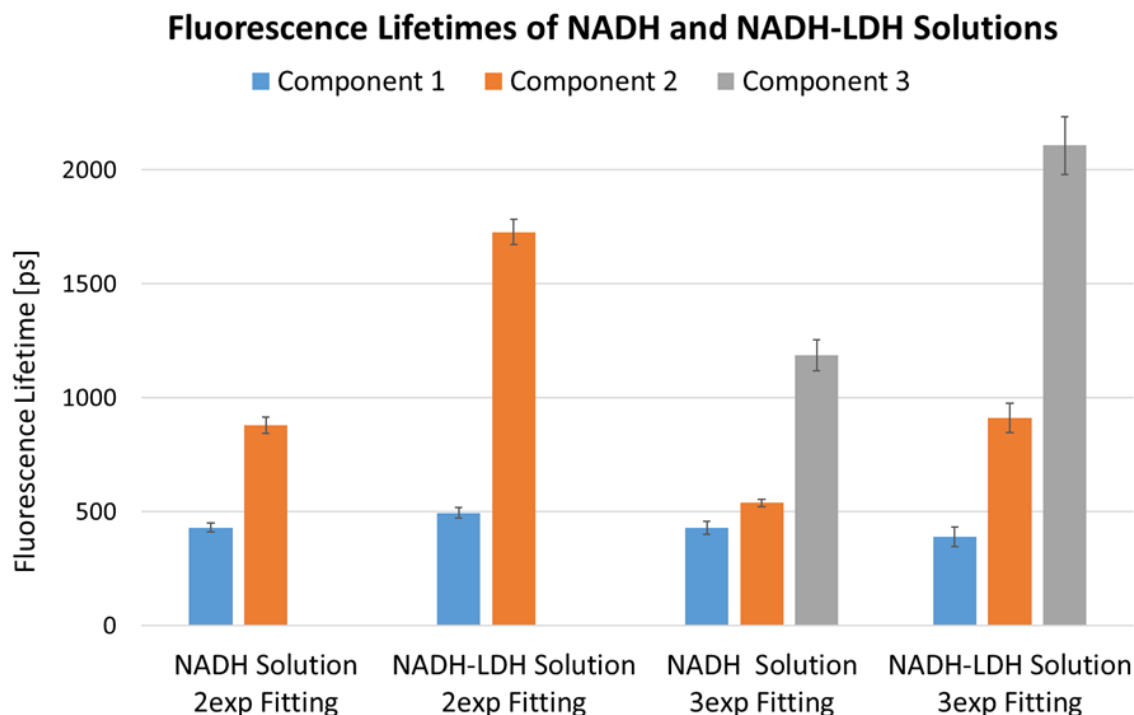


**Figure 4.3:** Double-, and triple-exponential fluorescence lifetime decay fittings of pure NADH in solution and a mixture of NADH and LDH (16:1) in solution. For NADH, the double-exponential fit and for the NADH-LDH mixture, the triple-exponential fit is the appropriate fitting model.

The double exponential fit of NADH resulted in a short fluorescence lifetime component of 0.4 ns and a long fluorescence lifetime component of 0.9 ns which agree well with literature and stand for a possibly folded (0.4 ns) and extended (0.9 ns) conformation of free NADH [9, 12]. A triple-exponential fit of pure NADH in solution resulted in over-fitting, which can be identified by two almost identical lifetime components with lifetimes of 0.4 ns and 0.5 ns. The double-exponential fit of the NADH-LDH mixture resulted in a significant increase of lifetime for the long lifetime component to 1.7 ns compared to pure NADHs long lifetime component of 0.9 ns. The triple-exponential fit of the NADH-LDH solution introduced a third lifetime component at 2.1 ns additionally to the two known NADH lifetime components of 0.4 ns and 0.9 ns from pure NADH in solution. It is therefore assumed that the double-exponential fit for pure NADH and the triple-exponential fit for the NADH-



LDH mix are the appropriate models for the fluorescence lifetime analysis. The third lifetime component of the NADH-LDH mix at 2.1 ns represents the fluorescence lifetime of LDH-bound NADH. When NADH and LDH were combined, NADH fluorescence lifetimes of approximately 0.4 ns (71% contribution), 0.9 ns (22% contribution), and 2.1 ns (7% contribution) were observed. Introducing LDH caused an increase in lifetime component number and a decrease of the relative contribution of the shortest lifetime component and a related increase in the contribution of the middle-lifetime component.

#### 4.1.4 Reagents

Solvent	Reagent	Concentration	pH Value
Glycolysis Stress Test Media			$7.02 \pm 0.03$
	Glucose	10mM	$7.05 \pm 0.02$
	Oligomycin	1 $\mu$ M	$7.07 \pm 0.03$
	2-DG	100 mM	$7.06 \pm 0.02$
	Forskolin	5 $\mu$ M	$7.07 \pm 0.02$
	Epinephrine	0.5 $\mu$ M	$7.09 \pm 0.04$
Mitochondria Stress Test Media			$7.08 \pm 0.02$
	Oligomycin	1 $\mu$ M	$7.16 \pm 0.04$
	FCCP	1 $\mu$ M	$7.15 \pm 0.05$
	Rotenone/AA	0.5 $\mu$ M	$7.14 \pm 0.06$
	Forskolin	5 $\mu$ M	$7.17 \pm 0.03$
	Epinephrine	0.5 $\mu$ M	$7.19 \pm 0.03$

**Table 4.2:** The effect on external pH-value of the glycolysis stress test media (2 mM glutamine) and mitochondria stress test media (10 mM glucose, 1 mM pyruvate, 2 mM glutamine) after injection of pharmacological reagents.

The pH of a solution is known to impact the fluorescence lifetime of a dissolved fluorophore [139]. Intracellular pH is an important factor for understanding cellular conditions. While the shape of the autofluorescence spectrum remains unchanged with intracellular pH, the average fluorescence lifetime of NADH and FAD become shorter as the intracellular pH increases. Additionally, the fluorescence lifetime of NADH is not uniform inside a cell and externally induced intra-cellular pH-changes result in different fluorescence lifetimes in several cellular areas [139]. Fluorescence lifetimes of adipocytes' NADH changed significantly after injection of several pharmacological reagents. To confirm whether the fluorescence lifetime change was indeed based on metabolic changes rather than change in extracellular pH, media

acidity was monitored using a pH meter (Table 4.2). Individual injections of pharmacological reagents were performed in the same concentration and media as in cell experiments.

This experiment was able to show that none of the reagents at given concentration resulted in a significant change in pH.

## 4.2 NADH Lifetime Analysis

### 4.2.1 Spatial Binning

Spatial binning of the decay curve has a significant effect on subsequent fluorescence lifetime analysis. Recent articles describe NADHs fluorescence lifetime by using a double exponential fit and high spatial binning ( $>35 \mu m^2$ ), which yields two distinct fluorescence lifetimes [21, 140]. The use of spatial binning increases the number of pixels and photon counts that contribute to the fluorescence decay while decreasing the effective resolution and spatial detail. However, other recent publications showed that NADH in cerebral tissue and cancer cells can have up to four distinct fluorescence lifetimes [9, 12]. In contrast to studies showing only two fluorescence lifetimes for NADH, these publications made use of high resolution imaging and low spatial binning ( $<10 \mu m^2$ ). To determine if spatial binning affects the number of uniquely detected NADH lifetimes of adipocytes, identical FLIM data sets using different levels of binning were analyzed.

The results show that reducing spatial binning from 9 x 9 pixels ( $14 \mu m^2$ ) to 3 x 3 pixels ( $1.5 \mu m^2$ ) during FLIM analysis of NADH causes an increase in the number of unique lifetime components.

In the case of exponential fitting, high spatial binning (9 x 9 pixels) and therefore, low effective spatial resolution ( $14 \mu m^2$ ), resulted in two fluorescence lifetimes for NADH (Fig. 4.4), while low spatial binning (3 x 3 pixels) and therefore, high effective spatial resolution ( $1.5 \mu m^2$ ), clearly resulted in four distinct lifetime components. Similarly, phasor analysis of high spatial binning images (9 x 9 pixels) resulted in two clear lifetime contributions that are represented by two projected points on the universal semicircle. While the phasor plot generated by low spatial binning (3 x 3 pixels) is not as straightforward to interpret. The triangular arrangement strongly suggests that more than two fluorescence lifetimes were present, even though they cannot be directly distinguished with the principal component analysis.

A common method to separate components having the same phasor location but different lifetime distributions is the multi-harmonic lifetime analysis, where higher harmonics of the laser repetition rate are used [132]. For this study, this method did not result in improved separation of the phasor populations.

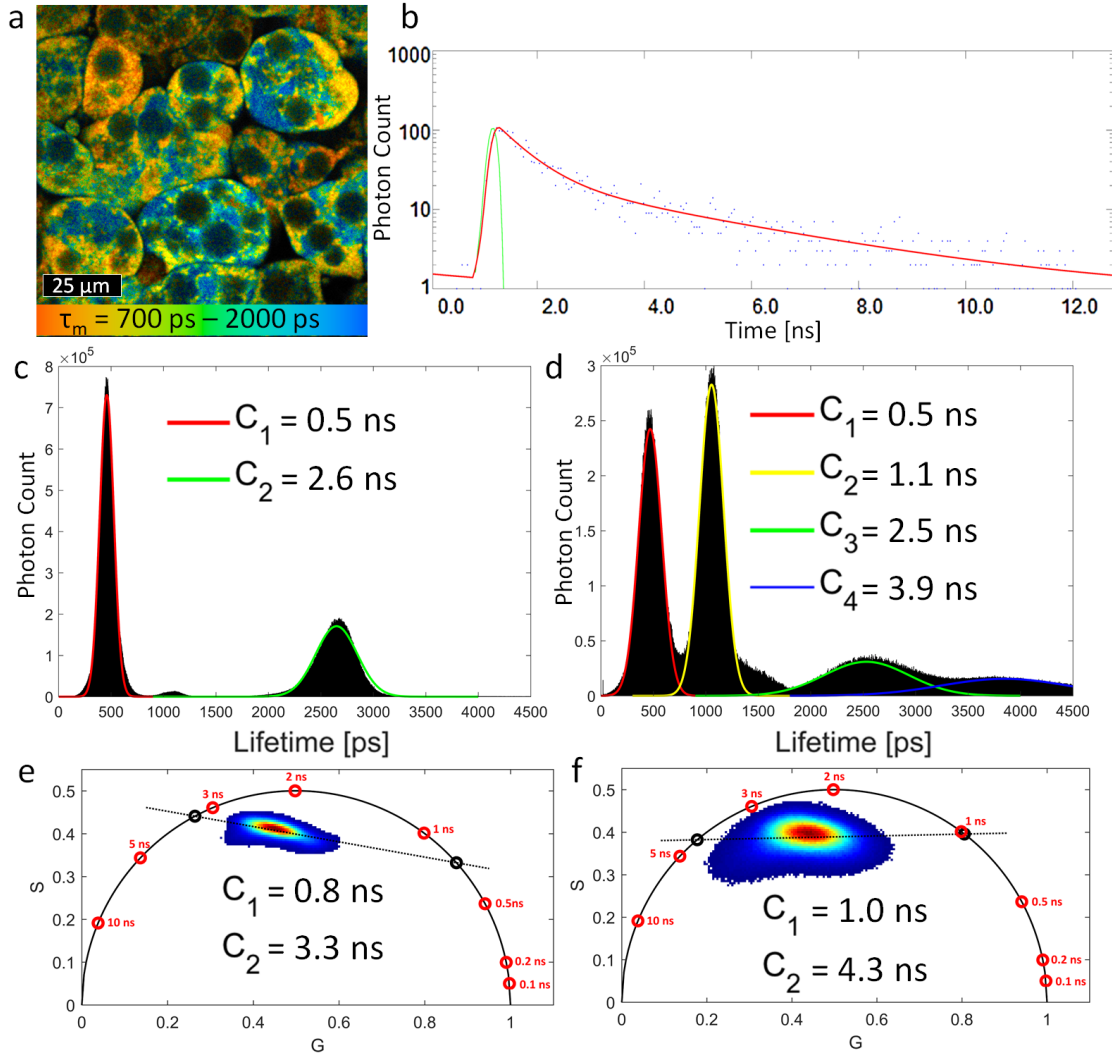


**Figure 4.4:** Effect of spatial binning on the NADH fluorescence lifetime distribution of adipocytes using the phasor approach and exponential fitting of the decay curve. (a) FLIM image of NADH of in vitro 3T3-L1 adipocytes color coded for the average fluorescence lifetime. (b) Fluorescence decay curve of several spatially binned pixels of the FLIM image. NADH histogram based on the intensity and lifetime of all pixels of the FLIM image using bi-exponential fitting with a spatial binning of (c)  $9 \times 9$  pixels ( $14 \mu\text{m}^2$ ) and (d)  $3 \times 3$  pixels ( $1.5 \mu\text{m}^2$ ). Phasor plots of all pixels of the FLIM image showing the NADH lifetime distribution for (e)  $9 \times 9$  pixels spatial binning and (f)  $3 \times 3$  pixels spatial binning. For low spatial binning (f), the phasor analysis is not suitable as the interpretation of a broad phasor distribution is often not possible. The attempt of an interpretation by using principal component analysis (f) results in only two fluorescence lifetimes compared to four lifetimes using exponential fitting (d).

### 4.2.2 Temporal Binning

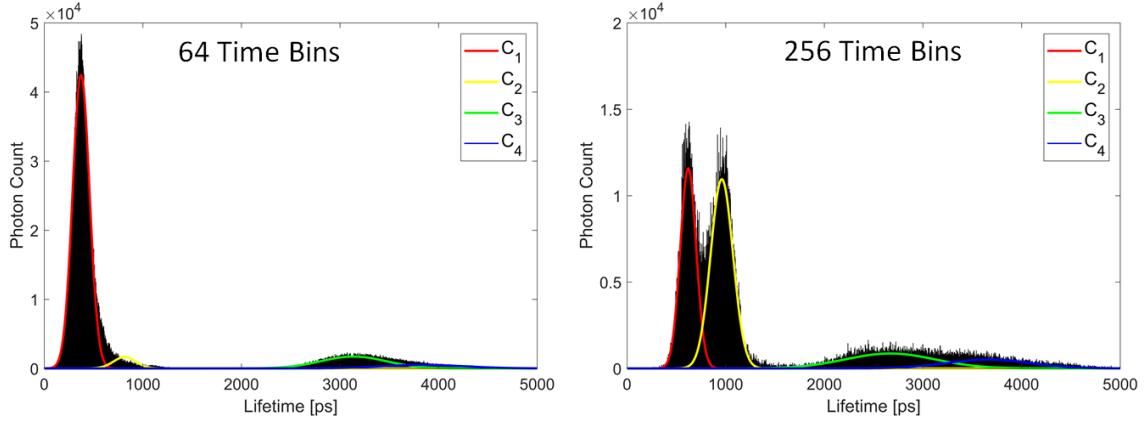


**Figure 4.5:** Temporal resolution of measured decay curves of NADH of adipocytes was collected into 64 and 256 time bins over 12.5 ns. The NADH distribution for 64 time bins shows three distinct lifetime components while for 256 time bins, four distinct lifetime components are detected.

Recent publication showed that temporal binning, just like spatial binning, can be used to improve fit accuracy and decrease image acquisition time [46]. Therefore, the temporal resolution of the measured decay curves of NADH of adipocytes was reduced from 256 time bins over 12.5 ns to 64 by summing the number of photons in 4 consecutive time bins. The new fluorescence decay curves were analyzed and lifetime parameters were evaluated. This technique theoretically improves the fit accuracy by combining the photons in consecutive time bins within a pixel and therefore, the error due to shot noise in the time bin is reduced. However, multiple bins combined also result in a loss of signal detail.

Fig. 4.5 shows a similar effect on the NADH lifetime distribution as spatial binning and a reduction from four distinct lifetimes at 256 time bins to three lifetimes at 64 time bins. While lifetime component  $C_1$  and  $C_3$  are still prominent, component  $C_2$  is markedly reduced in contribution to the total fluorescence intensity and component  $C_4$  cannot be detected anymore. The fourfold decrease of time bins and subsequent increase of gating time from 50 ps to 200 ps altered the NADH fluorescence lifetime distribution significantly. This was expected since the fluorescence lifetime peaks of component  $C_1$  and  $C_2$  are only separated by 500 ps with FWHM of up to 320 ps which results in significant overlap (Fig. 4.5). It can be assumed that by reducing the amount of time bins even further, only two fluorescence lifetimes will be determined. Therefore, it was concluded that reducing the amount of time bins failed to accurately represent all four lifetime components and the standard amount of 256 time bins was used for all fluorescence lifetime investigations.

### 4.2.3 Lifetime Localization

For low spatial binning and bi-exponential fitting the NADH fluorescence lifetime distribution of an adipocyte FLIM image shows four distinct fluorescence lifetimes. Even though 4 distinct fluorescence lifetimes for NADH are found, only two components are fit at each pixel. The 4 lifetimes components are only identified across different pixels and not within one fluorescence decay. The reason is that the use of a bi-exponential model to fit the fluorescence decay always returns two fluorescence lifetimes, regardless of how many lifetimes the analyzed pixel actually has. The two-lifetime model was selected out of practical reasons such as speed and ease of use as attempts to fit the data with three lifetime components did not deliver a significant improvement based on the quality of the fit as discussed in Subsection 3.2.1. By analyzing each pixel individually, it became clear that the lifetime components occur in pairs: the lifetime component  $C_1$  at 0.5 ns is predominantly accompanied by component  $C_3$  at 2.3 ns (Fig. 4.6 b) and lifetime component  $C_2$  at 1 ns is accompanied

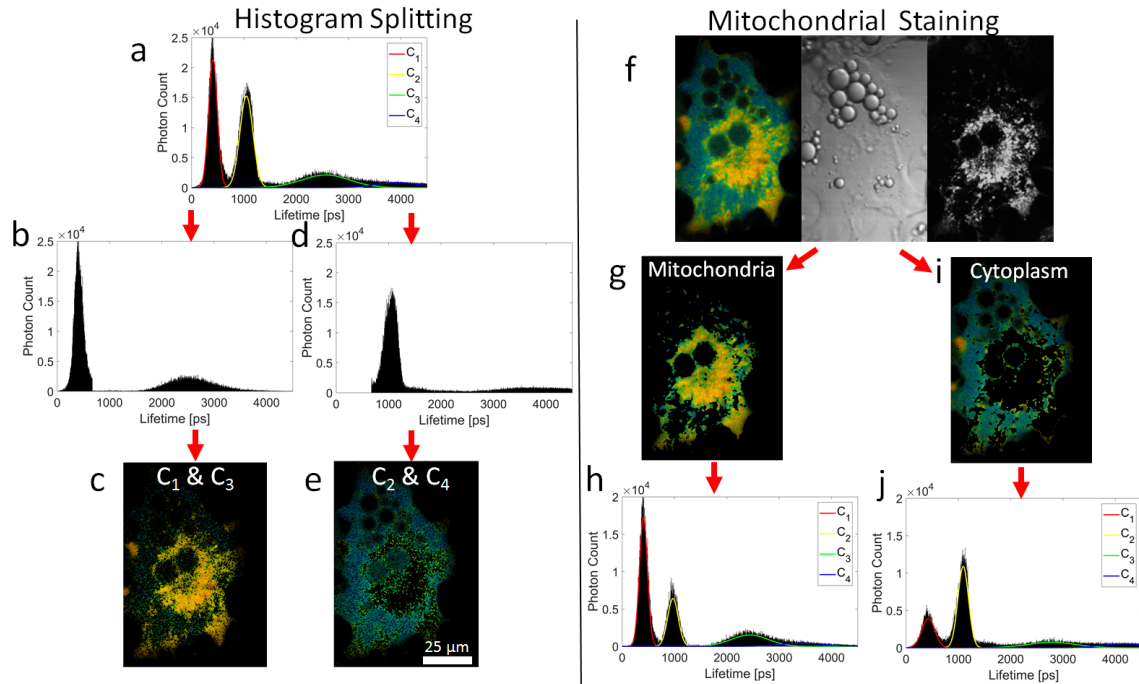


**Figure 4.6:** (a) NADH lifetime distribution of the entire cell and Gaussian fitting of each lifetime component. (b,c) FLIM image and fluorescence lifetime distribution that only consist of lifetime pair  $C_1$  and  $C_3$ . (d,e) FLIM image and lifetime distribution that only consist of lifetime pair  $C_2$  and  $C_4$ . (f) FLIM, trans-illumination, and mitochondrial-stain image of a single 3T3-L1 fat cell. (g,h) Fluorescence lifetime distribution and FLIM image of mitochondria. (i,j) Fluorescence lifetime distribution and FLIM image of the cytoplasm.

nied by component  $C_4$  at 3.7 ns (Fig. 4.6d). Based on this information, two FLIM images were generated: one that shows the spatial distribution of lifetime pair  $C_1$ ,  $C_3$  (Fig. 4.6 c) and another one for lifetime pair  $C_2$ ,  $C_4$  (Fig. 4.6 e). As NADH fluorescence is known to arise from mitochondria, the cellular mitochondria distribution was determined using the stain tetra-methyl-rhodamine ethyl ester (TMRE) and MitoTracker Green FM. The mitochondrial stain, trans-illumination and FLIM image enabled the generation of FLIM images that belong to specific cellular regions such as mitochondria and the cytoplasm. Interestingly, these FLIM images of specific cellular regions show significant differences in fluorescence lifetime distribution. The mitochondrial lifetime distribution (Fig. 4.6 h) and the cytoplasmic distribution (Fig. 4.6 j) indicate that the NADH fluorescence lifetime of mitochondria favors lifetime components  $C_1$  and  $C_3$  while the cytoplasm favors components  $C_2$  and  $C_4$ . Comparing the images revealed that the mitochondrial-stain derived mitochondria FLIM image (Fig. 4.6 g) shows a high correlation ( $R = 0.75$ ) with the  $C_1$  and  $C_3$  FLIM lifetime pair image (Fig. 4.6 c) and that the cytoplasm FLIM image (Fig. 4.6 i) has a similarly strong correlation ( $R = 0.67$ ) with the  $C_2$  and  $C_4$  FLIM lifetime pair image (Fig. 4.6 e).

This supports the conclusion that lifetime components  $C_1$  and  $C_3$ , are associated with mitochondria, and components  $C_2$  and  $C_4$  are observed to arise from the cytoplasm.

This theory of regional differences of NADH species was further investigated by analysis of isolated mitochondria of 3T3-L1 adipocytes. According to the findings of this section, the analysis of isolated mitochondria should result in NADH fluorescence that predominately exhibits lifetime components  $C_1$  and  $C_3$  as shown in the next section.

#### 4.2.4 Isolated Mitochondria

Isolated mitochondria from adipocyte cell cultures and adipose tissues are relatively easy to study, depending on the mitochondrial density. Brown adipose tissue as well as differentiated 3T3-L1 cells contain high amounts of mitochondria and therefore, the isolated mitochondrial population is statistically representative for the tissue and culture [141]. For white adipose tissue, the mitochondrial density is low, resulting in very low mitochondrial yields. Therefore, large amounts of adipose tissue have to be collected to isolate sufficient amounts of mitochondria. However, monolayer cell cultures of 3T3-L1 adipocytes generated sufficient amounts of mitochondria using a glass homogenizer and standard protocols [141]. The isolated mitochondrial population was analyzed to reveal intra-cellular fluorescence lifetime differences of NADH. Isolated mitochondria were stained with TMRE to test for impurities within the cell extract. Even though some impurities were detected as highlighted in Fig. 4.7, most of the fluorescence signal originated from mitochondria. As predicted in



Subsection 4.2.3, isolated mitochondria predominately exhibit NADH fluorescence of lifetime component  $C_1$  and  $C_3$ . This finding strengthens the claim that distinct fluorescence lifetimes are specific to intracellular cellular features.

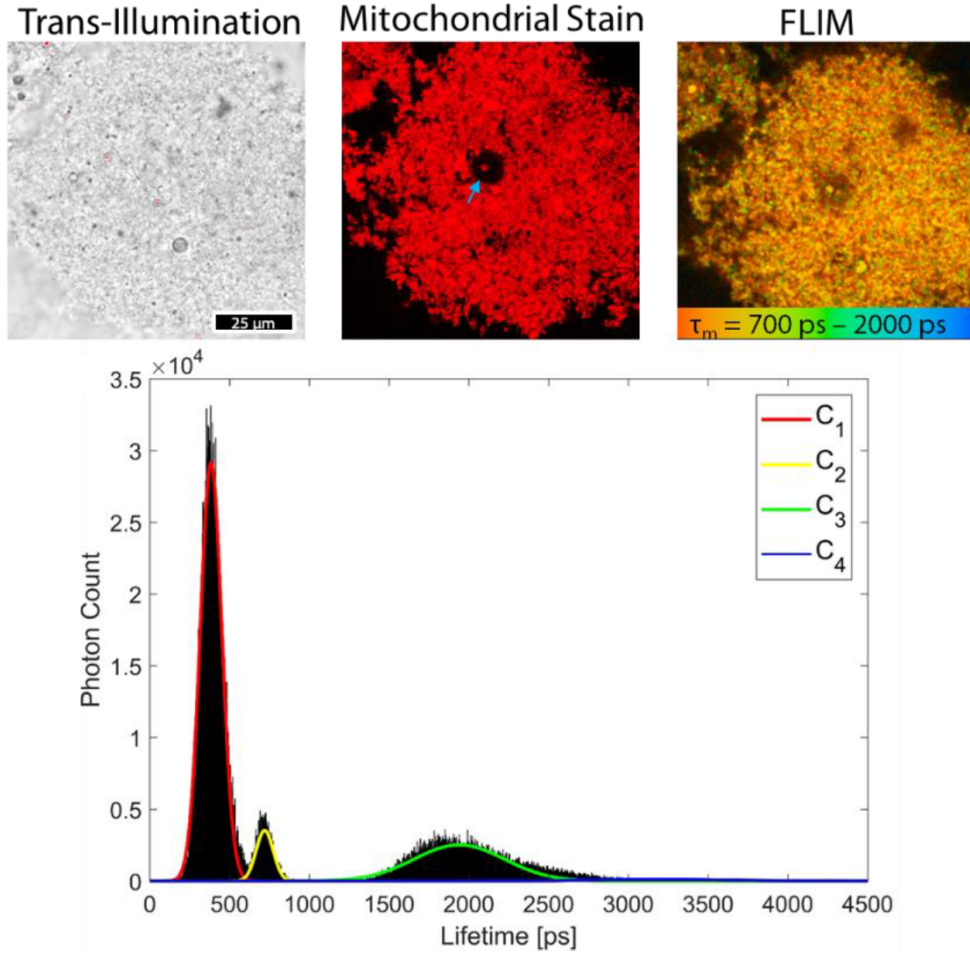


**Figure 4.7:** Fluorescence lifetime distribution of NADH of isolated mitochondria of 3T3-L1 adipocytes. Trans-illumination image, TMRE mitochondrial stain image, and FLIM image of isolated mitochondria. The blue arrow highlights impurities such as a cell nucleus within the isolated mitochondria. The fluorescence lifetime distribution of isolated mitochondria consisted predominantly of component  $C_1$  and  $C_3$ .

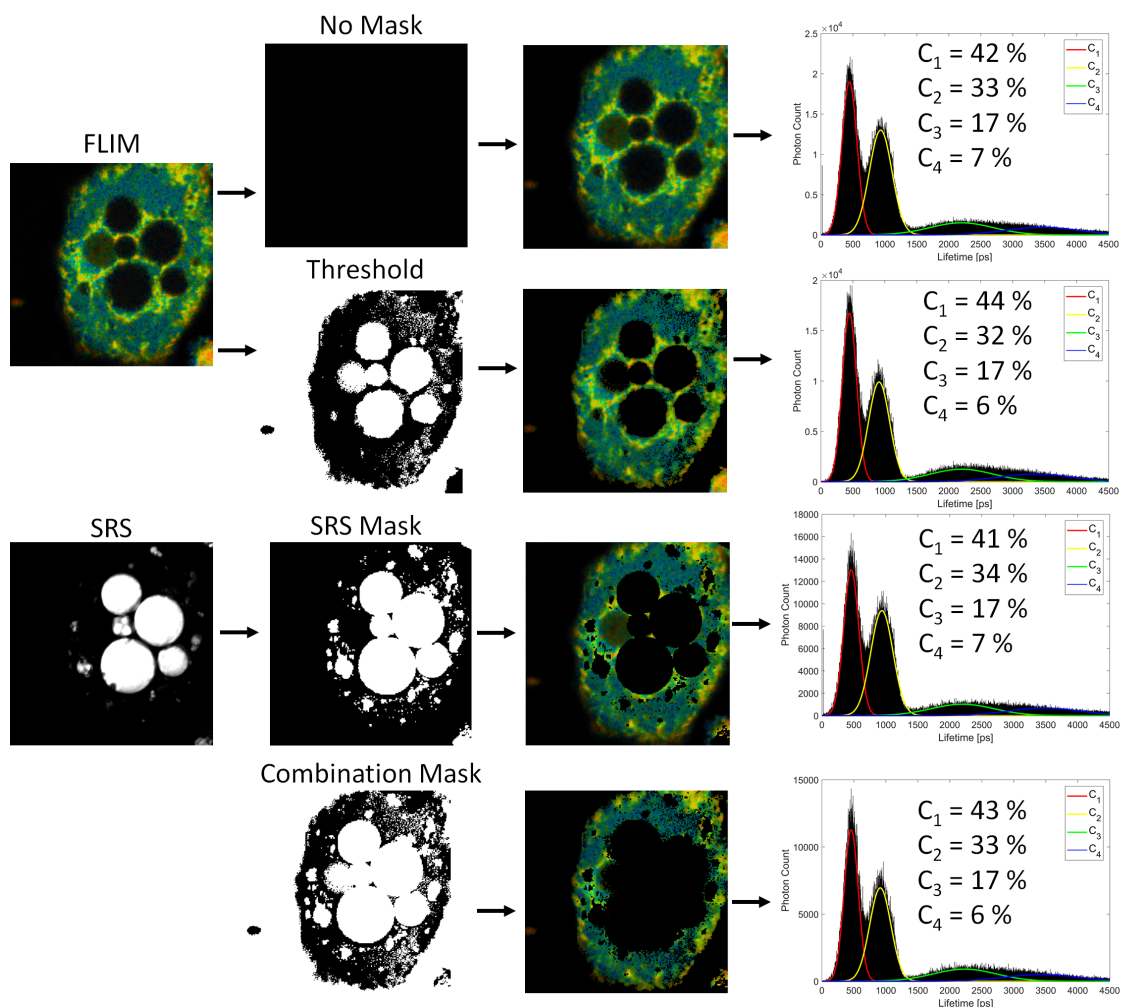


**Figure 4.8:** FLIM and SRS image of a single 3T3-L1 adipocyte. An intensity based adaptive threshold was used to create a mask to remove low fluorescence intensity areas such as the background, nuclei, and lipid droplets. SRS signals were used to generate masks containing lipids and lipofuscin. The last row shows a combination masks generated by addition of all other masks. The masks were used to removed certain features of the FLIM image for the fluorescence lifetime analysis and the resulting lifetime distributions are shown in the column on the right.



### 4.2.5 Detection of Lipids and Lipofuscin

Lipofuscin is mainly present in post mitotic cells. It consists of lipids, proteins, carbohydrates and a small amount of metals. Lipofuscin has been investigated concerning its lipid and protein composition and several authors described a protein fraction of 20% to 70% and a lipid fraction of 20 to 50 wt% [142, 143]. Stimulated Raman Scattering (SRS) microscopy is highly sensitive to the detection of lipids. Due to the lipid rich composition of lipofuscin, this imaging modality is able to reliably detect lipofuscin [144]. The contrast of the SRS signal in the lipid droplets arises from the Raman response of the abundant C-H bonds in the lipid molecules [145]. Thus, laser scanning stimulated Raman scattering microscopy is applied to visualize lipid droplets in cells and tissues. There are several publications using fluorescent dyes for labeling of lysosomes and lipids such as LysoTracker to detect lipofuscin [146, 147]. Colocalization studies using stimulated Raman scattering microscopy showed high correlation with these fluorescent dyes for imaging of lipid and lysosome-related organelles [148, 149]. Therefore, SRS was used to detect lipofuscin and other lipid-rich components in Fig. 4.8.

To eliminate the influence of lipid and lipofuscin fluorescence on the analysis of NADH fluorescence, regions containing lipid and lipofuscin were removed from the analysis. These regions were determined by SRS and fluorescence intensity as shown in Fig. 4.8. While initially analyzing the entire image, several masks were applied such as an intensity based adaptive threshold mask, a mask based on the SRS signal of lipids and a combination of all the masks. The analysis of the fluorescence lifetime distribution after application of these masks, which eliminate the fluorescence from lipids and therefore also from lipofuscin, resulted in 4 distinct lifetime components for NADH. Additionally, several publications showed a long mono exponential fluorescence lifetime for lipids, which can be excited and detected with the same setup as for NADH imaging [21, 144]. There is a possibility, that the 4 fluorescence lifetimes detected could be a mix of NADH and lipid fluorescence, especially at the transition zones from lipid droplet to other cellular areas. Therefore, a SRS mask which was

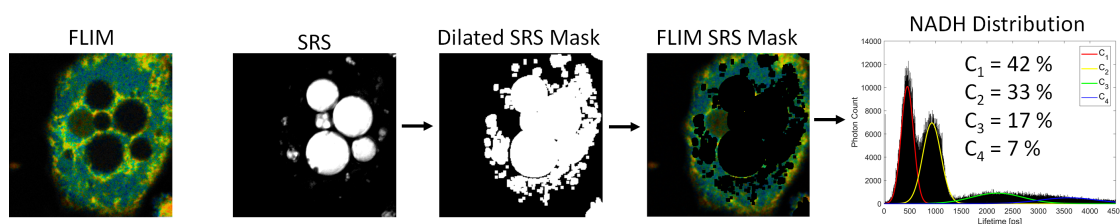


**Figure 4.9:** FLIM and SRS image of a single 3T3-L1 adipocyte. SRS signals were used to generate a binary mask which was morphologically dilated by two pixels and then subtracted from the FLIM image. The resulting FLIM image was analyzed and a NADH lifetime distribution was generated.

morphologically dilated by 2 pixels was applied to the FLIM image and the NADH distribution was analyzed (Fig. 4.9). The dilated mask consequently avoids an overlap between spatial regions that could potentially contain both NADH and lipid droplets. It is notable that under this extreme condition, where lipid droplets and peri-droplet regions are strongly selected out, still four distinct fluorescence lifetime peaks can be seen. These lifetime components are proposed to arise from the mitochondria and cytoplasm, which are contained in the regions of the cell left behind after application of the lipid droplet mask. However, it is important to note that there have been other reports, showing four lifetime components for NADH in cells or tissue that do not contain high concentrations of lipid droplets: cerebral tissue, rat basophilic leukemia cells, and mammary adenocarcinoma cells [9, 12].

#### 4.2.6 Mitochondrial Movement

Mitochondria undergo trafficking, fusion, and fission, creating continuously changing networks to support mitochondrial function and accommodate cellular homeostasis. Due to their involvement in metabolism and their association with metabolic diseases, it would be beneficial to monitor the organization of mitochondria. A good way to investigate mitochondrial morphology relies on methods such as scanning microscopy in combination with mitochondria-specific dyes. Multiple fluorescence images of 3T3-L1 fat cells using the TMRE and MitoTracker Green FM mitochondrial stain were captured 6 s apart from each other to analyze the location and movement of individual mitochondria. The measurements revealed that most mitochondria are clustered in specific parts of the cell, especially close to the nuclei and

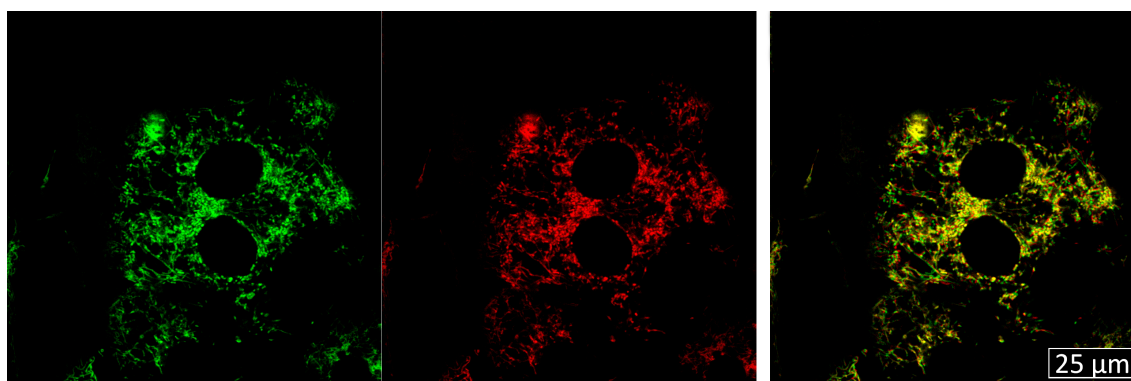


**Figure 4.10:** Mitochondrial stain image of a single 3T3-L1 fat cell captured once (green false color) and 6 second later (red false color). Additive combination of the green and red false color images reveal mitochondrial movement. In areas where the mitochondria are clustered it is not feasible to detect the displacement and a yellow color is visible (additive of green and red).

are more spread out in other cellular areas such as the periphery. Images taken 6 s apart from each other showed considerable mitochondrial movement (Fig. 4.10). While the movement analysis in areas where the mitochondria were clustered was not feasible, less clustered cellular areas were used to measure the displacement between frames. Image analysis revealed an average displacement of  $0.5\ \mu\text{m}$  movement within 6 s in less clustered areas of the cell. During the acquisition time of a FLIM image using the experimental setup (60 s) mitochondria were found to move up to  $5\ \mu\text{m}$ . The FLIM imaging system uses a 60x objective lens with 1.2 NA to excite very small focal volumes. Given the natural intracellular migration of mitochondria during the 60 s acquisition period, mitochondria inevitably enter and exit the focal plane throughout acquisition, leading to image blurriness as shown in Fig. 4.11 and thus having negative impact on the fluorescence lifetime analysis.

While there are still areas of the cell that only exhibit fluorescence of mitochondria or the cytoplasm during the acquisition time, there are also areas that display a mixture of cytosolic and mitochondrial fluorescence. The double-exponential model used in this work for fluorescence lifetime analysis is not suited for these mixtures of cytosolic and mitochondrial fluorescence, which leads to inaccurate fluorescence lifetimes. This inaccuracy induced by mitochondrial movement broadens the NADH lifetime distribution peaks of individual lifetime components and makes it difficult to separate each component individually.

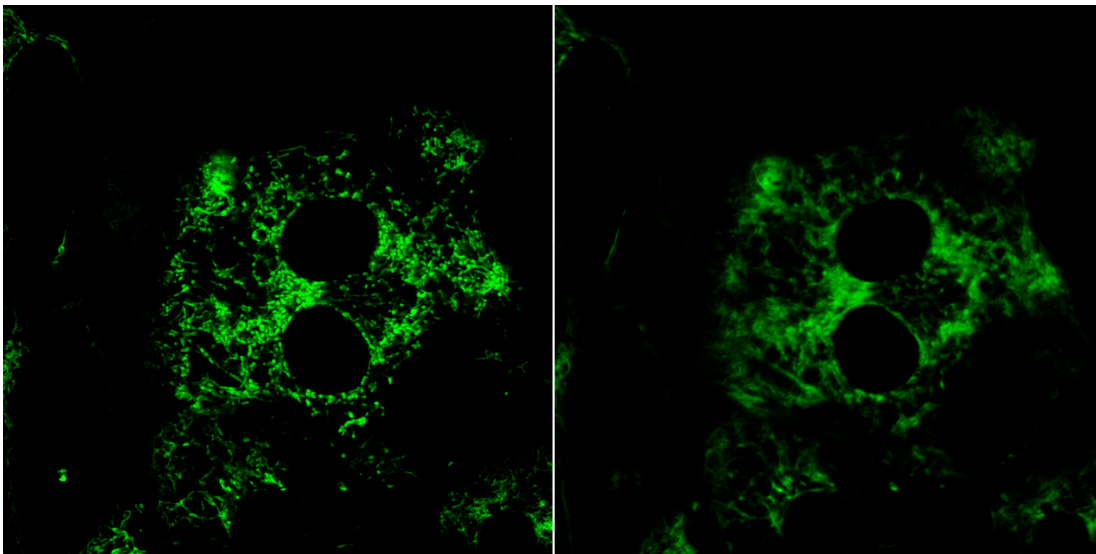


**Figure 4.11:** Mitochondrial stain image of a single 3T3-L1 fat cell taken within 6 seconds shows a great amount of detail and individual mitochondria. The same cell recorded continuously for 60 seconds (typical for FLIM applications) results in a blurry image with reduced detail.

### 4.2.7 NADH Phasor Plot

Fig. 4.4f presents a phasor plot that arranges in a broad cluster, making it impossible to extract the correct fluorescence lifetimes. Here, an approach to determine the fluorescence lifetimes of broadly clustered phasor plots is presented. The method combines a segmentation of exponential fitting derived lifetime histograms with the phasor analysis. The segmentation of the NADH lifetime histogram is aiming to split fluorescence of mitochondria and the cytoplasm. Therefore, the NADH lifetime distribution is split into the lifetime pairs  $C_1$  and  $C_3$  for mitochondrial fluorescence and pair  $C_2$  and  $C_4$  for cytoplasmic fluorescence (Fig. 4.12). The FLIM image pixels segmented by this histogram splitting method are then analyzed by the phasor approach. Phasor points generated by a segmentation of mitochondrial ( $C_1$  and  $C_3$ ) NADH fluorescence are closely arranged along a single line suggesting two NADH fluorescence lifetimes for this cellular compartment. The cytoplasmic ( $C_2$  and  $C_4$ )

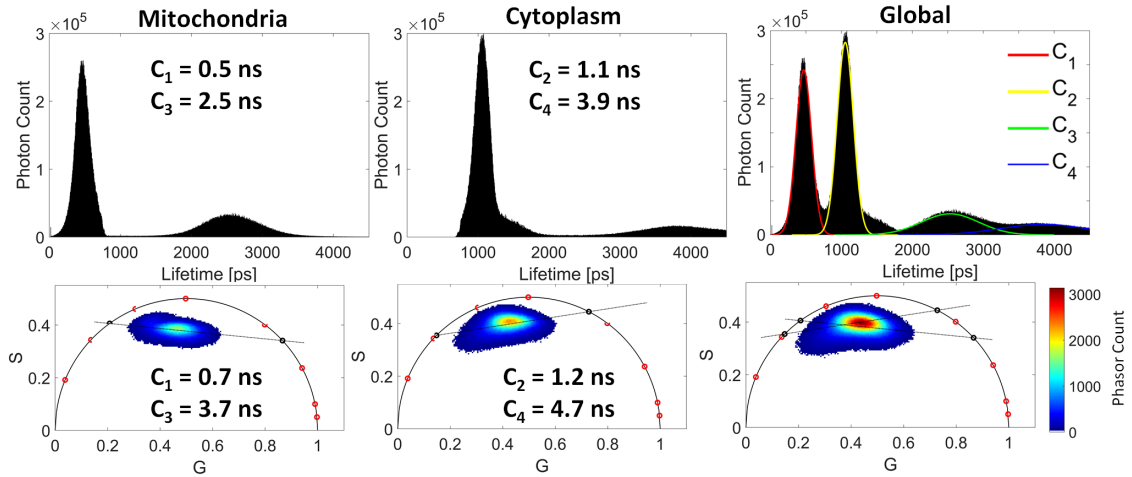


**Figure 4.12:** NADH lifetime distributions defined by exponential fitting and corresponding phasor plots. Mitochondrial lifetime pair  $C_1$  and  $C_3$ , cytoplasmic lifetime pair  $C_2$  and  $C_4$ , and the entire FLIM Image.  $n = 20$  FLIM images per group.

phasor point distribution of NADH fluorescence shows a slightly triangular shape. However, it is hypothesized that the use of improved mitochondrial and cytoplasmic segmentation should lead to a phasor point distribution along a single line, thus, representing two NADH fluorescence lifetimes for the cytoplasm. In Fig. 4.12, it can intuitively be observed that the global phasor plot can be described by individual fluorescence lifetimes of mitochondrial ( $C_1$  and  $C_3$ ) and cytoplasmic ( $C_2$  and  $C_4$ ) segmentation. Even though the NADH lifetimes determined by phasor analysis are slightly longer than the ones generated by bi-exponential fitting, the trends

match well with shorter lifetime pairs associated with mitochondrial fluorescence, and longer pairs for cytoplasmic fluorescence.

## 4.3 Assessment of Metabolic Activity

### 4.3.1 Mitochondrial Cytoplasmic Ratio

As the localization of each of the four lifetime components is highly specific to mitochondrial and cytoplasmic cellular features, a new metabolic ratio was defined, namely the mitochondrial-cytoplasmic-ratio (MCR), which is specific to changes in mitochondrial to cytoplasmic NADH fluorescence intensity:

$$MCR = \frac{\text{Mitochondrial NADH Fluorescence}}{\text{Cytoplasmic NADH Fluorescence}} = \frac{C_1 + C_3}{C_2 + C_4} \quad (4.1)$$

The MCR is sensitive to shifts in mitochondrial and cytoplasmic NADH concentration as well as shifts in spatial distribution of these cellular compartments. In this study, FLIM measurements were performed within minutes of the injection of pharmacological reagents. Therefore, it is likely that the MCR represents shifts in mitochondrial and cytoplasmic metabolism rather than changes in content. The following analysis of metabolic changes compares the MCR to traditional optical biomarkers such as the fluorescence lifetime based free-to-bound ratio of NADH and the fluorescence intensity based redox ratio of NADH and flavin adenine dinucleotide (FAD) which can be expressed as  $FAD / (FAD + NADH)$ .

### 4.3.2 Mitochondria Stress Test - Individual Injections

Mitochondrial respiration and extracellular acidification were analyzed using an extracellular flux analyzer and compared to the microscopically derived optical redox ratio, free-to-bound ratio and MCR. The mitochondria stress test presented here, consisted of 3 individual injections of pharmacological reagents, the first injection being oligomycin. Oligomycin inhibits ATP synthase and prevents protons from re-entering the mitochondrial matrix, causing the inhibition of oxidative phosphorylation and consequently causing a decrease in oxygen consumption rate (OCR) along with an increase in glycolysis (Fig. 4.13). As these changes drive an increase in mitochondrial NADH and decrease of FAD due to inhibition of the electron transport chain (ETC), both the optical free-to-bound ratio and MCR should increase significantly, while the redox ratio should decrease. As can be seen in Fig. 4.14, the optical free-to-bound ratio and MCR do indeed increase and the redox ratio

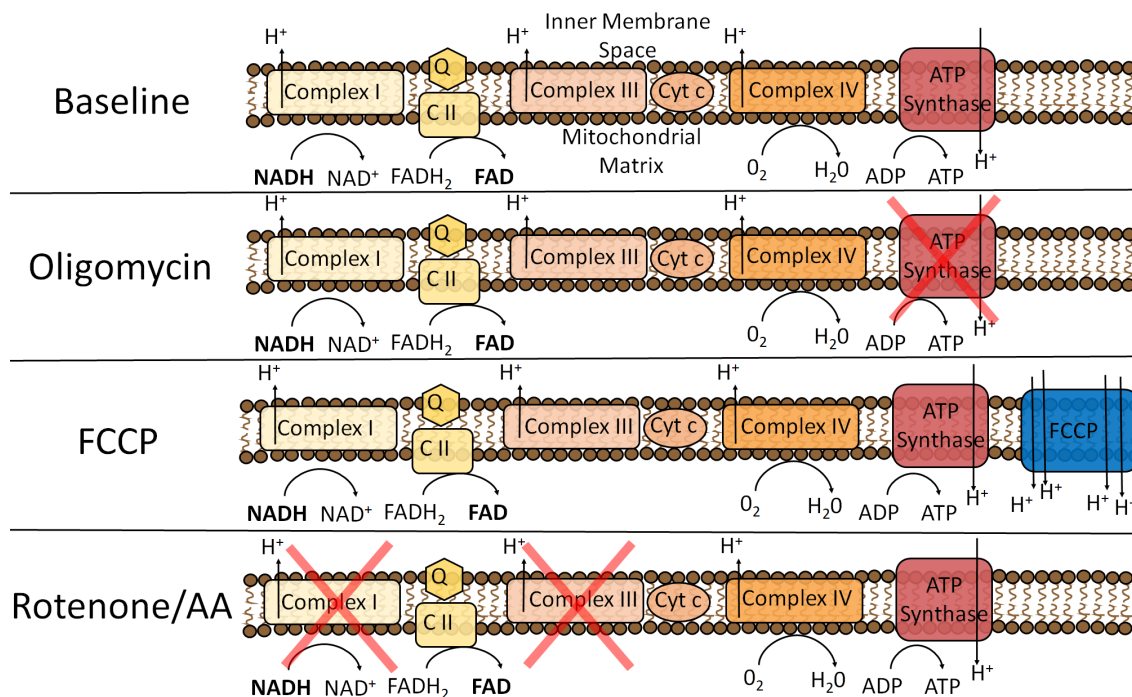


**Figure 4.13:** Simplified schematic of the electron transport chain and the effect of individual injections of each of the reagents of the mitochondria stress test.

decreases. Specifically, the contribution to the total fluorescence intensity of mitochondria lifetime components  $C_1$  and  $C_3$  is observed to rise, while the contribution of the cytoplasmic component  $C_2$  decreased. To compensate for the inhibition of the ETC, glycolytic ATP production is upregulated to sustain cellular demand, which explains the decrease of lifetime component  $C_2$ . As expected the oligomycin injection resulted in an increased extracellular acidification rate (ECAR) determined by monitoring extracellular pH changes measured by an extracellular flux analyzer. The second injection of the stress test is FCCP, which acts as a protonophore to translocate protons into the inner membrane of the mitochondria, accelerating respiration and thereby oxidizing NADH to non-fluorescent NAD<sup>+</sup> and FADH<sub>2</sub> to fluorescent FAD. The FCCP injection resulted in an increase in OCR as measured by the flux analyzer. By uncoupling oxidative phosphorylation from ATP production, FCCP causes cells to switch to glycolysis, which is marked by an increased ECAR measured by the flux analyzer. These changes cause the mitochondrial NADH pool to deplete due to higher activity of the ETC. The cytoplasmic NADH pool showed a slight increase in form of increased intensity of lifetime component  $C_2$ , due to significantly higher glycolytic function. As anticipated, the MCR was observed to decrease, with the mitochondrial  $C_1$  and  $C_3$  fluorescence intensity declining while the  $C_2$  intensity increased. The redox ratio does not show significant changes compared to the baseline after FCCP injection which has been reported previously [150, 151].



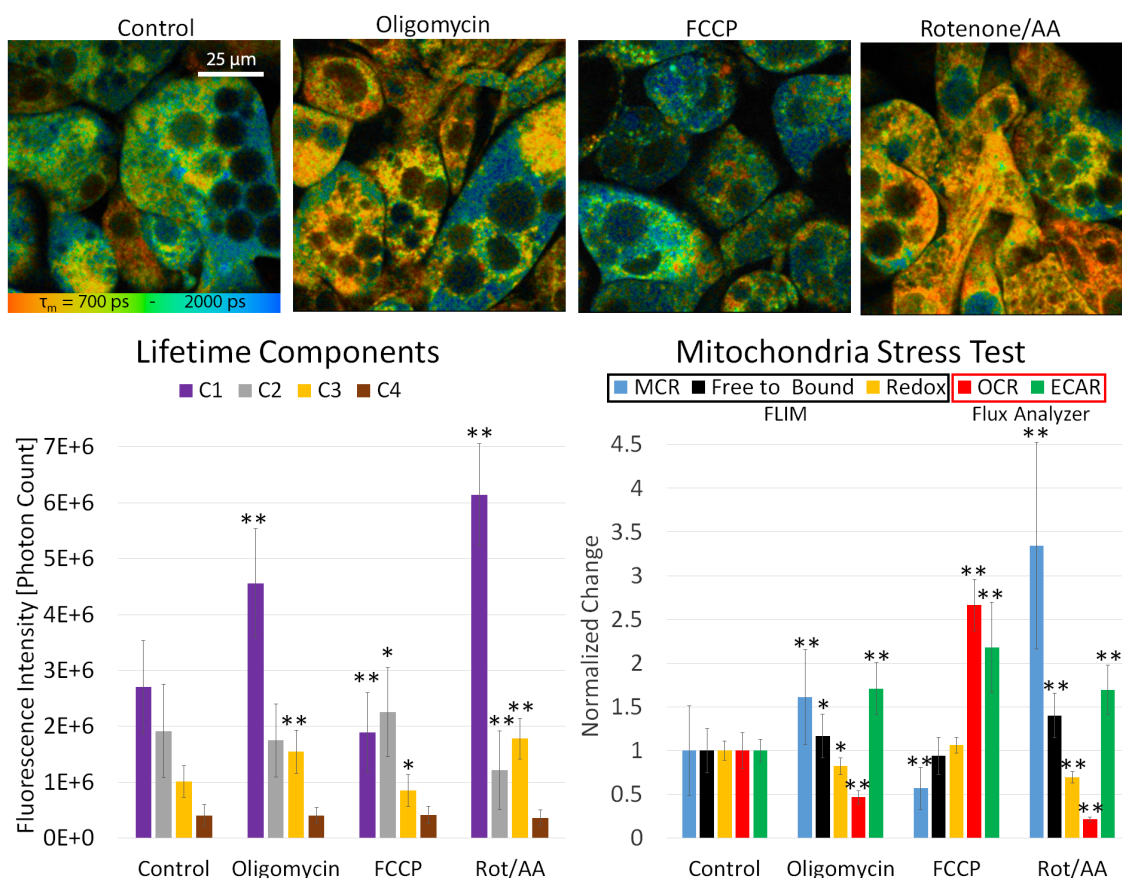


**Figure 4.14:** Mitochondria stress test - individual injections. Fluorescence intensity of the individual lifetime components of NADH for each step of the mitochondria stress test. The effect of individual injections of oligomycin, FCCP, and rotenone/antimycin on the FLIM-derived MCR, optical free-to-bound ratio, and redox ratio as well as on OCR and ECAR measured by an extracellular flux analyzer. Mean  $\pm$  SD of  $n = 40$  FLIM images per group. Significant differences of treatment groups to the control by Student's t-test with \*  $p < 0.05$ , \*\*  $p < 0.001$ .

The third injection of the stress test are respiratory chain inhibitors rotenone and antimycin which induce oxidative stress and maximize mitochondrial NADH by preventing its oxidation to  $\text{NAD}^+$ , as well as prevention of oxidation of  $\text{FADH}_2$  to FAD. Therefore, the redox ratio decreased significantly. As expected the rotenone/antimycin injection led to a decreased OCR measured by the flux analyzer and a corresponding increase in the FLIM-derived free-to-bound ratio and MCR due to inhibition of the ETC. The injection led to maximized mitochondrial NADH which increased the  $C_1$  and  $C_3$  fluorescence intensity. As a result of the oxidative phos-

## 4 Results

phorylation inhibition, glycolysis becomes upregulated in the cytoplasm, which can be seen by an increased ECAR.

### 4.3.3 Mitochondria Stress Test - Consecutive Injections

The results of the mitochondrial stress test with consecutive injections are almost identical to individual injections in Subsection 4.3.2. However, the microscopically

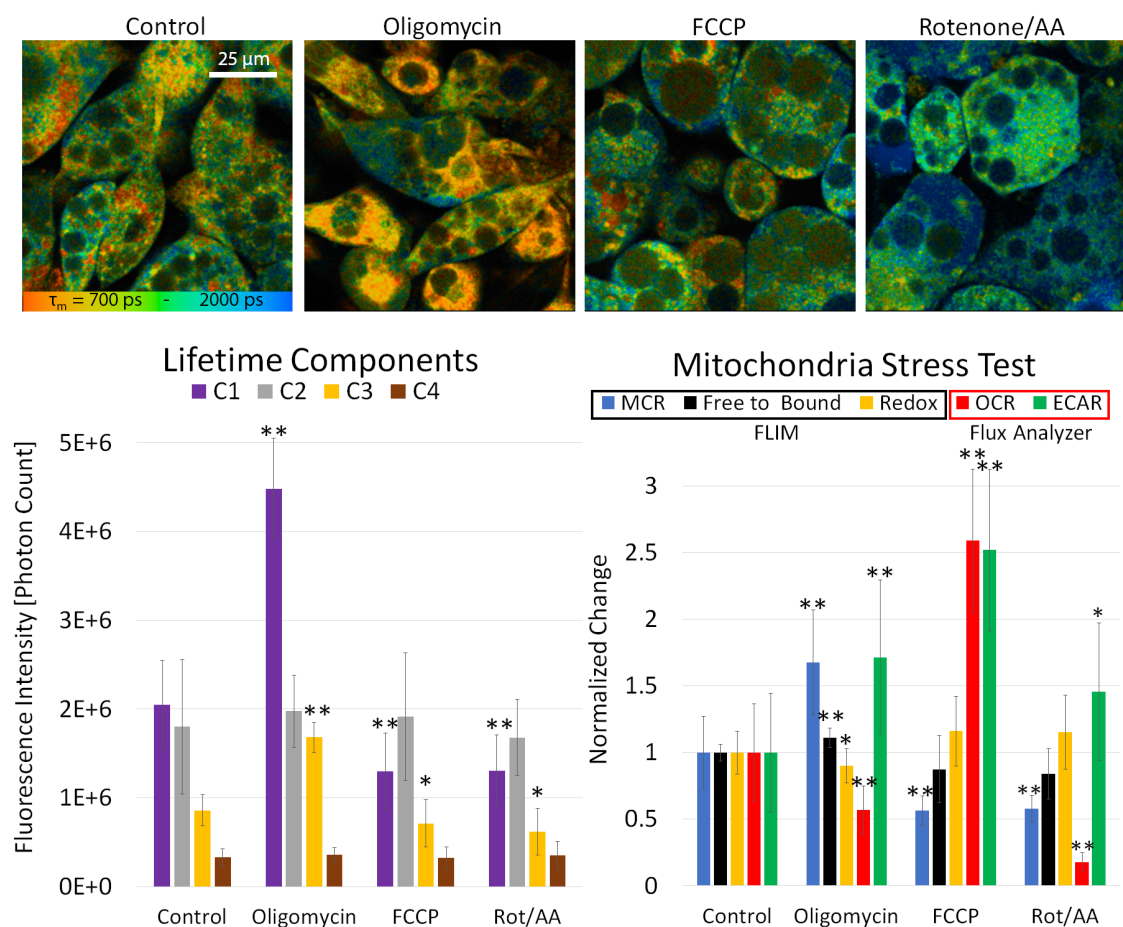


**Figure 4.15:** Mitochondria stress test - consecutive injections. Fluorescence intensity of the individual lifetime components of NADH for each step of the mitochondria stress test. The effect of consecutive injections of oligomycin, FCCP, and rotenone/antimycin on the FLIM-derived MCR, optical free-to-bound ratio, and redox ratio as well as on OCR and ECAR measured by an extracellular flux analyzer. Mean  $\pm$  SD of  $n = 20$  FLIM images per group. Significant differences of treatment groups to the control by Student's  $t$ -test with \*  $p < 0.05$ , \*\*  $p < 0.001$ .



derived biomarkers such as redox ratio, free-to-bound-ratio, MCR, and lifetime parameters differed significantly after injection of rotenone/antimycin. For consecutive injections, first FCCP is added to accelerate the ETC to maximum capacity and subsequently respiration is blocked by the complex I and III inhibitors rotenone and antimycin A. Usually, when these inhibitors are applied, the complex I and III mediated electron flow is stopped and therefore the mitochondrial NADH is not oxidized anymore and accumulates in the matrix. This results in decreased respiration, increased acidification, and change of the imaging biomarkers such as increasing contribution of mitochondrial lifetime components  $C_1$  and  $C_3$ . In contrast to the expectations, rotenone/antimycin injection in the presence of the ETC uncoupler FCCP resulted in no significant change of the mitochondrial lifetime component  $C_1$  and  $C_3$  or any other imaging biomarker compared to before the injection (Fig. 4.15). However, while there were no fluorescence lifetime parameter changes, the flux analyzer determined that respiration stopped, and acidification increased as expected. The inhibitor-uncoupler combination results in a mismatch between cellular respiration and the imaging parameters compared to individual injections.

#### 4.3.4 Glycolysis Stress Test

The glycolysis stress test is the standard assay for measuring glycolytic function, and for this particular stress test, cells are incubated in glucose- and pyruvate-free media. The glycolytic rate is determined by monitoring extracellular pH via changes in media lactate concentration. The glycolysis stress test presented here, consisted of 3 individual injections of pharmacological reagents.

In the first step of the test, injection of glucose leads to a saturation of glucose concentration within the cell, and triggers the start of catabolism through the glycolytic pathway. This catabolic process is accompanied by a discharge of protons into the media, which was observed to cause an increase in ECAR while the OCR remained unchanged. Surprisingly, the optical ratios also remained unchanged Fig. 4.16. However, the fluorescence intensity of lifetime components  $C_1$ ,  $C_2$ , and  $C_3$  increased significantly after the injection of glucose, suggesting higher metabolic activity. The increase of component  $C_2$  was expected and can be explained by reduction of  $\text{NAD}^+$  to NADH as glucose is broken down to pyruvate during glycolysis. The increase of mitochondrial components  $C_1$  and  $C_3$  are somewhat surprising, since no increase in OCR occurred. This could be explained by increased activity in the tricarboxylic acid cycle induced by pyruvate shuttled into the mitochondria [91].

In the second step, injection of oligomycin reveals the maximum glycolytic capacity by inhibition of mitochondrial energy production, causing a shift in the ATP production to glycolysis. The ECAR measured by the flux analyzer, and the FLIM-derived MCR,  $C_1$ ,  $C_3$  and  $C_4$  lifetime component fluorescence were observed to increase significantly after the injection of oligomycin, while the OCR decreased significantly.

## 4 Results

As expected, the oligomycin injection of the glycolysis stress test (Fig. 4.16) has an effect on the cells very similar to the mitochondria stress test (Fig. 4.14). Given both the microscopy- and flux analyzer-derived data, it is very likely that the changes of lifetime components  $C_1$  and  $C_3$  following oligomycin injection into the media are caused by inhibition of the ETC while fluorescence of component  $C_4$  increased due to higher glycolytic activity.

In the final stress test step, 2-DG is injected to inhibit glycolysis by binding to the

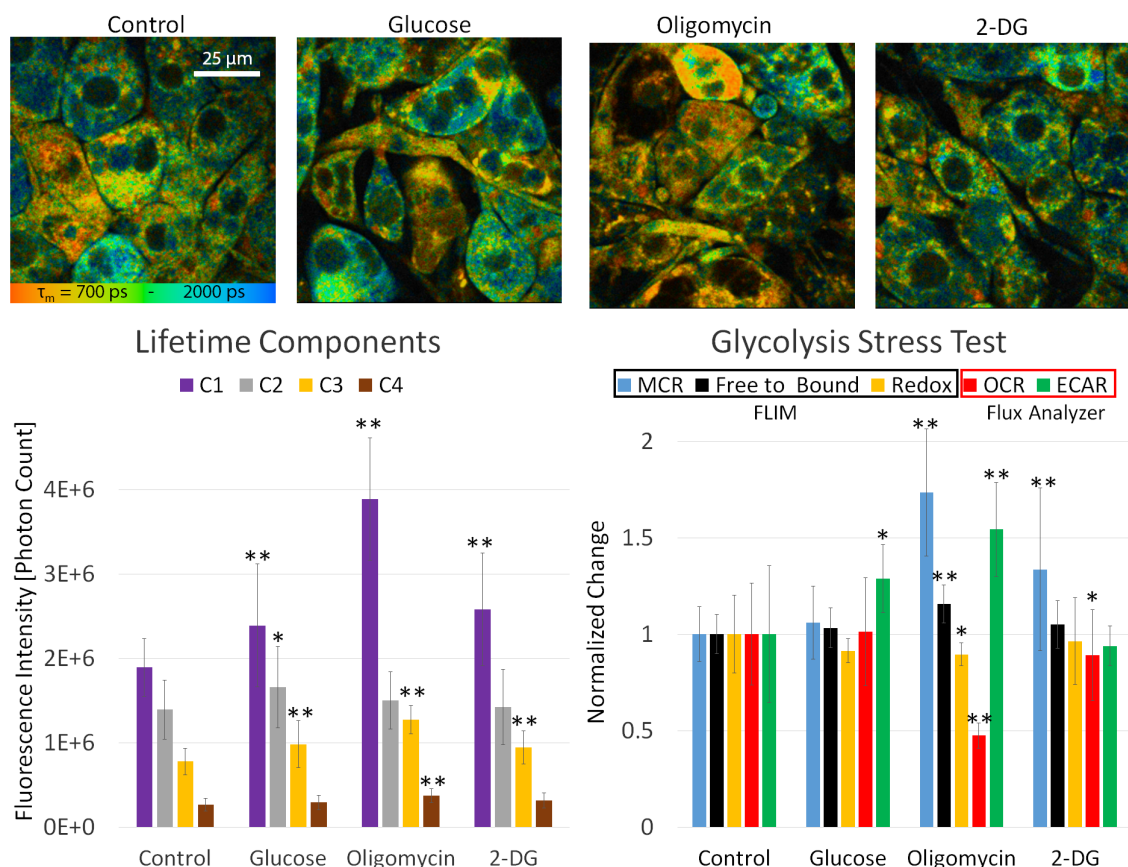


**Figure 4.16:** Glycolysis stress test. Fluorescence intensity of the individual lifetime components of NADH for each step of the glycolysis stress test. The effect of individual injections of glucose, oligomycin, and 2-DG on the FLIM-derived MCR, optical free-to-bound ratio, and redox ratio as well as on OCR and ECAR measured by an extracellular flux analyzer. Mean  $\pm$  SD of  $n = 40$  FLIM images per group. Significant differences of treatment groups to the control by Student's t-test with \*  $p < 0.05$ , \*\*  $p < 0.001$ .

first enzyme of the glycolytic pathway showing the non-glycolytic acidification of cells, leading to an observed decrease in OCR without a resulting change in ECAR as determined by the flux analyzer. Unchanged ECAR after 2-DG injection was an-

ticipated since control cells have a very low glycolytic rate due to the use of glucose- and pyruvate-free cell culture media. The FLIM-derived MCR, component  $C_1$  and  $C_3$  all increased compared to the control. These changes, which correspond to a decreased OCR measured by the flux analyzer, can be explained by reduced activity of the ETC.

### 4.3.5 Redox Ratio

The redox ratio originates from two fluorescent cofactors: NADH and FAD. Both molecules play crucial roles in electron transport in the cell and changes in their concentration can be used to determine the metabolic state of a cell.

The redox ratio and therefore the relative fluorescence intensity of NADH and FAD can be expressed as  $\text{FAD} / (\text{FAD} + \text{NADH})$ .

Literature shows that an increase in redox ratio values are linked to oxidative phosphorylation while a decrease in redox ratio means an increase in glycolytic metabolism [80]. Results of this study are shown in Fig. 4.17 and Fig. 4.18 which highlight changes of NADH intensity, FAD intensity, and redox ratio after individual non-subsequent injection of several pharmacological reagents of the mitochondria stress test and glycolysis stress test. Compared to the baseline with a redox ratio of 0.24, oligomycin and rotenone/AA injection decrease the redox ratio to 0.19 and 0.16, respectively. As expected, the injection of mitochondrial ETC uncoupler FCCP slightly increases the redox ratio by reduction of the mitochondrial NADH pool. For the glycolysis stress test, the individual non-subsequent injection of glucose, oligomycin, and 2-DG results in a decrease of the redox ratio compared to the control value of 0.22. These results and trends conform with other reports showing significant variations in redox ratio due to pharmacologically induced cellular metabolism [151, 150].

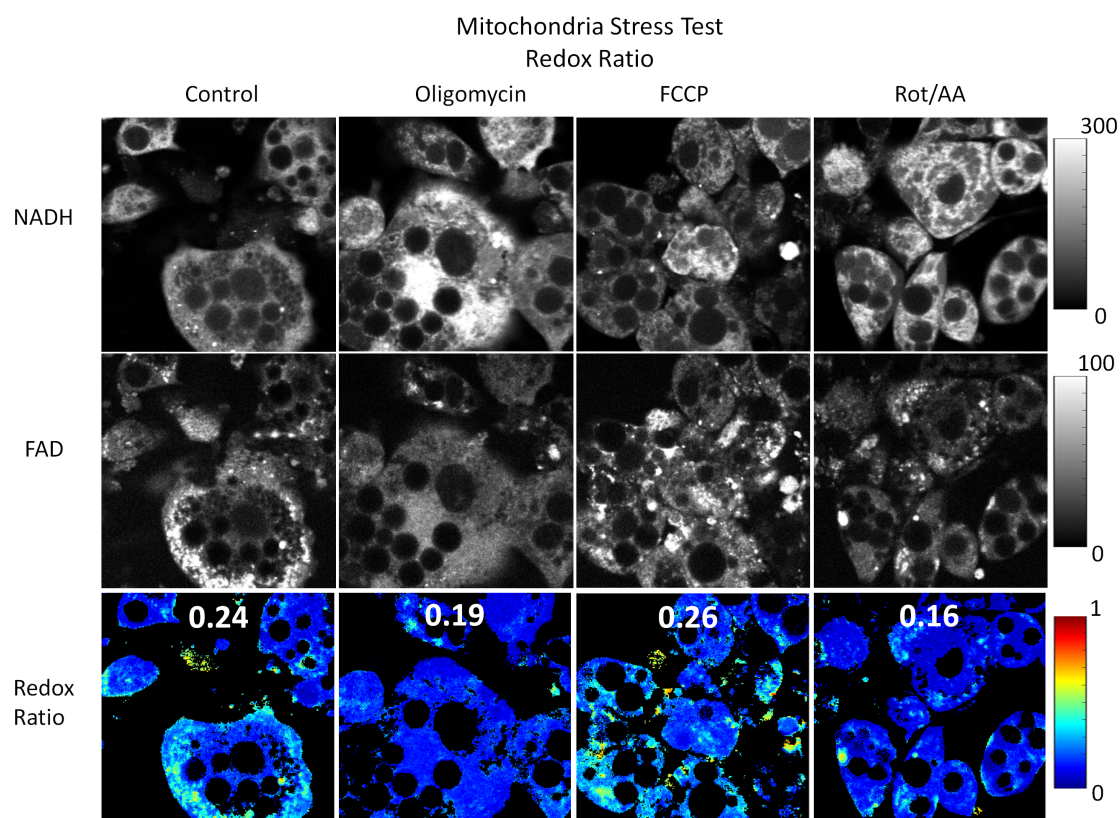


**Figure 4.17:** Redox ratio based on the fluorescence intensity of NADH and FAD for individual non-subsequent injections of the mitochondria stress test. Representative images of NADH, FAD and the calculated redox ratio ( $\text{FAD}/(\text{FAD} + \text{NADH})$ ) in response to individual non-subsequent injections of mitochondrial ETC inhibitors and uncouplers. All images were acquired from different cell plates of the same culture under identical conditions after individual non-subsequent injection of Oligomycin, FCCP, and Rotenone/AA indicated above the figure panels. The average value of the redox ratios are shown on top of the redox images.

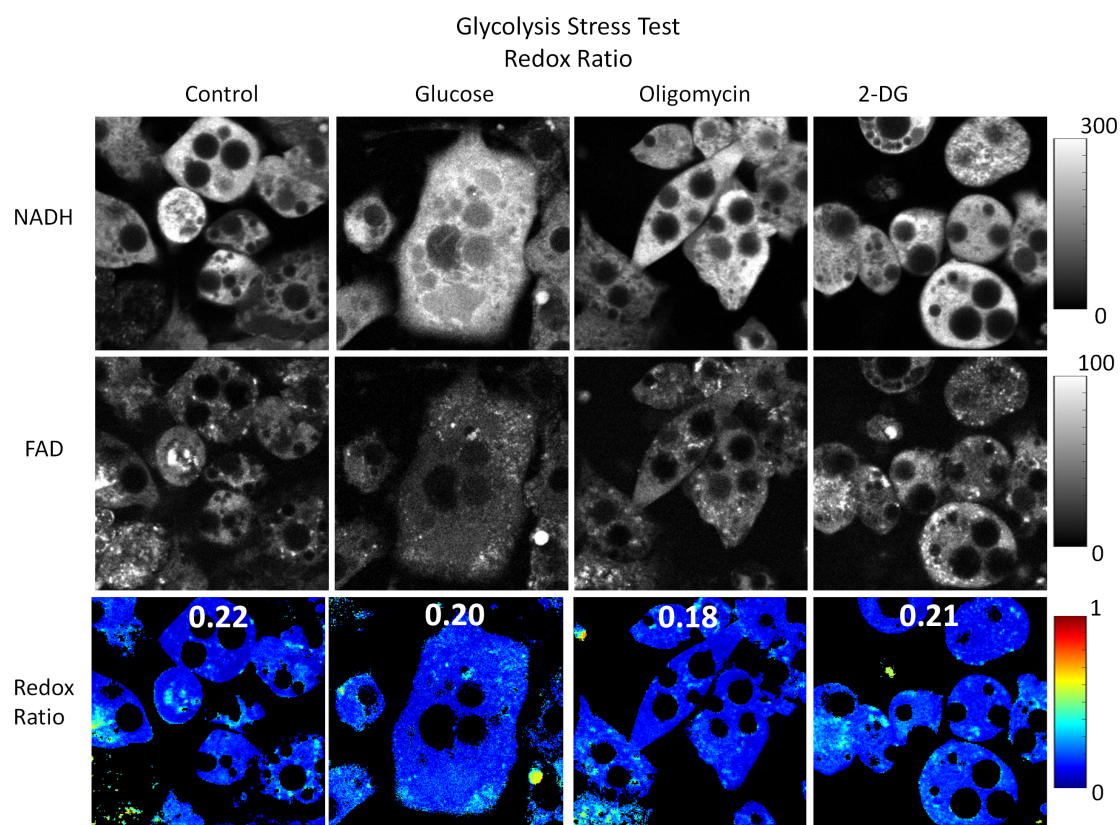


**Figure 4.18:** Redox ratio based on the fluorescence intensity of NADH and FAD for individual non-subsequent injections of the glycolysis stress test. Representative images of NADH, FAD and the calculated redox ratio ( $\text{FAD}/(\text{FAD} + \text{NADH})$ ) in response to individual non-subsequent injections of drugs changing the glycolic rate. All images were acquired from different cell plates of the same culture under identical conditions after individual non-subsequent injection of Glucose, Oligomycin, and 2-DG indicated above the figure panels. The average value of the redox ratios are shown on top of the redox images.



### 4.3.6 Browning of Adipocytes

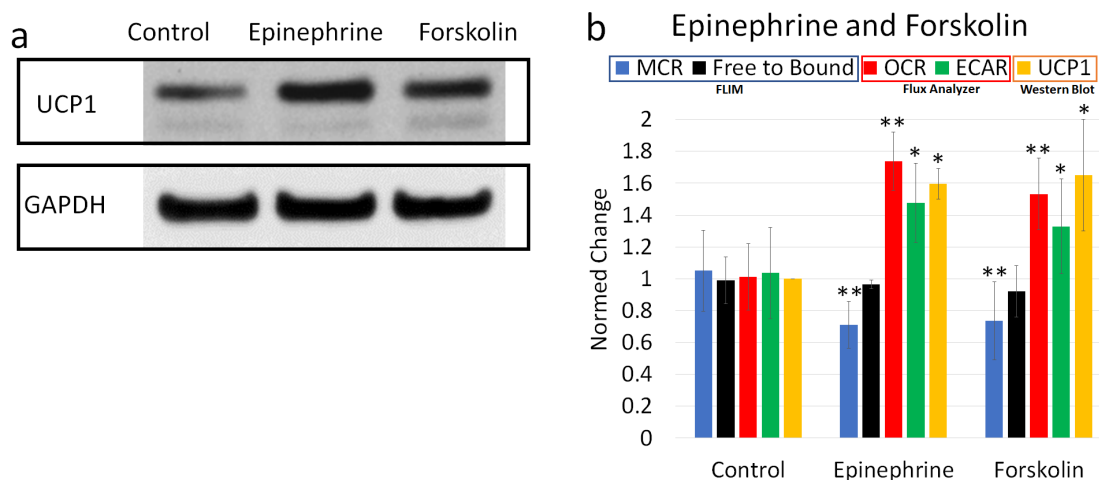


**Figure 4.19:** Murine white inguinal fat after 1-hour treatment with epinephrine and forskolin compared to untreated cells. (a) Expression of UCP1 and house-keeping gene GAPDH. UCP1 expression is normalized to the expression of GAPDH. (b) Effect on the FLIM-derived free-to-bound ratio and MCR, OCR and ECAR measured by the extracellular flux analyzer, and the gene expression of browning marker UCP1 analyzed by western blotting. Mean  $\pm$  SD of  $n = 20$  FLIM images per group. Significant differences of treatment groups to the control by Student's t-test with \*  $p < 0.05$ , \*\*  $p < 0.001$ .

Browning of white adipocytes has been described as an increase in UCP1 expression, resulting in thermogenic, fat-burning properties [152]. Though they initially show low levels of UCP1 expression, exposure of white adipocytes to mild cold or pharmacological reagents can activate a thermogenic pathway that induces the expression of UCP1, and lipolysis. To examine this effect, epinephrine and forskolin, which both promote lipolysis and are known to induce browning, were added to inguinal adipocytes in culture for 1 hour. Western blots (Fig. 4.19) show increased levels of UCP1 protein for treated cells compared to untreated cells. UCP1 expression was normalized to the expression of reference gene GAPDH which remained constant under investigation. Like the pharmacological reagent FCCP, UCP1 acts as a protonophore to facilitate proton translocation across the inner membrane of the mitochondria. Fig. 4.19 shows that like FCCP (Fig. 4.14), both epinephrine and forskolin cause a significant increase in OCR and ECAR. While the optical free-to-bound ratio had no significant change, it is interesting to note that the new MCR metric decreased due to small but significant changes in lifetime components  $C_1$  and  $C_2$  after treatment. Furthermore, it is shown that the MCR is inversely proportional to the OCR, further supporting the idea that this metric is sensitive to metabolic

changes of the ETC (Fig. 4.14, Fig. 4.16, Fig. 4.19).

## 4.4 Quantification of the new MCR Metric

### 4.4.1 MCR of Adipocytes

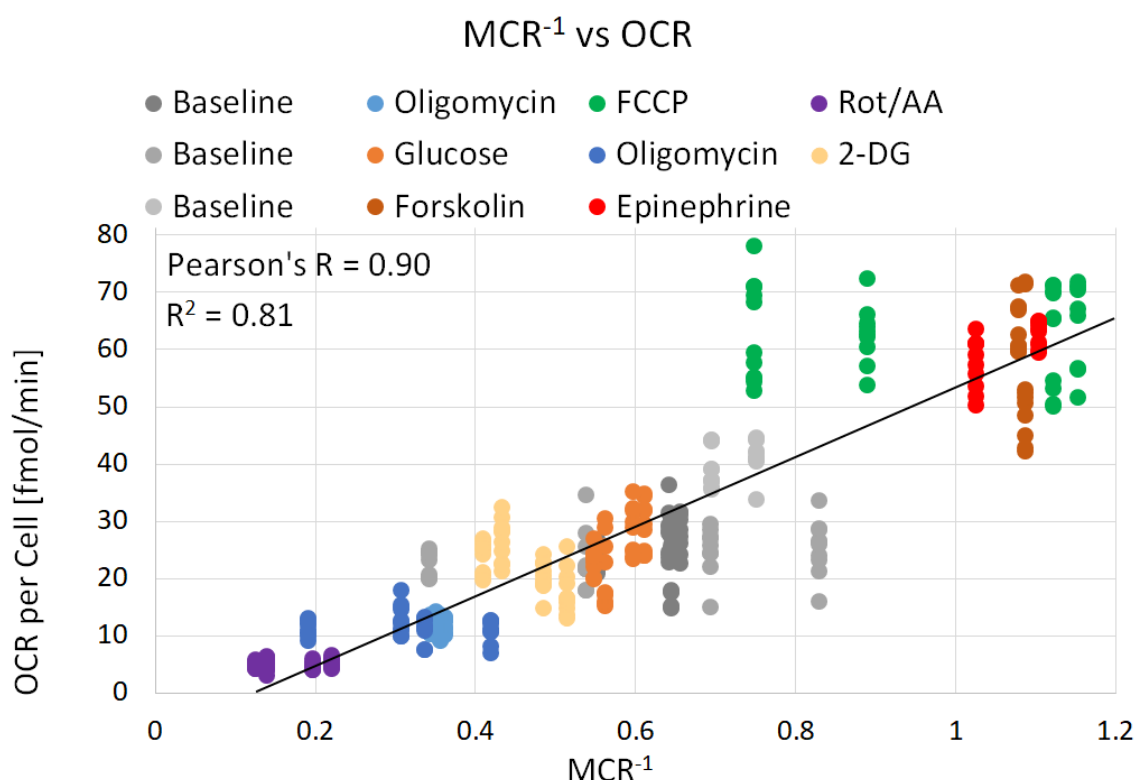


**Figure 4.20:** Scatter plot of OCR vs MCR<sup>-1</sup> for all experimental conditions at 20,000 cells per well. A linear regression was fitted through the OCR and MCR<sup>-1</sup> data of 3T3-L1 and primary inguinal adipocytes for controls and after injection of various pharmacological reagents. The  $R^2$  value which shows how close the data are to the fitted regression line was calculated. The Pearson's correlation shows the measure of strength and direction of association that exists between the OCR and MCR<sup>-1</sup>.

Mitochondrial stress test and glycolysis stress test experiments suggest that the MCR is inversely proportional to the OCR ((Fig. 4.14, Fig. 4.16). To analyze this hypothesis, the microscopic derived MCR data from all cell culture experiments of adipocytes such as mitochondria stress test, glycolytic function stress test, and browning experiments were plotted in combination with the corresponding OCRs

## 4 Results

measured by the flux analyzer Fig. 4.20. For visualization purposes and easier read-out, the inverse MCR ( $\text{MCR}^{-1}$ ) is used in Fig. 4.20.

As expected, it is shown that the  $\text{MCR}^{-1}$  is linearly proportional to the OCR, supporting the idea that this newly introduced metric is sensitive to metabolic changes of the ETC. A strong correlation exists between  $\text{MCR}^{-1}$  and OCR.

While some of the data points from the baseline and FCCP treatment appear to be scattered depending on the cell line and media used, overall, the experiments resulted in a good correlation ( $R^2=0.81$ ) with high  $\text{MCR}^{-1}$  values aligning with high OCRs and low  $\text{MCR}^{-1}$  values with low OCRs (Fig. 4.20). The values for the ECAR and  $\text{MCR}^{-1}$  of adipocytes did not result in a meaningful correlation.

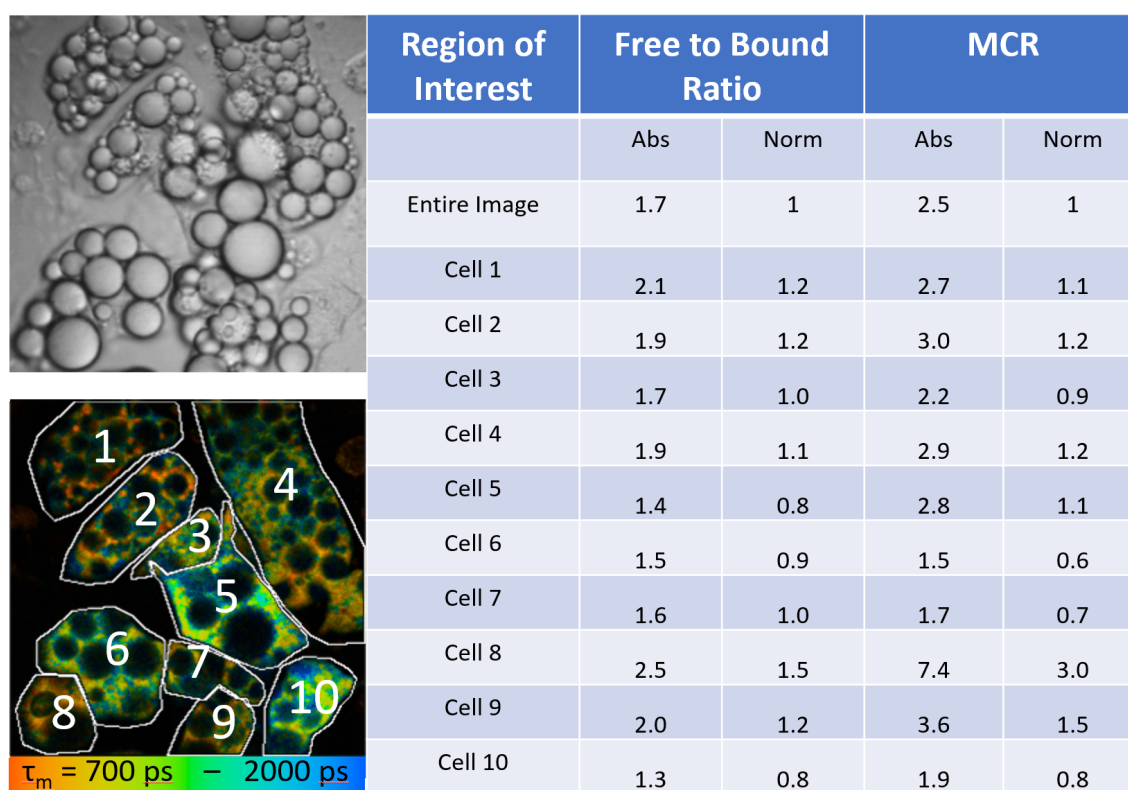


**Figure 4.21:** Manual segmentation of individual cells. Absolute and normalized free-to-bound ratios and MCRs of the entire image as well as for individual cells were calculated. Significant differences can be seen within this untreated monolayer cell culture of 3T3-L1 adipocytes. Normalized MCR values reveal a higher dynamic range compared to normalized free-to-bound ratios.

Furthermore, the free-to-bound ratios and MCRs of individual adipocytes within one field of view were analyzed Fig. 4.21. The individual adipocytes were manually segmented based on a transillumination image and a FLIM image. Afterwards, the



fluorescence lifetime parameters of each cell were calculated and compared to the fluorescence parameters of the entire field of view. The manual segmentation and analysis of individual cells highlights the heterogeneity of the adipocyte mono-layer cell culture. Even though, cells in close proximity have the same appearance, and were exposed to the same conditions, significant differences in free-to-bound ratio and MCR occur with absolute values of 1.3 to 2.5 and 1.5 to 7.4, respectively. There are no obvious correlations such as cell or lipid droplet size that could explain these differences.

The comparison of normalized free-to-bound ratio values and normalized MCR values reveals a higher dynamic range for the MCR analysis Fig. 4.21.

#### 4.4.2 Mixed Cell Cultures

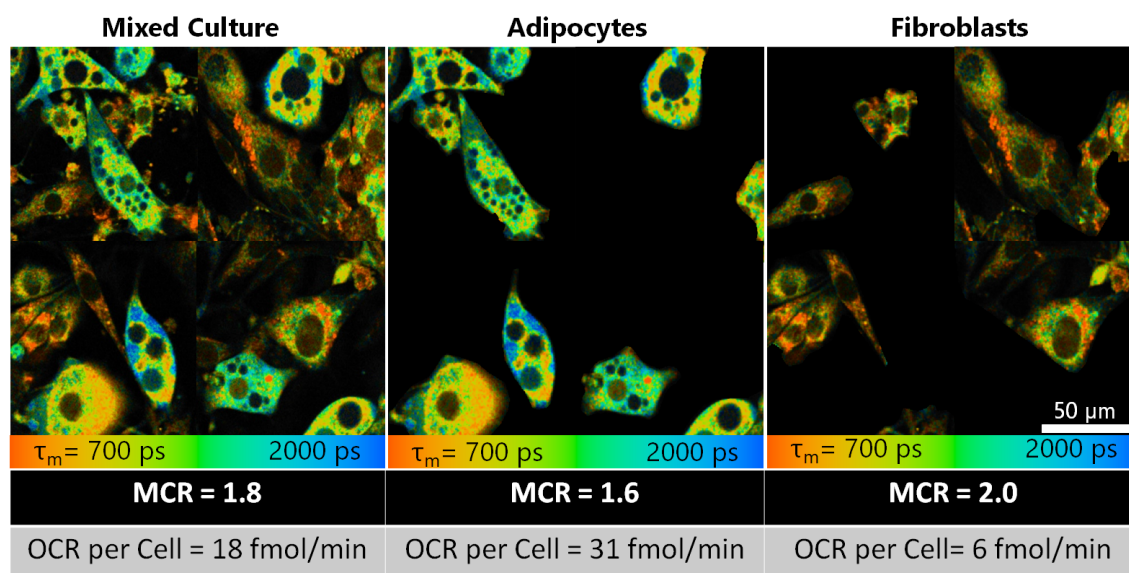


**Figure 4.22:** Mixed cell cultures of adipocytes and fibroblasts in a 1:1 ratio were analyzed with microscopic MCR measurements and flux analyzer derived OCR measurements. Manual segmentation was used for MCR calculations of adipocytes and fibroblasts only. For the OCR measurement by the flux analyzer additional cell cultures with adipocytes only and fibroblasts only were analyzed.

NIH 3T3 mouse embryonic fibroblast cells and differentiated 3T3-L1 adipocytes were used in mixed cell cultures. Fig. 4.22 shows 4 representative images stitched together of a mixed cell culture as well as manually segmented adipocytes and fibroblasts of the same cell culture. The manual selection was performed based on morphological differences such as lipid droplets and cellular shape. The color-coded FLIM images of the mixed cell culture show differences in fluorescence lifetime, with

shorter lifetimes for fibroblasts and longer lifetimes for adipocytes. Additionally, the fluorescence intensity is considerably higher for adipocytes compared to fibroblasts and the adipocyte MCR is lower than the fibroblast MCR. While the microscopic MCR metric can be calculated for the entire cell culture as well as for adipocytes and fibroblasts only, the flux analyzer derived OCR can only be measured for an entire cell culture. Hence, three different cell cultures were analyzed. A mixed culture with 10,000 adipocytes and 10,000 fibroblasts, an adipocyte only culture with 10,000 cells, and a fibroblast only culture with 10,000 cells. For adipocytes, the MCR has a value of 1.6 ( $\text{MCR}^{-1}=0.6$ ) which should result in an OCR per cell of around 30 fmol/min according to Fig. 4.20. As expected, an OCR of 31 fmol/min was measured by the flux analyzer for the adipocyte cell culture (Fig. 4.22). For fibroblasts, the MCR is noticeably higher with a value of 2.0 ( $\text{MCR}^{-1}=0.5$ ) which should result in a lower OCR per cell of around 25 fmol/min according to Fig. 4.20. However, the measured OCR only reaches a value of 6 fmol/min. This can be explained by the different cell type, since the results of Fig. 4.20 only apply to metabolic changes of adipocytes and might not be transferable to another cell line such as fibroblasts. As expected, the MCR and the OCR value of the mixed culture resemble a combination of both cell lines.

### 4.4.3 MCR of HEK cells

To evaluate if a cell line with different cellular structure, function, and origin than adipocytes also generates four distinct NADH fluorescence lifetime components, human embryonic kidney cells 293 (HEK 293) were analyzed. Further, pharmacological induced metabolic changes of HEK 293 cells were induced and microscopically and extracellular flux derived metabolic markers were evaluated and compared to results from adipocytes. Therefore, the mitochondria stress test was applied to this cell line. Mitochondrial respiration and extracellular acidification of HEK293 were analyzed using an extracellular flux analyzer and compared to the microscopically derived optical redox ratio, free-to-bound ratio and MCR. The mitochondria stress test presented here, consisted of 3 individual injections of oligomycin, FCCP, and rotenone/antimycin.

Oligomycin injection results in an increase in mitochondrial NADH and decrease of FAD which increases both the optical free-to-bound ratio and MCR, while the redox ratio decreases as can be seen in Fig. 4.23. Specifically, the contribution to the total fluorescence intensity of mitochondria lifetime components  $C_1$  is observed to rise, while the contribution of the cytoplasmic component  $C_4$  decreased. As shown for adipocytes, the oligomycin injection of HEK 293 cells resulted in a decreased OCR and an increased ECAR determined by an extracellular flux analyzer.

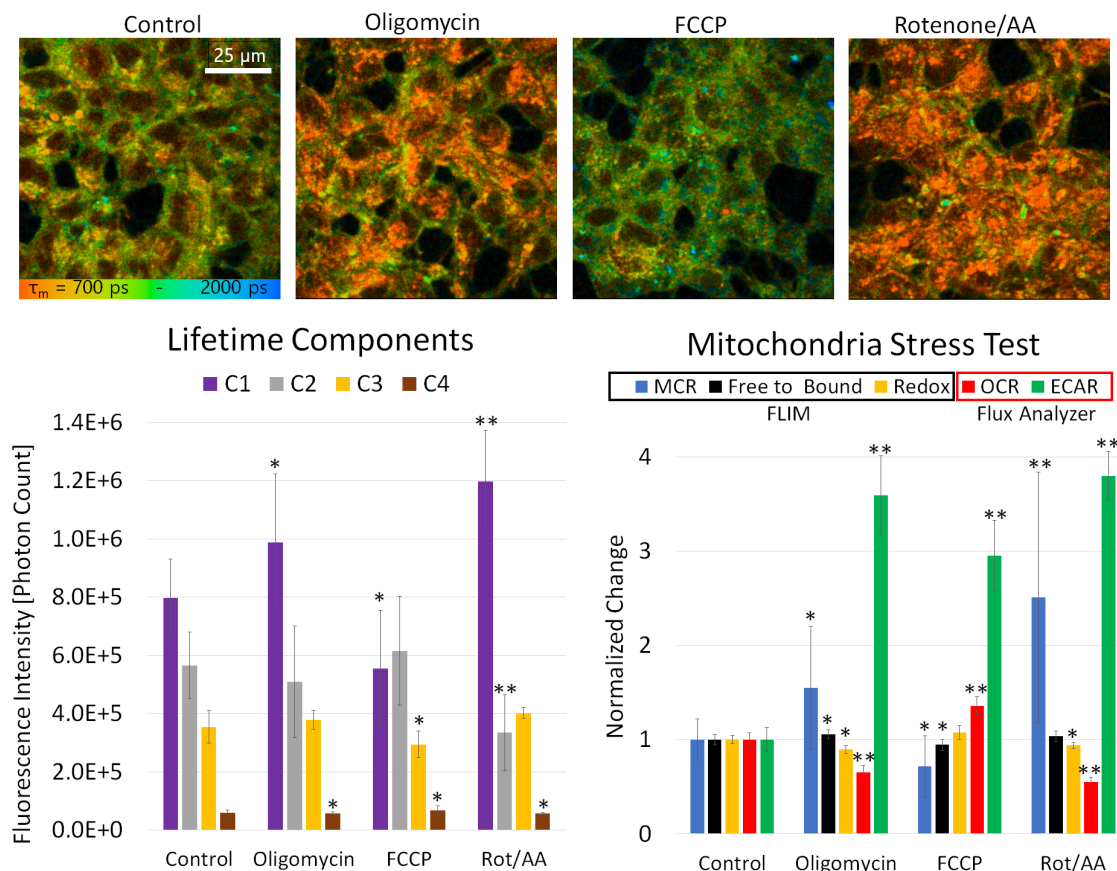


**Figure 4.23:** Mitochondria stress test of HEK 293 cells. Fluorescence intensity of the individual lifetime components of NADH for each step of the mitochondria stress test. The effect of individual injections of oligomycin, FCCP, and rotenone/antimycin on the FLIM-derived MCR, optical free-to-bound ratio, and redox ratio as well as on OCR and ECAR measured by an extracellular flux analyzer. Mean  $\pm$  SD of  $n \geq 10$  FLIM images per group. Significant differences of treatment groups to the control by Student's t-test with \*  $p < 0.05$ , \*\*  $p < 0.001$ .

The second individual injection is FCCP, which resulted in an increase in OCR and ECAR as measured by the flux analyzer. FCCP causes the mitochondrial NADH pool to deplete due to higher activity of the ETC, which resulted in a decrease in mitochondrial NADH fluorescence lifetime components  $C_1$  and  $C_3$ . As anticipated, the MCR was observed to decrease, with the mitochondrial  $C_1$  and  $C_3$  fluorescence intensity declining while the  $C_4$  intensity increased. While the free-to-bound ratio slightly decreased, the redox ratio does not show significant changes compared to the baseline after FCCP injection.

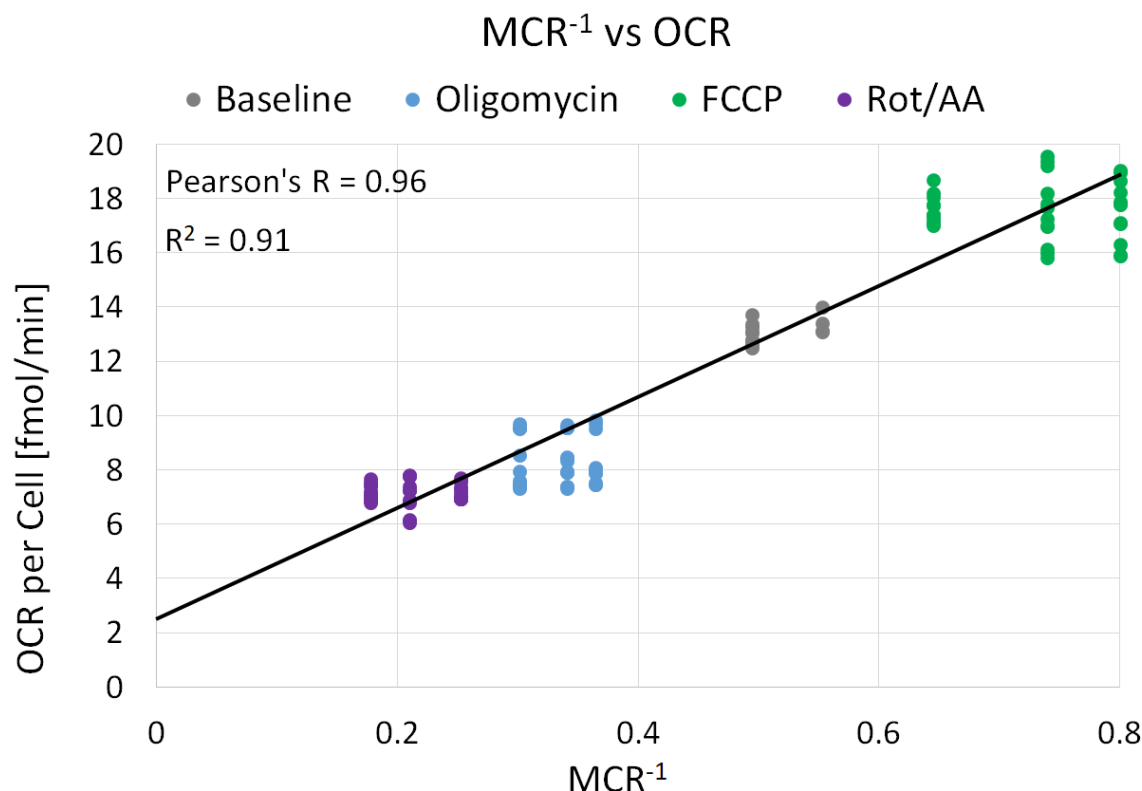


**Figure 4.24:** Scatter plot of OCR vs MCR<sup>-1</sup> for all experimental conditions at 20,000 cells per well. A linear regression was fitted through the OCR and MCR<sup>-1</sup> data of HEK 293 cells for baseline measurements and after injection of pharmacological reagents of the mitochondria stress test. The  $R^2$  value which shows how close the data are to the fitted regression line was calculated. The Pearson's correlation shows the measure of strength and direction of association that exists between the OCR and MCR<sup>-1</sup>.

The individual injection of respiratory chain inhibitors rotenone and antimycin induce oxidative stress and maximize the mitochondrial NADH pool while stopping FAD oxidation. This results in a redox ratio decrease and an increase in  $C_1$  fluorescence intensity as well as MCR. As expected the rotenone/antimycin injection led to a decreased OCR and an increased ECAR measured by the flux analyzer.

The induced metabolic changes of HEK 293 cells resulted in very similar lifetime component and metabolic marker shifts compared to adipocytes. This further strengthens the validation of the new MCR metric as well as the fact that even non-adipose cells exhibit four distinct NADH fluorescence lifetime components. Comparable to Fig. 4.20 a linear proportion between OCR and the inverse MCR (MCR<sup>-1</sup>) exists for HEK 293 cells. MCR<sup>-1</sup> data from mitochondria stress test cell culture experiments of HEK 293 cells were plotted in combination with the corresponding OCRs measured by a flux analyzer (Fig. 4.24). For this cell line an even stronger

correlation ( $R^2=0.91$ ) was found between  $\text{MCR}^{-1}$  and OCR compared to adipocytes ( $R^2=0.81$ ).

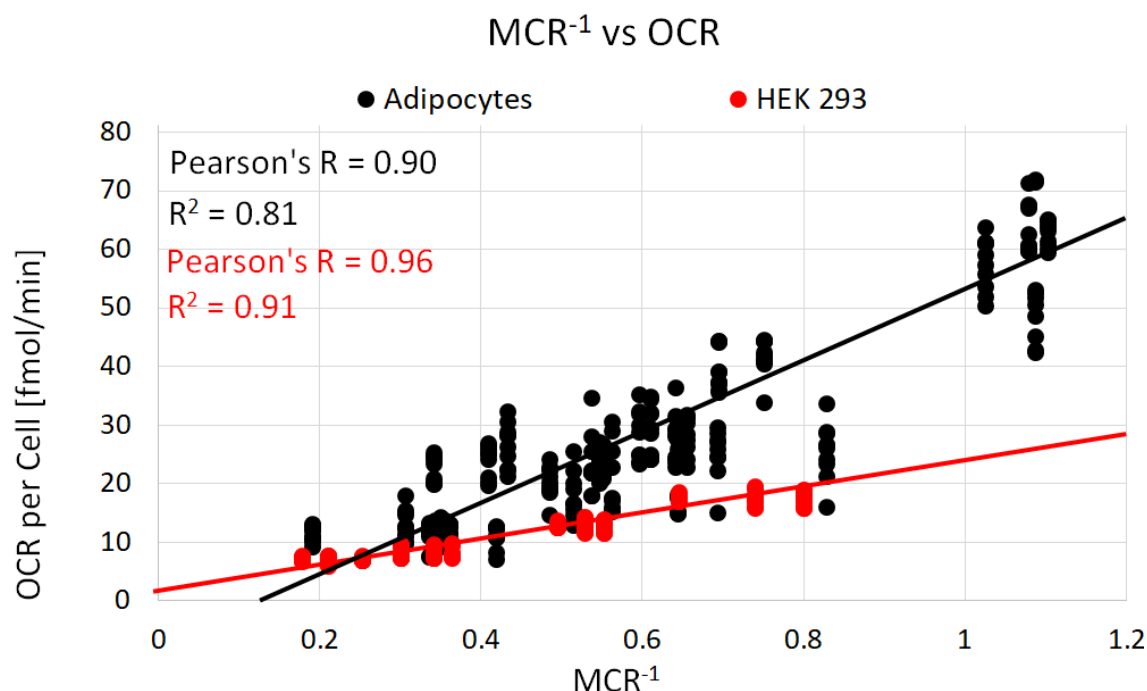


**Figure 4.25:** Scatter plot of OCR vs  $\text{MCR}^{-1}$  for all experimental conditions at 20,000 cells per well. A linear regression was fitted through the OCR and  $\text{MCR}^{-1}$  data of HEK 293 cells for baseline measurements and after injection of pharmacological reagents of the mitochondria stress test. The  $R^2$  value which shows how close the data are to the fitted regression line was calculated. The Pearson's correlation shows the measure of strength and direction of association that exists between the OCR and  $\text{MCR}^{-1}$ .

Fig. 4.25 compares the inverse MCR ( $\text{MCR}^{-1}$ ) vs OCR correlation between adipose cells and HEK 293 cells. Both cell lines show good correlation between  $\text{MCR}^{-1}$  and OCR and have the same trend with low  $\text{MCR}^{-1}$  values for low OCRs, and high  $\text{MCR}^{-1}$  values for high OCRs. However, the linear regression that was fitted through the data shows a lower slope for HEK 293 cells compared to adipocytes. While at  $\text{MCR}^{-1}$  values of 0.2 the OCR per cell for both cell lines is about 6 fmol/min, for higher  $\text{MCR}^{-1}$  values such as 0.8, the OCR per cell of HEK 293 cells is only at 20 fmol/min, while the OCR per cell of adipocytes is at 40 fmol/min. Therefore, the  $\text{MCR}^{-1}$  vs OCR correlation does not only depend on the metabolic state of a cell but also on the cell line.

## 4.5 Adipose Tissue

### 4.5.1 Epididymal, Inguinal, and Interscapular Mouse Fat

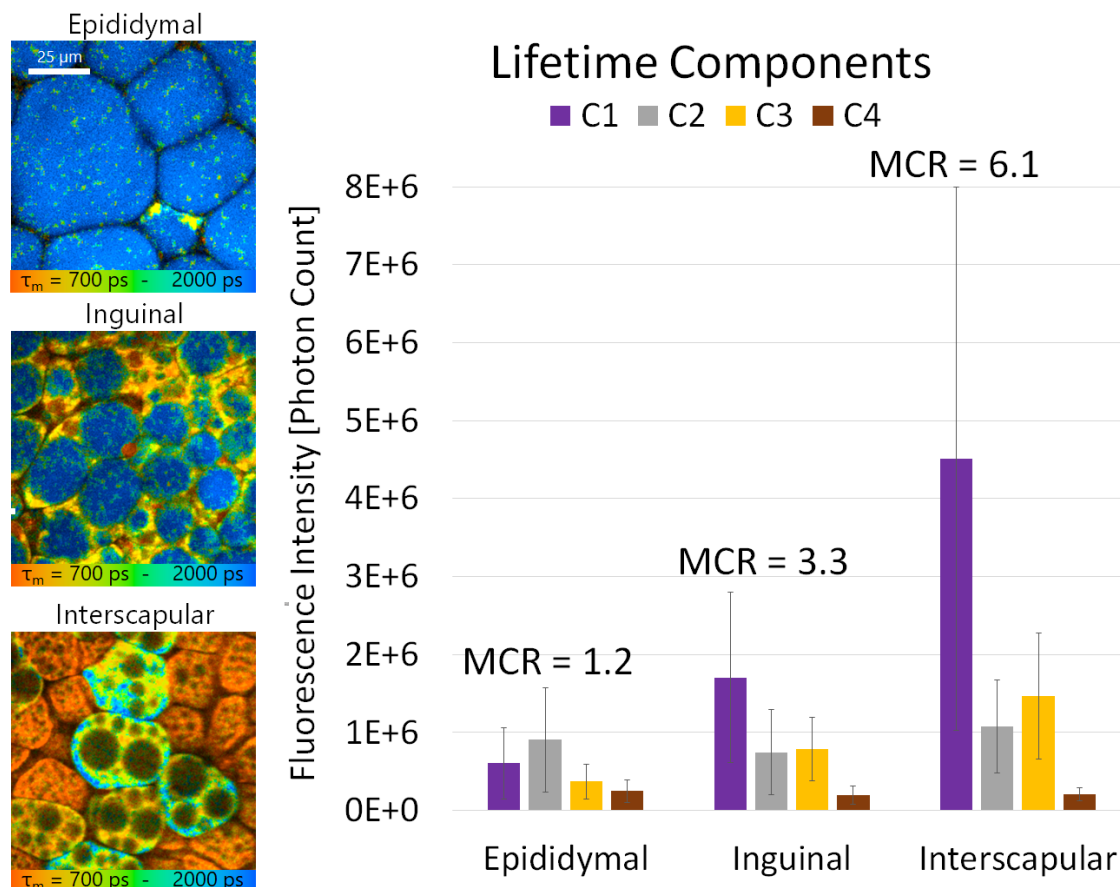


**Figure 4.26:** Representative NADH FLIM images of epididymal, inguinal, and interscapular fat and the individual fluorescence intensity of their lifetime components.

FLIM measurements on freshly excised fat pads were performed. Images were acquired from as deep as 50  $\mu\text{m}$  in tissue excised from the epididymal, inguinal, and interscapular fat depots of mice. Interscapular fat in mice is recognized as classical BAT with robust thermogenic properties. Epididymal fat is WAT which is often taken as a non-thermogenic control tissue as it is resistant to tissue browning. In contrast, inguinal fat is often called subcutaneous WAT (scWAT) that can turn into BeAT as it has the ability to form beige adipocytes with thermogenic properties. The lipid droplets of all tested types of fat depots had a long mono-exponential fluorescence lifetime decay around 6 to 7 ns that was distinct from the typical NADH-FLIM



signature. Therefore, the lipid droplets were removed from the fluorescence analysis with two methods used in combination. First, cellular features were identified by a detectable FAD fluorescence signal while lipid droplets were distinguished by weak to absent emission at the FAD channel. And secondly, CARS signals of the lipid droplets were used to mask out lipid content from the analysis.

Morphologically, clear differences can be drawn between the adipocytes of the three fat pads. Smaller sized lipid droplets and smaller sized cells are seen in BAT compared to scWAT and WAT (Fig. 4.26). Individual image fields were captured from between 5 to 10 separate locations across each tissue specimen to better sample any larger scale tissue heterogeneity. Especially in BAT, high cell heterogeneity was observed with cells having few relatively large lipid droplets with longer fluorescence lifetimes as well as cells with numerous small lipid droplets and shorter fluorescence lifetimes. More importantly, the images showed higher fluorescence intensity and shorter fluorescence lifetimes in BAT compared to both WAT depots. This is a reflection of both higher mitochondrial density, and higher turnover rates in the electron transport chain (ETC) in BAT compared to WAT [21]. Thus, it is not surprising that the distribution of the lifetime components and fluorescence intensity per field of view are different between the fat depots. Mentionable is the extremely small amount of non-lipid fluorescent cellular features in WAT, which results in low overall fluorescence intensity after removing lipid fluorescence from the analysis. Therefore, considerably more WAT FLIM images have to be analyzed compared to BAT FLIM images, to reach statistical significance. However, non-lipid cellular features of WAT exhibit a different fluorescence lifetime distribution compared to non-lipid cellular features of scWAT and BAT. Mitochondrial lifetime components  $C_1$  and  $C_3$  are very low which was expected as WAT is known to have very small amounts of mitochondria. Increasing mitochondrial content as seen in scWAT and BAT results in significantly higher total fluorescence of lifetime components  $C_1$  and  $C_3$  as well as higher overall fluorescence intensity per field of view.

Experiments showed that different adipose tissue types have diverse morphological and optical characteristics. WAT, scWAT, and BAT fat depots from mice differ significantly in NADH lifetime parameters, lipid droplet size, mitochondria content, and reaction to pharmacological reagents. WAT favors energy storage as seen by large lipid droplets which are utilized by circulation while BAT has many small lipid droplets for thermogenesis through fatty acid oxidation [21, 153]. ScWAT and BAT depict strong fluorescence of lifetime components  $C_1$  and  $C_3$  representing high mitochondrial density, potential to dissipate heat, and flux through oxidative phosphorylation. WAT on the other hand shows very low non-lipid fluorescence which predominately originates from lifetime component  $C_2$  and  $C_4$  demonstrating low mitochondrial density and flux through glycolysis. The notion that scWAT can turn into BeAT and adapt to a BAT-like metabolic profile is evident as the morphology and fluorescence parameters are fairly similar to BAT even without thermogenic activation.

### 4.5.2 Storage Influence on Fluorescence Lifetime

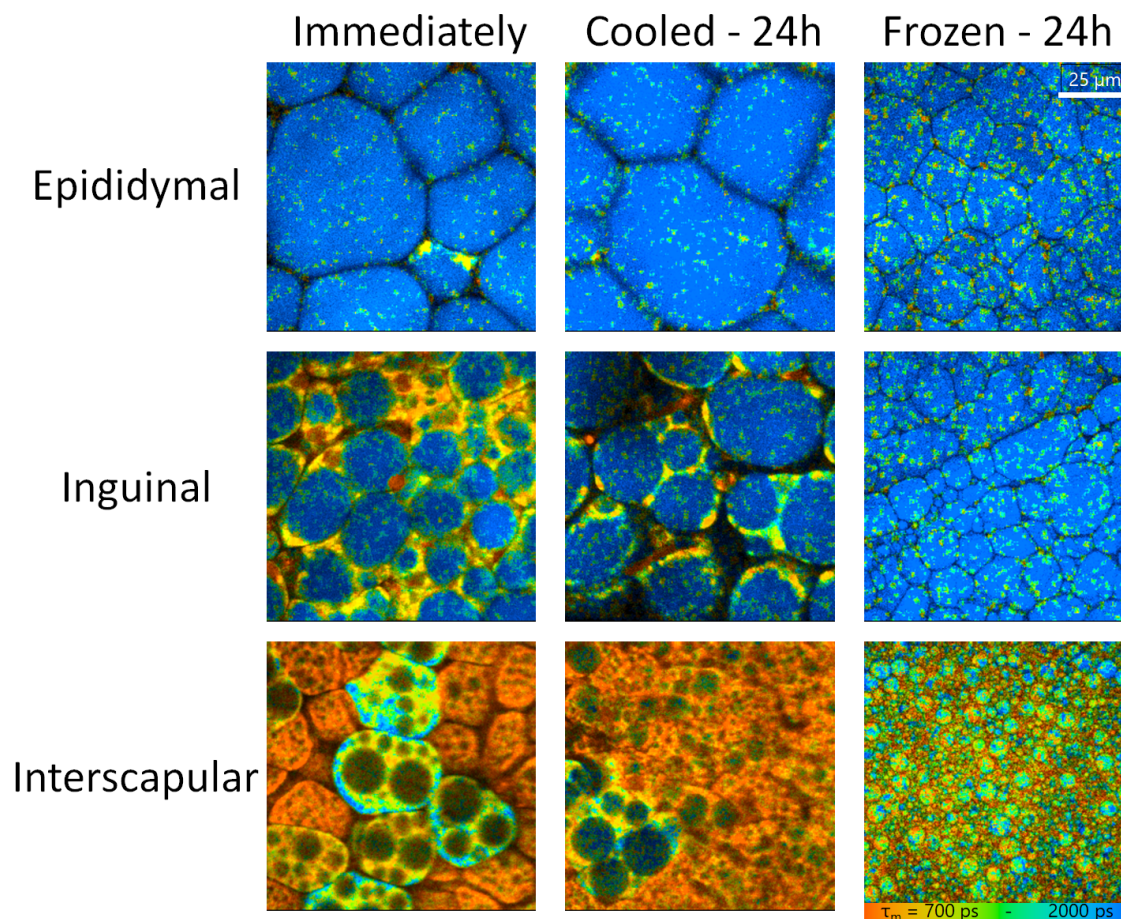


**Figure 4.27:** FLIM images of NADH of epididymal, inguinal, and interscapular fat pads. Imaging of the tissue was performed immediately after excision, after 24 hours at 4°C, and after snap freezing with liquid nitrogen and storage for 24 hours at -80°C.

Due to logistical problems, it is often not possible to analyze tissue specimen immediately after excision. Therefore, two common storage conditions were compared to the results of freshly imaged fatty tissue. The aim of these experiments was to determine if and how storage conditions effect fluorescence lifetime parameters. Epididymal, inguinal, and interscapular depots from mice were imaged at 37°C immediately after excision, after 24 hours in a refrigerator at 4°C, or after being frozen at -80°C for 24 hours. Fig. 4.27 shows an overview of representative FLIM images of the three different tissues at all storage conditions. While fresh and cooled tissue specimen have similar appearances, the frozen tissue underwent significant morphological changes. The lipid droplets of frozen tissue of all three fat depots



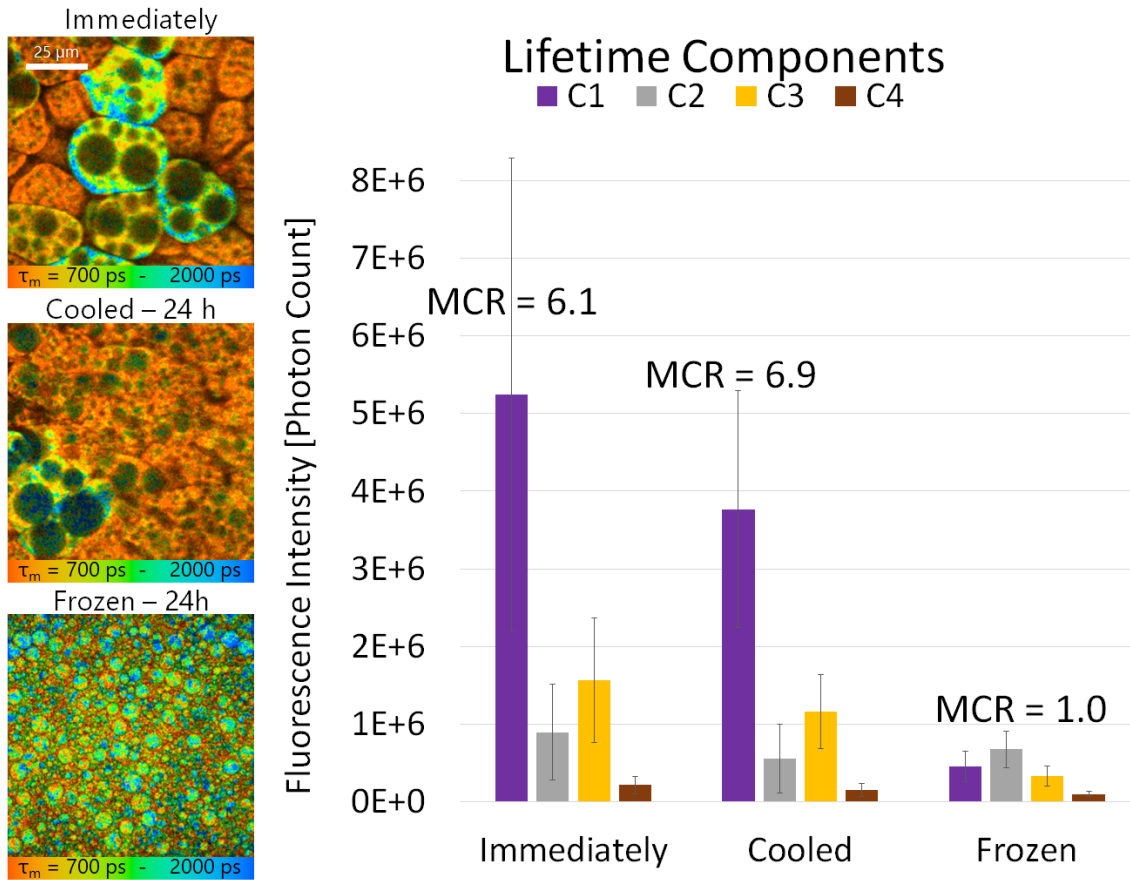


**Figure 4.28:** FLIM images of NADH of interscapular fat pads and the individual fluorescence intensity of their lifetime components. Imaging of the tissue was performed immediately after excision, after 24 hours at 4°C, and after 24 hours at -80°C.

are considerably smaller than for fresh and cooled tissue. The assumption is that during the freezing and thawing process the lipid membranes break which causes the lipid to leak out and form smaller lipid droplets. Additionally, all three frozen FLIM images have less heterogeneous fluorescence patterns and longer fluorescence lifetimes. This again can be explained by membrane breakage. Cooled scWAT and WAT FLIM images had lower amounts of non-lipid fluorescence than fresh specimen while cooled BAT FLIM images were comparable to fresh BAT images.

Fluorescence lifetime components of BAT revealed differences between storage conditions. Fresh BAT images exhibited high fluorescence intensity and as expected mitochondrial lifetime components  $C_1$  and  $C_3$  were especially distinctive. Compared to this, the distribution of cooled BAT was almost identical with overall lower fluorescence intensity. Frozen tissue samples demonstrated the lowest fluorescence

intensity of the three investigated conditions with low mitochondrial fluorescence. This indicates that frozen cells underwent serious morphological and fluorescence changes and shouldn't be used for accurate lifetime analysis. Taken together, these images demonstrate that functional metabolic imaging via TPEF of intrinsic NADH not only provides contrast between different functional types of adipose tissue, such as WAT, BeAT, and BAT but can also indicate tissue viability and metabolic states of the cells.

### 4.5.3 Metabolic Changes of Tissue

Like for mono-layer adipocyte cultures, optical metabolic readouts and flux analyzer measurements of the epididymal, inguinal, and interscapular depots from mice were analyzed after injection of pharmacological reagents. To quantify differences between tissues, algorithmic segmentation of cellular features and lipid compartments were applied in each image using combined fluorescence intensity, lifetime data and CARS signals.

Mean redox ratio, free-to-bound ratios, and MCRs were calculated for non-lipid regions, while a flux analyzer measured OCRs and ECARs for each tissue type. Due to logistical obstacles such as time constraints, tissue viability, and the need for immediate imaging, fewer tissue samples than needed for strong statistical significance were analyzed. Images had to be taken immediately after excision as Subsection 4.5.2 showed, that non-lipid fluorescence, especially in WAT, decreased significantly after tissue storage. Additionally, reproducibility is a lot more difficult with tissue samples than cell cultures where exact cell counts can be quantified. Using consistent size and weight of the tissue samples have been shown to result in satisfying and reproducible outcomes with the flux analyzer. For comparison of different tissue types one has to keep in mind that the three fatty tissues have differences in size and weight per cell. Nevertheless, experiments were carried out as consistent and precise as possible.

A big advantage of the flux analyzer is its capability to investigate up to 24 wells with tissue specimen at the same time, while microscopical imaging is restricted to one sample at a time. Analysis of the individual NADH lifetime components and imaging biomarkers revealed that metabolic changes of tissue have very similar trends compared to adipocyte cell cultures. Injections of FCCP mainly causes a decrease in mitochondrial NADH components  $C_1$  and  $C_3$  which account for the changes of the MCR. As expected, the flux analyzer derived OCR and ECAR of tissue experiments showed trends in the same direction as for cell culture experiments. However, the scope of the induced metabolic changes was less pronounced even though significantly higher pharmacological concentrations (8  $\mu$ M FCCP, 10  $\mu$ M Rot/AA) were applied. As expected, respiratory inhibitors rotenone and antimycin produced an increase of mitochondrial lifetime components  $C_1$  and  $C_3$ .

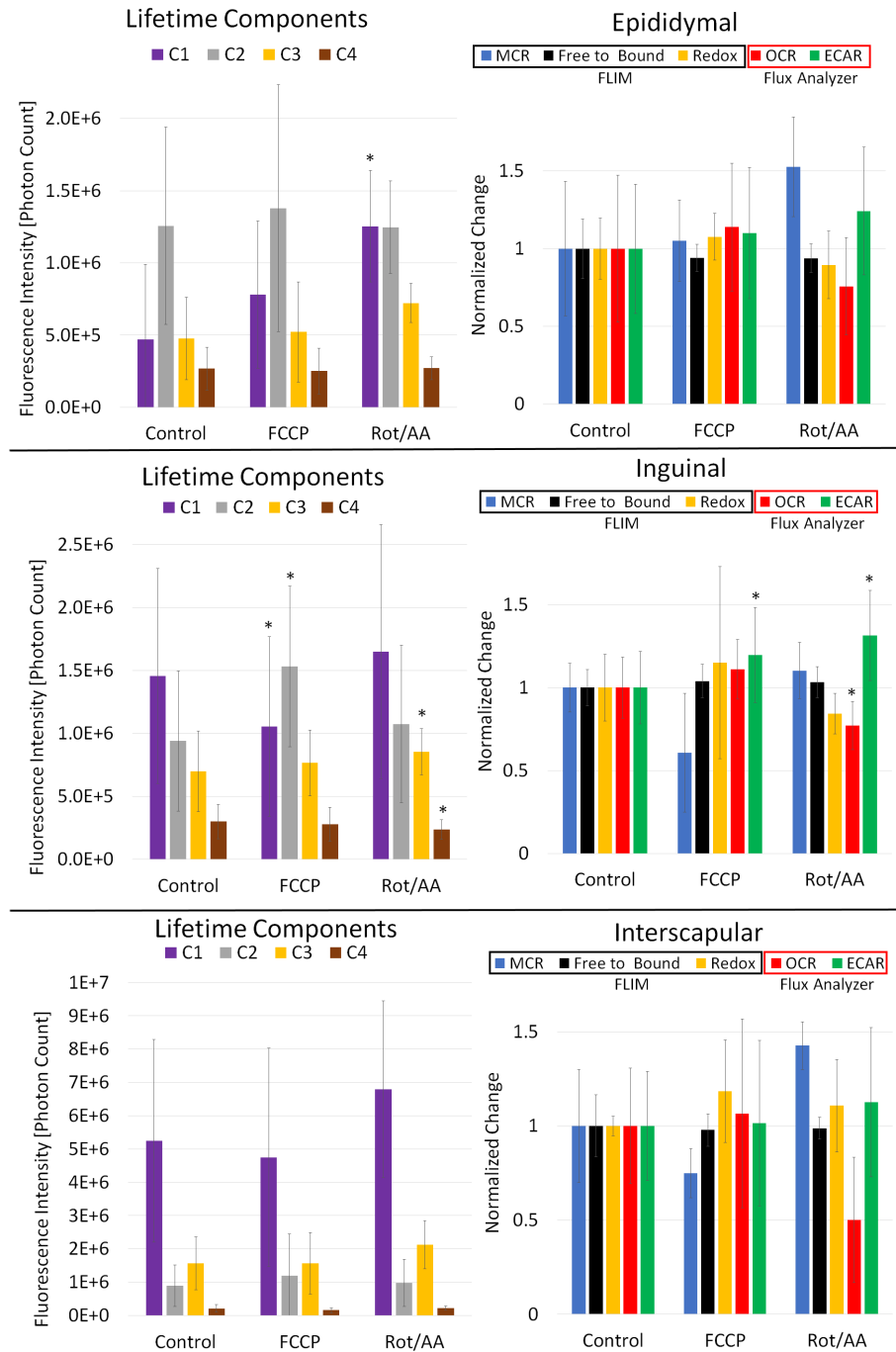


**Figure 4.29:** Fluorescence intensity of each lifetime component of NADH for epididymal, inguinal, and interscapular fat after individual injections of FCCP ( $8\mu\text{M}$ ) and rotenone/antimycin ( $10\mu\text{M}$ ). The effect of individual injections on the FLIM-derived MCR, optical free-to-bound ratio, and redox ratio as well as on OCR and ECAR measured by an extracellular flux analyzer. Mean  $\pm$  SD of  $n = 10$  FLIM images per group. Significant differences of treatment groups to the control by Student's  $t$ -test with \*  $p < 0.05$ .

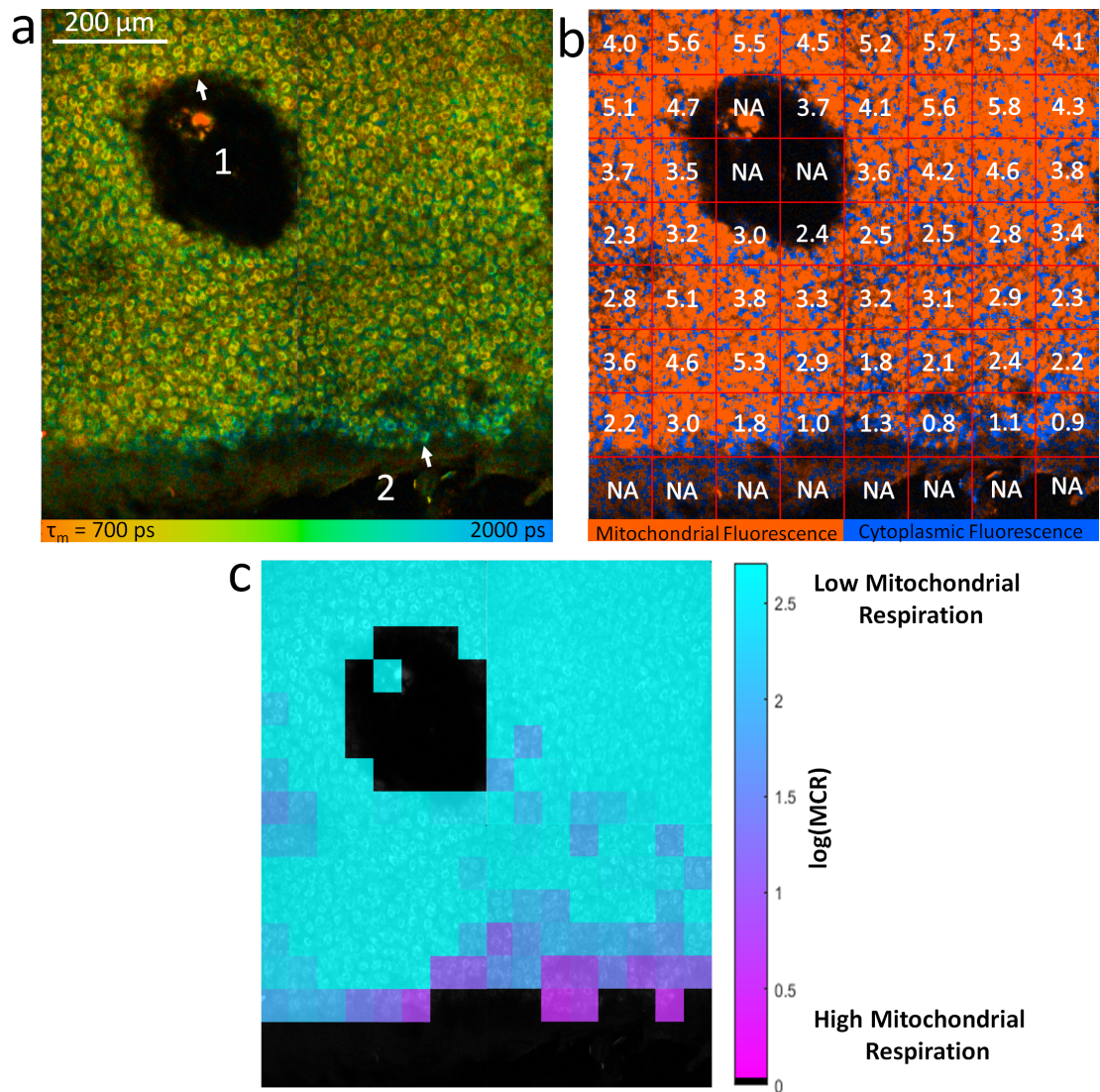


**Figure 4.30:** Metabolic imaging of human keratinocytes in living engineered skin inside the stratum granulosum at a depth of 50  $\mu\text{m}$ . **a:** FLIM image of epidermal skin equivalent with **1:** a CO<sub>2</sub> laser (20 mJ) induced fractional wound and **2:** a mechanically induced (1 mm punch biopsy) epidermal wound. Images were taken 24 hours after the wounds were induced. Arrows mark the edge of the wound. **b:** The image is divided into 64 equal squares and the MCR value for each individual area is displayed. Depending on the origin of the fluorescence, each pixel of the image was color coded. Red for predominantly mitochondrial fluorescence and blue if the fluorescence arises from the cytoplasm. **c:** A way of displaying the fluorescence information of epidermal skin with respect to metabolic activity. The image is divided into 256 equal squares and color-coded contingent on the logarithmic value of the MCR. Low  $\log(\text{MCR})$  values represent high metabolic activity while high  $\log(\text{MCR})$  values denote low metabolic activity. This representation highlights increased metabolic activity at the mechanically induced wound and no change in metabolism at the laser induced wound.

#### 4.5.4 Wound healing of Human Skin Equivalent

Preliminary data of wound healing experiments in human skin equivalents using NADH-FLIM show promising results. The cells at the edge of the mechanically induced epidermal wound, show a decreased MCR and increased fluorescence lifetime indicating higher cellular respiration (Fig. 4.30). Previous studies by Deka et al showed similar results at the closure of an epidermal wound where increased fluorescence lifetime was observed which indicates oxidative phosphorylation as the major source of energy production [154]. Metabolic imaging of wound healing of skin equivalents exhibited promising preliminary results which could be extended further to study metabolic reactions induced by wounds, drugs, cosmetics, and various natural and chemical reagents. For this purpose, skin equivalent, 3D engineered tissue as well as ex-vivo tissue samples could be analyzed.



## 5 Discussion

The objective of this thesis was the development of an imaging based NADH fluorescence biomarker that enhances quantification of cellular metabolic function compared to currently known biomarkers as well as assessment of individual cells in real time. Additionally, imaging biomarkers were compared and correlated to extracellular flux analysis to identify and understand underlying mechanisms and influencing dynamics and therefore trying to establish an improved optical evaluation methodology. Measuring endogenous NADH fluorescence is a well-known research technique allowing the evaluation of metabolic activity on a subcellular level. Even though NADH fluorescence and its promising implications have been discovered over 60 years ago by Chance et al, NADH autofluorescence measurements have not transcended into laboratories as the standard tool for bioenergetics [1]. The focus of numerous researchers has improved the optical NADH energy metabolism analysis tremendously over time by addition of intrinsic FAD fluorescence as well as usage of NADHs fluorescence lifetime [81, 3]. However, while these discoveries introduced new sensitive optical biomarkers such as the optical redox ratio and the NADH free-to-bound ratio, many technical challenges and analytical difficulties resulting in conflicting outcomes remain. NADH fluorescence is an indirect marker of cellular metabolic activity with many influencing dynamics such as pH, viscosity, temperature and protein composition further complicating analysis. At the moment, the extracellular flux analysis of cellular media determining oxygen consumption and extracellular acidification is the gold standard for measurement of cellular metabolism. Disadvantages of the current gold standard are lack of visual information for analysis and its restriction to averaged measurements of heterogeneous cell cultures and tissues.

### 5.1 NADH Lifetime Parameters and Localization

Before analyzing cellular metabolic changes, microscopical settings with respect to excitation and emission were optimized. To reach the strongest possible signal intensity and specificity for NADH without causing cellular damage, specific excitation wavelengths, irradiations, and durations were chosen as defined by damage threshold calculations. For reliable fluorescence emission detection and analysis,



high spatial and temporal resolution were found to be necessary for accurate results. Additionally, fluorescence photon yields were optimized under consideration of signal-to-noise-ratio, acquisition parameters, and cellular damage thresholds. Remarkable differences of NADH FLIM publications are found in the lifetime analysis procedure. While early publications of NADH fluorescence reported two fluorescence lifetimes, recent publications indicate the existence of up to eight lifetime components depending on cell type, protein composition and analytical method [4, 12, 9]. Even though up to eight unique lifetimes were detected, only four lifetimes regularly appear across different conditions and cells and the remaining four lifetimes were detected infrequently and without statistical significance [12].

In this work, optimization of imaging parameters like spatial binning and fluorescence decay analysis such as the fitting procedure also resulted in four NADH fluorescence lifetime components.

The approach of four individual lifetimes instead of two, increases the information encoded by shifts of each lifetime component and provides a basis for a new and enhanced NADH FLIM analysis. Therefore, this study shows, for the first time, that four fluorescence lifetime components exist for NADH in adipocytes, HEK 293 cells, and fibroblasts and that lifetime pairs can be localized to distinct cellular compartments. The fluorescence lifetime components  $C_1$  (0.5 ns) and  $C_3$  (2.3 ns) are predominantly found within mitochondria, while the lifetime components  $C_2$  (1 ns) and  $C_4$  (3.7 ns) predominantly arise from the cytoplasm. This is in contrast to the traditional two lifetime model for NADH, where the short fluorescence lifetime  $\tau_1$  (0.5 ns) represents the cytoplasm and the long fluorescence lifetime  $\tau_2$  (2.5 ns) is attributed to the mitochondria [155]. In the two-lifetime model, it is believed that the cytoplasm, where glycolysis occurs, is associated with free NADH and mitochondria, where oxidative phosphorylation takes place, are associated with bound NADH. Hence, the free-to-bound ratio has traditionally been thought of as a ratio of glycolysis to oxidative phosphorylation. In this traditional model, NADH within the mitochondria binds to several enzymes and proteins such as lactate dehydrogenase (LDH) and malate dehydrogenase (MDH) and a change of the free-to-bound ratio can therefore be seen as a change in enzyme binding.

This traditional explanation, which relies on the theory that bound NADH is mainly found in mitochondria, is however limited in its application since it is well documented that NADH also binds to cytosolic enzymes such as glyceraldehyde phosphate dehydrogenase (GAPDH) and LDH (Fig. 2.14) [140, 156]. Additionally, literature and experiments of this work show that NADH in solution has two intrinsic fluorescence lifetimes which most likely represent different conformations of free NADH, possibly folded (0.4 ns) and extended (0.9 ns) [9, 12]. Interestingly, the fluorescence lifetimes of free NADH in solution measured in this work reasonably concur with lifetime components  $C_1$  (0.5 ns) and  $C_2$  (1 ns) of NADH in adipocytes. Additionally, we showed that mixing pure NADH in solution with LDH, an enzyme which is found in mitochondria as well as the cytoplasm, introduces a third fluo-

rescence lifetime component to the solution (Fig. 4.3). These findings, lead to the assertion that both cellular features must each have free and bound NADH fluorescence lifetimes. The difference between free and bound NADH lifetimes within mitochondria (0.5 ns and 2.3 ns) and within the cytoplasm (1 ns and 3.7 ns) may be attributable to different micro-environmental conditions such as pH, viscosity, and/or osmotic concentration. Therefore, several NADH solution experiments were analyzed.

NADH suspended in different solvents resulted in fluorescence lifetime parameter differences (Table 4.1). This lifetime change caused by solvent polarity also occurs inside cells, as polarity is essential for their physiological function. Solvent polarity can be expressed by the dielectric constant which describes the solvents ability to insulate charges of particles immersed in it. Polarity heavily influences the intracellular transportation of proteins and interactions and it is strongest across cellular membranes where a separation of solvents with different polarities create electrochemical gradients [157]. Therefore, various cellular features divided by cellular membranes such as mitochondria exhibit strong polarity differences which could be the reason for the observed lifetime parameter differences between mitochondria and the cytoplasm.

Even though fluorescence lifetime of NADH is commonly referred to be concentration independent, this work showed that this is only true for a specific concentration range. Fig. 4.1 presents that NADH at increasing concentration produced a steady decrease in fluorescence lifetime and increase of the contribution of the short lifetime component. This can be explained by the pile-up effect as well as self-quenching which occur at concentrations that are significantly higher than what is found physiologically. Although mitochondrial fluorescence intensity is higher, and its lifetime components are shorter (0.5 ns and 2.3 ns) comparable to the cytoplasm (1 ns and 3.7 ns), both effects are extremely unlikely to be the reason for that. The pile-up effect and self-quenching rarely occur in cell or tissue experiments as NADH concentration as well as fluorescence emission are significantly lower compared to solution experiments. Therefore, the micro-environmental conditions are most likely the cause for mitochondrial and cytoplasmic NADH lifetime parameters differences. We conclude that a 4-lifetime component model is entirely appropriate, with the mitochondrial to cytoplasmic NADH fluorescence intensity ratio (MCR) as a useful new tool to quantify mitochondrial and cytoplasmic NADH changes.

The detection of four distinct lifetime components of NADH has been accomplished using high spatial and temporal resolution imaging. This study also highlights the influence spatial and temporal binning have on the fluorescence lifetime analysis. While spatial and temporal binning do improve photon numbers and thus the precision of a given fit, binning can also average out spatial and temporal heterogeneity in the fluorescence lifetime decay traces, which would therefore result in a loss of in-

formation. Additionally, if the fluorescence decay of a sample exhibits several similar fluorescence lifetimes, temporal binning of the decays will lead to an averaging out of unique lifetime components. Therefore, there must be a balance between spatial binning size to preserve spatial information, number of time bins to save temporal information, and photon counts to achieve good parameter estimation, in either exponential or phasor analysis. It was shown that the number of NADH lifetime components varies from two for high spatial binning ( $3.7 \times 3.7 \mu\text{m}$ ) to four for low spatial binning ( $1.2 \times 1.2 \mu\text{m}$ ). Similar observations were shown for temporal binning where the reduction of 256 time bins over 12.5 ns to 64 time bins had comparable effects as increase of spatial binning. The conclusion is that several fluorescence lifetime components with similar lifetimes exist and that subcellular structures smaller than  $3.7 \mu\text{m}$  are related to the increase in number of lifetime components.

The localization of individual lifetime components revealed that there is a good correlation between mitochondria and lifetime components  $C_1$ ,  $C_3$  and components  $C_2$ ,  $C_4$  and the cytoplasm (Fig. 4.6). Analysis of mitochondria within adipocytes using mitochondrial stains indicated tubular shapes with diameters of around  $1 \mu\text{m}$  and lengths of up to  $6 \mu\text{m}$  [158]. These proportions fit the spatial binning size requirement ( $< 3.7 \mu\text{m}$ ) and could explain the impact of spatial binning on lifetime analysis. This theory of regional differences of NADH species was further confirmed by analysis of isolated mitochondria of differentiated murine adipocytes which resulted in a fluorescence lifetime distribution of predominately lifetime components  $C_1$  and  $C_3$  (Fig. 4.7).

The improved level of visual image detail compared to comparable studies resulted in the detection of four distinct lifetime components of NADH. This was achieved and could be further improved by using higher numerical aperture (NA) objective lenses and abstaining from spatial binning in the subsequent analysis. This combination of high NA and low spatial binning increased the spatial sampling resolution of the FLIM analysis significantly. It is worth noting that further reduction of spatial binning requires collection of far more photons to achieve the signal-to-noise ratio necessary to facilitate accurate fitting of the fluorescence decay traces. Even though higher photon yield could be achieved by longer imaging acquisition durations or higher excitation laser power, it might also lead to photobleaching, which could distort lifetime measurements and lead to significant error. Cellular photo damage threshold calculations as well as photobleaching experiments showed that the used laser parameters did not induce immediate or long-term cell damage (Table 3.1 and Fig. 3.6).

The discrepancy in fluorescence lifetime components between different studies is most likely attributable to several different experimental parameters and settings such as magnification, resolution, and binning. It has been shown that in cells with high oxidative phosphorylation, more of the NADH pool is enzyme bound, en-

abling FLIM and especially the free to bound ratio to provide insights into dynamic metabolic changes in living cells. Additionally, studies showed that cancer cells which rely on glycolysis exhibit an elevated level of free NADH compared to normal non-transformed cells of similar origin. While the FLIM-based free to bound ratio can distinguish between healthy and cancerous cells it is also capable to accurately detect subtle features of cellular metabolism such as confluence, serum starvation, and hypoxia at a higher accuracy than standard biochemical methods [92].

Here, a double exponential fitting procedure was performed for NADH instead of adding additional exponential components as shown by Yaseen et al, who used 2 constrained and 2 free lifetimes resulting in a quadruple-exponential fit [9]. The reason for that is most pixels of a NADH FLIM image only contain 2 fluorescence lifetime components and the 4 lifetime components are identified across different pixels and not within one fluorescence decay. Only a very small subset of pixels which simultaneously have cytoplasmic and mitochondrial fluorescence contain four fluorescence lifetime components. Therefore, using a double-exponential fitting procedure reliably represents the fluorescence lifetime and results in a faster data analysis. Additionally, using a quadruple-exponential analysis of low intensity autofluorescence with restricted lifetimes as well as non-restricted lifetimes can exceed the potential information and result in artificial non-existent lifetime components. To overcome this pixel-to-pixel variability, a combination of segmentation and phasor analysis may ultimately be a more powerful approach than exponential fitting, especially in heterogeneous cellular or tissue environments (e.g. a tumor) where simple model-based fitting approaches can fall short.

Therefore, this work introduced a method combining segmentation of exponential fitting derived lifetime histograms with the phasor analysis. While the exponential decay analysis of NADH resulted in four distinct fluorescence lifetimes, the corresponding phasor plots arranged in broad clusters, making the extraction of fluorescence lifetime parameters impossible. The method of splitting the phasor plot into mitochondrial and cytoplasmic fluorescence offered easy interpretation and analysis of complicated data (Fig. 4.12). Despite the generation of longer fluorescence lifetimes, the phasor plots of Fig. 4.12 agree with the bi-exponential fit and support the findings of four distinct NADH lifetimes. Future investigations will further explore and combine both analysis modalities as we see considerable potential to further improve FLIM analysis.

Although the fluorescence lifetime components yield a good correlation with distinct cellular compartments, there are several causes that impair this correlation. For instance, image analysis of mitochondria-labeled cells revealed an average displacement of up to 5  $\mu\text{m}$  during typical FLIM image acquisition time of 60 s for 256 x 256 pixel images (105  $\mu\text{m}$  x 105  $\mu\text{m}$ , Fig. 4.10 and Fig. 4.11). This amount of movement leads to mitochondria entering and exiting the focal plane during the acquisition time, causing blurring and impacting the fluorescence lifetime analysis as well as a reduced correlation between FLIM images and fluorescence images of

mitochondria (Fig. 4.6). The double-exponential model used in this work is not suited for pixels of the FLIM image that display a mixture of cytoplasmic and mitochondrial fluorescence, which can lead to suboptimal fitting of the fluorescence lifetimes. Any inaccuracy induced by mitochondrial movement acts to broaden the lifetime distribution peaks of the individual lifetime components and makes it difficult to easily separate each one: this ultimately is the reason why the cytoplasmic phasor plot has a triangular shape (Fig. 4.12). One way to reduce mitochondrial motion blur without stopping mitochondrial movement would be a reduction of the image acquisition time. The current spatial resolution of  $1.5\ \mu\text{m} \times 1.5\ \mu\text{m}$  for a single pixel means that it would take an average time of 15 s for a mitochondrion to travel through that area. Therefore, reducing imaging acquisition time by a factor of 5 down to 12 s should result in significant improvement of image quality and reduction of motion blur caused by movement of mitochondria. However, it is worth noting, that reducing image acquisition times currently carries its own set of problems, as an increase in laser power could lead to cell damage while fewer acquisition scans would lead to suboptimal photon statistics for analysis. Nevertheless, steps to increase acquisition speed and photon detection yields using the current setup are improved scan mechanistic (from sawtooth to bidirectional) and use of objective lenses with higher NA as seen in Eq. 2.4.

Finally, the possibility that the four NADH fluorescence lifetime components are influenced by other fluorophores was analyzed. It can be safely neglected that NADPH autofluorescence contributed to the results, since previous studies have shown that its intracellular concentration is 4 to 40 times lower than NADH, which also has a greater quantum yield [10, 80, 79]. Additionally, the type I collagen coating of the glass bottom dishes, could theoretically interfere with the results of NADH fluorescence due to its autofluorescence [159, 160]. However, a measurement of collagen coated dishes did not show any measurable fluorescence. FAD could contribute to the measured fluorescence signal but its emission peak at 525 nm, low excitation at 755 nm, and lower quantum yield than NADH make it a neglectable contributor to the NADH channel used in the FLIM system. Lipid droplets are known to have long mono-exponential fluorescence lifetime decays (6.5 – 7.8 ns) which interfere with the NADH fluorescence lifetime analysis [21, 144]. Also, another lipid-based fluorophore that interferes with the metabolic analysis is lipofuscin which excitation ranges from 360 to 660 nm with fluorescence emission from 510 to 700 nm and a fluorescence lifetime of about 3.2 ns [11, 161]. Therefore, fluorescence intensity thresholds, stimulated Raman scattering (SRS), and coherent anti-Stokes Raman scattering (CARS) were used to remove lipid and lipofuscin from the NADH analysis. Results showed that even after excluding transition zones from lipid droplet to other cellular areas from analysis, NADH still exhibited 4 distinct fluorescence lifetimes.

Additionally, HEK cells and fibroblasts which are known for low lipid and lipofuscin content generated 4 NADH fluorescence lifetime components which further strengthens the assumption that all four lifetime components arise from NADH.

## 5.2 MCR of Adipocytes, HEK 293 Cells, and Tissue

To quantify the metabolic readout of optical biomarkers, cellular energy metabolism was modified in a well-controlled way. This was accomplished by using inhibitors and uncouplers of the respiratory system of the cell and by monitoring the indirect metabolic changes with a flux analyzer. The mitochondria stress test with individual non-subsequent injections of oligomycin, FCCP, and rotenone/antimycin on adipocytes, HEK 293 cells and tissue showed significant changes of the intensity based redox ratio and the fluorescence lifetime based free-to-bound ratio and MCR. The optical redox ratio is described as  $\text{FAD}/(\text{NADH} + \text{FAD})$  and suggest intracellular changes in NADH and FAD concentrations. However, recent publications showed that the redox ratio is significantly correlated with the intracellular concentration ratio of  $\text{NAD}/(\text{NADH} + \text{NAD})$  rather than  $\text{FAD}/(\text{NADH} + \text{FAD})$  [79]. This surprising behavior which is most likely caused by FAD quenching through protein binding at high concentrations makes interpretation of the underlying pathways difficult. Nevertheless, the analysis of the redox ratio of this work conforms with literature where an increase is caused by enhanced oxidative phosphorylation and reduced redox ratios are associated with increase of glycolytic function [162]. While the intensity based redox ratio reflects changes in concentration, fluorescence lifetime is mostly independent of fluorophore concentration. Therefore, FLIM was used to detect changes in fluorescence lifetime and protein binding states which can be expressed and evaluated by the free-to-bound ratio and the newly introduced MCR metric. Compared to the 2-lifetime model of the free-to-bound ratio, the MCR analyzes the intensity of 4 individual lifetime components.

Fig. 4.13 showed that oligomycin blocks ATP synthase causing the inhibition of oxidative phosphorylation and consequently causing a decrease in oxygen consumption rate (OCR) and increasing mitochondrial NADH. The injection of rotenone/antimycin also inhibits the ETC, which maximizes NADH within the mitochondria. This leads to an increase in fluorescence intensity contribution for mitochondria-associated lifetime components  $C_1$  and  $C_3$  and a decrease for cytoplasmic-associated lifetime component  $C_2$  as seen in Fig. 5.1. The increase of absolute fluorescence intensity of  $C_1$  and  $C_3$  was expected since Vergen et al showed that inhibition of the ETC leads to an increase in mitochondrial NADH and quantum yield [12]. FCCP acts to increase mitochondrial respiration by uncoupling ATP phosphorylation from the ETC and thereby oxidizing NADH to non-fluorescent  $\text{NAD}^+$  which depletes the mitochondrial NADH pool. While this metabolic alteration does not affect the traditional free-to-bound and redox ratios, a significant change can be detected with the MCR metric (Fig. 4.14). This highlights the strength of the 4-lifetime analysis of NADH, as the decreased MCR arises from subtle changes of lifetime components  $C_1$  (0.5 ns) and  $C_2$  (1.0 ns) which are undetectable in the traditional two-lifetime analysis. Fig. 5.1 simplifies the relationship of NADH lifetime components depend-



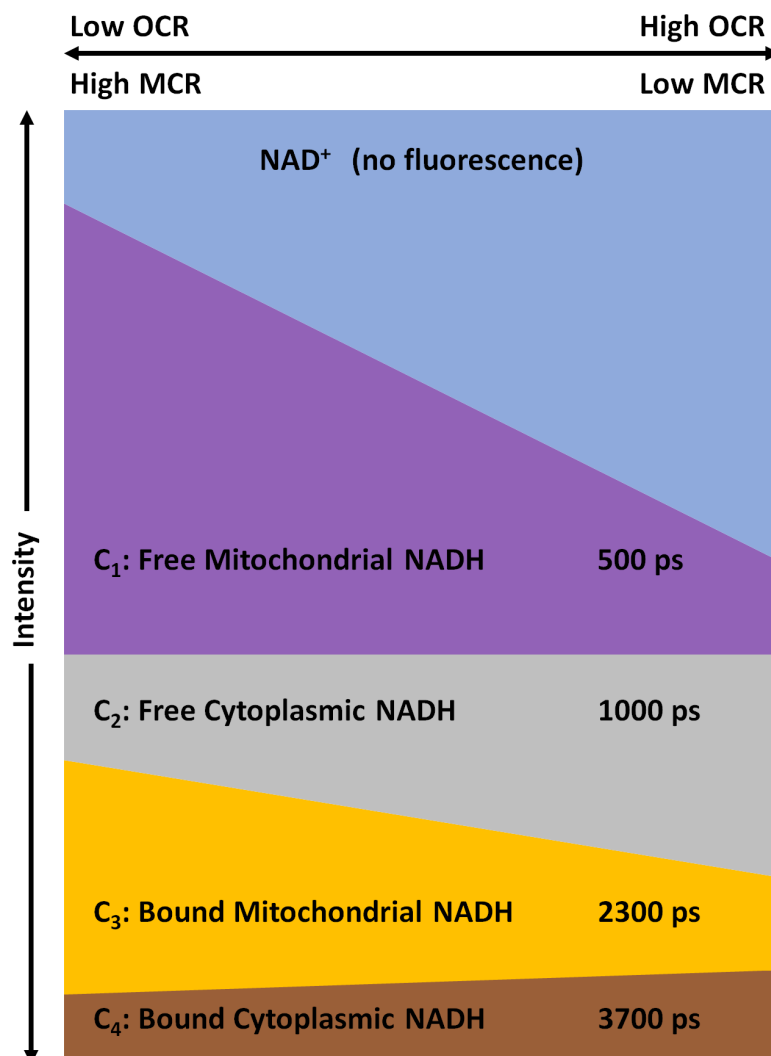


**Figure 5.1:** Scheme of NAD<sup>+</sup> and NADH lifetime component distribution upon metabolic changes under the assumption of a stable NAD<sup>+</sup>/NADH pool. The scheme shows the correlation between OCR and MCR as well as the fluorescence lifetime component distribution depending on the metabolic state of the cell. High OCR/ low MCR by uncoupling ATP phosphorylation from the ETC means increased mitochondrial respiration and thereby oxidizing NADH to non-fluorescent NAD<sup>+</sup> which depletes the mitochondrial NADH pool ( $C_1$  and  $C_3$ ) and increases the cytoplasmic NADH pool ( $C_2$  and  $C_4$ ). Low OCR/ high MCR by inhibition of the ETC maximizes NADH within the mitochondria and this leads to an increase in fluorescence intensity contribution for mitochondria-associated lifetime components  $C_1$  and  $C_3$  and a decrease for cytoplasmic-associated lifetime component  $C_2$  and  $C_4$ .



ing on metabolic activity. The results of the mitochondria test suggest that while the free-to-bound ratio, the redox ratio and the MCR have reproducible results in adipocytes and HEK 293 cells, the MCR has a greater magnitude of response to changes of the ETC.

While the mitochondria stress test injections of the ETC uncoupler FCCP and respiration inhibitor rotenone/antimycin showed similar trends in tissue as for cell culture experiments, the magnitude of the effect was significantly lower for all biomarkers. This can be explained by a significantly lower number of cells since only the tissue surface get in contact with the pharmacological reagent. Future studies with tissue specimen will therefore use higher reagent concentrations and longer measuring periods. The reproducibility was also more difficult with tissue samples than cell cultures where exact cell counts can be quantified. Additionally, the harvesting method resulted in tissue samples of the same weight but different sizes, shapes, and surface areas. Nevertheless, there were no principally different outcomes using tissue compared to cell cultures and the trends of the biomarkers let assume that an increasing number of experiments, optimized sample preparation, and higher reagent concentration will lead to results comparable to cell cultures.

Compared to individual non-subsequent injections of pharmacological reagents of the mitochondria stress test, consecutive injection showed significant differences. Rotenone/antimycin in succession to the ETC uncoupler FCCP resulted in untypical low fluorescence intensity for the ETC inhibitors. While the inhibitors should have maximized mitochondrial NADH, the contrary was observed and lifetime components  $C_1$  and  $C_3$  decreased compared to the baseline (Fig. 4.15). However, the flux analyzer determined decreasing OCR and increasing ECAR as expected. This mismatch between cellular respiration and the imaging parameters for an inhibitor-uncoupler combination was also discovered by Schaefer et al [163]. Additionally, they showed that a reverse injection strategy with injection of respiration inhibitors rotenone/antimycin first and injecting FCCP afterwards led to the same outcome of decreased mitochondrial lifetime components and stopped respiration.

The consecutive injection experiment showed that NADH lifetime parameters do not purely correlate with respiration, especially when using the uncoupler FCCP. Most likely, the reason for this unexpected behavior after injection of inhibitor-uncoupler combinations is a disturbance of the membrane potential and the pH concentration gradient across the inner mitochondrial membrane [163]. The results suggest that not only NADH concentration and protein binding influence the lifetime parameters but also pH and membrane potential since rotenone/antimycin as well as FCCP are causing rapid mitochondrial depolarization of the membrane potential. This example of mitochondria in an uncoupled state indicates the limitations of metabolic imaging of NADH as a biomarker and replacement for the extracellular flux analyzer.

Even though, the underlying mechanisms and pathways for the FLIM NADH respiration mismatch should be further studied, it is also worth questioning if these mechanisms have physiological relevance and exist outside of pharmacological injections of the mitochondria stress test.

The glycolysis stress test (Fig. 4.16) showed changes that act to solely increase glycolytic activity, but that do not impact the ETC such as a glucose injection, only introduced insignificant variation by either the free-to-bound ratio, redox ratio or the MCR metric. While ECAR increased after glucose injection, the rest of the metabolic identifiers such as OCR, free-to-bound ratio and MCR remained unchanged. ECAR measures glycolytic acidification of the assay media by conversion of glucose to lactate<sup>-</sup> + H<sup>+</sup> and the export of products into the assay medium. Glucose catabolism to pyruvate would suggest an initial increase of cytoplasmic NADH through reduction of NAD<sup>+</sup>, which indeed can be seen by an increase in cytoplasmic fluorescence intensity of lifetime component  $C_2$  (Fig. 2.14). Nevertheless, the MCR did not change due to an equal fluorescence intensity increase of mitochondrial NADH. A possible explanation for this relatively small increase of NADH concentration within the cytoplasm could be the conversion of pyruvate to lactate, which involves the oxidation of NADH back to NAD<sup>+</sup> (Fig. 2.14) [91].

To confirm that fluorescence lifetime changes were based on cellular metabolism and intracellular pH-differences rather than pH changes of the media induced by the injection of pharmacological reagents from the mitochondria and glycolysis stress test; pH-meter measurements showed that none of the reagents resulted in a significant change of the pH-value of the media (Table 4.2). Fluorescence lifetime changes by alterations in protein content such as UCP1 are unlikely, as the pharmacological treatments release their effect within seconds to minutes whereas significant protein concertation changes are observed after minutes to hours as seen in Fig. 4.19. Upon uncoupling with FCCP as well as UCP1, a slight increase in temperature was reported of adipocytes in cell culture [164], which is the highest as the respiratory system is pumping protons in the intermembrane space, however solution experiments of this work showed that temperature changes in this realm have a negligible effect on fluorescence lifetime (Table 4.1).

The possibility of browning of white fat is a desirable prospect for the treatment of obesity and related disorders. Therefore, white inguinal mouse adipocytes were treated with epinephrine and forskolin which are known reagents to activate browning. Treated adipocytes showed a similar metabolic reaction (Fig. 4.19) as cells treated with the uncoupling agent FCCP (Fig. 4.14), which can be explained by upregulation of UCP1 as shown by gene expression. UCP1, which is similar to FCCP, acts as a protonophore to facilitate proton translocation across the inner membrane of the mitochondria, which acts to downregulate aerobic ATP synthesis

and up-regulate oxygen consumption [165]. Model calculations revealed consistent metabolic flux changes for both FCCP- and UCP1-mediated uncoupling, suggesting a common mechanism [165]. UCP1 expression and FCCP treatment increased glucose uptake and a substantial output of lactate as seen by an increased ECAR as well as increased mitochondrial respiration indicated by an increased OCR. These signs of increased metabolic activity which are signs of browning were also detected by the new FLIM derived MCR (Fig. 4.19). While epinephrine and forskolin induce browning in cell culture, they are not suitable for therapeutic treatment in humans as they have severe side effects.

Over the past years, FLIM flow cytometry and cell sorting have shifted into focus due to technological advances that allow faster image acquisition. These applications are often based on fluorescent dyes and antibodies due to weak fluorescence of endogenous fluorophores [166]. The fluorescence lifetime is mostly independent of emission intensity and can be used to distinguish between cell subpopulations that signal differently. This study demonstrated the ability of FLIM to determine different metabolic states of individual live adipocytes to isolate cell subpopulations by sorting using the MCR. Individual adipocyte analysis and mixed cell population analysis of adipocytes and fibroblasts showed that heterogeneity between cells exist and that this heterogeneity often cannot be distinguished by cellular appearance. However, endogenous FLIM constitutes a tool to detect these differences. While the NADH fluorescence emission of different cell types such as fibroblasts and adipocytes are almost identical, their lifetime parameters differ significantly. Compared to the flux analyzer, FLIM enables to distinguish metabolic states and cell types within pure and mixed cell populations. This ability to sort subpopulations enables further studies such as cell screening, flow cytometry, and cell isolation based on cell signaling and its metabolic state rather than cell type. This research can enhance the detection and understanding of how metabolic and physiologic subpopulations of the same cell type develop.

In this study, manual segmentation was used to outline cells and the new MCR metric enabled unmixing of cell type as well as metabolic state. The main objective of these experiments was to show its capability of cell sorting and potential use for flow cytometry since fluorescence lifetime enhances cytometric data with a quantitative parameter that is independent of the measured fluorescence intensity. Compared to the free-to-bound and redox ratio, the MCR represents dynamic metabolic changes with high sensitivity and enables FLIM as an imaging alternative to the flux analyzer and current flow cytometry, especially for applications in heterogeneous cell cultures and even tissue.

This work and the MCR metric may provide a sensitive and quantitative marker for new and developing fields for the assessment of the metabolic state. However, special focus of this work was put on the quantitative assessment of adipose tissue

function through functional metabolic imaging using purely endogenous fluorescence of NADH. The MCR can distinguish adipose tissue types such as WAT, scWAT, and BAT, and is sensitive to thermogenic activation of adipocyte cell cultures. Additionally, the MCR optical biomarker enhances sensitivity compared to established biomarkers such as the free-to-bound ratio and the optical redox ratio and it also provides the basis of a much needed toolset for non-invasive dynamic assessment of adipose tissue function. The MCR biomarker enhances understanding of adipocytes which is required towards the development of interventions for metabolic health in the context of obesity, and physiological functions of adipose tissue.

While FLIM of NADH did not manage to reflect stopped respiration after injection of an inhibitor-uncoupler combination such as FCCP and rotenone/antimycin (Fig. 4.15), it can still reliably be performed for metabolic analysis, as the reaction to the inhibitor-uncoupler injection was created artificially and might not be observed in physiological conditions.

**Probably the most interesting finding of this work was that the MCR is inversely correlated to the OCR.** This result supports the idea that the new MCR metric is sensitive to metabolic changes of the ETC (Fig. 4.20). While a strong correlation between the inverse MCR ( $\text{MCR}^{-1}$ ) and the OCR exists over all data points, some of them, especially of untreated adipocytes still have a wide spread and are less correlated. These not so well correlated data points of untreated baseline adipocytes can be explained by different cell culture conditions such as type of media and adipocyte cell line differences. This observation led to the assumption that the characteristics of the MCR and OCR correlation might be different for other cell lines. Therefore, the NADH fluorescent lifetime of NIH fibroblast and HEK 293 cells was analyzed.

As expected, the analysis of NIH fibroblasts and HEK 293 cells revealed four distinct NADH lifetime components, demonstrating that this feature is not unique to adipocytes. Therefore, the ratio of intensity of the four individual lifetime components allow for the generation of the MCR metric for these cell lines.

The inverse MCR ( $\text{MCR}^{-1}$ ) and OCR analysis of HEK 293 cells indicated an even stronger correlation compared to adipocytes. However, the comparison of adipocytes and HEK 293 cells revealed differences in the  $\text{MCR}^{-1}$  vs OCR relationship. At the same MCR values, the respiration per cell is lower for HEK 293 cells than for adipocytes. This discrepancy between cell lines was expected and can be explained by different cell morphology such as size and amount of mitochondria as well as cell origin and functionality.

These cellular differences mean that a direct conversion of MCR values to the absolute oxygen consumption rate per cell independent of cell type is not applicable. Nevertheless, the data suggests that as soon as a sufficient amount of information about a specific cell line is gathered, a linear conversion of  $\text{MCR}^{-1}$  to OCR values can

be performed. An effective way to gather a broad spectrum of MRC and OCR values are individual titrations of pharmacological reagents rotenone and FCCP which cover the range from stopped respiration to maximum respiration, respectively. We will look further into the predictive relationship of  $\text{MCR}^{-1}$  and OCR and the applicability for intact tissues. Ultimately, the future goal is to develop a biomarker that allows for optical determination of OCR under consideration of factors that affect quantification like cell dimension and mitochondrial distribution.

### 5.3 Tissue Preparation, Imaging, and Wound Healing

To highlight the significance of quantitative optical biomarkers, imaging of adipose tissue was demonstrated. While the potential therapeutic effect through modification of lipid metabolism is important, many controversies and contradictory results remain. Therefore, the potential of fluorescence imaging as an analytical tool for adipose metabolism was compared to analysis by an extracellular flux analyzer. Additionally, optimized imaging condition in reference to sample preparation were evaluated. Optical signatures reflect bioenergetic function and biosynthetic pathways associated with the different types of adipose tissue. Distribution of the NADH lifetime components give insight about cellular functions and morphology such as energy storage, dissipation capabilities, and mitochondria content. Tissue heterogeneity, especially in BAT, might be an indicator of several subpopulations within the fat depot with different thermogenic onset times depending on thermoregulation demands.

In cell culture experiments, increased respiration through uncouplers like FCCP was associated with decreased MCR and increase of the mean fluorescence lifetime (Fig. 4.14). Therefore, one would assume that BAT, which has the highest basal respiration compared to WAT and scWAT, has similar fluorescence lifetime characteristics. Additionally, BAT contains large amounts of UCP1, which works in similar ways as FCCP.

However, contrary to the expectations, UCP1-rich BAT has the highest MCR and lowest mean fluorescence lifetime compared to UCP1 deficient WAT and scWAT. This can be explained by morphological and functional differences of the tissue types compared to cell culture experiments.

In cell culture, NADH lifetime changes upon FCCP injection are immediate and therefore caused by dynamic metabolic actions of the ETC rather than change in mitochondrial content or protein composition. In comparison to that, fluorescence differences of the three tissues are mostly caused by mitochondrial content and protein composition. High expression of UCP1 in BAT induces increased electron flux through the ETC and therefore oxidation of mitochondrial NADH to  $\text{NAD}^+$ ,

which depletes mitochondrial lifetime components  $C_1$  and  $C_3$ . However, the number and density of mitochondria is so high that even small mitochondrial NADH pools dominate BATs fluorescence signature. With decreasing number and density of mitochondria, fluorescence lifetimes prolong, fluorescence intensity decreases and mitochondrial lifetime components  $C_1$  and  $C_3$  are less dominant as seen for WAT and scWAT.

This means, the MCR of the metabolic baseline of cells and tissues is useful on giving information on the mitochondrial content but it does not correlate with the OCR. However, once the MCR and OCR of the metabolic baseline are established, the MCR is great at detecting dynamic metabolic changes from the baseline and correlates well to the OCR.

Due to logistical difficulties, sample freezing and thawing is a common approach in FLIM microscopy [168, 169, 21]. Though, freezing is known to lead to loss of NADH and to affect the fluorescence emission characteristics [170]. Freezing of adipose tissue, revealed that not only fluorescence emission but also cellular morphology was affected (Fig. 4.27 and Fig. 4.28). Morphological features and unresponsive behavior to injection of pharmacological reagents, confirmed viability loss of frozen tissue samples. On the other hand, cooled samples showed satisfactory cellular structure and fluorescence emission 24 hours after excision. However, extended periods of storage under these conditions will most likely also result in loss of fluorescence intensity and tissue viability. Additionally, storage at 4°C of these thermoregulating tissues might also induce unwanted changes as BAT in mice is known to increase UCP1 content in response to cold exposure.

Therefore, immediate imaging of tissues constitutes the only reliable and most reproducible way of measurement. If due to logistical reasons imaging immediately after excision is not possible, cooling is the preferred method and freezing the tissue should be avoided. However, as our understanding of how different storage and preparation conditions affect the outcome of metabolic FLIM imaging, it is likely that the time interval between tissue harvesting and imaging can be increased.

Wound healing experiments in human skin equivalents using NADH-FLIM show increased metabolic activity at the edge of a mechanically induced wound indicating higher cellular proliferation. There was no increase of metabolic activity at the edge of wounds created by fractional laser ablation. This can be explained by the limitation of the skin equivalent model which is not capable of removing the laser induced coagulation zone and therefore hindering cells to proliferate. Nevertheless, these preliminary results could be extended further to study metabolic reactions of tissue engineered cells and organs with specific metabolic traits as it is a very promising field of biomedical and cosmetic research. Due to accessibility and ease of use, these models enable non-invasive assessment and evaluation of the physiology. Moreover, applications of these models and improved versions as platforms for analytical evaluation in combination with non-destructive readouts could enable high throughput and screening experiments without the need for animals models or clinical studies.



## 6 Conclusion

In this thesis time-domain fluorescence lifetime imaging microscopy (FLIM) was applied to analyze the metabolism of biological systems exploiting the naturally occurring fluorophore NADH. FLIM imaging has existed in the field of biomedical optics for the past several decades, yet much is left to be explored. The purpose of the work was to effectively develop a powerful label-free, non-invasive tool to enhance the quantification of metabolic changes in multiple important biological samples.

We have shown, for the first time in adipocytes, HEK cells, and fibroblasts, that four fluorescence lifetime components exist for NADH. The origin of each individual lifetime component of the NADH FLIM signal was localized to specific cellular features such as mitochondria and cytoplasm. This was accomplished by using a combination of high numerical aperture imaging, high temporal binning, and low spatial binning for the fluorescence lifetime analysis. By comparing standardized metabolic stress tests, it was shown that changes of the electron transport chain (ETC) and therefore of oxidative phosphorylation significantly altered the ratio of the four fluorescence lifetime components. Based on these findings, we defined a new optical biomarker named mitochondrial-cytoplasmic-ratio (MCR) that accurately reflects shifts in mitochondrial and cytoplasmic NADH concentration and the binding state.

We found that the MCR has an increased response and dynamic range to metabolic changes compared to traditional optical assessments such as the frequently used optical free-to-bound ratio and redox ratio. Moreover, we demonstrated its sensitivity to metabolic changes especially for cellular respiration through the electron transport chain (ETC) in live cell culture and ex-vivo tissue samples. The microscopically derived MCR metric correlates inversely linear with the flux analyzer derived oxygen consumption rate. While the linear correlation differs between cell lines such as adipocytes and HEK 293 cells, this optical biomarker could prove highly advantageous in the prediction of metabolic respiration of individual cells after an initial calibration.

The use of this novel biomarker and analysis technique by NADH FLIM allows to be superior to the flux analyzer for individual cell analysis as well as for mixed cell populations. Once the metabolic activity is determined, the information can be used as a mapping tool to identify or pictorially highlight cells within the cell culture or tissue based on metabolic activity. Our results show that non-invasive detection of



dynamic metabolic changes and even browning of live adipocytes are enabled by label-free monitoring of the fluorescence lifetime analysis of NADH.

Additionally, we demonstrated for the first time, a combination of exponential and phasor analysis using label-free imaging in adipocytes. This combination of segmentation of an exponential fitting derived fluorescence lifetime histogram with a subsequent phasor analysis enables the evaluation of otherwise not interpretable phasor plots. This new phasor analysis approach is a promising, non-invasive tool to quantify and evaluate biological systems. As shown in this work, phasor analysis of FLIM allows an efficient way to uniquely identify, intrinsic autofluorescence of NADH in cell cultures.

Furthermore, we have demonstrated that two photon excited fluorescence microscopy can quantitatively assess adipose tissue function through functional metabolic imaging with subcellular resolution using purely intrinsic contrast. Imaging biomarkers such as the new MCR metric and fluorescence intensity contribution of NADHs lifetime components can distinguish energy-storage driven white adipose tissue (WAT) from energy-dissipative brown adipose tissue (BAT). These bioenergetics analysis techniques provide the basis of a promising tool set for non-invasive dynamic assessment of adipose tissue function towards developing metabolic health solutions in the context of metabolic diseases such as obesity and diabetes, and towards a deeper understanding of complex biological roles of the adipose organ.

Although this study mainly focused on quantification of metabolic activity of adipocytes, this approach is widely applicable and constitutes a powerful tool for application to monitor cellular metabolism. The results demonstrate that NADH-FLIM is a robust technique for assessing and indexing cellular features of several cell lines and therefore, this method could prove beneficial for drug development and screening studies, especially for cell cultures, and for tissue models. Furthermore, the use of endogenous fluorophores as intrinsic biomarkers of metabolism makes this technique label-free, therefore facilitating the possibility of in vivo measurements. Overall this work has contributed to the advancement of FLIM for use in functional imaging of individual cells and mixed cell cultures.

## 7 Outlook

Even though NADH fluorescence principles are relatively well understood, the measurement of NADH FLIM still presents a number of challenges, notably linked to the photophysical processes, the need for appropriate controls and the effects of dynamic interactions. However, the outcomes and findings described in this thesis exposed several future directions and chances to be investigated using label-free FLIM. While we demonstrated a novel approach of analyzing NADH with four fluorescence lifetime components and combining exponential and phasor analysis, this technique can be enhanced further. The ultimate goal is the development of absolute quantification of OCR by only optical label-free analysis under consideration of cell size and mitochondria number and density. The advantage of this technique is label-free metabolic imaging with single cell resolution, which would demonstrate a powerful non-invasive imaging technique for flow cytometry and cell sorting. However, current acquisition times for these kinds of measurements are too long. Therefore, several studies investigated techniques to improve acquisition speed by temporal binning, improved phasor analysis, volumetric imaging through light-sheet microscopy, wide-field FLIM, higher numerical aperture, the use of analog detection and many more [46, 171, 172, 173].

Combining our analysis and overall FLIM settings with faster acquisition could enable several new research areas including cell sorting based on metabolism which might enable flow cytometric detection of cancerous cells and activated immune cells as well as assessing metabolic state during embryo development. Further investigations could also include the study of live animals, examination of neurodegenerative diseases, further investigation of obesity related diseases like diabetes, and the analysis of mitochondrial activity especially in aging cells. Additionally, endoscopes can minimize surgical invasiveness of FLIM microscopy in accessing fat depots or other organs in live subjects. Moreover, cellular metabolism can be monitored over time. Thus, this non-destructive technique will find potential application in drug discovery and safety screening, especially effects of drugs as well as understanding diseases and therapies. Future studies could also analyze the influence of wound healing drugs and ointments using skin equivalents for improving wound care. Metabolic imaging of tissue models can be possible due to the ease with which two-photon microscopy can be applied to complex 3D structures. A list of potential procedures and applications that could benefit from improved metabolic FLIM imaging is shown in Table 7.1.

NADH Fluorescence Lifetime Imaging Microscopy	
Technique/Procedure	Advantage/ Application
Macroscopic Imaging [174]	Large field of view at cellular resolution for whole tissue/tumor observation
Wide-field FLIM [175]	Fast measurement and large field of view at low resolution
Light sheet microscopy [176, 177]	Fast three-dimensional volumetric imaging with microscopic resolution and concentration independent contrast using a CCD camera
Endoscopy [178, 179]	Deep tissue imaging and evaluation to provide a comprehensive insight for diagnostics and detection
Parallel excitation and emission multiplexing [180]	Rapid measurements by modulating multiple laser lines to provide a low cost solution to implement FLIM with multiple excitation and emission channels
Phasor approach for metabolic, genomic, and disease pathways [181, 182]	Definition of subcellular dynamics of impaired metabolism and epigenetic modifiers to establish biophysical signatures and pathways
Viability measurements [183]	Identifying and extracting metabolic signatures of apoptosis and necrosis in single cells, tissue environments, and within the living organisms
Cell screening, sorting, and flow cytometry [172, 184]	High-throughput single-cell screening by label-free non-invasive metabolic imaging. Has the potential to become a blood screening tool and is expected to be widely used regarding detection, identification, and personalized therapy
Drug screening [185]	Information obtained may complement and facilitate the design of new experiments and interpretations and possibly open new avenues of drugs development
Combination with other endogenous fluorophores [186]	Capability to detect molecular changes with higher sensitivity due to additional information: predictors of drug response and in assessing the efficacy of treatment
Combination with fluorescent probes [163]	Illustration of additional quantitative information such as mitochondria content and pH-changes for high-resolution cellular imaging
Combination with OCT [187]	Simultaneously visualize cross-sectional morphology and biochemical compositional information of biological tissue
Combination with Raman and harmonic generation microscopy [188, 144]	Provides valuable additional diagnostic information such as refractive index changes and visualization of tissue boundaries
3D Tissue and tissue constructs [189, 131]	Interpretation of metabolic changes in 3D models and efficient control of energetic, developmental, and disease parameters
Human skin and xenograft mouse models [190]	Rapid, non-invasive and sensitive assessment of skin disease progression as well as a diagnostic tool for detection
Wound healing [191]	Evaluation of the efficacy and healing mechanisms of wound-healing drugs in real time
Real time histology [192]	Simultaneously image and quantify the cellular morphology and microenvironment of live tissues without conventional biopsy or fluorescent dyes

**Table 7.1:** New and future techniques in acquisition, analysis and sample preparation of NADH FLIM and their advantages and applications.

---

Overall, future technical advancements of imaging techniques such as FLIM and the combination of them with smart algorithms to correlate data with physiological function will generate a substantial progression in functional imaging. Additionally, the rapid growth of processing power and the use of machine learning algorithm in the interpretation of data can soon establish real-time imaging and data analysis of complex physiologies and metabolic changes with increasing spatial and temporal resolution.





## 8 Abbreviations

2-DG	2-deoxy-D-glucose
AA	antimycin A
ADC	analogue to digital converter
ADP	adenosine diphosphate
ATP	adenosine triphosphate
BAT	brown adipose tissue
BeAT	beige adipose tissue
BS	beam splitter
CARS	coherent anti-Stokes Raman scattering
DMEM	Dulbecco's modified Eagle medium
ECAR	extracellular acidification rate
ECM	extracellular matrix
EFT	EpiDerm full thickness
EOM	electro-optic amplitude modulator
ETC	electron transport chain
FAD	oxidized flavin adenine dinucleotide
FADH <sub>2</sub>	reduced flavin adenine dinucleotide
FBS	fetal bovine serum
FCCP	carbonyl cyanide-4-(trifluoromethoxy)-phenylhydrazone
FLIM	fluorescence lifetime imaging microscopy
GAPDH	glyceraldehyde 3-phosphate dehydrogenase
GLP	Glan-laser polarizer
HEK 293	human embryonic kidney cells 293
HWP	half-wave plate
IRF	instrument response function
LD	laser diode
LDH	lactate dehydrogenase
MCR	mitochondrial-cytoplasmic-ratio
MDH	malate dehydrogenase
NA	numerical aperture
NAD <sup>+</sup>	oxidized nicotinamide adenine dinucleotide
NADH	reduced nicotinamide adenine dinucleotide
NADPH	reduced nicotinamide adenine dinucleotide phosphate
NIR	near infrared
OCR	oxygen consumption rate
OCT	optical coherence tomography
OXPHOS	oxidative phosphorylation
PBS	phosphate-buffered saline
PET-CT	positron emission tomography- computed tomography
PLIM	phosphorescence lifetime imaging microscopy
PMT	photo multiplier tube



---

PD	photo diode
QWP	quarter-wave plate
ROI	regions of interest
ROS	reactive oxygen species
scWAT	subcutaneous white adipose tissue
SHG	second harmonic generation
SRG	stimulated Raman gain
SRL	stimulated Raman loss
SRS	stimulated Raman scattering
TAC	time-to-amplitude converter
TBS	tris-buffered saline
TCA	tricarboxylic acid
TCSPC	time correlated single photon counting
TMRE	tetramethylrhodamine ethyl ester
TPEF	two-photon excited fluorescence
UCP1	uncoupling protein 1
UV	ultra violet
scWAT	subcutaneous white adipose tissue
vWAT	visceral depot of white adipose tissue
WAT	white adipose tissue



## List of Figures

2.1	Jablonski Diagram . . . . .	7
2.2	Stoke's Shift . . . . .	9
2.3	Optical Absorption Coefficients . . . . .	12
2.4	Mono- and Bi-Exponential Fluorescence Decay . . . . .	17
2.5	Fluorescence Lifetime Fitting . . . . .	18
2.6	Simplified Schematic of Time Domain FLIM . . . . .	20
2.7	Simplified Schematic of Frequency Domain FLIM . . . . .	21
2.8	Simplified Schematic of Phasor Plot . . . . .	23
2.9	Fluorescence Decay to Phasor Plot . . . . .	25
2.10	Diagram of the Rayleigh and Raman Scattering Processes . . . . .	29
2.11	Energy Level Diagrams for Raman Processes . . . . .	31
2.12	SRS and CARS Microscopy Setup . . . . .	33
2.13	Signal Characteristics in CARS and SRS . . . . .	35
2.14	Simplified Schematic of Glycolysis and Oxidative Metabolism . . . . .	37
2.15	NADH and FAD Excitation and Emission . . . . .	41
2.16	NADH, NADPH and FAD molecule Structure . . . . .	42
2.17	Developmental Lineages of Brown, Beige, and White Adipocytes . . . . .	47
3.1	Confocal and FLIM Setup Scheme . . . . .	54
3.2	Redox Ratio . . . . .	56
3.3	Optical Setup of CARS and SRS . . . . .	57
3.4	Optical Setup of Pump and Stokes Beam . . . . .	58
3.5	Raman Imaging of Cell Cultures and Tissue . . . . .	59
3.6	Photobleaching . . . . .	62
3.7	Photobleaching of Continuous and Intervall Imaging . . . . .	63
3.8	Apoptosis . . . . .	64
3.9	Photodamage by Laser Irradiation . . . . .	65
3.10	Decay Curve Fitting . . . . .	68
3.11	Fluorescence Lifetime Fitting . . . . .	69
3.12	Commercial vs Custom Software . . . . .	70
3.13	SHG of Urea Crystals . . . . .	71
3.14	Synthetic IRF Calculation . . . . .	72
3.15	Synthetic IRF Decay vs Measured IRF Decay . . . . .	73
3.16	Synthetic IRF Distribution vs Measured IRF Distribution . . . . .	74
3.17	Phasor Plot Comparison . . . . .	74

## List of Figures

---

3.18	Schematic of Phasor Plot Properties . . . . .	75
3.19	Multi-Harmonic Phasor Analysis Scheme . . . . .	76
3.20	Multi-Harmonic Phasor Analysis of NADH . . . . .	78
3.21	IRF Phasor Calibration . . . . .	79
3.22	NADH Phasor Segmentation . . . . .	80
3.23	Region of Interest Selection . . . . .	81
3.24	Spatial Binning of NADH Fluorescence . . . . .	82
3.25	Temporal Binning of NADH Fluorescence . . . . .	83
3.26	Seahorse XFe24 Analyzer . . . . .	88
3.27	Mitochondrial Respiration Stress Test . . . . .	89
3.28	Glycolytic Function Stress Test . . . . .	90
4.1	NADH Solutions . . . . .	94
4.2	NADH Lifetime Component Contribution . . . . .	95
4.3	NADH-LDH Solution . . . . .	96
4.4	Effect of Spatial Binning on NADH Distribution . . . . .	99
4.5	Effect of Temporal Binning on NADH Distribution . . . . .	100
4.6	Lifetime Component Localization . . . . .	101
4.7	NADH Lifetime Distribution of Isolated Mitochondria . . . . .	103
4.8	SRS Lipid Detection . . . . .	104
4.9	Redox Ratio Glycolysis Stress Test . . . . .	105
4.10	Mitochondria Movement Measurement . . . . .	106
4.11	Mitochondria Movement Blurr . . . . .	107
4.12	NADH Phasor Segmentation . . . . .	108
4.13	Effect of Reagents on the ETC . . . . .	110
4.14	Mitochondria Stress Test - Individual Injections . . . . .	111
4.15	Mitochondria Stress Test - Consecutive Injections . . . . .	112
4.16	Glycolysis Stress Test . . . . .	114
4.17	Redox Ratio Mitochondria Stress Test . . . . .	116
4.18	Redox Ratio Glycolysis Stress Test . . . . .	117
4.19	Effect of Browning Reagents . . . . .	118
4.20	$MCR^{-1}$ vs OCR . . . . .	119
4.21	Individual Cell Analysis . . . . .	120
4.22	Mixed Cell Culture . . . . .	121
4.23	Mitochondria Stress Test of HEK 293 . . . . .	123
4.24	$MCR^{-1}$ vs OCR of HEK 293 . . . . .	124
4.25	$MCR^{-1}$ vs OCR of Adipocytes and HEK 293 . . . . .	125
4.26	Representative NADH FLIM Images of Adipose Tissue . . . . .	126
4.27	Effect of Storage Conditions on Tissue . . . . .	128
4.28	Effect of Storage Conditions on BAT . . . . .	129
4.29	Metabolic Changes of Tissue . . . . .	131
4.30	Epidermal Wound . . . . .	132

5.1	NADH Lifetime Component Distribution Scheme . . . . .	142
-----	---	-----



## List of Tables

2.1	Absorbed Photons per Pulse . . . . .	11
2.2	Fluorophores . . . . .	14
3.1	Damage Threshold . . . . .	60
4.1	NADH Lifetimes in Solution . . . . .	93
4.2	Effect of Reagents on pH-Value . . . . .	97
7.1	Outlook . . . . .	152





## Bibliography

- [1] B. Chance, "Spectrophotometry of Intracellular Respiratory Pigments," *Science*, vol. 120, pp. 767–775, Nov. 1954.
- [2] J. G. White and W. B. Amos, "Confocal microscopy comes of age," July 1987.
- [3] J. R. Lakowicz, *Principles of Fluorescence Spectroscopy*. New York: Springer, 3rd edition ed., Mar. 2011.
- [4] J. R. Lakowicz, H. Szmacinski, K. Nowaczyk, and M. L. Johnson, "Fluorescence lifetime imaging of free and protein-bound NADH," *Proceedings of the National Academy of Sciences*, vol. 89, pp. 1271–1275, Feb. 1992.
- [5] W. Becker, A. Bergmann, M. A. Hink, K. König, K. Benndorf, and C. Biskup, "Fluorescence lifetime imaging by time-correlated single-photon counting," *Microscopy Research and Technique*, vol. 63, pp. 58–66, Jan. 2004.
- [6] Y. Sun, J. Phipps, D. S. Elson, H. Stoy, S. Tinling, J. Meier, B. Poirier, F. S. Chuang, D. G. Farwell, and L. Marcu, "Fluorescence lifetime imaging microscopy: in vivo application to diagnosis of oral carcinoma," *Optics Letters*, vol. 34, pp. 2081–2083, July 2009.
- [7] P. a. A. De Beule, C. Dunsby, N. P. Galletly, G. W. Stamp, A. C. Chu, U. Anand, P. Anand, C. D. Benham, A. Naylor, and P. M. W. French, "A hyperspectral fluorescence lifetime probe for skin cancer diagnosis," *The Review of Scientific Instruments*, vol. 78, p. 123101, Dec. 2007.
- [8] Z. Wang, P. Luan, J. Qu, Y. Zheng, D. Zhao, Z. Zhao, L. Liu, P. Artem, F. Zhu, and J. Liu, "Application of fluorescence lifetime imaging in clinical medicine," *Journal of Innovative Optical Health Sciences*, vol. 11, July 2017.
- [9] M. A. Yaseen, S. Sakadžić, W. Wu, W. Becker, K. A. Kasischke, and D. A. Boas, "In vivo imaging of cerebral energy metabolism with two-photon fluorescence lifetime microscopy of NADH," *Biomedical Optics Express*, vol. 4, p. 307, Feb. 2013.
- [10] K. Drozdowicz-Tomsia, A. G. Anwer, M. A. Cahill, K. N. Madlum, A. M. Maki, M. S. Baker, and E. M. Goldys, "Multiphoton fluorescence lifetime imaging microscopy reveals free-to-bound NADH ratio changes associated with

- metabolic inhibition,” *Journal of biomedical optics*, vol. 19, no. 8, pp. 086016–086016, 2014.
- [11] C. Stringari, R. A. Edwards, K. T. Pate, M. L. Waterman, P. J. Donovan, and E. Gratton, “Metabolic trajectory of cellular differentiation in small intestine by Phasor Fluorescence Lifetime Microscopy of NADH,” *Scientific Reports*, vol. 2, Aug. 2012.
  - [12] J. Vergen, C. Hecht, L. V. Zholudeva, M. M. Marquardt, R. Hallworth, and M. G. Nichols, “Metabolic Imaging Using Two-Photon Excited NADH Intensity and Fluorescence Lifetime Imaging,” *Microscopy and Microanalysis*, vol. 18, pp. 761–770, Aug. 2012.
  - [13] M. A. Digman, V. R. Caiolfa, M. Zamai, and E. Gratton, “The Phasor Approach to Fluorescence Lifetime Imaging Analysis,” *Biophysical Journal*, vol. 94, pp. L14–L16, Jan. 2008.
  - [14] C. Stringari, A. Cinquin, O. Cinquin, M. A. Digman, P. J. Donovan, and E. Gratton, “Phasor approach to fluorescence lifetime microscopy distinguishes different metabolic states of germ cells in a live tissue,” *Proceedings of the National Academy of Sciences of the United States of America*, vol. 108, pp. 13582–13587, Aug. 2011.
  - [15] S. Qian, H. Huang, and Q. Tang, “Brown and beige fat: the metabolic function, induction, and therapeutic potential,” *Frontiers of Medicine*, Jan. 2015.
  - [16] S. Wang, N. Moustaid-Moussa, L. Chen, H. Mo, A. Shastri, R. Su, P. Bapat, I. Kwun, and C.-L. Shen, “Novel insights of dietary polyphenols and obesity,” *The Journal of Nutritional Biochemistry*, vol. 25, pp. 1–18, Jan. 2014.
  - [17] C. Hilton, F. Karpe, and K. E. Pinnick, “Role of developmental transcription factors in white, brown and beige adipose tissues,” *Biochimica et Biophysica Acta (BBA) - Molecular and Cell Biology of Lipids*, vol. 1851, pp. 686–696, May 2015.
  - [18] S. Nirengi, T. Yoneshiro, H. Sugie, M. Saito, and T. Hamaoka, “Human brown adipose tissue assessed by simple, noninvasive near-Infrared time-resolved spectroscopy,” *Obesity*, vol. 23, pp. 973–980, May 2015.
  - [19] L. Sidossis and S. Kajimura, “Brown and beige fat in humans: thermogenic adipocytes that control energy and glucose homeostasis,” *Journal of Clinical Investigation*, vol. 125, pp. 478–486, Feb. 2015.
  - [20] J. Wu, P. Cohen, and B. M. Spiegelman, “Adaptive thermogenesis in adipocytes: Is beige the new brown?,” *Genes & Development*, vol. 27, pp. 234–250, Feb. 2013.

- 
- [21] C. A. Alonzo, S. Karaliota, D. Pouli, Z. Liu, K. P. Karalis, and I. Georgakoudi, "Two-photon excited fluorescence of intrinsic fluorophores enables label-free assessment of adipose tissue function," *Scientific Reports*, vol. 6, p. 31012, Aug. 2016.
- [22] U. Gehlsen, A. Oetke, M. Szaszák, N. Koop, F. Paulsen, A. Gebert, G. Huettmann, and P. Steven, "Two-photon fluorescence lifetime imaging monitors metabolic changes during wound healing of corneal epithelial cells in vitro," *Graefe's Archive for Clinical and Experimental Ophthalmology*, vol. 250, pp. 1293–1302, Sept. 2012.
- [23] A. W. C. Chua, Y. C. Khoo, B. K. Tan, K. C. Tan, C. L. Foo, and S. J. Chong, "Skin tissue engineering advances in severe burns: review and therapeutic applications," *Burns & Trauma*, vol. 4, Feb. 2016.
- [24] Z. Wang, Y. Zheng, D. Zhao, Z. Zhao, L. Liu, A. Pliss, F. Zhu, J. Liu, J. Qu, and P. Luan, "Applications of fluorescence lifetime imaging in clinical medicine," *Journal of Innovative Optical Health Sciences*, vol. 11, p. 1830001, July 2017.
- [25] B. E. A. Saleh and M. C. Teich, *Fundamentals of Photonics*. Hoboken, N.J: Wiley-Interscience, 2 edition ed., Mar. 2007.
- [26] M. Kasha, "Characterization of electronic transitions in complex molecules," *Discussions of the Faraday society*, vol. 9, pp. 14–19, 1950.
- [27] F. X. Kärtner, *Few-Cycle Laser Pulse Generation and Its Applications*. Springer Science & Business Media, Sept. 2004. Google-Books-ID: wgbno3SFx34C.
- [28] Y. Pu, W. Wang, Y. Yang, and R. R. Alfano, "Stokes shift spectroscopic analysis of multifluorophores for human cancer detection in breast and prostate tissues," *Journal of Biomedical Optics*, vol. 18, p. 017005, Jan. 2013.
- [29] R. K. Benninger and D. W. Piston, "Two-Photon Excitation Microscopy for the Study of Living Cells and Tissues," *Current protocols in cell biology / editorial board, Juan S. Bonifacino ... [et al.]*, vol. 0 4, pp. Unit–4.1124, June 2013.
- [30] P. T. C. So, C. Y. Dong, B. R. Masters, and K. M. Berland, "Two-Photon Excitation Fluorescence Microscopy," *Annu. Rev. Biomed. Eng.*, p. 42, 2000.
- [31] W. Denk, J. H. Strickler, and W. W. Webb, "Two-Photon Laser Scanning Fluorescence Microscopy," *Science*, vol. 248, no. 4951, pp. 73–76, 1990.

- [32] S. Tang, T. B. Krasieva, Z. Chen, G. Tempea, and B. J. Tromberg, "Effect of pulse duration on two-photon excited fluorescence and second harmonic generation in nonlinear optical microscopy," *Journal of Biomedical Optics*, vol. 11, no. 2, p. 020501, 2006.
- [33] A. Hopt and E. Neher, "Highly nonlinear photodamage in two-photon fluorescence microscopy," *Biophysical journal*, vol. 80, no. 4, pp. 2029–2036, 2001.
- [34] A. Diaspro, P. Bianchini, G. Vicidomini, M. Faretta, P. Ramoino, and C. Usai, "Multi-photon excitation microscopy," *BioMedical Engineering OnLine*, vol. 5, p. 36, June 2006.
- [35] N. G. Horton, K. Wang, D. Kobat, C. G. Clark, F. W. Wise, C. B. Schaffer, and C. Xu, "In vivo three-photon microscopy of subcortical structures within an intact mouse brain," *Nature Photonics*, vol. 7, pp. 205–209, Mar. 2013.
- [36] A. Vogel and V. Venugopalan, "Mechanisms of Pulsed Laser Ablation of Biological Tissues," *Chemical Reviews*, vol. 103, pp. 577–644, Feb. 2003.
- [37] S.-W. Chu, M.-C. Chan, S.-P. Tai, S. Keller, S. P. DenBaars, and C.-K. Sun, "Simultaneous four-photon luminescence, third-harmonic generation, and second-harmonic generation microscopy of GaN," *Optics Letters*, vol. 30, pp. 2463–2465, Sept. 2005.
- [38] G. Baryshnikov, B. Minaev, and H. Ågren, "Theory and Calculation of the Phosphorescence Phenomenon," *Chemical Reviews*, vol. 117, pp. 6500–6537, May 2017.
- [39] N. Ramanujam, "Fluorescence Spectroscopy of Neoplastic and Non-Neoplastic Tissues," *Neoplasia (New York, N.Y.)*, vol. 2, pp. 89–117, Jan. 2000.
- [40] R. B. Mujumdar, L. A. Ernst, S. R. Mujumdar, C. J. Lewis, and A. S. Waggoner, "Cyanine dye labeling reagents: sulfoindocyanine succinimidyl esters," *Bioconjugate chemistry*, vol. 4, no. 2, pp. 105–111, 1993.
- [41] C. V. Bindhu, S. S. Harilal, G. K. Varier, R. C. Issac, V. P. N. Nampoori, and C. P. G. Vallabhan, "Measurement of the absolute fluorescence quantum yield of rhodamine B solution using a dual-beam thermal lens technique," *Journal of Physics D: Applied Physics*, vol. 29, no. 4, p. 1074, 1996.
- [42] D. V. O'Connor, *Time-correlated single photon counting*. London ; Orlando: Academic Press, 1984.
- [43] R. Laine, *Fluorescence lifetime spectroscopy and imaging of FRET probes for the study of cell signalling*. PhD thesis, Imperial College London, 2013.
- [44] B. Valeur, *Molecular fluorescence: principles and applications*. Weinheim ; New York: Wiley-VCH, 2002. HOLLIS number: 008977994.

- 
- [45] D. F. Swinehart, "The beer-lambert law," *J. Chem. Educ.*, vol. 39, no. 7, p. 333, 1962.
- [46] A. J. Walsh, J. T. Sharick, M. C. Skala, and H. T. Beier, "Temporal binning of time-correlated single photon counting data improves exponential decay fits and imaging speed," *Biomedical Optics Express*, vol. 7, p. 1385, Apr. 2016.
- [47] C. B. Talbot, R. Patalay, I. Munro, S. Warren, F. Ratto, P. Matteini, R. Pini, H. G. Breunig, K. König, A. C. Chu, G. W. Stamp, M. A. A. Neil, P. M. W. French, and C. Dunsby, "Application of ultrafast gold luminescence to measuring the instrument response function for multispectral multiphoton fluorescence lifetime imaging," *Optics Express*, vol. 19, p. 13848, July 2011.
- [48] H. C. Ishikawa-Ankerhold, R. Ankerhold, and G. P. C. Drummen, "Advanced Fluorescence Microscopy Techniques—FRAP, FLIP, FLAP, FRET and FLIM," *Molecules*, vol. 17, pp. 4047–4132, Apr. 2012.
- [49] W. Becker, *The bh TCSPC Handbook*. Becker & Hickl GmbH, 6th edition ed., 2014.
- [50] W. Becker, "Fluorescence lifetime imaging – techniques and applications," *Journal of Microscopy*, vol. 247, pp. 119–136, Aug. 2012.
- [51] B. Spring and R. Clegg, "Image analysis for denoising full-field frequency-domain fluorescence lifetime images," *Journal of Microscopy*, vol. 235, pp. 221–237, Aug. 2009.
- [52] P. C. Schneider and R. M. Clegg, "Rapid acquisition, analysis, and display of fluorescence lifetime-resolved images for real-time applications," *Review of Scientific Instruments*, vol. 68, pp. 4107–4119, Nov. 1997.
- [53] Squire, Verveer, and Bastiaens, "Multiple frequency fluorescence lifetime imaging microscopy," *Journal of Microscopy*, vol. 197, pp. 136–149, Feb. 2000.
- [54] D. B. Papkovsky and R. I. Dmitriev, "Imaging of oxygen and hypoxia in cell and tissue samples," *Cellular and Molecular Life Sciences*, vol. 75, pp. 2963–2980, Aug. 2018.
- [55] W. Becker, V. Shcheslavskiy, and A. Rück, "Simultaneous Phosphorescence and Fluorescence Lifetime Imaging by Multi-Dimensional TCSPC and Multi-Pulse Excitation," in *Multi-Parametric Live Cell Microscopy of 3D Tissue Models* (R. I. Dmitriev, ed.), Advances in Experimental Medicine and Biology, pp. 19–30, Cham: Springer International Publishing, 2017.
- [56] A. Periasamy and R. M. Clegg, eds., *FLIM Microscopy in Biology and Medicine*. Boca Raton: Chapman and Hall/CRC, 1 edition ed., July 2009.

- [57] G. I. Redford and R. M. Clegg, "Polar Plot Representation for Frequency-Domain Analysis of Fluorescence Lifetimes," *Journal of Fluorescence*, vol. 15, pp. 805–815, Sept. 2005.
- [58] Y.-C. Chen and R. M. Clegg, "Fluorescence lifetime-resolved imaging," *Photosynthesis Research*, vol. 102, p. 143, Dec. 2009.
- [59] S. Kefayati, "Confocal and two-photon microscopy: Image enhancement," Master's thesis, Brock University (Canada), Canada, 2008.
- [60] A. Ustione and D. W. Piston, "A simple introduction to multiphoton microscopy," *Journal of Microscopy*, vol. 243, pp. 221–226, Sept. 2011.
- [61] S. L. Jacques, "Optical properties of biological tissues: a review," *Physics in Medicine and Biology*, vol. 58, pp. R37–R61, June 2013.
- [62] M. Oheim, E. Beaurepaire, E. Chaigneau, J. Mertz, and S. Charpak, "Two-photon microscopy in brain tissue: parameters influencing the imaging depth," *Journal of Neuroscience Methods*, vol. 111, pp. 29–37, Oct. 2001.
- [63] P. Theer and W. Denk, "On the fundamental imaging-depth limit in two-photon microscopy," *JOSA A*, vol. 23, pp. 3139–3149, Dec. 2006.
- [64] N. J. Durr, C. T. Weisspfennig, B. A. Holfeld, and A. Ben-Yakar, "Maximum imaging depth of two-photon autofluorescence microscopy in epithelial tissues," *Journal of Biomedical Optics*, vol. 16, Feb. 2011.
- [65] Y. Yu, P. V. Ramachandran, and M. C. Wang, "Shedding new light on lipid functions with CARS and SRS microscopy," *Biochimica et biophysica acta*, vol. 1841, pp. 1120–1129, Aug. 2014.
- [66] R. W. Boyd, "Chapter 1 - The Nonlinear Optical Susceptibility," in *Nonlinear Optics (Third Edition)*, pp. 1–67, Burlington: Academic Press, 2008.
- [67] A. Folick, W. Min, and M. C. Wang, "Label-free imaging of lipid dynamics using Coherent Anti-stokes Raman Scattering (CARS) and Stimulated Raman Scattering (SRS) microscopy," *Current Opinion in Genetics & Development*, vol. 21, pp. 585–590, Oct. 2011.
- [68] C. L. Evans and X. S. Xie, "Coherent Anti-Stokes Raman Scattering Microscopy: Chemical Imaging for Biology and Medicine," *Annual Review of Analytical Chemistry*, vol. 1, no. 1, pp. 883–909, 2008.
- [69] W. J. Tipping, M. Lee, A. Serrels, V. G. Brunton, and A. N. Hulme, "Stimulated Raman scattering microscopy: an emerging tool for drug discovery," *Chemical Society Reviews*, vol. 45, no. 8, pp. 2075–2089, 2016.



- 
- [70] M. J. Winterhalder and A. Zumbusch, “Beyond the borders — Biomedical applications of non-linear Raman microscopy,” *Advanced Drug Delivery Reviews*, vol. 89, pp. 135–144, July 2015.
- [71] J. H. Postlethwait and J. L. Hopson, *Modern biology*. Orlando: Holt, Rinehart and Winston, 2009. OCLC: 226360402.
- [72] E. Enger, F. C. Ross, and D. Bailey, *Concepts in Biology*. New York: McGraw-Hill Education, 14 edition ed., Jan. 2011.
- [73] B. Alberts, A. Johnson, J. Lewis, M. Raff, K. Roberts, and P. Walter, “The Mitochondrion,” *Molecular Biology of the Cell*. 4th edition, 2002.
- [74] J. M. Berg, J. L. Tymoczko, and L. Stryer, “Oxidative Phosphorylation,” *Biochemistry*. 5th edition, 2002.
- [75] G. M. Cooper, “The Mechanism of Oxidative Phosphorylation,” *The Cell: A Molecular Approach*. 2nd edition, 2000.
- [76] K. A. Young, J. A. Wise, P. DeSaix, D. H. Kruse, B. Poe, E. Johnson, J. E. Johnson, O. Korol, J. G. Betts, and M. Womble, *Anatomy & Physiology*. OpenStax College, 1st edition ed., Jan. 2013.
- [77] M. Serajul Islam, M. Honma, T. Nakabayashi, M. Kinjo, and N. Ohta, “pH Dependence of the Fluorescence Lifetime of FAD in Solution and in Cells,” *International journal of molecular sciences*, vol. 14, pp. 1952–1963, Jan. 2013.
- [78] G. H. Patterson, S. M. Knobel, P. Arkhammar, O. Thastrup, and D. W. Piston, “Separation of the glucose-stimulated cytoplasmic and mitochondrial NAD(P)H responses in pancreatic islet  $\beta$  cells,” *Proceedings of the National Academy of Sciences*, vol. 97, pp. 5203–5207, May 2000.
- [79] K. P. Quinn, G. V. Sridharan, R. S. Hayden, D. L. Kaplan, K. Lee, and I. Georgakoudi, “Quantitative metabolic imaging using endogenous fluorescence to detect stem cell differentiation,” *Scientific Reports*, vol. 3, Dec. 2013.
- [80] M. C. Skala, K. M. Riching, D. K. Bird, A. Gendron-Fitzpatrick, J. Eickhoff, K. W. Eliceiri, P. J. Keely, and N. Ramanujam, “In vivo multiphoton fluorescence lifetime imaging of protein-bound and free nicotinamide adenine dinucleotide in normal and precancerous epithelia,” *Journal of Biomedical Optics*, vol. 12, no. 2, p. 024014, 2007.
- [81] B. Chance, B. Schoener, R. Oshino, F. Itshak, and Y. Nakase, “Oxidation-reduction ratio studies of mitochondria in freeze-trapped samples. NADH and flavoprotein fluorescence signals,” *Journal of Biological Chemistry*, vol. 254, pp. 4764–4771, June 1979.

- [82] R. Scholz, R. G. Thurman, J. R. Williamson, B. Chance, and T. Bücher, "Flavin and Pyridine Nucleotide Oxidation-Reduction Changes in Perfused Rat Liver," *Journal of Biological Chemistry*, vol. 244, pp. 2317–2324, May 1969.
- [83] J. V. Rocheleau, W. S. Head, and D. W. Piston, "Quantitative NAD(P)H/Flavoprotein Autofluorescence Imaging Reveals Metabolic Mechanisms of Pancreatic Islet Pyruvate Response," *Journal of Biological Chemistry*, vol. 279, pp. 31780–31787, July 2004.
- [84] O. Warburg, F. Wind, and E. Negelein, "The Metabolism of Tumors in the Body," *The Journal of General Physiology*, vol. 8, pp. 519–530, Mar. 1927.
- [85] J. H. Ostrander, C. M. McMahon, S. Lem, S. R. Millon, J. Q. Brown, V. L. Seewaldt, and N. Ramanujam, "Optical Redox Ratio Differentiates Breast Cancer Cell Lines Based on Estrogen Receptor Status," *Cancer research*, vol. 70, June 2010.
- [86] N. D Kirkpatrick, C. Zou, M. Brewer, W. R Brands, R. A Drezek, and U. Utzinger, "Endogenous Fluorescence Spectroscopy of Cell Suspensions for Chemopreventive Drug Monitoring," *Photochemistry and photobiology*, vol. 81, pp. 125–34, Jan. 2005.
- [87] Mujat Claudia, Greiner Cherry, Baldwin Amy, Levitt Jonathan M., Tian Fenghua, Stucenski Lee A., Hunter Martin, Kim Young L., Backman Vadim, Feld Michael, Mürger Karl, and Georgakoudi Irene, "Endogenous optical biomarkers of normal and human papillomavirus immortalized epithelial cells," *International Journal of Cancer*, vol. 122, pp. 363–371, Oct. 2007.
- [88] W. S. Kunz and W. Kunz, "Contribution of different enzymes to flavoprotein fluorescence of isolated rat liver mitochondria," *Biochimica et Biophysica Acta (BBA) - General Subjects*, vol. 841, pp. 237–246, Sept. 1985.
- [89] Y. Wu, W. Zheng, and J. Y. Qu, "Sensing cell metabolism by time-resolved autofluorescence," *Optics Letters*, vol. 31, pp. 3122–3124, Nov. 2006.
- [90] T. S. Blacker, R. J. Marsh, M. R. Duchen, and A. J. Bain, "Activated barrier crossing dynamics in the non-radiative decay of NADH and NADPH," *Chemical Physics*, vol. 422, pp. 184–194, Aug. 2013.
- [91] I. Georgakoudi and K. P. Quinn, "Optical Imaging Using Endogenous Contrast to Assess Metabolic State," *Annual Review of Biomedical Engineering*, vol. 14, pp. 351–367, Aug. 2012.
- [92] D. K. Bird, "Metabolic Mapping of MCF10a Human Breast Cells via Multiphoton Fluorescence Lifetime Imaging of the Coenzyme NADH," *Cancer Research*, vol. 65, pp. 8766–8773, Oct. 2005.

- 
- [93] J. Gómez-Ambrosi, C. Silva, J. C. Galofré, J. Escalada, S. Santos, D. Millán, N. Vila, P. Ibañez, M. J. Gil, V. Valentí, F. Rotellar, B. Ramírez, J. Salvador, and G. Frühbeck, "Body mass index classification misses subjects with increased cardiometabolic risk factors related to elevated adiposity," *International Journal of Obesity*, vol. 36, pp. 286–294, Feb. 2012.
- [94] K. Jaworski, E. Sarkadi-Nagy, R. E. Duncan, M. Ahmadian, and H. S. Sul, "Regulation of Triglyceride Metabolism. IV. Hormonal regulation of lipolysis in adipose tissue," *American journal of physiology. Gastrointestinal and liver physiology*, vol. 293, pp. G1–G4, July 2007.
- [95] P. Trayhurn and J. H. Beattie, "Physiological role of adipose tissue: white adipose tissue as an endocrine and secretory organ," *Proceedings of the Nutrition Society*, vol. 60, pp. 329–339, Aug. 2001.
- [96] T. T. Tran, Y. Yamamoto, S. Gesta, and C. R. Kahn, "Beneficial Effects of Subcutaneous Fat Transplantation on Metabolism," *Cell metabolism*, vol. 7, pp. 410–420, May 2008.
- [97] M. B. Snijder, J. M. Dekker, M. Visser, L. M. Bouter, C. D. Stehouwer, P. J. Kostense, J. S. Yudkin, R. J. Heine, G. Nijpels, and J. C. Seidell, "Associations of hip and thigh circumferences independent of waist circumference with the incidence of type 2 diabetes: the Hoorn Study," *The American Journal of Clinical Nutrition*, vol. 77, pp. 1192–1197, May 2003.
- [98] B. A. Horwitz, J. S. Hamilton, and K. S. Kott, "GDP binding to hamster brown fat mitochondria is reduced during hibernation," *American Journal of Physiology-Regulatory, Integrative and Comparative Physiology*, vol. 249, pp. R689–R693, Dec. 1985.
- [99] I. Cavallini, M. A. Marino, C. Tonello, P. Marzola, E. Nicolato, P. F. Fabene, L. Calderan, P. Bernardi, R. M. Asperio, E. Nisoli, and A. Sbarbati, "The hydrolipidic ratio in age-related maturation of adipose tissues," *Biomedicine & Pharmacotherapy*, vol. 60, pp. 139–143, Apr. 2006.
- [100] A. Fedorenko, P. V. Lishko, and Y. Kirichok, "Mechanism of Fatty-Acid-Dependent UCP1 Uncoupling in Brown Fat Mitochondria," *Cell*, vol. 151, pp. 400–413, Oct. 2012.
- [101] P. Seale, B. Bjork, W. Yang, S. Kajimura, S. Kuang, A. Scime, S. Devarakonda, S. Chin, H. M. Conroe, H. Erdjument-Bromage, P. Tempst, M. A. Rudnicki, D. R. Beier, and B. M. Spiegelman, "PRDM16 Controls a Brown Fat/Skeletal Muscle Switch," *Nature*, vol. 454, pp. 961–967, Aug. 2008.

- [102] T. F. Hany, E. Gharehpapagh, E. M. Kamel, A. Buck, J. Himms-Hagen, and G. K. v. Schulthess, "Brown adipose tissue: a factor to consider in symmetrical tracer uptake in the neck and upper chest region," *European Journal of Nuclear Medicine and Molecular Imaging*, vol. 29, pp. 1393–1398, Oct. 2002.
- [103] N. Petrovic, T. B. Walden, I. G. Shabalina, J. A. Timmons, B. Cannon, and J. Nedergaard, "Chronic Peroxisome Proliferator-activated Receptor  $\gamma$  (PPAR $\gamma$ ) Activation of Epididymally Derived White Adipocyte Cultures Reveals a Population of Thermogenically Competent, UCP1-containing Adipocytes Molecularly Distinct from Classic Brown Adipocytes," *The Journal of Biological Chemistry*, vol. 285, pp. 7153–7164, Mar. 2010.
- [104] S. Cinti, "Transdifferentiation properties of adipocytes in the adipose organ," *American Journal of Physiology-Endocrinology and Metabolism*, vol. 297, pp. E977–E986, May 2009.
- [105] Q. A. Wang, C. Tao, R. K. Gupta, and P. E. Scherer, "Tracking adipogenesis during white adipose tissue development, expansion and regeneration," *Nature Medicine*, vol. 19, pp. 1338–1344, Oct. 2013.
- [106] X.-R. Peng, P. Gennemark, G. O'Mahony, and S. Bartsaghi, "Unlock the Thermogenic Potential of Adipose Tissue: Pharmacological Modulation and Implications for Treatment of Diabetes and Obesity," *Frontiers in Endocrinology*, vol. 6, Nov. 2015.
- [107] Y.-H. Lee, A. P. Petkova, A. A. Konkar, and J. G. Granneman, "Cellular origins of cold-induced brown adipocytes in adult mice," *The FASEB Journal*, vol. 29, pp. 286–299, Jan. 2015.
- [108] K. Ikeda, P. Maretich, and S. Kajimura, "The Common and Distinct Features of Brown and Beige Adipocytes," *Trends in Endocrinology & Metabolism*, vol. 29, pp. 191–200, Mar. 2018.
- [109] A. Vargas-Castillo, R. Fuentes-Romero, L. A. Rodriguez-Lopez, N. Torres, and A. R. Tovar, "Understanding the Biology of Thermogenic Fat: Is Browning A New Approach to the Treatment of Obesity?," *Archives of Medical Research*, vol. 48, pp. 401–413, July 2017.
- [110] K. K. Kaur, "Advances in BAT physiology for understanding and translating into Pharmacotherapies for obesity and comorbidities," *MOJ Drug Design Development & Therapy*, vol. 2, Sept. 2018.
- [111] P. Boström, J. Wu, M. P. Jedrychowski, A. Korde, L. Ye, J. C. Lo, K. A. Rasbach, E. A. Boström, J. H. Choi, J. Z. Long, S. Kajimura, M. C. Zingaretti, B. F. Vind, H. Tu, S. Cinti, K. Højlund, S. P. Gygi, and B. M. Spiegelman,

- “A PGC1 $\alpha$ -dependent myokine that drives browning of white fat and thermogenesis,” *Nature*, vol. 481, pp. 463–468, Jan. 2012.
- [112] S. Kajimura, B. M. Spiegelman, and P. Seale, “Brown and beige fat: Physiological roles beyond heat-generation,” *Cell metabolism*, vol. 22, pp. 546–559, Oct. 2015.
- [113] M. Petruzzelli, M. Schweiger, R. Schreiber, R. Campos-Olivas, M. Tsoli, J. Allen, M. Swarbrick, S. Rose-John, M. Rincon, G. Robertson, R. Zechner, and E. F. Wagner, “A Switch from White to Brown Fat Increases Energy Expenditure in Cancer-Associated Cachexia,” *Cell Metabolism*, vol. 20, pp. 433–447, Sept. 2014.
- [114] L. S. Sidossis, C. Porter, M. K. Saraf, E. Børsheim, R. S. Radhakrishnan, T. Chao, A. Ali, M. Chondronikola, R. Mlcak, C. C. Finnerty, H. K. Hawkins, T. Toliver-Kinsky, and D. N. Herndon, “Browning of Subcutaneous White Adipose Tissue in Humans,” *Cell metabolism*, vol. 22, pp. 219–227, Aug. 2015.
- [115] A. A. van der Lans, J. Hoeks, B. Brans, G. H. Vijgen, M. G. Visser, M. J. Vosselman, J. Hansen, J. A. Jörgensen, J. Wu, F. M. Mottaghy, P. Schrauwen, and W. D. van Marken Lichtenbelt, “Cold acclimation recruits human brown fat and increases nonshivering thermogenesis,” *The Journal of Clinical Investigation*, vol. 123, pp. 3395–3403, Aug. 2013.
- [116] F. Villarroja and A. Vidal-Puig, “Beyond the Sympathetic Tone: The New Brown Fat Activators,” *Cell Metabolism*, vol. 17, pp. 638–643, May 2013.
- [117] A. M. Cypess, L. S. Weiner, C. Roberts-Toler, E. F. Elia, S. H. Kessler, P. A. Kahn, J. English, K. Chatman, S. A. Trauger, A. Doria, and G. M. Kolodny, “Activation of Human Brown Adipose Tissue by a  $\beta$ 3-Adrenergic Receptor Agonist,” *Cell Metabolism*, vol. 21, pp. 33–38, Jan. 2015.
- [118] J. Orava, *Characterisation of Functional Brown Adipose Tissue In Adult Humans*. PhD thesis, University of Turku, Apr. 2014.
- [119] A. C. Carpentier, D. P. Blondin, K. A. Virtanen, D. Richard, F. Haman, and R. E. Turcotte, “Brown Adipose Tissue Energy Metabolism in Humans,” *Frontiers in Endocrinology*, vol. 9, 2018.
- [120] A. Meiliana and A. Wijaya, “Brown and Beige Fat: Therapeutic Potential in Obesity,” *The Indonesian Biomedical Journal*, vol. 6, p. 65, Aug. 2014.
- [121] K. Pearson, “VII. Mathematical contributions to the theory of evolution.—III. Regression, heredity, and panmixia,” *Phil. Trans. R. Soc. Lond. A*, vol. 187, pp. 253–318, Jan. 1896.

- [122] S. Yue, M. N. Slipchenko, and J.-X. Cheng, “Multimodal nonlinear optical microscopy,” *Laser & Photonics Reviews*, vol. 5, pp. 496–512, July 2011.
- [123] K. König, “Multiphoton microscopy in life sciences,” *Journal of microscopy*, vol. 200, no. 2, pp. 83–104, 2000.
- [124] X. Nan, E. O. Potma, and X. S. Xie, “Nonperturbative Chemical Imaging of Organelle Transport in Living Cells with Coherent Anti-Stokes Raman Scattering Microscopy,” *Biophysical Journal*, vol. 91, pp. 728–735, July 2006.
- [125] G. H. Patterson and D. W. Piston, “Photobleaching in two-photon excitation microscopy,” *Biophysical journal*, vol. 78, no. 4, pp. 2159–2162, 2000.
- [126] J. Pawley, ed., *Handbook of Biological Confocal Microscopy*. Springer US, 3 ed., 2006.
- [127] H. Oehring, I. Riemann, P. Fischer, K.-J. Halbhuber, and K. König, “Ultra-structure and reproduction behaviour of single CHO-K1 cells exposed to near infrared femtosecond laser pulses,” *Scanning*, vol. 22, pp. 263–270, July 2018.
- [128] A. C. E. Moor, “Signaling pathways in cell death and survival after photodynamic therapy,” *Journal of Photochemistry and Photobiology B: Biology*, vol. 57, pp. 1–13, Aug. 2000.
- [129] A. V. Meleshina, V. V. Dudenkova, M. V. Shirmanova, V. I. Shcheslavskiy, W. Becker, A. S. Bystrova, E. I. Cherkasova, and E. V. Zagaynova, “Probing metabolic states of differentiating stem cells using two-photon FLIM,” *Scientific Reports*, vol. 6, p. 21853, Feb. 2016.
- [130] J. Enderlein and R. Erdmann, “Fast fitting of multi-exponential decay curves,” *Optics Communications*, vol. 134, pp. 371–378, Jan. 1997.
- [131] P. H. Lakner, M. G. Monaghan, Y. Möller, M. A. Olayioye, and K. Schenke-Layland, “Applying phasor approach analysis of multiphoton FLIM measurements to probe the metabolic activity of three-dimensional in vitro cell culture models,” *Scientific Reports*, vol. 7, p. 42730, Feb. 2017.
- [132] S. Sanchez, L. Bakás, E. Gratton, and V. Herlax, “Alpha Hemolysin Induces an Increase of Erythrocytes Calcium: A FLIM 2-Photon Phasor Analysis Approach,” *PLoS ONE*, vol. 6, p. e21127, June 2011.
- [133] M. Štefl, N. G. James, J. A. Ross, and D. M. Jameson, “Applications of phasors to in vitro time-resolved fluorescence measurements,” *Analytical Biochemistry*, vol. 410, pp. 62–69, Mar. 2011.
- [134] “Seahorse XF Glycolysis Stress Test Kit User Guide,” p. 24.



- 
- [135] Z. Heiner, T. Roland, J. Leonard, S. Haacke, and G. I. Groma, “Kinetics of Light-Induced Intramolecular Energy Transfer in Different Conformational States of NADH,” *The Journal of Physical Chemistry B*, vol. 121, pp. 8037–8045, Aug. 2017.
- [136] A. Gafni and L. Brand, “Fluorescence decay studies of reduced nicotinamide adenine dinucleotide in solution and bound to liver alcohol dehydrogenase,” *Biochemistry*, vol. 15, no. 15, pp. 3165–3171, 1976.
- [137] Q. Yu and A. A. Heikal, “Two-photon autofluorescence dynamics imaging reveals sensitivity of intracellular NADH concentration and conformation to cell physiology at the single-cell level,” *Journal of Photochemistry and Photobiology B: Biology*, vol. 95, pp. 46–57, Apr. 2009.
- [138] T. G. Scott, R. D. Spencer, N. J. Leonard, and G. Weber, “Synthetic spectroscopic models related to coenzymes and base pairs. V. Emission properties of NADH. Studies of fluorescence lifetimes and quantum efficiencies of NADH, AcPyADH,[reduced acetylpyridineadenine dinucleotide] and simplified synthetic models,” *Journal of the American Chemical Society*, vol. 92, no. 3, pp. 687–695, 1970.
- [139] M. Islam, M. Honma, T. Nakabayashi, M. Kinjo, and N. Ohta, “pH Dependence of the Fluorescence Lifetime of FAD in Solution and in Cells,” *International Journal of Molecular Sciences*, vol. 14, pp. 1952–1963, Jan. 2013.
- [140] T. S. Blacker, Z. F. Mann, J. E. Gale, M. Ziegler, A. J. Bain, G. Szabadkai, and M. R. Duchon, “Separating NADH and NADPH fluorescence in live cells and tissues using FLIM,” *Nature Communications*, vol. 5, p. 3936, 2014.
- [141] B. Cannon and J. Nedergaard, “Studies of Thermogenesis and Mitochondrial Function in Adipose Tissues,” in *Adipose Tissue Protocols*, Methods in Molecular Biology<sup>TM</sup>, pp. 109–121, Humana Press, 2008.
- [142] S. Warburton, K. Southwick, R. M. Hardman, A. M. Secrest, R. K. Grow, H. Xin, A. T. Woolley, G. F. Burton, and C. D. Thulin, “Examining the proteins of functional retinal lipofuscin using proteomic analysis as a guide for understanding its origin,” *Molecular Vision*, vol. 11, pp. 1122–1134, Dec. 2005.
- [143] U. T. Brunk and A. Terman, “Lipofuscin: mechanisms of age-related accumulation and influence on cell function,” *Free Radical Biology and Medicine*, vol. 33, pp. 611–619, Sept. 2002.
- [144] R. Datta, A. Alfonso-García, R. Cinco, and E. Gratton, “Fluorescence lifetime imaging of endogenous biomarker of oxidative stress,” *Scientific Reports*, vol. 5, May 2015.



- [145] X. Nan, J.-X. Cheng, and X. S. Xie, “Vibrational imaging of lipid droplets in live fibroblast cells with coherent anti-Stokes Raman scattering microscopy,” *Journal of Lipid Research*, vol. 44, pp. 2202–2208, Nov. 2003.
- [146] J. R. Sparrow, C. A. Parish, M. Hashimoto, and K. Nakanishi, “A2e, a Lipofuscin Fluorophore, in Human Retinal Pigmented Epithelial Cells in Culture,” *Investigative Ophthalmology & Visual Science*, vol. 40, pp. 2988–2995, Nov. 1999.
- [147] W. Rice, D. Kaplan, and I. Georgakoudi, “Two-Photon Microscopy for Non-Invasive, Quantitative Monitoring of Stem Cell Differentiation,” *PloS one*, vol. 5, p. e10075, Apr. 2010.
- [148] M. Klapper, M. Ehmke, D. Palgunow, M. Böhme, C. Matthäus, G. Bergner, B. Dietzek, J. Popp, and F. Döring, “Fluorescence-based fixative and vital staining of lipid droplets in *Caenorhabditis elegans* reveal fat stores using microscopy and flow cytometry approaches,” *Journal of Lipid Research*, vol. 52, pp. 1281–1293, June 2011.
- [149] K. Yen, T. T. Le, A. Bansal, S. D. Narasimhan, J.-X. Cheng, and H. A. Tissenbaum, “A Comparative Study of Fat Storage Quantitation in Nematode *Caenorhabditis elegans* Using Label and Label-Free Methods,” *PloS one*, vol. 5, p. e12810, Sept. 2010.
- [150] J. Hou, H. J. Wright, N. Chan, R. Tran, O. V. Razorenova, E. O. Potma, and B. J. Tromberg, “Correlating two-photon excited fluorescence imaging of breast cancer cellular redox state with Seahorse flux analysis of normalized cellular oxygen consumption,” *Journal of Biomedical Optics*, vol. 21, June 2016.
- [151] K. Alhallak, L. G. Rebello, T. J. Muldoon, K. P. Quinn, and N. Rajaram, “Optical redox ratio identifies metastatic potential-dependent changes in breast cancer cell metabolism,” *Biomedical Optics Express*, vol. 7, pp. 4364–4374, Oct. 2016.
- [152] I. Shabalina, N. Petrovic, J. de Jong, A. Kalinovich, B. Cannon, and J. Nedergaard, “UCP1 in Brite/Beige Adipose Tissue Mitochondria Is Functionally Thermogenic,” *Cell Reports*, vol. 5, pp. 1196–1203, Dec. 2013.
- [153] J. Yu, S. Zhang, L. Cui, W. Wang, H. Na, X. Zhu, L. Li, G. Xu, F. Yang, M. Christian, and P. Liu, “Lipid droplet remodeling and interaction with mitochondria in mouse brown adipose tissue during cold treatment,” *Biochimica et Biophysica Acta (BBA) - Molecular Cell Research*, vol. 1853, pp. 918–928, May 2015.

- 
- [154] G. Deka, W.-W. Wu, and F.-J. Kao, "In vivo wound healing diagnosis with second harmonic and fluorescence lifetime imaging," *Journal of biomedical optics*, vol. 18, p. 061222, June 2013.
- [155] H. D. Vishwasrao, "Conformational Dependence of Intracellular NADH on Metabolic State Revealed by Associated Fluorescence Anisotropy," *Journal of Biological Chemistry*, vol. 280, pp. 25119–25126, Apr. 2005.
- [156] C. J. Valvona, H. L. Fillmore, P. B. Nunn, and G. J. Pilkington, "The Regulation and Function of Lactate Dehydrogenase A: Therapeutic Potential in Brain Tumor: Regulation and Function of Lactate Dehydrogenase A," *Brain Pathology*, vol. 26, pp. 3–17, Jan. 2016.
- [157] K. Orlando and W. Guo, "Membrane Organization and Dynamics in Cell Polarity," *Cold Spring Harbor Perspectives in Biology*, vol. 1, Nov. 2009.
- [158] V. Jayashankar and S. M. Rafelski, "Integrating mitochondrial organization and dynamics with cellular architecture," *Current Opinion in Cell Biology*, vol. 26, pp. 34–40, Feb. 2014.
- [159] M. Y. Berezin and S. Achilefu, "Fluorescence Lifetime Measurements and Biological Imaging," *Chemical Reviews*, vol. 110, pp. 2641–2684, May 2010.
- [160] A. Zoumi, A. Yeh, and B. J. Tromberg, "Imaging cells and extracellular matrix in vivo by using second-harmonic generation and two-photon excited fluorescence," *Proceedings of the National Academy of Sciences*, vol. 99, no. 17, pp. 11014–11019, 2002.
- [161] D. Chorvat and A. Chorvatova, "Multi-wavelength fluorescence lifetime spectroscopy: a new approach to the study of endogenous fluorescence in living cells and tissues," *Laser Physics Letters*, vol. 6, pp. 175–193, Mar. 2009.
- [162] A. V. Meleshina, V. V. Dudenkova, A. S. Bystrova, D. S. Kuznetsova, M. V. Shirmanova, and E. V. Zagaynova, "Two-photon FLIM of NAD(P)H and FAD in mesenchymal stem cells undergoing either osteogenic or chondrogenic differentiation," *Stem Cell Research & Therapy*, vol. 8, p. 15, Jan. 2017.
- [163] P. M. Schaefer, D. Hilpert, M. Niederschweiberer, L. Neuhauser, S. Kalinina, E. Calzia, A. Rueck, B. v. Einem, and C. A. F. v. Arnim, "Mitochondrial matrix pH as a decisive factor in neurometabolic imaging," *Neurophotonics*, vol. 4, p. 045004, Nov. 2017.
- [164] S. Kiyonaka, T. Kajimoto, R. Sakaguchi, D. Shinmi, M. Omatsu-Kanbe, H. Matsuura, H. Imamura, T. Yoshizaki, I. Hamachi, T. Morii, and Y. Mori, "Genetically encoded fluorescent thermosensors visualize subcellular thermoregulation in living cells," *Nature Methods*, vol. 10, pp. 1232–1238, Dec. 2013.

- [165] Y. Si, H. Shi, and K. Lee, “Metabolic flux analysis of mitochondrial uncoupling in 3t3-L1 adipocytes,” *PloS one*, vol. 4, no. 9, 2009.
- [166] J. P. Houston, Z. Yang, J. Sambrano, W. Li, K. Nichani, and G. Vacca, “Overview of Fluorescence Lifetime Measurements in Flow Cytometry,” in *Flow Cytometry Protocols* (T. S. Hawley and R. G. Hawley, eds.), Methods in Molecular Biology, pp. 421–446, New York, NY: Springer New York, 2018.
- [167] T. Sanchez, D. Needleman, and C. Racowsky, “Metabolic imaging to assess mitochondrial function in human embryos cultured in low versus ultra-low oxygen tension,” *Fertility and Sterility*, vol. 108, p. e59, Sept. 2017.
- [168] J. Phipps, Y. Sun, R. Saroufeem, N. Hatami, and L. Marcu, “Fluorescence lifetime imaging microscopy for the characterization of atherosclerotic plaques,” *Proceedings of SPIE—the International Society for Optical Engineering*, vol. 7161, 2009.
- [169] D. Elson, J. Requejo-Isidro, I. Munro, F. Reavell, J. Siegel, K. Suhling, P. Tadrous, R. Benninger, P. Lanigan, J. McGinty, C. Talbot, B. Treanor, S. Webb, A. Sandison, A. Wallace, D. Davis, J. Lever, M. Neil, D. Phillips, G. Stamp, and P. French, “Time-domain fluorescence lifetime imaging applied to biological tissue,” *Photochemical & Photobiological Sciences*, vol. 3, no. 8, p. 795, 2004.
- [170] L. Marcu, “Fluorescence Lifetime Techniques in Medical Applications,” *Annals of Biomedical Engineering*, vol. 40, pp. 304–331, Feb. 2012.
- [171] M. Eibl, S. Karpf, D. Weng, H. Hakert, T. Pfeiffer, J. P. Kolb, and R. Huber, “Single pulse two photon fluorescence lifetime imaging (SP-FLIM) with MHz pixel rate,” *Biomedical Optics Express*, vol. 8, pp. 3132–3142, June 2017.
- [172] D.-H. Lee, X. Li, N. Ma, M. A. Digman, and A. P. Lee, “Rapid and label-free identification of single leukemia cells from blood in a high-density microfluidic trapping array by fluorescence lifetime imaging microscopy,” *Lab on a Chip*, vol. 18, pp. 1349–1358, May 2018.
- [173] R. Hartig, Y. Prokazov, E. Turbin, and W. Zusratter, “Wide-Field Fluorescence Lifetime Imaging with Multi-anode Detectors,” in *Fluorescence Spectroscopy and Microscopy: Methods and Protocols* (Y. Engelborghs and A. J. Visser, eds.), Methods in Molecular Biology, pp. 457–480, Totowa, NJ: Humana Press, 2014.
- [174] V. I. Shcheslavskiy, M. V. Shirmanova, V. V. Dudenkova, K. A. Lukyanov, A. I. Gavrina, A. V. Shumilova, E. Zagaynova, and W. Becker, “Fluorescence time-resolved macroimaging,” *Optics Letters*, vol. 43, pp. 3152–3155, July 2018.

- 
- [175] T. Hinsdale, C. Olsovsky, J. J. Rico-Jimenez, K. C. Maitland, J. A. Jo, and B. H. Malik, "Optically sectioned wide-field fluorescence lifetime imaging microscopy enabled by structured illumination," *Biomedical Optics Express*, vol. 8, pp. 1455–1465, Feb. 2017.
- [176] T. Funane, S. S. Hou, K. M. Zoltowska, S. J. van Veluw, O. Berezovska, A. T. N. Kumar, and B. J. Bacsikai, "Selective plane illumination microscopy (SPIM) with time-domain fluorescence lifetime imaging microscopy (FLIM) for volumetric measurement of cleared mouse brain samples," *Review of Scientific Instruments*, vol. 89, May 2018.
- [177] C. A. Mitchell, S. P. Poland, J. Seyforth, J. Nedbal, T. Gelot, T. Huq, G. Holst, R. D. Knight, and S. M. Ameer-Beg, "Functional in vivo imaging using fluorescence lifetime light-sheet microscopy," *Optics Letters*, vol. 42, pp. 1269–1272, Apr. 2017.
- [178] H. Sparks, S. Warren, J. Guedes, N. Yoshida, T. C. Charn, N. Guerra, T. Tatla, C. Dunsby, and P. French, "A flexible wide-field FLIM endoscope utilising blue excitation light for label-free contrast of tissue," *Journal of Biophotonics*, vol. 8, pp. 168–178, Jan. 2015.
- [179] J. Bec, J. E. Phipps, D. Gorpas, D. Ma, H. Fatakdawala, K. B. Margulies, J. A. Southard, and L. Marcu, "In vivo label-free structural and biochemical imaging of coronary arteries using an integrated ultrasound and multispectral fluorescence lifetime catheter system," *Scientific Reports*, vol. 7, Aug. 2017.
- [180] M. Zhao, Y. Li, and L. Peng, "Parallel excitation-emission multiplexed fluorescence lifetime confocal microscopy for live cell imaging," *Optics Express*, vol. 22, pp. 10221–10232, Apr. 2014.
- [181] L. Aguilar-Arnal, S. Ranjit, C. Stringari, R. Orozco-Solis, E. Gratton, and P. Sassone-Corsi, "Spatial dynamics of SIRT1 and the subnuclear distribution of NADH species," *Proceedings of the National Academy of Sciences of the United States of America*, vol. 113, pp. 12715–12720, Nov. 2016.
- [182] S. Sameni, A. Syed, J. L. Marsh, and M. A. Digman, "The phasor-FLIM fingerprints reveal shifts from OXPHOS to enhanced glycolysis in Huntington Disease," *Scientific Reports*, vol. 6, Oct. 2016.
- [183] A. J. Bower, M. Marjanovic, Y. Zhao, J. Li, E. J. Chaney, and S. A. Boppart, "Label-free in vivo cellular-level detection and imaging of apoptosis," *Journal of biophotonics*, vol. 10, pp. 143–150, Jan. 2017.
- [184] R. Cao, P. Jenkins, W. Peria, B. Sands, M. Naivar, R. Brent, and J. P. Houston, "Phasor plotting with frequency-domain flow cytometry," *Optics Express*, vol. 24, pp. 14596–14607, June 2016.

- [185] C. García, A. Losada, M. A. Sacristán, J. F. Martínez-Leal, C. M. Galmarini, and M. P. Lillo, “Dynamic cellular maps of molecular species: Application to drug-target interactions,” *Scientific Reports*, vol. 8, Jan. 2018.
- [186] S. R. Alam, H. Wallrabe, Z. Svindrych, A. K. Chaudhary, K. G. Christopher, D. Chandra, and A. Periasamy, “Investigation of Mitochondrial Metabolic Response to Doxorubicin in Prostate Cancer Cells: An NADH, FAD and Tryptophan FLIM Assay,” *Scientific Reports*, vol. 7, Sept. 2017.
- [187] H. S. Nam, W. J. Kang, M. W. Lee, J. W. Song, J. W. Kim, W.-Y. Oh, and H. Yoo, “Multispectral analog-mean-delay fluorescence lifetime imaging combined with optical coherence tomography,” *Biomedical Optics Express*, vol. 9, pp. 1930–1947, Mar. 2018.
- [188] S. Ranjit, A. Dvornikov, E. Dobrinskikh, X. Wang, Y. Luo, M. Levi, and E. Gratton, “Measuring the effect of a Western diet on liver tissue architecture by FLIM autofluorescence and harmonic generation microscopy,” *Biomedical Optics Express*, vol. 8, pp. 3143–3154, June 2017.
- [189] A. Alfonso-Garcia, J. Shklover, B. E. Sherlock, A. Panitch, L. G. Griffiths, and L. Marcu, “Fiber-based fluorescence lifetime imaging of recellularization processes on vascular tissue constructs,” *Journal of Biophotonics*, vol. 11, p. e201700391, Sept. 2018.
- [190] M. N. Pastore, H. Studier, C. S. Bonder, and M. S. Roberts, “Non-invasive metabolic imaging of melanoma progression,” *Experimental Dermatology*, vol. 26, pp. 607–614, July 2017.
- [191] J. Li, A. J. Bower, Z. Arp, E. J. Olson, C. Holland, E. J. Chaney, M. Marjanovic, P. Pande, A. Alex, and S. A. Boppart, “Investigating the healing mechanisms of an angiogenesis-promoting topical treatment for diabetic wounds using multimodal microscopy,” *Journal of Biophotonics*, vol. 11, p. e201700195, Mar. 2018.
- [192] H. Wang, X. Liang, Y. H. Mohammed, J. A. Thomas, K. R. Bridle, C. A. Thorling, J. E. Grice, Z. P. Xu, X. Liu, D. H. G. Crawford, and M. S. Roberts, “Real-time histology in liver disease using multiphoton microscopy with fluorescence lifetime imaging,” *Biomedical Optics Express*, vol. 6, pp. 780–792, Feb. 2015.

## Resume

Name: Michael Evers  
Birthdate: June 21st 1989  
Birthplace: Wismar, Germany  
Nationality: German  
Marital status: Single  
Email: Michaelevers@gmx.net  
Telephone: +1-857-204-3627



### Education

05/14-01/19 **University of Lübeck, Germany**  
Doctoral degree in Natural Sciences  
Focus on fluorescence lifetime imaging microscopy

12/11-02/14 **University of Lübeck, Germany**  
Master of Science in Medical Engineering Science  
Focus on laser tissue interaction

10/08-12/11 **University of Lübeck, Germany**  
Bachelor of Science in Medical Engineering Science  
Focus on biomedical optics and imaging

09/99-06/08 **Geschwister Scholl Gymnasium**  
(High School), Wismar  
German Abitur (A level)  
Main course: English, Mathematics

## Work and Research Experience

- 06/2016 – present      **Senior Research Technologist** at Cutaneous Biology Research Center, Massachusetts General Hospital, Harvard Medical School, Boston, MA, USA
- 02/14 – 06/16          **Graduate Research Assistant** at Cutaneous Biology Research Center, Massachusetts General Hospital, Harvard Medical School, Boston, MA, USA
- 05/13 – 11/13          **Non Employee Student** at Cutaneous Biology Research Center, Massachusetts General Hospital, Harvard Medical School, Boston, MA, USA
- 10/12 – 03/13          **Non Employee Student** at the Wellman Center for Photomedicine , Massachusetts General Hospital, Harvard Medical School, Boston, MA, USA
- 01/12 – 08/12          **Student Assistant** at the Institute for Software Engineering and Programming Languages, University of Lübeck, Germany
- 07/11 – 12/11          **Student Assistant** at the Institute of Biomedical Optics, University of Lübeck, Germany



# Publications and Presentations

## Publications

1. Kepp T., Droigk C., Casper M., Evers M., Huettmann G., Salma N., Manstein D., Heinrich M.P., Handels H., “Segmentation of several mouse skin layers in optical coherence tomography image data using deep convolutional neural networks”, Biomed Opt Express, Jun. 2019
2. Casper M., Schulz-Hildebrandt H., Evers M., Manstein D., Huettmann G., “Optimization-based vessel segmentation for robust quantification of capillary networks in skin with optical coherence tomography angiography” J Biomed Opt, Apr. 2019
3. Evers M., Salma, N., Osseiran S., Casper M., Birngruber R., Evans C. L., Manstein D., “Enhanced quantification of metabolic activity for individual adipocytes by label-free FLIM”, Sci Rep, no. 8, Jun. 2018.
4. Evers M., Ha M.L., Casper M., Welford D., Kositratna G., Birngruber R., Manstein D., “Assessment of skin lesions produced by focused, tunable, mid-infrared chalcogenide laser radiation”, Lasers Surg Med, Apr. 2018.
5. Kepp T., Droigk C., Casper M., Evers M., Salma N., Manstein D., Handels H., “Segmentation of subcutaneous fat within mouse skin in 3D OCT image data using random forests”, Proc. SPIE 10574, Medical Imaging 2018: Image Processing, Mar. 2018.
6. Kositratna G, Evers M, Sajjadi A, Manstein D., “Rapid fibrin plug formation within cutaneous ablative fractional CO2 laser lesions”, Lasers Surg Med. 48(2):125-32, Feb. 2016.

### Presentations

1. Evers M., Salma N., Birngruber R., Evans C.L., Manstein D., “Improved NADH fluorescence lifetime analysis: A label-free bioenergetic marker for assessment of wounds”, Presentation at ASLMS Laser2019, Denver, Colorado
2. Evers M., Salma N., Osseiran S., Casper M., Birngruber R., Evans C.L., Manstein D., “Phasor fluorescence lifetime microscopy of NADH to analyze metabolic activity of adipocytes”, Presentation at Photonics West SPIE 2018, San Francisco, California
3. Evers M., Salma N., Birngruber R., Evans C.L., Manstein D., “Label-free Analysis of dynamic metabolic Changes using FLIM”, Presentation at ASLMS Laser2017, San Diego, California
4. Evers M., Salma N., Birngruber R., Evans C.L., Manstein D., “A new and highly sensitive method of analyzing metabolic activity using fluorescence lifetime imaging microscopy of NADH”, Presentation at Photonics West SPIE 2017, San Francisco, California
5. Evers M., Salma N., Birngruber R., Evans C.L., Manstein D., “Real-time analysis of metabolic activity within adipocytes by fluorescence lifetime imaging microscopy”, Presentation at ASLMS Laser2015, Orlando, Florida
6. Evers M., Ha L., Welford D., Birngruber R., Manstein D., “Wavelength-dependence of fractional ablations in ex-vivo human skin using a tunable  $\text{Cr}^{2+}:\text{ZnSe}/\text{S}$  infrared laser”, Presentation at ASLMS Laser2014, Phoenix, Arizona
7. Evers M., Welford D., Manstein D., Birngruber R., “Mid-infrared laser spectroscopy using a tunable gain-switched  $\text{Cr}^{2+}:\text{ZnSe}$  laser”, Student Conference Medical Engineering Science 2013, Lübeck

## Acknowledgements

I would like to express my sincere gratitude to my mentors and advisors Prof. Reginald Birngruber and Prof. Dieter Manstein for giving me the opportunity to work on such an interesting and unique project. They always gave me encouragement and freedom to pursue this project in a self-determinant way allowing me to learn a lot. I'm thankful for Reginald's continuous help and support, and his immense knowledge and Dieter's enthusiasm and creativity towards science which was a great motivation for me.

Special thanks go to Prof. Conor Evans for making this project possible by trusting me and letting me use his equipment. Furthermore, he was always available to discuss my project, helping in interpreting the data and advice on experiments.

I would like to thank my colleague and friend Dr. Nunciada Salma for teaching and helping me with cell culture and sample preparation and for many great conversations.

A very special thanks goes to Malte Casper for being a true friend who is always supportive and encouraging, and for all the time we spend together which I absolutely enjoyed and am thankful for.

Many thanks to my colleagues Dr. Garuna Kositratna, Dr. Cuc Nguyen, Naja Meyer-Schell, Dr. Martin Jaspan, and Dr. David Welford for the great teamwork and for making everyday life in the lab more fun!

I also want to thank all the members of the Evans group for welcoming me into their lab and the nice atmosphere. Thanks go to Dr. Sam Osseiran and Joachim Api Pruessner for teaching me imaging and helping me with problems on the two-photon microscope.

Working in Boston together with all these experts was a wonderful experience which I am absolutely grateful for.

Finally, I thank all my friends and family, especially my sister Jule and my parents Birgit and Dieter for their constant love and support!